MOMENTUM-BASED BEAM AND PIPE THEORIES WITH APPLICATIONS TO OCEAN ENGINEERING

A Dissertation

by

SHANRAN TANG

Submitted to the Office of Graduate and Professional Studies of
Texas A&M University
in partial fulfillment of the requirements for the degree of

DOCTOR OF PHILOSOPHY

Chair of Committee,	Bert Sweetman
Committee Members,	Jeffrey Falzarano
	Richard Mercier
	Ping Wang
Head of Department,	Sharath Girimaji

May 2019

Major Subject: Ocean Engineering

ABSTRACT

Floating offshore wind turbines may be the most practical offshore wind energy technology for deep waters. The dynamics of floating wind turbine systems is highly complicated as they are subject to irregular winds and waves, and platform motions are coupled by gyroscopic effects of the whirling blades. Computing the blade vibration is particularly challenging. The blades are highly flexible and spin around a shaft on a moving tower, introducing large deformations and irregular non-inertial frames. Blade vibration, turbine spin, and platform motion each have distinctively different frequency range, resulting in a multi-scale problem. This study is motivated by solving vibration of blades on a floating offshore wind turbine, in which the underlying theory is the dynamics of arbitrarily-shaped beams having large deformations and overall motions.

Developments of two new fundamental dynamic theories are presented; a separation of displacements technique and a linearization method for small angles and small strains are proposed. A geometrically-exact nonlinear beam theory is developed based on conservation of momentum for application to arbitrarily-shaped beams having large deformations and overall motions. Coordinate transformations are used to derive the nonlinear inertial forces and moments and the nonlinear relationships between displacements and strains, enabling rigorous consideration of kinematic and geometric nonlinearities. A geometrically-exact nonlinear theory is subsequently developed for pipes conveying fluid. The derivation follows that of momentum-based beam theory: the dynamic effects of the fluid are included based on the total momentum balance of both the fluid and pipe. The fluid is viscous and is assumed to be incompressible and homogeneous. The resulting pipe theory addresses geometric and kinematic nonlinearities and inertial coupling effects. The separation of displacements technique combined with the linearization method enables nonlinear beam or pipe dynamics to be rigorously reduced to a series of piecewise-linear models.

The practical value of these theoretical developments is demonstrated through numerical implementation and examples. The finite volume method is conveniently used for discretization because the underlying theories are based on a conservation law. Two piecewise-linear dynamic solvers, each for beams and pipes, are shown to capture nonlinear dynamics using linear solutions without iteration at each time-step. Momentum-based beam theory combined with multibody momentum cloud method is applied to model the fully aero-hydro-servo-elastic coupling dynamics of floating wind turbine systems. The momentum-based theory for pipes conveying fluid is demonstrated through practical application to model a top-tensioned marine riser.

DEDICATION

To my mother, my father, and my grandmother.

ACKNOWLEDGMENTS

This dissertation is the main result of my research since I enrolled in Texas A&M University in 2013. I would like to express my sincerest gratitude to my advisor, Professor Bert Sweetman, for his constructive guidance and full confidence in me. This work would not have been possible without either the creative discussions with him or the insightful suggestions from him, both of which inspired me to explore scientific boundaries and to extend the limits on my capabilities.

Sincere thanks are expressed to Professor Richard Mercier, Professor Jeffrey Falzarano, and Dr. Ping Wang, for serving as my committee members during their busy schedule. I greatly appreciate their valuable advice on my research and constructive comments on this dissertation.

I would like to thank Professor Jun Zhang, Dr. Amanda Wood, Dr. Juan Horrillo, Dr. Jens Figlus, and Professor Marc Perlin for their help and support during my study in the Department of Ocean Engineering. I would also like to thank my friends, Yujiao Sun, Shu Dai, Ju Gao, Changqun Zhang, Dapeng Li, Chengxue Li, He Yang, Chenrui Qu, Dr. Wei Cheng, and Dr. Lili Qu for helping me in my personal life. Last but not least, I would like to thank my family for their consistent encouragement that motivated me to finish this study.

CONTRIBUTORS AND FUNDING SOURCES

Contributors

This work was supported by a dissertation committee consisting of Professor Bert Sweetman and Professor Jeffrey Falzarano of the Department of Ocean Engineering, Professor Richard Mericer of the Zachry Department of Civil Engineering, and Assistant Professor Ping Wang of the Department of Maritime Administration.

All the work conducted for the dissertation was completed by the student independently.

Funding Sources

Graduate study was supported by a graduate teaching assistantship from Texas A&M University and Summer Graduate Student Support from the Texas Institute of Oceanography.

TABLE OF CONTENTS

Page

ABSTRACT ii

DEDICATION iv

ACKNOWLEDGMENTS v

CONTRIBUTORS AND FUNDING SOURCES vi

TABLE OF CONTENTS vii

LIST OF FIGURES x

LIST OF TABLES xii

1. INTRODUCTION AND LITERATURE REVIEW 1

  1.1 Background and Motivation 1
  1.2 Literature Review 5
    1.2.1 Beam Theories 5
    1.2.2 Pipes Conveying Fluid 9
    1.2.3 Floating Offshore Wind Turbines 11
  1.3 Main Contributions 13
  1.4 Organization of Dissertation 15

2. MOMENTUM-BASED BEAM THEORY 17

  2.1 Introduction 17
  2.2 Governing Equations 18
    2.2.1 Coordinate Systems 18
    2.2.2 Displacements and Kinematics 19
    2.2.3 Momentum Balance 21
    2.2.4 Strain Measures and Internal Forces and Moments 22
    2.2.5 Equations of Motion 25
    2.2.6 Relation to Existing GEBT 26
  2.3 Linearization, Simplification, and Discretization 28
    2.3.1 Linearized MBBT 28
    2.3.2 Simplifications for Practical Engineering Cases 31
      2.3.2.1 Beams in Inertial Frames 31
      2.3.2.2 Straight Beams without Initial Curve or Twist 31
      2.3.2.3 2D Beams Having Negligible Axial Deformation 32

2.3.3 Spatial Discretization 33
2.4 Piecewise-linear MBBT 36
2.4.1 Theory 36
2.4.2 Discretized Matrix Formulation 40
2.4.3 Implementation 45
2.5 Numerical Examples 46
2.5.1 Convergence and Order of Accuracy 47
2.5.2 Initially-curved Beam 50
2.5.3 Rotating Straight Beam 51
2.5.4 Initially-twisted Wind Turbine Blade 52
2.6 Conclusions 55

3. MOMENTUM-BASED THEORY FOR PIPES CONVEYING FLUID 56

3.1 Introduction 56
3.2 Governing Equations 57
3.2.1 Assumptions 57
3.2.2 Coordinate Systems 57
3.2.3 Displacements and Kinematics 58
3.2.4 Strain Measures and Elastic Forces and Moments 59
3.2.5 Flow Model 61
3.2.6 Momentum Balance 64
3.3 Separation of Displacements and Linearization 66
3.3.1 Separation of Displacements 67
3.3.2 Piecewise Linearization 70
3.4 Numerical Implementation 73
3.4.1 Finite Volume Discretization 73
3.4.2 Evolving Base Configuration 75
3.4.3 Boundary Conditions and Assembled System 77
3.5 Numerical Examples 78
3.5.1 Rotating Cantilever Pipe 79
3.5.2 Semi-circular Curved Pipe 80
3.5.3 Top-tensioned Riser 82
3.6 Conclusions 87

4. NONLINEAR COUPLED DYNAMICS OF FLOATING OFFSHORE WIND TURBINES 88

4.1 Introduction 88
4.2 Nonlinear FOWT Systems 89
4.3 Nonlinear Blade Dynamics 90
4.4 Dynamic Coupling 91
4.4.1 Rigid-flexible-body Coupling 91
4.4.2 Computational Method 92
4.5 Simulations 93
4.5.1 Structure Configurations 93
4.5.2 Environmental Conditions 95

4.5.3 Validation Test 95
4.5.4 Simulation Cases 96
4.6 Results and Discussion 98
4.6.1 Highly-compliant FOWT 98
4.6.2 Control-induced Platform Oscillations 101
4.6.3 Imbalanced Aerodynamic Loads 101
4.6.4 Coupled Dynamics 104
4.6.5 Fatigue Loading Comparison 106
4.7 Conclusions 108

5. SUMMARY 109

5.1 Conclusions 109
5.2 Future Work 110

REFERENCES 112

APPENDIX A. ELASTIC STIFFNESS MATRICES OF A BASE CONFIGURATION 129

LIST OF FIGURES

FIGURE Page

1.1 Nonlinearities of beam dynamics. 3

1.2 Coupling framework used in FOWT simulation. 15

2.1 Coordinate systems of a beam. 19

2.2 Linear strain of a beam. 23

2.3 The nth beam finite control volume. 34

2.4 Base configuration and coordinate systems of a beam. 38

2.5 Change of root-mean-square error with element size. 48

2.6 The cantilever beam subject to tip moment. 49

2.7 $45°$-curved cantilever beam. 50

2.8 The cantilever beam subject to static and dynamic loads and rotation. 52

2.9 Time-histories of blade tip displacements. 54

2.10 Time-histories of blade root bending moments. 54

3.1 Coordinate systems of a pipe. 58

3.2 Linear strain of a pipe. 61

3.3 Base configuration and coordinate systems of a pipe. 68

3.4 The nth pipe finite control volume. 75

3.5 Rotating cantilever pipe conveying fluid. 79

3.6 Static deformation of rotating cantilever pipe conveying fluid. 81

3.7 Semi-circular curved pipe conveying fluid. 81

3.8 In-plane deformation of rotating semi-circular pipe conveying fluid. 83

3.9 Out-of-plane deformation of rotating semi-circular pipe conveying fluid. 83

3.10 Top-tensioned riser. 84

3.11 Riser deformations at various time-steps. 86

3.12 Maximum bending moments along the riser. 86

4.1 Nonlinearities associated with FOWT systems. 90

4.2 Coupling framework. 93

4.3 120-m spar design and 74-m truncated spar design. 94

4.4 Directions of motions. 96

4.5 Platform motions in validation tests. 97

4.6 Blade responses and reactions in validation tests. 97

4.7 Turbine performance of 74-m spar in the typical operational condition. 99

4.8 Platform motions of 74-m spar in the typical operational condition. 99

4.9 120-m spar and 74-m spar in the extreme operational condition. 100

4.10 Platform motions of 120-m spar in the typical operational condition. 102

4.11 Turbine performance of 120-m spar in the typical operational condition. 102

4.12 PSD's of 74-m spar in the typical operational condition. 103

4.13 Comparison of resultant aerodynamic yaw moment. 104

4.14 PSD's of the blade POM's for 120-m spar in the typical operational condition. 106

4.15 PSD of the first blade POM for 74-m spar in the typical operational condition. 106

LIST OF TABLES

TABLE Page

2.1 Convergence analysis on time-step size. 49

2.2 Tip coordinates (x,y,z) of the deformed curved beam. 51

2.3 Comparisons of blade tip displacements. 53

3.1 Dimensionless frequencies, μ_ω, of a cantilever pipe. 80

3.2 Dimensionless frequencies, μ^*_ω, for in-plane vibration of a semi-circular pipe. 82

4.1 Blade models. 91

4.2 Simulation cases. 98

4.3 Short-term damage-equivalent loads. 108

1. INTRODUCTION AND LITERATURE REVIEW

This dissertation focuses on the development of a new geometrically-exact nonlinear beam theory and a sister theory for pipes conveying fluid, and on the application of these theories to ocean engineering structures, including floating offshore wind turbines and a top-tensioned marine riser. Euler-Bernoulli beam theory was developed centuries ago to model linear bending. Timoshenko improved the Euler-Bernoulli theory in the 1920s by including shear deformation and rotational inertia. These classical linear beam theories are not sufficient for nonlinear beam dynamics, and geometrically-exact beam theory was developed in the 1980s to address beam nonlinearities. Use of time-domain computer simulations has significantly increased since that time and many practical applications would benefit from coupling advanced simulation techniques with nonlinear beam models. Unfortunately, it is difficult to couple the pre-existing geometrically-exact beam formulations in inertial frames with multibody system models, and difficult to discretize these formulations for numerical implementation. The proposed new beam model has been formulated from the outset in non-inertial reference frames, which has enabled significant improvements over pre-existing beam theories. The new formulation enables both better compatibility with multibody models and easier numerical discretization. The background and motivation of this dissertation is presented in Section 1.1. Relevant historical literature about beam theories, theories for pipes conveying fluid, and floating offshore wind turbines, are reviewed in Section 1.2. The main contributions and the organization of this dissertation are summarized in Section 1.3 and 1.4, respectively.

1.1 Background and Motivation

Placing wind farms in the ocean has distinct advantages over onshore locations: availability of adequate space near the electricity consumption centers in populated coastal areas; desirable wind characteristics including higher wind velocities and steadier wind fields, and the possibility of building larger, more efficient turbines because of reduced public concern about noise and visual impact. However, development of offshore wind has been hindered by deep waters, which makes bottom-fixed structures prohibitively expensive. Floating offshore wind turbines (FOWT's) may be the most practical offshore wind energy technology for deep waters. The first commercial floating offshore wind farm, Hywind Scotland, was commissioned in October 2017, which consists five of the 6-MW spar-type FOWT's [1]. Development of FOWT system has become an intensive research field in recent years.

The dynamics of FOWT systems is highly complicated as they are subject to irregular and nonlinear loads induced by both winds and waves, and global rotational motions of floating platforms are coupled by gyroscopic effects of the whirling blades. Blade vibration, turbine spin, and platform motion each have distinctively different frequency range, resulting in a multi-scale problem. Computing the coupled dynamics between turbine blade vibration and floating platform motions is particularly challenging because blades spin around a shaft at the top of a moving tower, introducing irregular non-inertial frames. The system dynamics becomes more challenging for the more advanced FOWT designs. Increasing turbine size leads to longer, slender, and more flexible blades that are subject to large deformations. Highly-compliant floating platform designs are proposed for FOWT to reduce manufacture and installation costs [2, 3, 4], but these lower-cost floating platforms are subject to large angular motions. Wang and Sweetman develop the momentum cloud method for multibody systems and apply it to FOWT's, in which a FOWT is modeled as three rigid bodies [5] or six rigid bodies [6]. The existing in-house momentum cloud method code for FOWT solves the equations of motion expressed in terms of sequenced Euler angles, such that the code does not rely on small angular displacement assumptions. That code is directly applicable to highly-compliant FOWT's, but in the work by Sweetman and Wang the blades are modeled as rigid bodies.

The present work develops new theory directly applicable to computing the dynamics of the blades on FOWT's. These blades are flexible slender structures and the dynamics of the blades present unique technical challenges: turbine blades have complicated 3-dimensional (3D) geometry including irregular cross-sections and structural twist along the axial direction; the blades are heavily loaded by aerodynamic loads and gravity inducing large deformations, and they are also

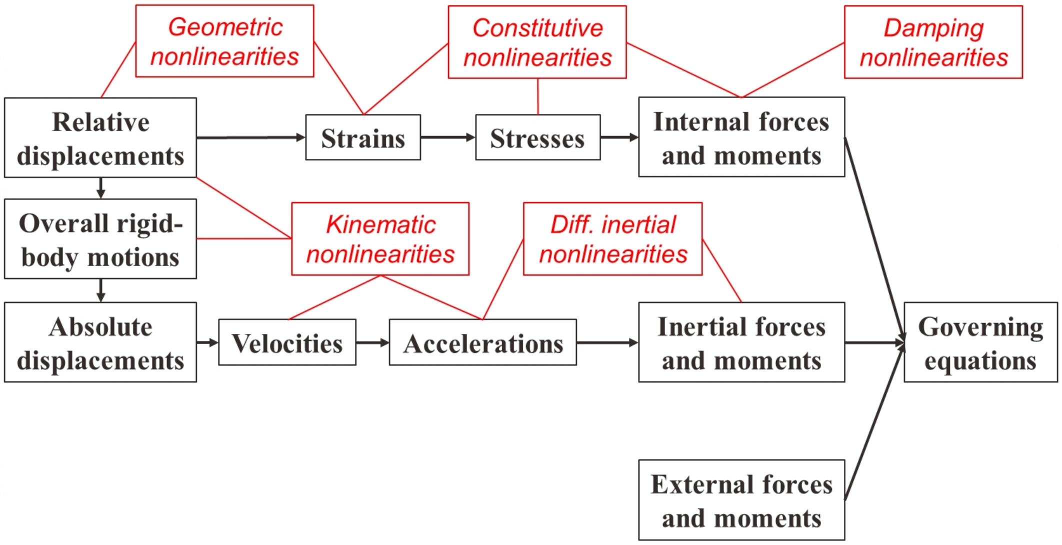

Figure 1.1: Nonlinearities of beam dynamics.

subject to complicated overall motions resulting from turbine spin and platform motions, introducing non-inertial frames. The underlying theory for such blade structures is the nonlinear dynamics of arbitrarily-shaped beams having large deformation and overall motions.

There are several types of nonlinearities inherently associated with beam dynamics (Fig. 1.1): (a) geometric nonlinearities are nonlinear relationships between displacements and strains, which are induced by large deformations and cause geometric stiffening [7, 8]; (b) constitutive nonlinearities are nonlinear relationships between stress and strain resulting from material properties, or nonlinear relationships between stress and resultant forces and moments resulting from geometric deformations; (c) kinematic nonlinearities are nonlinear relationships among displacements, velocities, and accelerations that are associated with overall rotations and/or angular deformations, such as centrifugal and Coriolis effects; (d) differential inertial nonlinearities occur when mass properties of differential cross-sectional elements measured in local coordinates, such as moment of inertia per unit length, depend on cross-sectional deformations; non-differential changes to the mass moment of inertia associated with global beam deformations are included in kinematic nonlinearities; (e) various nonlinear structural damping effects also exist.

Modeling of FOWT blades as beam structures poses significant challenges because these irregularly-shaped blades are subject to large deformations, geometric stiffening, global rotations, and irregular motions with the floating platform. Inclusion of geometric and kinematic nonlinearities is important for accurate modeling of FOWT blades. Constitutive equations used in beam theories are commonly obtained from a separate cross-sectional analysis, including effects of irregular cross-sections and composite materials. It is reasonable to treat mass properties of differential cross-sectional elements of relatively stiff beams as constants. Therefore, differential inertial nonlinearities are commonly negligible for the blades, while still preserving nonlinear inertial forces and moments associated with kinematic nonlinearities.

Linear Euler-Bernoulli beam theory has been employed in early blade solvers, but important effects of structural coupling and large deflections were neglected in those models. A combined multibody and linear Timoshenko beam element representation has been used to model wind turbine blades as well, in which individual blade elements are considered as deformable bodies represented by linear finite elements (FE's). Nonlinear beam dynamic theories, such as geometrically-exact beam theory (GEBT), have been applied with some success. Kim et al. [9] and Zhao and Wu [10] apply geometrically-exact theories to 3D beams having simple planar rotation. Application of GEBT to beams having large deformations and general overall motions is found in a few studies: Hodges [11, 12] presents a GEBT formulation similar to the one proposed by Simo and Vu-Quoc [13], in which dynamic quantities are referred to inertial frames in both formulations.

GEBT can properly address the geometric and kinematic nonlinearities and inertial effects of blades having large deformations and overall motions. However, applying GEBT to FOWT blades is rather difficult. First, the existing GEBT formulations are developed in inertial reference frames such that the overall rigid-body motions are implicitly coupled with local deformations in the governing equations, which makes these formulations difficult to combine with a multibody representation of a complete FOWT system. Second, the application of numerical methods to GEBT is complicated because interpolation of rotations requires special treatment to address the nonlinear character of 3D finite rotations [14, 15, 16, 17]. The conventional FE method interpolates a continuous quantity between nodes as a sum of shape functions, which is not directly applicable to 3D finite rotations because most rotation parameterizations are non-additive quantities. Numerical implementation of the existing GEBT becomes even more complicated when beams undergo large overall motions. The overall motion of an undeformed beam and the rigid-body motion of each deformed element both need to be considered carefully to ensure strain remains invariant to rigid-body motions [18]. The overall rigid-body rotation and the local deformation rotation are also not directly additive. The new beam theory developed in this work is geometrically-exact and overcomes the shortcomings of the existing formulations. The new formulation is developed in a non-inertial frame with dynamic quantities referred to the moving frame. Overall rigid-body motions are explicitly included to enable direct coupling with multibody system models, which is critical for application to FOWT blades because multibody solvers are commonly used to solve the FOWT system motions. The new formulation in non-inertial frames combined with new techniques also allows straightforward application of finite discretization to beam models.

Many other flexible slender structures in ocean engineering are subject to large deformations and overall motions, such as floating pipelines and marine risers. Many theories have been previously developed to compute dynamic behaviors of flexible pipes conveying fluid, many of which are expansions of beam models to include internal flow, but no geometrically-exact theory for pipes conveying fluid has been derived. This work also presents the development of the first geometrically-exact nonlinear dynamic theory for pipe-fluid system, including large deformations and overall motions.

1.2 Literature Review

1.2.1 Beam Theories

Beam theories are used to reduce 3D slender structures to one-dimensional (1D) beam models. The Euler-Bernoulli beam theory was developed in the mid 18th century and continues to be widely used today. Timoshenko improves the Euler-Bernoulli beam theory by including the effects of shear deformation and rotational inertia. These classical beam theories are inadequate to properly address nonlinear behaviors of some beam structures. Nonlinear strain measures are used with classical beam theories in order to partially address geometric nonlinearities, yet this approach relies on the same fundamental assumptions made in the Euler or Timoshenko theories.

Modern beam theories are developed to address beam nonlinearities. GEBT is a class of nonlinear beam theories [19, 20], which allows for nonlinear displacement-strain relationships and nonlinear beam kinematics. Reissner [21] derives the nonlinear strain measures using the principle of virtual work for static two-dimensional (2D) beams. Reissner [22, 23] extends the derivation from a 2D plane to a 3D space to develop a large-displacement static theory for space-curved beams. Simo [24] and Simo and Vu-Quoc [25] derive nonlinear kinematics and strain measures for beams in a 3D space and propose a geometrically-exact dynamic beam theory. Simo and Vu-Quoc [26] further develop the theory to include shear and torsion-warping deformations. Bauchau and Hong [27, 28] develop a small-strain nonlinear beam model in which cross-sections do not deform in their planes while St. Venant warping functions are used for out-of-plane deformations. Danielson and Hodges [29] derive a nonlinear displacement-strain relationship for curved and twisted beams with large displacements and rotations, and significantly simplify the strain measures based on small-strain and small-local-rotation assumptions. Danielson and Hodges [30] further develop this work into a static nonlinear beam theory for moderate local rotation. Hodges [11] derives a mixed-form intrinsic formulation of GEBT by extending the static theory to dynamic cases using a variational calculus approach to apply Hamilton's principle. Other GEBT formulations also exist: Bauchau and Hong [28] establish a displacement-based formulation; Zupan and Saje [31] and Su and Cesnik [32] establish a strain-based formulation.

Constitutive relationships play an important role in nonlinear beam theories. Deriving constitutive equations from strain energy functions is a widely used approach in early work [24, 11, 26]. Using a separate cross-sectional analysis to reduce dimensions (3D body to 1D beam) and to derive constitutive equations are more popular in the recent literature, especially for composite beams. Variational asymptotic beam sectional analysis (VABS) is proposed in which the variational asymptotic method is used to evaluate the constitutive properties of cross-sections [33, 34, 35, 36, 37]. Cross-sections are modeled using 2D FE's in VABS such that a 3D geometrically nonlinear analysis for slender structures is split into a 2D cross-sectional analysis and a 1D nonlinear beam analysis. Recent studies on composite wind turbine blades [38, 39] show that VABS is sufficient to provide cross-sectional constitutive matrices including effects such as cross-section warping, irregular shape, and varying properties of composite materials. Additional assumptions may be applied in cross-sectional analyses depending on how the constitutive equations are derived: different material models can be assumed with different strain energy functions, and certain cross-sectional strains or warping measures often are assumed to be small.

Flexible beam structures having large overall motions are found in many engineering applications, such as wind turbine blades, satellite antennas, and robotic arms. Many recent studies of beam dynamics address coupling effects between overall beam motion and local beam deformation. Vibration of simply rotating beams has been extensively investigated, including application of classical beam theories and nonlinear strains in many studies [40, 41, 42, 43, 44, 45, 46]. Simo and Vu-Quoc [47, 48] apply GEBT to planar beams having large deformations and simple rotations. Kim et al. [9] and Zhao and Wu [10] apply similar geometrically-exact theories to 3D beams having planar rotations. Dynamics of 3D beams undergoing general overall motions also has been studied, including application of classical beam theories [49, 50, 51, 52]; these formulations generally neglect some of the effects of structure coupling and large deformations. Application of GEBT to 3D beams having large deformations and general overall motions is found in a few studies, e.g., Simo and Vu-Quoc [13] and Hodges [11, 12]. Hodges [12] presents an inertial frame formulation similar to the one proposed by Simo and Vu-Quoc [13]: dynamic quantities are relative to inertial frames in both GEBT formulations.

Implementation of modern nonlinear beam theories relies on numerical methods, most commonly the FE method. The conventional FE method interpolates a continuous quantity between nodes as a sum of shape functions, which is not directly applicable to 3D finite rotations as most rotation parameterizations are non-additive quantities. Application of the FE method to GEBT is complicated: interpolation of rotations requires special treatment to address the nonlinear character of 3D finite rotations [14, 15, 16, 17]. Strain-based and intrinsic formulations of GEBT are employed to allow application of FE interpolation to additive quantities [53, 54], in which rotations are not interpolated as primary valuables but are reconstructed through other quantities. Numerical implementation becomes even more complicated for beams undergoing large general overall motions. The overall rigid-body rotation of an undeformed beam and the local rigid-body rotation of each deformed element are not directly additive, and both need to be considered carefully to ensure strain is invariant with rigid-body motion [18]. Removal of rigid-body rotation prior to numerical interpolation is proposed by Wang et al. [55]; the rigid-body rotation is then restored after interpolation to establish the governing equations in a inertial frame.

Several numerical methods are developed for moving beams in the context of flexible multibody dynamics [56]: (a) the floating frame method, (b) the incremental FE approach, (c) the finite segment method, (d) the large rotation vector method, and (e) the absolute nodal coordinate approach. The floating frame method includes two sets of coordinates: one set is the intermediate floating frame that describes the rigid-body motion of a beam; the other set describes the local deformations in the floating frame. Local deformations are usually solved using classical beam theories because the formulation of a modern nonlinear beam theory in an intermediate non-inertial frame is not commonly available [49, 50]. The incremental FE approach is based on convected coordinate systems in which individual beam elements are considered as deformable multibodies. The finite segment method differs from the incremental FE approach in that beam segments are assumed as rigid multibodies connected by springs and/or dampers. Both the incremental FE method and the finite segment method make use of multibody dynamic theories to compute the body motion of each beam element [57, 58]. The large rotation vector method is equivalent to application of the FE method to nonlinear beam theories in inertial frames, which requires special interpolation of finite rotations [14, 15, 59]. The absolute nodal coordinate approach differs from the large rotation vector method in that the rotational variables are eliminated from the formulation: higher-order global shape functions are used to interpolate absolute translational displacements only, such that rotations are included implicitly [60, 61, 62].

1.2.2 Pipes Conveying Fluid

Pipes conveying fluid are widely used in many industries and have been studied extensively for decades. Numerous studies have been well documented in review papers [63, 64, 65, 66, 67] and books [68, 69]. Both beam and shell models have been used to describe the static and dynamic behaviors of pipes conveying fluid. Beam models are generally applied to slender pipes having relatively thick walls, which are suitable for the most engineering applications. The present work extends the new momentum-based beam model to include dynamic fluid effects.

Linear theories based on Euler-Bernoulli or Timoshenko beams are well established and have been applied to pipes conveying fluid; recent studies focus on more advanced theories for pipe structures. Semler et al. [70], Stangl et al. [71], and Ghayesh et al. [72] apply Euler-Bernoulli beam theory to straight pipes with nonlinear axial strains in order to account for foreshortening in the axial direction caused by lateral displacements. Wadham-Gagnon et al. [73] develop a 3D model for straight cantilever pipes conveying fluid similarly based on Euler-Bernoulli beam theory plus nonlinear axial strains; the model is expanded to include intermediate spring supports [74, 75] and tip-mass [76, 77, 78]. Pipe structures having various boundary conditions and supporting constraints are shown to have significantly different dynamic behaviors and stability characteristics [79, 80]; Kheiri et al. [81] and Zhang et al. [82] derive pipe models that directly incorporate general elastic boundary conditions in the governing equations.

Pipeline curvature should be properly considered in displacement-strain relationships and system kinematics for initially-curved pipes or highly-flexible large-displacement pipes. Misra et al. [83, 84] develop linear inextensible and extensible models for curved pipes including initial curvatures. Dupuis and Rousselet [85, 86] derive a nonlinear extensible model for curved pipes based on Timoshenko beam theory and partially include the geometric and kinematic nonlinearities with infinitesimal strain theory. Jung and Chung [87] model a semi-circular pipe conveying fluid as a curved Euler-Bernoulli beam with an extensible centerline using the Lagrange strain theory. Various methods are used to simulate the dynamic motions of curved pipes conveying fluid, including the transfer matrix method [88], the differential quadrature method [89], and the isogeometric analysis [90]. A 3D nonlinear beam model recently has been developed for highly-flexible pipes conveying fluid and compared with experimental results [91, 92].

Pipes conveying fluid subject to overall motions are common, including hydraulic lines on aircraft or heavy machinery, onshore pipelines impacted by earthquakes, and offshore pipelines moving with vessels or floating platforms. The inertial loads associated with internal flow and inertial coupling between overall rigid-body motions and the pipe deformations can significantly affect the dynamic response of these structures. Studies of inertial effects for pipes conveying fluid are less common. [93, 94] study rotating cantilever pipes conveying fluid based on Euler-Bernoulli beam theory. [95] develop a 3D nonlinear model for straight pipes conveying fluid that is similar to the one proposed by [73], but accounts for large translational overall motions using the Kane's method. [96] apply Euler-Bernoulli beam theory to the dynamic stability and responses of a 3D cantilever pipe subject to under base excitation at the fixed-end and having a tip-mass. Geometric and kinematic nonlinearities are often significant when a pipe structure: (a) is subject to non-negligible axial stresses and strains; (b) has a complicated 3D geometry; (c) is highly flexible or experiences large deformations, or (d) is subject overall motions translating or rotating in space. However, no geometrically-exact theory is believed to exist for pipes conveying fluid.

A separate group of studies addresses fluid-conveying pipe theories applicable to marine risers and offshore pipelines. Chucheepsakul and co-workers [97, 98, 99] propose 2D and 3D models for flexible marine risers, in which large nonlinear axial strains are considered while shear strains and rotational inertia are neglected as the underlying model is Euler-Bernoulli beam. Chatjigeorgiou [100, 101] develops a 3D nonlinear model for extensible catenary risers, in which the Euler angle formulations are used to represent large displacements and geometric and kinematic nonlinearities only for initially-straight pipes. Multi-phase flows including gas, fluids, and solids, are commonly found in offshore oil and gas applications. Some recent studies investigate the effects of multi-phase internal flow on pipe dynamics through physical experiments [102, 103, 104] and numerical modeling [105, 106, 107, 108]. The pipe structures in offshore applications are different from their onshore counterparts in environmental loads: current, wave, and vortex shedding all induce excitations to pipes. Special techniques, such as Morison's equation, are required to compute the environmental excitations [109, 110, 111, 112].

1.2.3 Floating Offshore Wind Turbines

Fully-coupled aero-hydro-servo-elastic modeling is necessary for complete analysis and design of FOWT systems. Detailed simulation of these highly nonlinear systems should ideally include aeroelastic effects of turbine blades, hydrostatic and hydrodynamic loads on the floating platform, control mechanism of the electromechanical/generator systems, structural dynamics of flexible components, inertial effects of the overall multibody system, and forcing of mooring system. Advanced analyses are applied to assess FOWT systems. Studies on rotating blades of bottom-fixed wind turbines show that blade vibration is critical for accurate estimation of aerodynamic loads, power output, and fatigue life [113, 114, 115, 116, 117, 118, 119]. Tran and Kim use computational fluid dynamics (CFD) simulation and a fluid-body interaction approach to analyze the aerodynamics and hydrodynamics of a moving FOWT, in which the FOWT is modeled as a rigid structure [120, 121, 122, 123]. Use of high-fidelity CFD simulation techniques has become increasingly popular for aerodynamic and hydrodynamic modeling in the recent years [124, 125, 126], but these techniques have mainly been applied to FOWT's that are assumed to be multi-rigid-body systems, because coupled simulation with structure flexibility and fluid interaction using CFD is extremely costly. Blade element momentum (BEM) and generalized dynamic wake (GDW) theories are commonly applied to aerodynamic modeling, and are available in existing FOWT software packages. Aero-hydro-coupled modeling is made possible by combing BEM or GDW aerodynamic models with conventional hydrodynamic methods used in oil and gas industry, such as Morison's equation or potential flow theory [127]. The National Renewable Energy Lab (NREL, USA) develops a fully-coupled package called "Fatigue, Aerodynamics, Structures, and Turbulence" (FAST), which uses a modular framework and employs small angular displacement assumptions in its solution to the governing equations and in its hydrodynamic module [128]. The International Energy Agency (IEA) has conducted several rounds of code-to-code comparisons for FOWT modeling. IEA has found the simulations to be reasonably accurate but also indicated specific areas for potential enhancements [129, 130, 131]. One of the identified potential improvements is dynamic modeling for FOWT blades [132, 133].

Highly-compliant floating platform designs are proposed for FOWT's to reduce manufacture and installation costs [2, 3, 4], but these platforms will be subject to large angular motions. Wang and Sweetman develop the momentum cloud method for multibody systems and apply it to highly-compliant FOWT's. The momentum cloud method (MCM) is based on applying the conservation of momentum directly to a multi-rigid-body system, and makes use of prescribed motions between each contiguous body [6]. The absolute translation of the center of mass of the system and the rotation of a base body within the system are chosen to be the reference coordinates. The relative rotations between the base body and contiguous bodies along the kinematic chain within the system are chosen to be relative coordinates, the effects of which are captured as a series of cascading transformation matrices. The final result is that the motion of an N-body system can be conveniently represented using six equations of motion (EOM's) that are updated at each time-step for the evolving configuration of the system. The solutions to three coupled rotational EOM's based on conservation of angular momentum of the system are Euler angles describing the rotation of the base body. The solutions to three coupled translational EOM's based on conservation of linear momentum of the system are the translation of the system measured at its center of mass, which are then transferred into translation of the base body. Additionally, inverse dynamic analysis can be used to obtain internal forcing between any two contiguous bodies. The advantage of MCM is that only six EOM's are to be solved as long as the relative motions between adjoining bodies are prescribed, regardless the complexity of the multibody system. An in-house multibody code has been developed using MCM. The resulting code has been applied to several FOWT models, each of which consists of two rigid bodies [2], three rigid bodies[5], or six rigid bodies [6]. This code does not rely on small angular displacement assumptions and it is applicable to highly-compliant FOWT's. Blades were modeled as rigid bodies in the pre-existing code.

FOWT blades are irregularly-shaped beam-like structures that are typically made of composite materials and that are subject to large deformations and overall motions. The composite materials used for the blades are generally treated as being anisotropic linear elastic. A separate 2D linear cross-sectional analysis is commonly employed to obtain constitutive matrices, in which structural coupling effects are included through the off-diagonal terms of the resulting constitutive matrices. Cross-sectional eccentricity generally exists because of the particular construction of the blades. Cross-sectional deformations of the blades are generally negligible, such that differential inertial nonlinearities can reasonably be neglected. FOWT blade dynamics are solved using linear Euler-Bernoulli beam model in the early blade codes, such as FLEX [134] and FAST ElastoDyn [135], neglecting the effects of structure coupling and large deflections. A combined multibody and linear Timoshenko beam element representation has been used to model blades in SIMPACK Wind [127], Blade [136], and HAWC2 [137], in which individual blade elements are considered as deformable bodies represented by linear finite elements. GEBT is first applied in BeamDyn, the latest blade module of FAST package [138], to compute the dynamics of wind turbine blades. Wiener-Milenković rotation parameters are used in BeamDyn to represent 3D rotations. Special treatments and complicated numerical techniques are used in BeamDyn: rigid-body rotation is removed before interpolation in each Legendre spectral finite element and is restored after interpolation to formulate the nonlinear governing equations in an inertial frame, which are solved using Newton–Raphson iterative method [55, 139].

1.3 Main Contributions

A geometrically-exact nonlinear beam theory is derived in this dissertation using a momentum-based approach, which is called momentum-based beam theory (MBBT). MBBT is a new formulation of GEBT that is derived in non-inertial reference frames such that the overall rigid-body motions of a beam are explicit in the governing equations, which makes the resulting formulation is readily compatible with multibody dynamic models. Coordinate transformation matrices are used throughout the derivation such that MBBT can be expressed in arbitrary coordinate systems, which enables the application of separation of displacements technique to establish general Lagrangian formulations with respect to arbitrary configurations. The derivation is based on conservation of momentum in vector form and the resulting EOM's retain intuitive physical significance, which allows rational linearization using practical engineering assumptions. The value of rational linearization is demonstrated by the development of several linearized and simplified versions of MBBT. A linearized updated Lagrangian formulation is achieved using a new separation of displacements technique and local linearization method based on small angles and small strains. The resulting formulation can effectively represent nonlinear beam dynamics using a series of piecewise-linear models, and can be solved using linear solutions without iteration at each time-step. The conventional linear FE or finite volume (FV) methods are directly applicable to the piecewise-linear beam models. The FV method is selected for use in this study. It is the most straightforward discretization method because the underlying beam theory is based on a conservation law.

A sister momentum-based theory for pipes conveying fluid is also developed as part of this dissertation. The new theory is the first dynamic theory for pipes conveying fluid that rigorously addresses geometric and kinematic nonlinearities of the pipe and inertial coupling effects between the pipe and fluid. The new theory is derived following the derivation methodology of MBBT. The dynamic effects of internal flow are included by summing the total momentum of both the fluid and pipe. The interactions between fluid and pipe wall, such as well pressure and wall friction, are implicitly included because internal effects do not affect the total momentum balance. The new pipe theory is formulated in non-inertial frames, similarly to MBBT, and addresses large deformations and overall motions, which makes it particularly suitable for ocean engineering applications, such as marine risers. Separation of displacements and local linearization techniques are similarly applied to the momentum-based theory for pipes conveying fluid to reduce the nonlinear dynamics to a series of piecewise-linear pipe models. The new theory is numerically implemented and demonstrated using the FV method.

The practical value of these two new theories are demonstrated through ocean engineering applications: MBBT is combined with MCM to model the fully-coupled FOWT systems, including a highly-compliant design; the momentum-based theory for pipes conveying fluid is applied to simulate a top-tensioned marine riser moving with a floating platform. A multi-scale weakly-coupled scheme is proposed for the coupled dynamic analyses of FOWT systems (Fig. 1.2), in

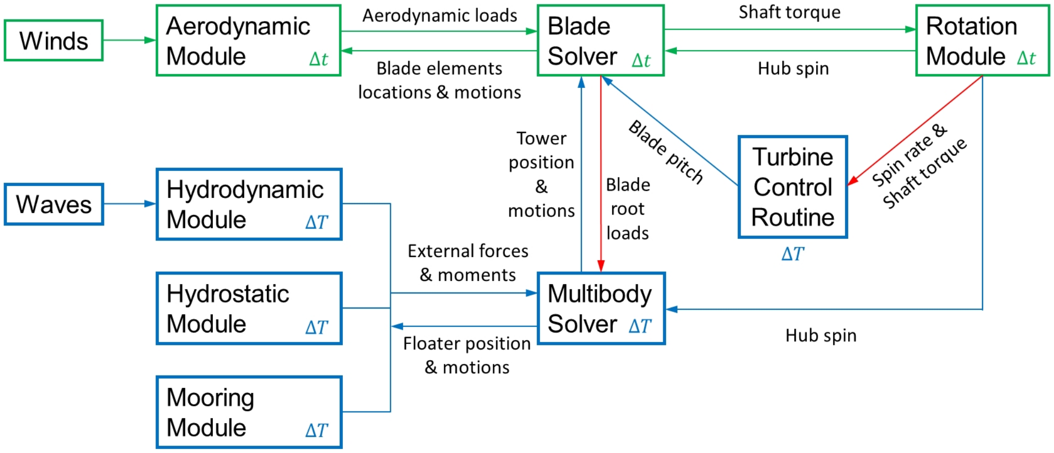

Figure 1.2: Coupling framework used in FOWT simulation.

which blade dynamics are computed using a smaller time-step size Δt and platform motions are computed using a larger time-step size ΔT. An advanced numerical simulation tool is developed for fully aero-hydro-servo-elastic-coupled simulations of FOWT's. Interesting dynamic behaviors are demonstrated in the simulations of FOWT's and the riser, enabling valuable insights into these ocean engineering systems.

1.4 Organization of Dissertation

The new MBBT is derived in Chapter 2. A set of coordinate systems are introduced for beam kinematics. Coordinate transformations and rotational displacements can be parameterized using any three-valuable finite rotation formulation. Nonlinear inertial forces and moments are derived based on conservation of momentum. The nonlinear relationships between displacements and strains are rigorously considered, enabling full consideration of geometric and kinematic nonlinearities. General nonlinear EOM's are first derived in a differential form, and then are simplified using practical engineering assumptions, including developments of a linearized model for small angles and small strains and a discretized model using the FV method. A separation of displacements technique is developed, which enables nonlinear beam dynamics to be rigorously reduced to a series of piecewise-linear models. The proposed model is unique amongst existing geometrically-exact beam formulations in that it is formulated using dynamic quantities relative to intermediate non-inertial coordinates, allowing general Lagrangian formulations to be established in floating frames with inertial coupling effects, which is compatible with multibody models. The theoretical developments is demonstrated through numerical implementation and convergence analyses.

The momentum-based theory for pipes conveying fluid is developed in Chapter 3. This nonlinear geometrically-exact theory is derived based on the total momentum balance of the fluid and pipe. The fluid is viscous and is assumed to be incompressible and homogeneous, and the varying fluid pressures along a pipe are considered. The fully nonlinear differential governing equations are derived in floating non-inertial frames, which rigorously account for geometric and kinematic nonlinearities and inertial coupling effects for pipes having large displacements and overall rigid-body motions. The separation of displacements technique combined with a small incremental displacement assumption are used to subsequently derive a linearized updated Lagrangian formulation, which allows large-displacement nonlinear dynamics to be rigorously reduced to a series of piecewise-linear models. The resulting time-stepping scheme is numerically implemented using the FV method. The effectiveness of these theoretical developments is demonstrated in several numerical examples, including a marine riser subject to top tension and forced motion.

Fully-coupled dynamic analyses for FOWT systems are presented in Chapter 4. The combination of the latest developments in nonlinear beam theory and multibody dynamics, MBBT and MCM, enables aero-hydro-servo-elastic-coupled analyses of FOWT's. MBBT that is formulated in floating non-inertial frames is particularly suitable for floating wind turbine applications. The MBBT nonlinear blade model is coupled with a multibody momentum cloud model through a multi-time-scale coupling scheme. The value of the proposed method is demonstrated through several numerical examples, including a highly-compliant FOWT design. Frequency-domain analysis and singular value decomposition are used in the coupled dynamic analyses. Key findings are discussed, including platform oscillations caused by blade pitch control, imbalance yaw moment caused by axial-asymmetric blade deflections, and the basic feasibility and potential fatigue loading on the blades of a complete highly-compliant FOWT design.

Conclusions and recommendations on future work are presented in Chapter 5.

2. MOMENTUM-BASED BEAM THEORY*

2.1 Introduction

The new beam theory presented in this chapter was originally motivated by the desire to model the dynamic response of blades on highly-compliant floating offshore wind turbines, in which the blades undergo planar rotation combined with complicated irregular large overall motions. The blades are also heavily loaded, such that nonlinearities are important in predicting the overall response. The specific objective of this chapter is to develop a new geometrically-exact model for arbitrarily-shaped beams having large deformations and large overall motions in non-inertial floating frames, and to verify this new theory through implementation of an effective numerical method that can be quantitatively compared with existing methods to compute nonlinear beam dynamics. The resulting momentum-based beam theory (MBBT) has been shown to rigorously include the effects of geometric and kinematic nonlinearities, and to include the inertial coupling effects introduced by floating frames. The new theory is different from other existing geometrically-exact beam theory (GEBT) formulations: it is formulated in a floating frame with dynamic quantities relative to the non-inertial frame, which enables the total Lagrangian formulation [140] to be established including inertial coupling effects. The resulting formulation explicitly includes overall rigid-body motion, which makes it readily compatible with multibody dynamic models. The derivation is based on conservation of momentum in vector form and use of coordinate transformation matrices. The resulting EOM's retain intuitive physical significance, which allows rational linearization using practical engineering assumptions. The value of the coordinate transformation and of rational linearization is demonstrated by the subsequent development of a separation of displacements technique and derivation of a linearized updated Lagrangian formulation. This chapter includes the complete derivation of MBBT and its further theoretical developments, as well as numerical implementation of these developments. MBBT is derived in Section 2.2, and is linearized, simpli-

---

*Reprinted with permission from "A geometrically-exact momentum-based non-linear theory applicable to beams in non-inertial frames" by Shanran Tang and Bert Sweetman, 2019. International Journal of Non-Linear Mechanics, Copyright [2019] by Elsevier .

fied, and discretized in Section 2.3. Separation of displacements and the resulting piecewise-linear MBBT are presented in Section 2.4, including linearization of the EOM's about a deformed configuration. A static and a dynamic MBBT numerical solver are each developed in Section 2.5, in which convergence analyses and several numerical examples are presented.

2.2 Governing Equations

MBBT is derived using two fundamental assumptions: (a) cross-sectional deformations are assumed to be small, such that cross-sectional mass properties, mass and mass moment of inertia per unit length, are constant in time, the result of which is that differential inertial nonlinearities are not considered; (b) the cross-sectional elastic forces and moments are functions of strain measures and/or time derivatives of strain measures, such that the constitutive relations do not introduce new unknowns to the system of governing equations. The derivation includes rigorous consideration of geometric and kinematic nonlinearities subject to these assumptions.

2.2.1 Coordinate Systems

The coordinate systems used in MBBT are presented in Fig. 2.1. An inertial Cartesian coordinate system, $\boldsymbol{XYZ}$, with origin O fixed to the earth, is denoted as global coordinate g. A non-inertial Cartesian coordinate, $\boldsymbol{xyz}$, is fixed to the undeformed beam at point W, and is defined as floating coordinate f. Translations and rotations of f relative to g represent the overall rigid-body motion of an undeformed beam. Curvilinear coordinate s is attached to the elastic axis of an undeformed, unstressed beam; another curvilinear coordinate S is similarly attached to the elastic axis of the deformed beam. Two sets of local coordinates are defined at each point along s and S. The non-inertial local undeformed coordinate l is fixed to elastic center P_0, and includes Cartesian coordinates $\boldsymbol{abc}$ with $\boldsymbol{b}$ and $\boldsymbol{c}$ on the cross-sectional plane and $\boldsymbol{a}$ tangent to the undeformed elastic axis s at P_0. Correspondingly, deformed local coordinate d includes Cartesian coordinates $\boldsymbol{ABC}$, with origin P fixed to the elastic center of the displaced cross-section. Deformed local coordinate d rotates with the cross-section such that $\boldsymbol{B}$ and $\boldsymbol{C}$ remain on the cross-sectional plane but $\boldsymbol{A}$ is not generally tangent to the deformed elastic axis S.

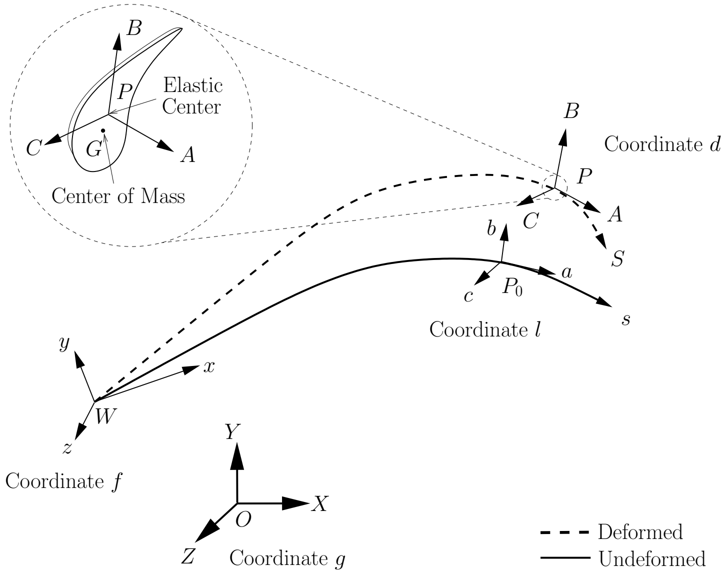

Figure 2.1: Coordinate systems of a beam.

2.2.2 Displacements and Kinematics

The absolute displacement measured in global coordinate g of any point along the beam can be expressed as a sum of two parts: the displacement resulting from a prescribed overall rigid-body motion of the undeformed beam, plus the unknown displacements resulting from the local beam deformation. The unknown displacements are measured in local undeformed coordinate l: translational displacements $u_i(s,t)$ are the components of a vector from P_0 to P resolved onto the $\boldsymbol{abc}$ coordinates; rotational displacements $\theta_i(s,t)$ are defined using three rotational variables that describe the 3D finite rotations from coordinate l to d, in which s is the location of P_0; t is time, and $i = 1, 2, 3$. Translational and rotational displacements can be expressed as 3D first-order tensors in vector form: $\boldsymbol{u}_l = [u_1, u_2, u_3]^T$; $\boldsymbol{\theta} = [\theta_1, \theta_2, \theta_3]^T$. Bold font is used to indicate vectors or matrices throughout this dissertation.

Coordinate transformation matrices are used to transfer vectors from one coordinate system to another. The subscripts of a transformation matrix indicate the post- and pre-transformation coordinates, and the subscript of a vector indicate in which coordinate the vector is resolved. For example, transformation matrix $\boldsymbol{T}_{dl}$ enables a translational displacement vector resolved in local undeformed coordinate l to be resolved in deformed coordinate d as: $\boldsymbol{u}_d = \boldsymbol{T}_{dl}\boldsymbol{u}_l$. Transformation matrices represent the change of directions between coordinates and are equivalent to rotation tensors that describe the rotation between basis vectors. The resulting transformation matrices are orthogonal: $\boldsymbol{T}_{ld} = \boldsymbol{T}_{dl}^T = \boldsymbol{T}_{dl}^{-1}$ and $\boldsymbol{u}_l = \boldsymbol{T}_{ld}\boldsymbol{u}_d$. No Einstein summation convention is applied. Transformation matrices are functions with respect to s and t, and can be computed using rotational displacements.

Angular velocities and accelerations are expressed using transformation matrices:

$$\begin{aligned}
\tilde{\boldsymbol{\omega}}_d &= \boldsymbol{T}_{dl}\dot{\boldsymbol{T}}_{ld} && (2.1)\\
\tilde{\boldsymbol{\Omega}}_f &= \boldsymbol{T}_{fg}\dot{\boldsymbol{T}}_{gf} && (2.2)\\
\dot{\tilde{\boldsymbol{\omega}}}_d &= \frac{\partial}{\partial t}(\boldsymbol{T}_{dl}\dot{\boldsymbol{T}}_{ld}) = \dot{\boldsymbol{T}}_{dl}\dot{\boldsymbol{T}}_{ld} + \boldsymbol{T}_{dl}\ddot{\boldsymbol{T}}_{ld} && (2.3)\\
\dot{\tilde{\boldsymbol{\Omega}}}_f &= \frac{\partial}{\partial t}(\boldsymbol{T}_{fg}\dot{\boldsymbol{T}}_{gf}) = \dot{\boldsymbol{T}}_{fg}\dot{\boldsymbol{T}}_{gf} + \boldsymbol{T}_{fg}\ddot{\boldsymbol{T}}_{gf} && (2.4)
\end{aligned}$$

in which vector $\boldsymbol{\omega}_d$ is the angular velocity of local deformation at a cross-section measured in coordinate d; vector $\boldsymbol{\Omega}_f$ is the angular velocity of overall rigid-body motion measured in coordinate f; $\dot{(\,)}$ and $\ddot{(\,)}$ denote the first and second time derivatives, and $\tilde{(\,)}$ denotes the skew-symmetric matrix of a vector, which can be used to represent cross products as matrix multiplications.

The absolute translational velocity of a differential cross-sectional element on a beam is measured in inertial coordinate g. Taking the time derivative of position vector $\boldsymbol{R}_g^{OG} = \boldsymbol{R}_g^{OW} + \boldsymbol{T}_{gf}\boldsymbol{R}_f^{WP_0} + \boldsymbol{T}_{gf}\boldsymbol{T}_{fl}\boldsymbol{u}_l + \boldsymbol{T}_{gf}\boldsymbol{T}_{fl}\boldsymbol{T}_{ld}\boldsymbol{R}_d^{PG}$ yields the absolute translational velocity:

$$\boldsymbol{v}_g^G = \boldsymbol{v}_g^W + \dot{\boldsymbol{T}}_{gf}\boldsymbol{R}_f^{WP_0} + \dot{\boldsymbol{T}}_{gf}\boldsymbol{T}_{fl}\boldsymbol{u}_l + \boldsymbol{T}_{gf}\boldsymbol{T}_{fl}\dot{\boldsymbol{u}}_l + \dot{\boldsymbol{T}}_{gf}\boldsymbol{T}_{fl}\boldsymbol{T}_{ld}\boldsymbol{e}_d + \boldsymbol{T}_{gf}\boldsymbol{T}_{fl}\dot{\boldsymbol{T}}_{ld}\boldsymbol{e}_d \qquad (2.5)$$

in which $\boldsymbol{e}_d = \boldsymbol{R}_d^{PG}$ is the eccentricity measured in coordinate d, and $\boldsymbol{v}_g^W = \dot{\boldsymbol{R}}_g^{OW}$. Time derivatives of $\boldsymbol{R}_f^{WP_0}$ and $\boldsymbol{T}_{fl}$ are equal to zero because there is no relative motion between the local undeformed coordinates and floating coordinate f. Cross-sectional eccentricity is assumed to be constant in time, $\dot{\boldsymbol{e}}_d = \boldsymbol{0}$, because cross-sectional deformations are assumed to be small.

2.2.3 Momentum Balance

Momentum balance is applicable to the absolute momentum measured in an inertial coordinate system. Any change in momentum results from the sum of forces and moments acting on each differential cross-sectional element:

$$\begin{aligned} \dot{\boldsymbol{L}}_g &= \sum \boldsymbol{F}_g &&= \boldsymbol{F}_g^{ext} + \boldsymbol{F}_g^{int} \qquad (2.6) \\ \dot{\boldsymbol{H}}_g^G &= \sum \boldsymbol{M}_g^G &&= \boldsymbol{M}_g^{ext,G} + \boldsymbol{M}_g^{int,G} \qquad (2.7) \end{aligned}$$

where $\boldsymbol{L}_g = m\boldsymbol{v}_g^G$ is the absolute linear momentum; $\boldsymbol{H}_g^G = \boldsymbol{T}_{gf}\boldsymbol{T}_{fl}\boldsymbol{T}_{ld}\boldsymbol{I}_d^G\boldsymbol{T}_{dl}\boldsymbol{T}_{lf}\boldsymbol{\Omega}_f + \boldsymbol{T}_{gf}\boldsymbol{T}_{fl}\boldsymbol{T}_{ld}\boldsymbol{I}_d^G\boldsymbol{\omega}_d$ is the absolute angular momentum about the center of mass G; m is the mass per unit length and $\boldsymbol{I}_d^G$ is the mass moment of inertia about G; $\boldsymbol{F}_g^{ext}$ and $\boldsymbol{M}_g^{ext,G}$ are the total forces and moments about G resulting from external loads; $\boldsymbol{F}_g^{int}$ and $\boldsymbol{M}_g^{int,G}$ are the total internal forces and moments about G resulting from beam deformation.

The left-hand side of Eq. (2.6) results from taking the time derivative of the absolute translational velocity expressed as Eq. (2.5):

$$\begin{aligned} \dot{\boldsymbol{L}}_g = m(&\boldsymbol{a}_g^W + \ddot{\boldsymbol{T}}_{gf}\boldsymbol{R}_f^{WP_0} + \ddot{\boldsymbol{T}}_{gf}\boldsymbol{T}_{fl}\boldsymbol{u}_l + 2\dot{\boldsymbol{T}}_{gf}\boldsymbol{T}_{fl}\dot{\boldsymbol{u}}_l + \boldsymbol{T}_{gf}\boldsymbol{T}_{fl}\ddot{\boldsymbol{u}}_l \\ &+ \ddot{\boldsymbol{T}}_{gf}\boldsymbol{T}_{fl}\boldsymbol{T}_{ld}\boldsymbol{e}_d + 2\dot{\boldsymbol{T}}_{gf}\boldsymbol{T}_{fl}\dot{\boldsymbol{T}}_{ld}\boldsymbol{e}_d + \boldsymbol{T}_{gf}\boldsymbol{T}_{fl}\ddot{\boldsymbol{T}}_{ld}\boldsymbol{e}_d) \qquad (2.8) \end{aligned}$$

in which $\boldsymbol{a}_g^W = \dot{\boldsymbol{v}}_g^W$ is the absolute acceleration of point W.

Multiplying the combination of Eqs. (2.6) and (2.8) by $\boldsymbol{T}_{fg}$ and substituting Eqs. (2.1) - (2.4) into the result yields a physically-intuitive formula that represents the change in linear momentum in non-inertial floating coordinate f:

$$\begin{aligned} \boldsymbol{F}_f^{ext} + \boldsymbol{F}_f^{int} = m[&\boldsymbol{a}_f^W + \dot{\tilde{\boldsymbol{\Omega}}}_f(\boldsymbol{R}_f^{WP_0} + \boldsymbol{T}_{fl}\boldsymbol{u}_l + \boldsymbol{T}_{fl}\boldsymbol{T}_{ld}\boldsymbol{e}_d) + \tilde{\boldsymbol{\Omega}}_f\tilde{\boldsymbol{\Omega}}_f(\boldsymbol{R}_f^{WP_0} + \boldsymbol{T}_{fl}\boldsymbol{u}_l + \boldsymbol{T}_{fl}\boldsymbol{T}_{ld}\boldsymbol{e}_d) \\ &+ \boldsymbol{T}_{fl}\boldsymbol{T}_{ld}(\dot{\tilde{\boldsymbol{\omega}}}_d\boldsymbol{e}_d + \tilde{\boldsymbol{\omega}}_d\tilde{\boldsymbol{\omega}}_d\boldsymbol{e}_d) + 2\tilde{\boldsymbol{\Omega}}_f\boldsymbol{T}_{fl}(\dot{\boldsymbol{u}}_l + \boldsymbol{T}_{ld}\tilde{\boldsymbol{\omega}}_d\boldsymbol{e}_d) + \boldsymbol{T}_{fl}\ddot{\boldsymbol{u}}_l] \qquad (2.9) \end{aligned}$$

The derivation for angular momentum balance in floating coordinate f follows the same logic: computing the time derivative of $\boldsymbol{H}_g^G$, multiplying the combination of Eq. (2.7) and $\dot{\boldsymbol{H}}_g^G$ by $\boldsymbol{T}_{fg}$, and substituting Eqs. (2.1) - (2.4) into the result yields:

$$\begin{aligned}\boldsymbol{M}_f^{ext,G} + \boldsymbol{M}_f^{int,G} =& \tilde{\boldsymbol{\Omega}}_f \boldsymbol{T}_{fl} \boldsymbol{T}_{ld} \boldsymbol{I}_d^G (\boldsymbol{T}_{dl} \boldsymbol{T}_{lf} \boldsymbol{\Omega}_f + \boldsymbol{\omega}_d) + \boldsymbol{T}_{fl} \boldsymbol{T}_{ld} \tilde{\boldsymbol{\omega}}_d \boldsymbol{I}_d^G (\boldsymbol{T}_{dl} \boldsymbol{T}_{lf} \boldsymbol{\Omega}_f + \boldsymbol{\omega}_d) \\ &+ \boldsymbol{T}_{fl} \boldsymbol{T}_{ld} \boldsymbol{I}_d^G (\boldsymbol{T}_{dl} \boldsymbol{T}_{lf} \dot{\boldsymbol{\Omega}}_f + \dot{\boldsymbol{\omega}}_d) - \boldsymbol{T}_{fl} \boldsymbol{T}_{ld} \boldsymbol{I}_d^G \tilde{\boldsymbol{\omega}}_d \boldsymbol{T}_{dl} \boldsymbol{T}_{lf} \boldsymbol{\Omega}_f \end{aligned} \tag{2.10}$$

2.2.4 Strain Measures and Internal Forces and Moments

The relationships between unknown displacements, $\boldsymbol{u}_l$ and $\boldsymbol{\theta}$, along the beam and the associated internal forces and moments are needed for solution of Eqs. (2.9) and (2.10). Angular strains are computed from curvature vectors; linear strains are computed using differential position vectors.

The curvature vector $\boldsymbol{k}_l$ of the undeformed curvilinear coordinate s, and $\boldsymbol{k}_d$ of the deformed curvilinear coordinate S, each describe the change in direction of a curvilinear coordinate per unit length, measured in the local Cartesian coordinates l and d respectively. The skew-symmetric matrix of the local curvature vector at any point can be computed as $\tilde{\boldsymbol{k}}_l = \boldsymbol{T}_{lf} \boldsymbol{T}'_{fl}$ or $\tilde{\boldsymbol{k}}_d = \boldsymbol{T}_{df} \boldsymbol{T}'_{fd}$, in which $\boldsymbol{T}_{df} = \boldsymbol{T}_{dl} \boldsymbol{T}_{lf}$ and $(\ )'$ denotes spatial derivatives with respect to s. The local angular strain, $\boldsymbol{\kappa}$, can be computed along the beam as the difference between these curvature vectors:

$$\begin{aligned}\boldsymbol{\kappa} =& \boldsymbol{k}_d - \boldsymbol{k}_l \\ =& \text{axial}(\boldsymbol{T}_{dl} \boldsymbol{T}_{lf} \boldsymbol{T}'_{fl} \boldsymbol{T}_{ld} + \boldsymbol{T}_{dl} \boldsymbol{T}_{lf} \boldsymbol{T}_{fl} \boldsymbol{T}'_{ld}) - \text{axial}(\boldsymbol{T}_{lf} \boldsymbol{T}'_{fl}) \\ =& \text{axial}(\boldsymbol{T}_{dl} \tilde{\boldsymbol{k}}_l \boldsymbol{T}_{ld} + \boldsymbol{T}_{dl} \boldsymbol{T}'_{ld} - \tilde{\boldsymbol{k}}_l) \end{aligned} \tag{2.11}$$

where axial( ) denotes the axial vector computed from a skew-symmetric matrix.

Derivation of linear strain follows a similar logic applied to differential position vectors instead of curvature vectors. Differential position vectors $\boldsymbol{r}'_l$ of the undeformed curvilinear coordinate s, and $\boldsymbol{r}'_d$ of the deformed curvilinear coordinate S, each describe the change in shape of a differential

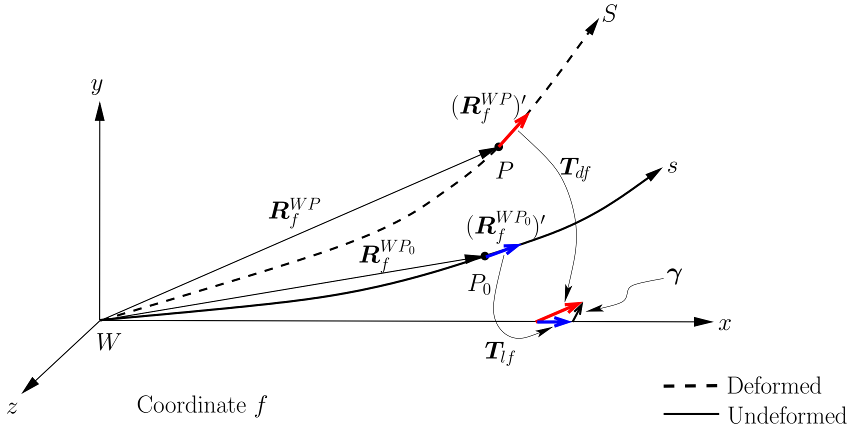

Figure 2.2: Linear strain of a beam.

element along the beam axis, measured in the local Cartesian coordinates l and d respectively. Differential position vectors at a point can be computed as $\boldsymbol{r}'_l = \boldsymbol{T}_{lf}(\boldsymbol{R}_f^{WP_0})'$ and $\boldsymbol{r}'_d = \boldsymbol{T}_{df}(\boldsymbol{R}_f^{WP})'$. Transformation matrices $\boldsymbol{T}_{lf}$ and $\boldsymbol{T}_{df}$ effectively rotate the spatial derivatives of position vectors to the common coordinate system f (Fig. 2.2), such that these vectors can be subtracted. The resulting linear strain, $\boldsymbol{\gamma}$, includes axial and shear strains and excludes rigid element rotations:

$$\begin{aligned}\boldsymbol{\gamma} &= \boldsymbol{r}'_d - \boldsymbol{r}'_l \\ &= \boldsymbol{T}_{df}(\boldsymbol{R}_f^{WP})' - \boldsymbol{T}_{lf}(\boldsymbol{R}_f^{WP_0})' \\ &= \boldsymbol{T}_{dl}\boldsymbol{T}_{lf}[\boldsymbol{T}'_{fl}\boldsymbol{R}_l^{WP_0} + \boldsymbol{T}_{fl}(\boldsymbol{R}_l^{WP_0})' + \boldsymbol{T}'_{fl}\boldsymbol{u}_l + \boldsymbol{T}_{fl}\boldsymbol{u}'_l] - \boldsymbol{T}_{lf}[\boldsymbol{T}'_{fl}\boldsymbol{R}_l^{WP_0} + \boldsymbol{T}_{fl}(\boldsymbol{R}_l^{WP_0})'] \\ &= \boldsymbol{T}_{dl}(\boldsymbol{e}_1 + \tilde{\boldsymbol{k}}_l\boldsymbol{u}_l + \boldsymbol{u}'_l) - \boldsymbol{e}_1 \qquad (2.12)\end{aligned}$$

in which $\boldsymbol{r}'_l = \tilde{\boldsymbol{k}}_l\boldsymbol{R}_l^{WP_0} + (\boldsymbol{R}_l^{WP_0})' = \boldsymbol{e}_1$ and $\boldsymbol{e}_1 = [1, 0, 0]^T$ is a unit vector, because $\boldsymbol{r}'_l$ yields a tangent unit vector that is always aligned with the $\boldsymbol{a}$-direction of local undeformed coordinate l.

Eqs. (2.11) and (2.12) represent the strain measures of a beam subject to large angular and translational deflections, and include full consideration of geometrical nonlinearities. These strain measures are invariant for rigid-body motions. The elastic force and moment of a cross-section at

s are assumed to be functions of strain measures and/or the time derivatives of strain measures:

$$\boldsymbol{F}_d(s,t) = \boldsymbol{F}_d(\boldsymbol{\gamma}, \boldsymbol{\kappa}, \dot{\boldsymbol{\gamma}}, \dot{\boldsymbol{\kappa}}) \tag{2.13}$$

$$\boldsymbol{M}_d^P(s,t) = \boldsymbol{M}_d^P(\boldsymbol{\gamma}, \boldsymbol{\kappa}, \dot{\boldsymbol{\gamma}}, \dot{\boldsymbol{\kappa}}) \tag{2.14}$$

in which $\boldsymbol{F}_d$ is the cross-sectional elastic force measured in deformed local coordinate d, and $\boldsymbol{M}_d^P$ is the cross-sectional elastic moment about elastic center in coordinate d. Eqs. (2.13) and (2.14) represent the constitutive relations for a material, and are applicable for linear elastic, hyperelasic, or viscoelastic models.

Momentum balance equations, (2.9) and (2.10), are expressed about the mass center of the differential element. The total internal force exerted on the differential element can be computed directly as the sum of cross-sectional elastic forces, but the total internal moment must be transfered from the elastic center to the mass center including the effects of elastic forces and eccentricities. Internal forces are exerted at each end of a differential element (s^- and s^+). The total internal force exerted on an element is:

$$\boldsymbol{F}_f^{int} = \frac{1}{\partial s}[\boldsymbol{T}_{fd}(s^+)\boldsymbol{F}_d(s^+) - \boldsymbol{T}_{fd}(s^-)\boldsymbol{F}_d(s^-)] = (\boldsymbol{T}'_{fl}\boldsymbol{T}_{ld} + \boldsymbol{T}_{fl}\boldsymbol{T}'_{ld})\boldsymbol{F}_d + \boldsymbol{T}_{fl}\boldsymbol{T}_{ld}\boldsymbol{F}'_d \tag{2.15}$$

The total of the internal moments exerted at each end of the element expressed about the mass center, including elastic forces and eccentricities is:

$$\begin{aligned} \boldsymbol{M}_f^{int,G} =& \frac{1}{\partial s}[\boldsymbol{T}_{fd}(s^+)\boldsymbol{M}_d^P(s^+) - \boldsymbol{T}_{fd}(s^-)\boldsymbol{M}_d^P(s^-)] \\ &+\frac{1}{\partial s}[\boldsymbol{T}_{fd}(s^+)(\widetilde{\boldsymbol{R}_d^{GP} + \boldsymbol{R}_d^{PP+}})\boldsymbol{F}_d(s^+) - \boldsymbol{T}_{fd}(s^-)(\widetilde{\boldsymbol{R}_d^{GP} + \boldsymbol{R}_d^{PP-}})\boldsymbol{F}_d(s^-)] \\ =& (\boldsymbol{T}'_{fl}\boldsymbol{T}_{ld} + \boldsymbol{T}_{fl}\boldsymbol{T}'_{ld})\boldsymbol{M}_d^P + \boldsymbol{T}_{fl}\boldsymbol{T}_{ld}(\boldsymbol{M}_d^P)' \\ &-\boldsymbol{T}_{fl}\boldsymbol{T}_{ld}\tilde{\boldsymbol{e}}_d\tilde{\boldsymbol{k}}_d\boldsymbol{F}_d - \boldsymbol{T}_{fl}\boldsymbol{T}_{ld}\tilde{\boldsymbol{e}}_d\boldsymbol{F}'_d + \boldsymbol{T}_{fl}\boldsymbol{T}_{ld}(\tilde{\boldsymbol{\gamma}} + \tilde{\boldsymbol{e}}_1)\boldsymbol{F}_d \end{aligned} \tag{2.16}$$

in which $\boldsymbol{R}_d^{GP} = -\boldsymbol{e}_d$ and $\frac{\partial}{\partial s}(\boldsymbol{R}_d^{PP+} - \boldsymbol{R}_d^{PP+}) = \frac{\partial}{\partial s}(\boldsymbol{R}_d^{P-P+}) = \boldsymbol{r}'_d = \boldsymbol{\gamma} + \boldsymbol{e}_1$ as per Eq. (2.12).

2.2.5 Equations of Motion

Translational and rotational EOM's are derived based on conservation of momentum in non-inertial coordinate f by substituting Eqs. (2.15) and (2.16) into Eqs. (2.9) and (2.10), respectively:

$$\begin{aligned}
& \boldsymbol{F}_f^{ext} + (\boldsymbol{T}'_{fl}\boldsymbol{T}_{ld} + \boldsymbol{T}_{fl}\boldsymbol{T}'_{ld})\boldsymbol{F}_d + \boldsymbol{T}_{fl}\boldsymbol{T}_{ld}\boldsymbol{F}'_d \\
= \; & m\boldsymbol{a}_f^W + m\dot{\tilde{\boldsymbol{\Omega}}}_f(\boldsymbol{R}_f^{WP_0} + \boldsymbol{T}_{fl}\boldsymbol{u}_l + \boldsymbol{T}_{fl}\boldsymbol{T}_{ld}\boldsymbol{e}_d) + m\tilde{\boldsymbol{\Omega}}_f\tilde{\boldsymbol{\Omega}}_f(\boldsymbol{R}_f^{WP_0} + m\boldsymbol{T}_{fl}\boldsymbol{u}_l + \boldsymbol{T}_{fl}\boldsymbol{T}_{ld}\boldsymbol{e}_d) \\
& + m\boldsymbol{T}_{fl}\boldsymbol{T}_{ld}(\dot{\tilde{\boldsymbol{\omega}}}_d\boldsymbol{e}_d + \tilde{\boldsymbol{\omega}}_d\tilde{\boldsymbol{\omega}}_d\boldsymbol{e}_d) + 2m\tilde{\boldsymbol{\Omega}}_f\boldsymbol{T}_{fl}(\dot{\boldsymbol{u}}_l + \boldsymbol{T}_{ld}\tilde{\boldsymbol{\omega}}_d\boldsymbol{e}_d) + m\boldsymbol{T}_{fl}\ddot{\boldsymbol{u}}_l \qquad (2.17)
\end{aligned}$$

$$\begin{aligned}
& \boldsymbol{M}_f^{ext,G} + (\boldsymbol{T}'_{fl}\boldsymbol{T}_{ld} + \boldsymbol{T}_{fl}\boldsymbol{T}'_{ld})\boldsymbol{M}_d^P + \boldsymbol{T}_{fl}\boldsymbol{T}_{ld}(\boldsymbol{M}_d^P)' \\
& - \boldsymbol{T}_{fl}\boldsymbol{T}_{ld}\tilde{\boldsymbol{e}}_d\tilde{\boldsymbol{k}}_d\boldsymbol{F}_d - \boldsymbol{T}_{fl}\boldsymbol{T}_{ld}\tilde{\boldsymbol{e}}_d\boldsymbol{F}'_d + \boldsymbol{T}_{fl}\boldsymbol{T}_{ld}(\tilde{\gamma} + \tilde{\boldsymbol{e}}_1)\boldsymbol{F}_d \\
= \; & \tilde{\boldsymbol{\Omega}}_f\boldsymbol{T}_{fl}\boldsymbol{T}_{ld}\boldsymbol{I}_d^G(\boldsymbol{T}_{dl}\boldsymbol{T}_{lf}\boldsymbol{\Omega}_f + \boldsymbol{\omega}_d) + \boldsymbol{T}_{fl}\boldsymbol{T}_{ld}\tilde{\boldsymbol{\omega}}_d\boldsymbol{I}_d^G(\boldsymbol{T}_{dl}\boldsymbol{T}_{lf}\boldsymbol{\Omega}_f + \boldsymbol{\omega}_d) \\
& + \boldsymbol{T}_{fl}\boldsymbol{T}_{ld}\boldsymbol{I}_d^G(\boldsymbol{T}_{dl}\boldsymbol{T}_{lf}\dot{\boldsymbol{\Omega}}_f + \dot{\boldsymbol{\omega}}_d) - \boldsymbol{T}_{fl}\boldsymbol{T}_{ld}\boldsymbol{I}_d^G\tilde{\boldsymbol{\omega}}_d\boldsymbol{T}_{dl}\boldsymbol{T}_{lf}\boldsymbol{\Omega}_f \qquad (2.18)
\end{aligned}$$

Eqs. (2.17) and (2.18) are the nonlinear 6-DOF EOM's expressed using transformation matrices in the floating frame. These EOM's are established as a part of a total Lagrangian formulation; the primary unknown variables are displacements $\boldsymbol{u}_l$ and $\boldsymbol{\theta}$ relative to non-inertial coordinate l, which represents the undeformed configuration. A complete, displacement-based formulation of MBBT is represented by the EOM's of Eqs. (2.17) - (2.18), constitutive relations of Eqs. (2.13) - (2.14), strain measures of Eqs. (2.11) - (2.12), angular motions of Eqs. (2.1) - (2.4), and the rotation formulations for transformation matrices. Any three-variable finite rotation formulation can be used to compute transformation matrices $\boldsymbol{T}_{ld}$ and $\boldsymbol{T}_{dl}$ as functions of $\boldsymbol{\theta}$, such as Euler angles, Rodrigues' formula, or Lie group. Inertial forces and moments associated with the overall rigid-body motion of an undeformed beam are explicitly included in Eqs. (2.17) and (2.18). Significant inertial forces and moments generally result from translational acceleration, $\boldsymbol{a}_f^W$, rotational velocity, $\boldsymbol{\Omega}_f$, and rotational acceleration, $\dot{\boldsymbol{\Omega}}_f$. The inertial term that includes $\tilde{\boldsymbol{\Omega}}_f\tilde{\boldsymbol{\Omega}}_f$ in Eq. (2.17) represents the centrifugal force introduced by rigid-body motion. The inertial term that includes

$2\tilde{\boldsymbol{\Omega}}_f$ in Eq. (2.17) represents the Coriolis effect. The first term in the right-hand-side of Eq. (2.18) implies that rigid-body motion alone ($\boldsymbol{\Omega}_f \neq 0$, $\boldsymbol{\omega}_d = 0$) can cause an inertial moment in the floating frame. The explicit representation of rigid-body motion in MBBT enables the beam theory to be readily coupled with multibody dynamics in which rigid-body motion and local deformation can be numerically solved either by separate codes or by a coupled routine.

The floating coordinate system represents the arbitrary absolute motion of an undeformed beam described by vectors $\boldsymbol{a}_f^W$, $\boldsymbol{\Omega}_f$, and $\dot{\boldsymbol{\Omega}}_f$ in Eqs. (2.17) - (2.18). MBBT enables computation of local dynamics relative to the floating coordinate system. Moreover, Eqs. (2.17) - (2.18) can be transferred to global inertial coordinate g or to local deformed (material) coordinate d through multiplication of the EOM's by transformation matrices $\boldsymbol{T}_{fg}$ or $\boldsymbol{T}_{fd}$, respectively. No re-derivation of the EOM's is required because the original EOM's include full consideration of relative motions among these coordinate systems.

2.2.6 Relation to Existing GEBT

MBBT is unique amongst other GEBT formulations in that dynamic quantities are relative to non-inertial frames and coordinate transformation matrices are used throughout the derivation. The vector-based formulation and the overall framework of the derivation are both useful for subsequent theoretical developments. The vector-based formulation using the relative dynamic quantities retains physical significance for each term and enables rigorous application of practical engineering assumptions, which leads to rational linearization in Section 2.3.1 and subsequent simplification in Section 2.3.2. The overall derivation framework using transformation matrices is essential for the separation of displacements technique developed in Section 2.4.1.

The final nonlinear result fo MBBT can be shown to be mathematically equivalent to the existing inertial frame formulation of GEBT, as would be expected because each derivation is based on the same physical assumptions. An inertial frame formulation of MBBT can be developed following the non-inertial frame formulation. Multiplying Eq. (2.6) by $\boldsymbol{T}_{dl}\boldsymbol{T}_{lf}\boldsymbol{T}_{fg}$ and substituting

Eq. (2.15) into the resulting equation yields:

$$\begin{aligned}
& \boldsymbol{F}_d^{ext} + \boldsymbol{T}_{dl}\boldsymbol{T}_{lf}(\boldsymbol{T}'_{fl}\boldsymbol{T}_{ld} + \boldsymbol{T}_{fl}\boldsymbol{T}'_{ld})\boldsymbol{F}_d + (\boldsymbol{F}_d)' \\
= \; & \boldsymbol{F}_d^{ext} + \tilde{\boldsymbol{k}}_d\boldsymbol{F}_d + (\boldsymbol{F}_d)' \\
= \; & \boldsymbol{T}_{dl}\boldsymbol{T}_{lf}\boldsymbol{T}_{fg} m \frac{\partial}{\partial t}(\boldsymbol{T}_{gf}\boldsymbol{T}_{fl}\boldsymbol{T}_{ld}\boldsymbol{v}_d^G) \\
= \; & \underline{\tilde{\boldsymbol{\Omega}}_d}\boldsymbol{L}_d + \dot{\boldsymbol{L}}_d
\end{aligned} \tag{2.19}$$

where $\underline{\boldsymbol{\Omega}_d} = \boldsymbol{\Omega}_d + \boldsymbol{\omega}_d = \boldsymbol{T}_{df}\boldsymbol{\Omega}_f + \boldsymbol{\omega}_d$ is the absolute angular velocity, and $\boldsymbol{L}_d = m\boldsymbol{v}_d^G = m(\boldsymbol{v}_d^P + \underline{\tilde{\boldsymbol{\Omega}}_d}\boldsymbol{e}_d)$ is the absolute linear momentum measured in coordinate d. The absolute angular momentum about the elastic center can be computed in inertial coordinate g:

$$\boldsymbol{H}_g^P = \boldsymbol{T}_{gd}\boldsymbol{H}_d^P = \boldsymbol{T}_{gd}(\tilde{\boldsymbol{e}}_d\boldsymbol{L}_d + \boldsymbol{I}_d^G\underline{\boldsymbol{\Omega}_d}) = \tilde{\boldsymbol{e}}_g\boldsymbol{L}_g + \boldsymbol{H}_g^G \tag{2.20}$$

Multiplying the time derivative of Eq. (2.20) by $\boldsymbol{T}_{dl}\boldsymbol{T}_{lf}\boldsymbol{T}_{fg}$ and combining Eqs. (2.6), (2.7), (2.15), and (2.16) with the resulting equation yields:

$$\begin{aligned}
& \dot{\boldsymbol{H}}_d^P + \underline{\tilde{\boldsymbol{\Omega}}_d}\boldsymbol{H}_d^P \\
= \; & \boldsymbol{T}_{dl}\boldsymbol{T}_{lf}\boldsymbol{T}_{fg}(\dot{\tilde{\boldsymbol{e}}}_g\boldsymbol{L}_g + \tilde{\boldsymbol{e}}_g\dot{\boldsymbol{L}}_g + \dot{\boldsymbol{H}}_g^G) \\
= \; & \underline{\tilde{\boldsymbol{\Omega}}_d}\tilde{\boldsymbol{e}}_d\boldsymbol{L}_d + \tilde{\boldsymbol{e}}_d[\boldsymbol{F}_d^{ext} + \tilde{\boldsymbol{k}}_d\boldsymbol{F}_d + (\boldsymbol{F}_d)'] + \boldsymbol{M}_d^{ext,G} + \tilde{\boldsymbol{k}}_d\boldsymbol{M}_d^P \\
& +(\boldsymbol{M}_d^P)' - \tilde{\boldsymbol{e}}_d[\tilde{\boldsymbol{k}}_d\boldsymbol{F}_d + (\boldsymbol{F}_d)'] + (\tilde{\boldsymbol{\gamma}} + \tilde{\boldsymbol{e}}_1)\boldsymbol{F}_d \\
= \; & -\tilde{\boldsymbol{v}}_d^P\boldsymbol{L}_d + \boldsymbol{M}_d^{ext,P} + \tilde{\boldsymbol{k}}_d\boldsymbol{M}_d^P + (\boldsymbol{M}_d^P)' + (\tilde{\boldsymbol{\gamma}} + \tilde{\boldsymbol{e}}_1)\boldsymbol{F}_d
\end{aligned} \tag{2.21}$$

where $\underline{\tilde{\boldsymbol{\Omega}}_d}\tilde{\boldsymbol{e}}_d\boldsymbol{L}_d = (\tilde{\boldsymbol{v}}_d^G - \tilde{\boldsymbol{v}}_d^P)m\boldsymbol{v}_d^G = -\tilde{\boldsymbol{v}}_d^P\boldsymbol{L}_d$ is the inertial-coupling term that represents the moment about the elastic center introduced by the inertial force acting at the center of mass, which does not exist if the EOM is established about the mass center. Eqs. (2.19) and (2.21) are the inertial frame formulation, and are identical to the EOM's presented as Eqs. (1a) and (1b) in [12], in which dynamic quantities ($\underline{\boldsymbol{\Omega}_d}$ and $\boldsymbol{v}_d^P$) and the underlying displacements are relative to an inertial frame.

Hodges' formulation or Eqs. (2.19) and (2.21) can also be used as the basis for an alternate derivation of MBBT in a non-inertial frame. This alternate derivation is approximately as complicated as the proposed MBBT derivation, and does not offer the useful intermediate results that makes MBBT valuable. The alternate derivation includes several steps: (a) transfer the reference coordinate into the non-inertial frame using variable transformation matrices; (b) transfer the reference point of angular momentum from the elastic center to the center of cross-sectional mass using Eq. (2.20); (c) Algebraically re-formulate the resulting dynamic quantities, and finally (d) derive the non-inertial frame formulation using the identity regarding antisymmetric operations: $\tilde{\boldsymbol{\alpha}}\tilde{\boldsymbol{\beta}} = \tilde{\boldsymbol{\beta}}\tilde{\boldsymbol{\alpha}} + (\widetilde{\tilde{\boldsymbol{\alpha}}\boldsymbol{\beta}})$, in which $\boldsymbol{\alpha}$ and $\boldsymbol{\beta}$ are arbitrary 3D vectors.

2.3 Linearization, Simplification, and Discretization

The governing equations of the fully nonlinear MBBT are linearized based on physical engineering assumptions. The linearized MBBT is then further simplified for application to three practical engineering cases. The linearized formulation is also re-derived in a discretized integral format using the FV method.

2.3.1 Linearized MBBT

Three additional assumptions are introduced for the linearization of MBBT: (a) rotational deformations along the beam are assumed to be small; (b) strain measures are assumed to be small, and (c) constitutive equations are assumed to be linear functions of strain measures. Transformation matrices $\boldsymbol{T}_{ld}$ and $\boldsymbol{T}_{dl}$ and derivatives of these matrices can be simplified considerably if the magnitudes of rotational displacements and their derivatives are small: $|\boldsymbol{\theta}(s,t)|$, $|\dot{\boldsymbol{\theta}}(s,t)|$, $|\ddot{\boldsymbol{\theta}}(s,t)|$, and $|\boldsymbol{\theta}'(s,t)| \ll 1$. The 1-2-3 sequenced Euler angle formulation is selected here to compute coordinate transformation matrices [6]. This Euler angle formulation is straightforward and no singularity issues arise in this application, which is limited to small angles. Alternate rotation formulations could be applied. Assuming $\sin(\theta) \approx \theta$ and $\cos(\theta) \approx 1$ in Euler angle formulation yields the simplified transformation matrices $\boldsymbol{T}_{ld}$ and $\boldsymbol{T}_{dl}$ for small angles:

$$\boldsymbol{T}_{ld} \approx \boldsymbol{I} + \tilde{\boldsymbol{\theta}} \tag{2.22}$$

$$\boldsymbol{T}_{dl} = \boldsymbol{T}_{ld}^T \approx \boldsymbol{I} - \tilde{\boldsymbol{\theta}} \tag{2.23}$$

in which $\boldsymbol{I}$ is identity matrix.

Linearized angular velocity and acceleration are obtained by substituting Eqs. (2.22) - (2.23) into Eqs. (2.1) and (2.3) and neglecting all terms of second-order and higher in θ_i, $\dot{\theta}_i$, and $\ddot{\theta}_i$:

$$\boldsymbol{\omega}_d \approx \left[\dot{\theta}_1, \dot{\theta}_2, \dot{\theta}_3\right]^T = \dot{\boldsymbol{\theta}} \tag{2.24}$$

$$\dot{\boldsymbol{\omega}}_d \approx \left[\ddot{\theta}_1, \ddot{\theta}_2, \ddot{\theta}_3\right]^T = \ddot{\boldsymbol{\theta}} \tag{2.25}$$

The spatial derivatives of translational displacements are small under small-strain assumption: $|\boldsymbol{\kappa}|$, $|\boldsymbol{\gamma}|$, and $|\boldsymbol{u}_l'(s,t)| \ll 1$. The linearized strain measures are found by substituting Eqs. (2.22) - (2.23) into Eqs. (2.11) - (2.12) and neglecting all terms of second-order and higher:

$$\boldsymbol{\kappa} \approx \text{axial}(\tilde{\boldsymbol{k}}_l\tilde{\boldsymbol{\theta}} - \tilde{\boldsymbol{\theta}}\tilde{\boldsymbol{k}}_l + \tilde{\boldsymbol{\theta}}') = \tilde{\boldsymbol{k}}_l\boldsymbol{\theta} + \boldsymbol{\theta}' \tag{2.26}$$

$$\boldsymbol{\gamma} \approx \tilde{\boldsymbol{e}}_1\boldsymbol{\theta} + \tilde{\boldsymbol{k}}_l\boldsymbol{u}_l + \boldsymbol{u}_l' \tag{2.27}$$

Internal forces and moments are computed using the strain measures and constitutive matrices assuming linear elasticity, such that Eqs. (2.13) and (2.14) can be expressed as:

$$\begin{bmatrix} \boldsymbol{F}_d(s,t) \\ \boldsymbol{M}_d(s,t) \end{bmatrix} = \boldsymbol{K} \begin{bmatrix} \boldsymbol{\gamma}(s,t) \\ \boldsymbol{\kappa}(s,t) \end{bmatrix} = \begin{bmatrix} \boldsymbol{K}_{11} & \boldsymbol{K}_{12} \\ \boldsymbol{K}_{21} & \boldsymbol{K}_{22} \end{bmatrix} \begin{bmatrix} \boldsymbol{\gamma}(s,t) \\ \boldsymbol{\kappa}(s,t) \end{bmatrix} \tag{2.28}$$

where $\boldsymbol{K}$ is the cross-sectional constitutive matrix, which is constant in time. The constitutive matrix can be obtained using one of several existing cross-sectional analysis methods, some of which enable inclusion of small cross-sectional deformations [34, 35, 36].

The linearized EOM's of MBBT are derived by substituting Eqs. (2.22) - (2.28) into the nonlinear Eqs. (2.17) - (2.18) and neglecting the terms of second-order and higher in those quantities assumed to be small:

$$\begin{aligned}
\boldsymbol{F}_f^{ext} \approx\ & m[\boldsymbol{a}_f^W + (\dot{\tilde{\boldsymbol{\Omega}}}_f + \tilde{\boldsymbol{\Omega}}_f\tilde{\boldsymbol{\Omega}}_f)(\boldsymbol{R}_f^{WP_0} + \boldsymbol{T}_{fl}\boldsymbol{e}_d) \\
& \quad + (\dot{\tilde{\boldsymbol{\Omega}}}_f + \tilde{\boldsymbol{\Omega}}_f\tilde{\boldsymbol{\Omega}}_f)\boldsymbol{T}_{fl}\boldsymbol{u}_l + 2\tilde{\boldsymbol{\Omega}}_f\boldsymbol{T}_{fl}\dot{\boldsymbol{u}}_l + \boldsymbol{T}_{fl}\ddot{\boldsymbol{u}}_l \\
& \quad - (\dot{\tilde{\boldsymbol{\Omega}}} + \tilde{\boldsymbol{\Omega}}_f\tilde{\boldsymbol{\Omega}}_f)\boldsymbol{T}_{fl}\tilde{\boldsymbol{e}}_d\boldsymbol{\theta} - 2\tilde{\boldsymbol{\Omega}}_f\boldsymbol{T}_{fl}\tilde{\boldsymbol{e}}_d\dot{\boldsymbol{\theta}} - \boldsymbol{T}_{fl}\tilde{\boldsymbol{e}}_d\ddot{\boldsymbol{\theta}}] \\
& -\boldsymbol{T}_{fl}'[\boldsymbol{K}_{11}(\tilde{\boldsymbol{e}}_1\boldsymbol{\theta} + \tilde{\boldsymbol{k}}_l\boldsymbol{u}_l + \boldsymbol{u}_l') + \boldsymbol{K}_{12}(\tilde{\boldsymbol{k}}_l\boldsymbol{\theta} + \boldsymbol{\theta}')] \\
& -\boldsymbol{T}_{fl}[\boldsymbol{K}_{11}(\tilde{\boldsymbol{e}}_1\boldsymbol{\theta} + \tilde{\boldsymbol{k}}_l\boldsymbol{u}_l + \boldsymbol{u}_l') + \boldsymbol{K}_{12}(\tilde{\boldsymbol{k}}_l\boldsymbol{\theta} + \boldsymbol{\theta}')]'
\end{aligned} \tag{2.29}$$

$$\begin{aligned}
\boldsymbol{M}_f^{ext,G} \approx\ & \tilde{\boldsymbol{\Omega}}_f\boldsymbol{T}_{fl}\boldsymbol{I}_d^G\boldsymbol{T}_{lf}\boldsymbol{\Omega}_f + \boldsymbol{T}_{fl}\boldsymbol{I}_d^G\boldsymbol{T}_{lf}\dot{\boldsymbol{\Omega}}_f + \boldsymbol{T}_{fl}\boldsymbol{I}_d^G\ddot{\boldsymbol{\theta}} \\
& +[\tilde{\boldsymbol{\Omega}}_f\boldsymbol{T}_{fl}\boldsymbol{I}_d^G + \boldsymbol{T}_{fl}\boldsymbol{I}_d^G\widetilde{(\boldsymbol{T}_{lf}\boldsymbol{\Omega}_f)} - \boldsymbol{T}_{fl}\widetilde{(\boldsymbol{I}_d^G\boldsymbol{T}_{lf}\boldsymbol{\Omega}_f)}]\dot{\boldsymbol{\theta}} \\
& +[\tilde{\boldsymbol{\Omega}}_f\boldsymbol{T}_{fl}\boldsymbol{I}_d^G\widetilde{(\boldsymbol{T}_{lf}\boldsymbol{\Omega}_f)} - \tilde{\boldsymbol{\Omega}}_f\boldsymbol{T}_{fl}\widetilde{(\boldsymbol{I}_d^G\boldsymbol{T}_{lf}\boldsymbol{\Omega}_f)}]\boldsymbol{\theta} \\
& +[\boldsymbol{T}_{fl}\boldsymbol{I}_d^G\widetilde{(\boldsymbol{T}_{lf}\dot{\boldsymbol{\Omega}}_f)} - \boldsymbol{T}_{fl}\widetilde{(\boldsymbol{I}_d^G\boldsymbol{T}_{lf}\dot{\boldsymbol{\Omega}}_f)}]\boldsymbol{\theta} \\
& -\boldsymbol{T}_{fl}'[\boldsymbol{K}_{21}(\tilde{\boldsymbol{e}}_1\boldsymbol{\theta} + \tilde{\boldsymbol{k}}_l\boldsymbol{u}_l + \boldsymbol{u}_l') + \boldsymbol{K}_{22}(\tilde{\boldsymbol{k}}_l\boldsymbol{\theta} + \boldsymbol{\theta}')] \\
& -\boldsymbol{T}_{fl}[\boldsymbol{K}_{21}(\tilde{\boldsymbol{e}}_1\boldsymbol{\theta} + \tilde{\boldsymbol{k}}_l\boldsymbol{u}_l + \boldsymbol{u}_l') + \boldsymbol{K}_{22}(\tilde{\boldsymbol{k}}_l\boldsymbol{\theta} + \boldsymbol{\theta}')]' \\
& +\boldsymbol{T}_{fl}\tilde{\boldsymbol{e}}_d\tilde{\boldsymbol{k}}_l[\boldsymbol{K}_{11}(\tilde{\boldsymbol{e}}_1\boldsymbol{\theta} + \tilde{\boldsymbol{k}}_l\boldsymbol{u}_l + \boldsymbol{u}_l') + \boldsymbol{K}_{12}(\tilde{\boldsymbol{k}}_l\boldsymbol{\theta} + \boldsymbol{\theta}')] \\
& +\boldsymbol{T}_{fl}\tilde{\boldsymbol{e}}_d[\boldsymbol{K}_{11}(\tilde{\boldsymbol{e}}_1\boldsymbol{\theta} + \tilde{\boldsymbol{k}}_l\boldsymbol{u}_l + \boldsymbol{u}_l') + \boldsymbol{K}_{12}(\tilde{\boldsymbol{k}}_l\boldsymbol{\theta} + \boldsymbol{\theta}')]' \\
& -\boldsymbol{T}_{fl}\tilde{\boldsymbol{e}}_1[\boldsymbol{K}_{11}(\tilde{\boldsymbol{e}}_1\boldsymbol{\theta} + \tilde{\boldsymbol{k}}_l\boldsymbol{u}_l + \boldsymbol{u}_l') + \boldsymbol{K}_{12}(\tilde{\boldsymbol{k}}_l\boldsymbol{\theta} + \boldsymbol{\theta}')]
\end{aligned} \tag{2.30}$$

Eqs. (2.29) and (2.30) are the linearized translational and rotational EOM's of MBBT resolved in non-inertial coordinate f. No additional equations are required to solve for the unknown displacements $\boldsymbol{u}_l$ and $\boldsymbol{\theta}$, because the linearized rotation formulations and strain measures have been substituted into the EOM's. Significant engineering insights into moving beam structures can be inferred from Eqs. (2.29) and (2.30): structural coupling between translational and rotational responses is captured by strain measures in the elastic terms, and dynamic coupling between translation and rotation is captured by eccentricity in the inertial terms.

2.3.2 Simplifications for Practical Engineering Cases

Three reduced formulations of linearized MBBT are derived for practical engineering applications. Linearized MBBT is shown to be equivalent to Timoshenko beam theory for straight, non-twisted beams in an inertial coordinate system. Linearized MBBT also can be recognized as an extension of Timoshenko beam theory for more complicated beam structures that have eccentricities, irregular shapes, fully-populated stiffness matrices, or overall rigid-body motion.

2.3.2.1 Beams in Inertial Frames

Coordinate f becomes an inertial system if $\boldsymbol{a}_f^W = \boldsymbol{0}$, $\boldsymbol{\Omega}_f = \boldsymbol{0}$, and $\dot{\boldsymbol{\Omega}}_f = \boldsymbol{0}$. The EOM's for beams in an inertial coordinate system can be simplified from Eqs. (2.29) and (2.30):

$$\begin{aligned} \boldsymbol{F}_f^{ext} \approx\ & m\boldsymbol{T}_{fl}\ddot{\boldsymbol{u}}_l - m\boldsymbol{T}_{fl}\tilde{\boldsymbol{e}}_d\ddot{\boldsymbol{\theta}} \\ & -\boldsymbol{T}_{fl}'[\boldsymbol{K}_{11}(\tilde{\boldsymbol{e}}_1\boldsymbol{\theta} + \tilde{\boldsymbol{k}}_l\boldsymbol{u}_l + \boldsymbol{u}_l') + \boldsymbol{K}_{12}(\tilde{\boldsymbol{k}}_l\boldsymbol{\theta} + \boldsymbol{\theta}')] \\ & -\boldsymbol{T}_{fl}[\boldsymbol{K}_{11}(\tilde{\boldsymbol{e}}_1\boldsymbol{\theta} + \tilde{\boldsymbol{k}}_l\boldsymbol{u}_l + \boldsymbol{u}_l') + \boldsymbol{K}_{12}(\tilde{\boldsymbol{k}}_l\boldsymbol{\theta} + \boldsymbol{\theta}')]' \end{aligned} \tag{2.31}$$

$$\begin{aligned} \boldsymbol{M}_f^{ext,G} \approx\ & \boldsymbol{T}_{fl}\boldsymbol{I}_d^G\ddot{\boldsymbol{\theta}} \\ & -\boldsymbol{T}_{fl}'[\boldsymbol{K}_{21}(\tilde{\boldsymbol{e}}_1\boldsymbol{\theta} + \tilde{\boldsymbol{k}}_l\boldsymbol{u}_l + \boldsymbol{u}_l') + \boldsymbol{K}_{22}(\tilde{\boldsymbol{k}}_l\boldsymbol{\theta} + \boldsymbol{\theta}')] \\ & -\boldsymbol{T}_{fl}[\boldsymbol{K}_{21}(\tilde{\boldsymbol{e}}_1\boldsymbol{\theta} + \tilde{\boldsymbol{k}}_l\boldsymbol{u}_l + \boldsymbol{u}_l') + \boldsymbol{K}_{22}(\tilde{\boldsymbol{k}}_l\boldsymbol{\theta} + \boldsymbol{\theta}')]' \\ & +\boldsymbol{T}_{fl}\tilde{\boldsymbol{e}}_d\tilde{\boldsymbol{k}}_l[\boldsymbol{K}_{11}(\tilde{\boldsymbol{e}}_1\boldsymbol{\theta} + \tilde{\boldsymbol{k}}_l\boldsymbol{u}_l + \boldsymbol{u}_l') + \boldsymbol{K}_{12}(\tilde{\boldsymbol{k}}_l\boldsymbol{\theta} + \boldsymbol{\theta}')] \\ & +\boldsymbol{T}_{fl}\tilde{\boldsymbol{e}}_d[\boldsymbol{K}_{11}(\tilde{\boldsymbol{e}}_1\boldsymbol{\theta} + \tilde{\boldsymbol{k}}_l\boldsymbol{u}_l + \boldsymbol{u}_l') + \boldsymbol{K}_{12}(\tilde{\boldsymbol{k}}_l\boldsymbol{\theta} + \boldsymbol{\theta}')]' \\ & -\boldsymbol{T}_{fl}\tilde{\boldsymbol{e}}_1[\boldsymbol{K}_{11}(\tilde{\boldsymbol{e}}_1\boldsymbol{\theta} + \tilde{\boldsymbol{k}}_l\boldsymbol{u}_l + \boldsymbol{u}_l') + \boldsymbol{K}_{12}(\tilde{\boldsymbol{k}}_l\boldsymbol{\theta} + \boldsymbol{\theta}')] \end{aligned} \tag{2.32}$$

2.3.2.2 Straight Beams without Initial Curve or Twist

The EOM's for beams in an inertial coordinate system can be further simplified if the beam is straight, such that local undeformed coordinate l is aligned with Cartesian coordinate system xyz.

Substituting $\boldsymbol{T}_{fl} = \boldsymbol{I}$ and $\boldsymbol{k}_l = \boldsymbol{0}$ into Eqs. (2.31) and (2.32) yields:

$$\boldsymbol{F}_l^{ext} \approx m\ddot{\boldsymbol{u}}_l - m\tilde{\boldsymbol{e}}_d\ddot{\boldsymbol{\theta}} - [\boldsymbol{K}_{11}(\tilde{\boldsymbol{e}}_1\boldsymbol{\theta} + \boldsymbol{u}_l') + \boldsymbol{K}_{12}\boldsymbol{\theta}']' \tag{2.33}$$

$$\begin{aligned}\boldsymbol{M}_l^{ext,G} \approx\ & \boldsymbol{I}_d^G\ddot{\boldsymbol{\theta}} - [\boldsymbol{K}_{21}(\tilde{\boldsymbol{e}}_1\boldsymbol{\theta} + \boldsymbol{u}_l') + \boldsymbol{K}_{22}\boldsymbol{\theta}']' \\ & + \tilde{\boldsymbol{e}}_d[\boldsymbol{K}_{11}(\tilde{\boldsymbol{e}}_1\boldsymbol{\theta} + \boldsymbol{u}_l') + \boldsymbol{K}_{12}\boldsymbol{\theta}']' \\ & - \tilde{\boldsymbol{e}}_1[\boldsymbol{K}_{11}(\tilde{\boldsymbol{e}}_1\boldsymbol{\theta} + \boldsymbol{u}_l') + \boldsymbol{K}_{12}\boldsymbol{\theta}']\end{aligned} \tag{2.34}$$

Eqs. (2.33) and (2.34) can be simplified further if the beam is symmetric such that eccentricity is zero ($\boldsymbol{e}_d = \boldsymbol{0}$):

$$\boldsymbol{F}_l^{ext} \approx m\ddot{\boldsymbol{u}}_l - \boldsymbol{K}_{11}'(\tilde{\boldsymbol{e}}_1\boldsymbol{\theta} + \boldsymbol{u}_l') - \boldsymbol{K}_{11}(\tilde{\boldsymbol{e}}_1\boldsymbol{\theta} + \boldsymbol{u}_l')' \tag{2.35}$$

$$\boldsymbol{M}_l^{ext} \approx \boldsymbol{I}_d^G\ddot{\boldsymbol{\theta}} - \boldsymbol{K}_{22}'\boldsymbol{\theta}' - \boldsymbol{K}_{22}\boldsymbol{\theta}'' - \tilde{\boldsymbol{e}}_1\boldsymbol{K}_{11}(\tilde{\boldsymbol{e}}_1\boldsymbol{\theta} + \boldsymbol{u}_l') \tag{2.36}$$

2.3.2.3 2D Beams Having Negligible Axial Deformation

The EOM's represented by Eqs. (2.35) and (2.36) can be simplified further if axial force and deformation are negligible. The resulting equations are applicable to straight 2D beams with loading limited to shear and bending in xy-plane. Eqs. (2.37) and (2.38) are commonly used to represent Timoshenko beam theory:

$$m\frac{\partial^2 u_y}{\partial t^2} - F_y^{ext}(x,t) \approx \frac{\partial}{\partial x}[K_1(\frac{\partial u_y}{\partial x} - \theta_z)] \tag{2.37}$$

$$I_{zz}\frac{\partial^2 \theta_z}{\partial t^2} - M_z^{ext}(x,t) \approx \frac{\partial}{\partial x}(K_2\frac{\partial \theta_z}{\partial x}) + K_1(\frac{\partial u_y}{\partial x} - \theta_z) \tag{2.38}$$

in which I_{zz} is moment of inertia per unit length; x is the beam axis; $K_1 = \kappa AG$ and $K_2 = EI$, where κ is Timoshenko shear coefficient, A is the cross-section area, G is the shear modulus, E is the elastic modulus, and I is the second moment of area.

2.3.3 Spatial Discretization

A spatially discretized model of linearized MBBT is derived to demonstrate that conventional discretization methods can be applied directly to the linearized formulation without special treatment. The FV method is selected because the discretized formulation can be established easily for a control finite volume, as MBBT is based on a conservation law. The discretization could alternatively be done using the FE method, which is more common to structural dynamics, although the discretization would be slightly more complicated.

A finite control volume attached to a deformed beam segment is shown in Fig. 2.3. The jth and (j+1)st cross-sections are end boundaries of the nth segment. The balance of absolute linear momentum is derived for the nth finite volume in integral form:

$$\frac{d}{dt}\int_{s^j}^{s^{j+1}} m(s)\boldsymbol{v}_g^G(s,t)ds = \boldsymbol{F}_g^{n,ext} + \boldsymbol{F}_g^{n,int} \tag{2.39}$$

in which $\boldsymbol{F}_g^{n,ext}$ and $\boldsymbol{F}_g^{n,int}$ are the total external and internal forces exerted on the nth segment, respectively. The total internal force, $\boldsymbol{F}_g^{n,int}$, is the sum of elastic forces applied at the jth and (j+1)st cross-sections, which can be computed using Eq. (2.28). There is no momentum flux term in the right-hand side of Eq. (2.39) because the control volume itself moves and deforms with the beam segment. Substituting Eq. (2.5) into Eq. (2.39), multiplying the resulting equation by $\boldsymbol{T}_{fg}$, and then applying the small-angle and small-strain assumptions (Eqs. (2.22) - (2.27)) yields:

$$\begin{aligned}
&M^n[\boldsymbol{a}_f^W + (\dot{\tilde{\boldsymbol{\Omega}}}_f + \tilde{\boldsymbol{\Omega}}_f\tilde{\boldsymbol{\Omega}}_f)(\boldsymbol{R}_f^n + \boldsymbol{T}_{fl}^n\boldsymbol{e}^n) + (\dot{\tilde{\boldsymbol{\Omega}}}_f + \tilde{\boldsymbol{\Omega}}_f\tilde{\boldsymbol{\Omega}}_f)\boldsymbol{T}_{fl}^n\boldsymbol{u}_l^n + 2\tilde{\boldsymbol{\Omega}}_f\boldsymbol{T}_{fl}^n\dot{\boldsymbol{u}}_l^n + \boldsymbol{T}_{fl}^n\ddot{\boldsymbol{u}}_l^n \\
&\quad - (\dot{\tilde{\boldsymbol{\Omega}}} + \tilde{\boldsymbol{\Omega}}_f\tilde{\boldsymbol{\Omega}}_f)\boldsymbol{T}_{fl}^n\tilde{\boldsymbol{e}}^n\boldsymbol{\theta}^n - 2\tilde{\boldsymbol{\Omega}}_f\boldsymbol{T}_{fl}^n\tilde{\boldsymbol{e}}^n\dot{\boldsymbol{\theta}}^n - \boldsymbol{T}_{fl}^n\tilde{\boldsymbol{e}}^n\ddot{\boldsymbol{\theta}}^n] \\
&\approx \boldsymbol{F}_f^{n,ext} - \boldsymbol{T}_{fl}^n\boldsymbol{T}_l^{nj}(\boldsymbol{K}_{11}^j\boldsymbol{\gamma}^j + \boldsymbol{K}_{12}^j\boldsymbol{\kappa}^j) + \boldsymbol{T}_{fl}^n\boldsymbol{T}_l^{nj+1}(\boldsymbol{K}_{11}^{j+1}\boldsymbol{\gamma}^{j+1} + \boldsymbol{K}_{12}^{j+1}\boldsymbol{\kappa}^{j+1})
\end{aligned} \tag{2.40}$$

in which M^n is the total mass of the nth segment:

$$M^n = \int_{s^j}^{s^{j+1}} m ds$$

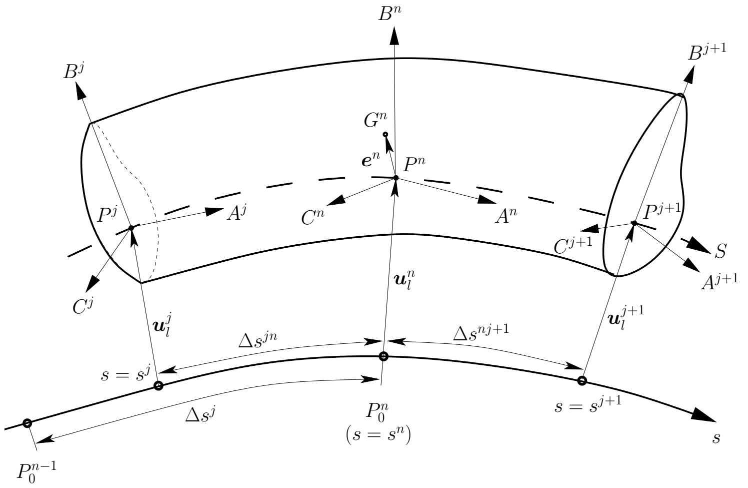

Figure 2.3: The nth beam finite control volume.

$\boldsymbol{R}_f^n$ is the position vector pointing from W to the elastic center P_0^n averaged over the nth segment in the undeformed configuration:

$$\boldsymbol{R}_f^n = \frac{\int_{s^j}^{s^{j+1}} m\boldsymbol{R}^{WP_0} ds}{M^n}$$

$\boldsymbol{T}_{fl}^n$ is the transformation matrix between coordinates f and l averaged over the nth segment:

$$\boldsymbol{T}_{fl}^n = \frac{\int_{s^j}^{s^{j+1}} m\boldsymbol{T}_{fl} ds}{M^n}$$

$\boldsymbol{e}^n$ is the eccentricity averaged over cross-sections along the undeformed nth segment:

$$\boldsymbol{e}^n = \frac{\int_{s^j}^{s^{j+1}} m\boldsymbol{T}_{fl}\boldsymbol{e}_d ds}{\int_{s^j}^{s^{j+1}} m\boldsymbol{T}_{fl} ds}$$

$\boldsymbol{u}_l^n$ is the unknown translational displacement averaged over the nth segment:

$$\boldsymbol{u}_l^n = \frac{\int_{s^j}^{s^{j+1}} m\boldsymbol{T}_{fl}\boldsymbol{u}_l ds}{\int_{s^j}^{s^{j+1}} m\boldsymbol{T}_{fl} ds}$$

$\boldsymbol{\theta}^n$ is the unknown rotational displacement averaged over the nth segment:

$$\boldsymbol{\theta}^n = \frac{\int_{s^j}^{s^{j+1}} m\boldsymbol{T}_{fl}\boldsymbol{\theta} ds}{\int_{s^j}^{s^{j+1}} m\boldsymbol{T}_{fl} ds}$$

$\boldsymbol{F}_f^{n,ext}$ is the sum of external forces exerted on the nth segment measured in coordinate f; $\boldsymbol{T}_l^{nj}$ and $\boldsymbol{T}_l^{nj+1}$ are the transformation matrices among different undeformed local coordinates at s^j, s^n, and s^{j+1}; $\boldsymbol{K}_{11}^j$ and $\boldsymbol{K}_{12}^j$ are the cross-sectional constitutive matrices of the jth cross-section, and vectors $\boldsymbol{\gamma}^j$ and $\boldsymbol{\kappa}^j$ are the linear and angular strains at s^j. Cross-sectional constitutive matrices, M^n, $\boldsymbol{R}_f^n$, $\boldsymbol{T}_{fl}^n$, $\boldsymbol{T}_l^{nj}$, $\boldsymbol{T}_l^{nj+1}$, and $\boldsymbol{e}^n$ are known constants related only to the undeformed beam properties.

A deformed local coordinate, d^n, is introduced with origin fixed to P^n and Cartesian coordinates $\boldsymbol{A}^n\boldsymbol{B}^n\boldsymbol{C}^n$ (Fig. 2.3). The translation and rotation of coordinate d^n are specified by the averaged displacements, $\boldsymbol{u}_l^n$ and $\boldsymbol{\theta}^n$. The mass moment of inertia of the nth finite control volume, $\boldsymbol{I}_{d^n}^n$, is evaluated in coordinate d^n about the center of mass, G^n.

The mass moment $\boldsymbol{I}_{d^n}^n$ is generally a time-dependent parameter that has a nonlinear relationship with the instantaneous deformation of the nth segment, but which can reasonably be assumed constant for most structural applications having relatively small finite segments and small strains. The balance of absolute angular momentum for the nth segment similarly is derived in a linear, discretized form by setting $\boldsymbol{I}_{d^n}^n$ to a constant value of $\boldsymbol{I}^n$:

$$\begin{aligned}
&\tilde{\boldsymbol{\Omega}}_f\boldsymbol{T}_{fl}^n\boldsymbol{I}^n\boldsymbol{T}_{lf}^n\boldsymbol{\Omega}_f + \boldsymbol{T}_{fl}^n\boldsymbol{I}^n\boldsymbol{T}_{lf}^n\dot{\boldsymbol{\Omega}}_f + \boldsymbol{T}_{fl}^n\boldsymbol{I}^n\ddot{\boldsymbol{\theta}}^n + [\tilde{\boldsymbol{\Omega}}_f\boldsymbol{T}_{fl}^n\boldsymbol{I}^n + \boldsymbol{T}_{fl}^n\boldsymbol{I}^n(\widetilde{\boldsymbol{T}_{lf}^n\boldsymbol{\Omega}_f}) - \boldsymbol{T}_{fl}^n(\widetilde{\boldsymbol{I}^n\boldsymbol{T}_{lf}^n\boldsymbol{\Omega}_f})]\dot{\boldsymbol{\theta}}^n \\
&+[\tilde{\boldsymbol{\Omega}}_f\boldsymbol{T}_{fl}^n\boldsymbol{I}^n(\widetilde{\boldsymbol{T}_{lf}^n\boldsymbol{\Omega}_f}) - \tilde{\boldsymbol{\Omega}}_f\boldsymbol{T}_{fl}^n(\widetilde{\boldsymbol{I}^n\boldsymbol{T}_{lf}^n\boldsymbol{\Omega}_f})]\boldsymbol{\theta}^n + [\boldsymbol{T}_{fl}^n\boldsymbol{I}^n(\widetilde{\boldsymbol{T}_{lf}^n\dot{\boldsymbol{\Omega}}_f}) - \boldsymbol{T}_{fl}^n(\widetilde{\boldsymbol{I}^n\boldsymbol{T}_{lf}^n\dot{\boldsymbol{\Omega}}_f})]\boldsymbol{\theta}^n \\
\approx\ &\boldsymbol{M}_f^{n,ext} + \boldsymbol{T}_{fl}^n(\tilde{\boldsymbol{e}}^n + \tilde{\boldsymbol{R}}_l^{P^jP^n})\boldsymbol{T}_l^{nj}(\boldsymbol{K}_{11}^j\boldsymbol{\gamma}^j + \boldsymbol{K}_{12}^j\boldsymbol{\kappa}^j) \\
&-\boldsymbol{T}_{fl}^n(\tilde{\boldsymbol{e}}^n - \tilde{\boldsymbol{R}}_l^{P^nP^{j+1}})\boldsymbol{T}_l^{nj+1}(\boldsymbol{K}_{11}^{j+1}\boldsymbol{\gamma}^{j+1} + \boldsymbol{K}_{12}^{j+1}\boldsymbol{\kappa}^{j+1}) \\
&-\boldsymbol{T}_{fl}^n\boldsymbol{T}_l^{nj}(\boldsymbol{K}_{21}^j\boldsymbol{\gamma}^j + \boldsymbol{K}_{22}^j\boldsymbol{\kappa}^j) + \boldsymbol{T}_{fl}^n\boldsymbol{T}_l^{nj+1}(\boldsymbol{K}_{21}^{j+1}\boldsymbol{\gamma}^{j+1} + \boldsymbol{K}_{22}^{j+1}\boldsymbol{\kappa}^{j+1}) \qquad (2.41)
\end{aligned}$$

where $\boldsymbol{M}_f^{n,ext}$ is the sum of external moments acting on the nth segment about the center of mass; $\boldsymbol{K}_{21}^j$ and $\boldsymbol{K}_{22}^j$ are the cross-sectional constitutive matrices of the jth cross-section, and $\boldsymbol{R}_l^{P^jP^n}$ and

$\boldsymbol{R}_l^{P^n P^{j+1}}$ are vectors pointing from elastic centers P^j to P^n and from P^n to P^{j+1}, respectively. Eqs. (2.40) and (2.41) are discretized FV formulations of the EOM's of linearized MBBT.

2.4 Piecewise-linear MBBT

A special formulation of MBBT is developed that allows application of linearized dynamic theory to large nonlinear structural displacements. Two critical advantages of the new MBBT over exiting GEBT formulations are the capacity for rational linearization of the EOM's and for expression of the EOM's relative to arbitrary non-inertial frames. The combined strength of these two capabilities enables development of a piecewise-linear version of MBBT using a separation of displacement technique. The piecewise-linear MBBT can be implemented in the time-domain when the incremental rotation within each time-step conforms to small-angle assumptions.

2.4.1 Theory

The theoretical basis of separation of displacements is to express the total deformation at any time as a sum of a quasi-static base configuration plus dynamic displacements relative to that base. This separation of displacements is a purely mathematical manipulation: an arbitrary beam configuration without any particular physical significance can be selected as the base configuration and considered to be quasi-static; the time derivatives of the dynamic displacements represent the total velocities and accelerations resulting from deformation. Selection of a base configuration such that dynamic rotations are sufficiently small for application of small-angle assumptions allows linearized MBBT to be used to solve for dynamic displacements, while nonlinearities associated with large displacements can be preserved for the base configuration.

The total translational and rotational displacements are each separated into a quasi-static displacement plus a dynamic displacement:

$$\boldsymbol{u}_l(s,t) = \boldsymbol{U}_l(s) + \boldsymbol{u}_l^*(s,t) \tag{2.42}$$

$$\boldsymbol{\phi}_l(s,t) = \boldsymbol{\Phi}_l(s) + \boldsymbol{\phi}_l^*(s,t) \tag{2.43}$$

in which $\boldsymbol{U}_l(s)$ is the quasi-static portion of the translational displacement measured from undeformed coordinate l; $\boldsymbol{u}_l^*(s,t)$ is the dynamic part of the translational displacement; total rotation vector $\boldsymbol{\phi}_l(s,t)$ describes the rotation of a differential element from its undeformed to deformed configurations; rotation vector $\boldsymbol{\Phi}_l(s)$ represents the rotation from the undeformed configuration to the base configuration, and vector $\boldsymbol{\phi}_l^*(s,t)$ is the dynamic rotation vector.

The base configuration is represented by an additional curvilinear coordinate system denoted as coordinate Q (Fig. 2.4). Coordinate Q shares the same origin as curvilinear coordinates s and S, but its curvilinear axis is through each cross-sectional elastic center for a prescribed base configuration. Coordinate Q is displaced from s by constant displacement $\boldsymbol{U}_l(s)$. A local element-fixed Cartesian coordinate system, $\boldsymbol{a}^*\boldsymbol{b}^*\boldsymbol{c}^*$, is introduced as coordinate q, with origin at the elastic center P^* and with directions described by rotation vector $\boldsymbol{\Phi}_l(s)$ (Fig. 2.4). The transformation matrices between coordinate q and coordinates l and d are given by $\boldsymbol{T}_{ld} = \boldsymbol{T}_{lq}\boldsymbol{T}_{qd}$ and $\boldsymbol{T}_{dl} = \boldsymbol{T}_{dq}\boldsymbol{T}_{ql}$. Eq. (2.42) is rewritten as:

$$\boldsymbol{u}_l(s,t) = \boldsymbol{U}_l(s) + \boldsymbol{T}_{lq}(s)\boldsymbol{u}_q^*(s,t) \tag{2.44}$$

in which $\boldsymbol{u}_q^* = [u_1^*, u_2^*, u_3^*]^T$ is the dynamic translational displacement measured in coordinate q. Taking time derivatives of Eq. (2.44) yields the translational velocity and acceleration:

$$\boldsymbol{v}_l = \frac{\partial}{\partial t}(\boldsymbol{U}_l + \boldsymbol{T}_{lq}\boldsymbol{u}_q^*) = \boldsymbol{T}_{lq}\dot{\boldsymbol{u}}_q^* \tag{2.45}$$

$$\boldsymbol{a}_l = \frac{\partial^2}{\partial t^2}(\boldsymbol{U}_l + \boldsymbol{T}_{lq}\boldsymbol{u}_q^*) = \boldsymbol{T}_{lq}\ddot{\boldsymbol{u}}_q^* \tag{2.46}$$

where $\dot{\boldsymbol{U}}_l = \ddot{\boldsymbol{U}}_l = \boldsymbol{0}$, and $\dot{\boldsymbol{T}}_{lq} = \ddot{\boldsymbol{T}}_{lq} = \boldsymbol{0}$.

Application of small-angle assumptions to Euler angles of the dynamic rotational displacements $(\theta_1^*, \theta_2^*, \theta_3^*)$ measured in coordinate q yields: $\boldsymbol{\phi}_q^* \approx \boldsymbol{\theta}^*$; $\boldsymbol{T}_{qd} \approx \boldsymbol{I} + \tilde{\boldsymbol{\theta}}^*$; $\boldsymbol{T}_{dq} \approx \boldsymbol{I} - \tilde{\boldsymbol{\theta}}^*$; $\boldsymbol{\omega}_d \approx \dot{\boldsymbol{\theta}}^*$, and $\dot{\boldsymbol{\omega}}_d \approx \ddot{\boldsymbol{\theta}}^*$.

Computation of strain measures necessarily is based on the total deformation including both quasi-static and dynamic displacements. The strain measures associated with the base config-

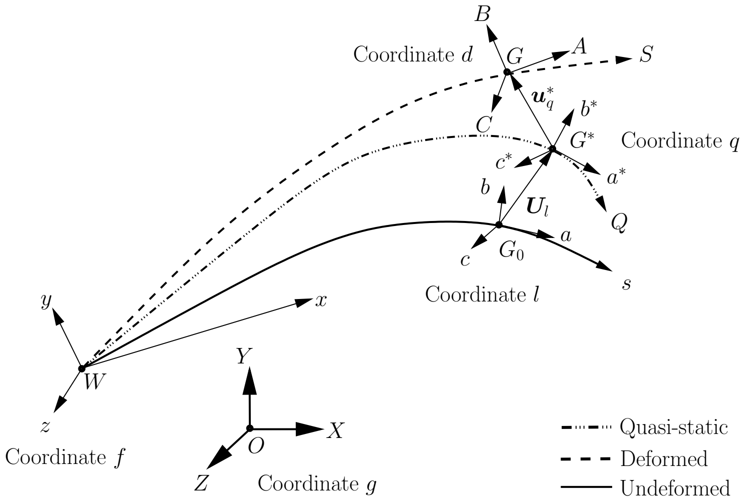

Figure 2.4: Base configuration and coordinate systems of a beam.

uration are computed using nonlinear strain and Euler angle formulation. The strain measures associated with dynamic displacements can be linearized about the base configuration by applying small-angle assumptions to the dynamic rotations. The total curvature vector is computed as:

$$\tilde{\boldsymbol{k}}_d = \boldsymbol{T}_{dl}\boldsymbol{T}_{lf}\boldsymbol{T}'_{fl}\boldsymbol{T}_{ld} + \boldsymbol{T}_{dl}\boldsymbol{T}'_{ld} \approx \tilde{\boldsymbol{k}}_q - \tilde{\boldsymbol{\theta}}^*\tilde{\boldsymbol{k}}_q + \tilde{\boldsymbol{k}}_q\tilde{\boldsymbol{\theta}}^* + \tilde{\boldsymbol{\theta}}^{*'} \tag{2.47}$$

in which $\tilde{\boldsymbol{k}}_q = \boldsymbol{T}_{qf}\boldsymbol{T}'_{fq} = \boldsymbol{T}_{ql}\boldsymbol{T}_{lf}\boldsymbol{T}'_{fl}\boldsymbol{T}_{lq} + \boldsymbol{T}_{ql}\boldsymbol{T}'_{lq}$ is the skew-symmetric matrix of the local curvature vector of the base configuration measured in coordinate q. Angular strain is linearized about the base configuration and is computed by substituting Eq. (2.47) into Eq. (2.11):

$$\boldsymbol{\kappa} = \text{axial}(\tilde{\boldsymbol{k}}_d - \tilde{\boldsymbol{k}}_l) \approx \boldsymbol{\kappa}_q + \tilde{\boldsymbol{k}}_q\boldsymbol{\theta}^* + \boldsymbol{\theta}^{*'} \tag{2.48}$$

where $\boldsymbol{\kappa}_q = \boldsymbol{k}_q - \boldsymbol{k}_l$ is the angular strain caused by deflection of base configuration.

The linear strain is treated in a similar fashion: substituting Eq. (2.44) into Eq. (2.12) assuming small dynamic angles. Linearizing the resulting equation yields an expression for strain linearized about the base configuration:

$$\boldsymbol{\gamma} \approx \boldsymbol{\gamma}_q + (\tilde{\boldsymbol{\gamma}}_q + \tilde{\boldsymbol{e}}_1)\boldsymbol{\theta}^* + \tilde{\boldsymbol{k}}_q \boldsymbol{u}_q^* + \boldsymbol{u}_q^{*'} \tag{2.49}$$

c in which $\boldsymbol{\gamma}_q = \boldsymbol{T}_{ql}(\boldsymbol{e}_1 + \tilde{\boldsymbol{k}}_l \boldsymbol{U}_l + \boldsymbol{U}_l') - \boldsymbol{e}_1$ is the strain caused by base configuration deflections.

Substituting Eqs. (2.44) - (2.46) into the nonlinear EOM's of Eqs. (2.17) - (2.18) yields the governing EOM's including separation of displacements. The resulting EOM's are linearized by applying small-angle assumptions, substituting (2.48) - (2.49), and then neglecting the second- and higher-order terms in dynamic displacements:

$$\begin{aligned}
\boldsymbol{F}_f^{ext} \approx m[&\boldsymbol{a}_f^B + (\dot{\tilde{\boldsymbol{\Omega}}} + \tilde{\boldsymbol{\Omega}}_f\tilde{\boldsymbol{\Omega}}_f)(\boldsymbol{R}_f^{WP_0} + \boldsymbol{T}_{fl}\boldsymbol{U}_l + \boldsymbol{T}_{fq}\boldsymbol{e}_d) \\
&+ (\dot{\tilde{\boldsymbol{\Omega}}}_f + \tilde{\boldsymbol{\Omega}}_f\tilde{\boldsymbol{\Omega}}_f)\boldsymbol{T}_{fq}\boldsymbol{u}_q^* + 2\tilde{\boldsymbol{\Omega}}_f\boldsymbol{T}_{fq}\dot{\boldsymbol{u}}_q^* + \boldsymbol{T}_{fq}\ddot{\boldsymbol{u}}_q^* \\
&- (\dot{\tilde{\boldsymbol{\Omega}}}_f + \tilde{\boldsymbol{\Omega}}_f\tilde{\boldsymbol{\Omega}}_f)\boldsymbol{T}_{fq}\tilde{\boldsymbol{e}}_d\boldsymbol{\theta}^* - 2\tilde{\boldsymbol{\Omega}}_f\boldsymbol{T}_{fq}\tilde{\boldsymbol{e}}_d\dot{\boldsymbol{\theta}}^* - \boldsymbol{T}_{fq}\tilde{\boldsymbol{e}}_d\ddot{\boldsymbol{\theta}}^*] \\
&- \boldsymbol{T}_{fq}'[\boldsymbol{K}_{11}(\boldsymbol{\gamma}_q + \tilde{\boldsymbol{\gamma}}_q\boldsymbol{\theta}^* + \tilde{\boldsymbol{e}}_1\boldsymbol{\theta}^* + \tilde{\boldsymbol{k}}_q\boldsymbol{u}_q^* + \boldsymbol{u}_q^{*'}) + \boldsymbol{K}_{12}(\boldsymbol{k}_q - \boldsymbol{k}_l + \tilde{\boldsymbol{k}}_q\boldsymbol{\theta}^* + \boldsymbol{\theta}^{*'})] \\
&- \boldsymbol{T}_{fq}[\boldsymbol{K}_{11}(\boldsymbol{\gamma}_q + \tilde{\boldsymbol{\gamma}}_q\boldsymbol{\theta}^* + \tilde{\boldsymbol{e}}_1\boldsymbol{\theta}^* + \tilde{\boldsymbol{k}}_q\boldsymbol{u}_q^* + \boldsymbol{u}_q^{*'}) + \boldsymbol{K}_{12}(\boldsymbol{k}_q - \boldsymbol{k}_l + \tilde{\boldsymbol{k}}_q\boldsymbol{\theta}^* + \boldsymbol{\theta}^{*'})]'
\end{aligned} \tag{2.50}$$

$$\begin{aligned}
\boldsymbol{M}_f^{ext,G} \approx &\tilde{\boldsymbol{\Omega}}_f\boldsymbol{T}_{fq}\boldsymbol{I}_d^G\boldsymbol{T}_{qf}\boldsymbol{\Omega}_f + \boldsymbol{T}_{fq}\boldsymbol{I}_d^G\boldsymbol{T}_{qf}\dot{\boldsymbol{\Omega}}_f + \boldsymbol{T}_{fq}\boldsymbol{I}_d^G\ddot{\boldsymbol{\theta}}^* \\
&+[\tilde{\boldsymbol{\Omega}}_f\boldsymbol{T}_{fq}\boldsymbol{I}_d^G - \boldsymbol{T}_{fq}(\widetilde{\boldsymbol{I}_d^G\boldsymbol{T}_{qf}\boldsymbol{\Omega}_f}) + \boldsymbol{T}_{fq}\boldsymbol{I}_d^G(\widetilde{\boldsymbol{T}_{qf}\boldsymbol{\Omega}_f})]\dot{\boldsymbol{\theta}}^* \\
&+[\tilde{\boldsymbol{\Omega}}_f\boldsymbol{T}_{fq}\boldsymbol{I}_d^G(\widetilde{\boldsymbol{T}_{qf}\boldsymbol{\Omega}_f}) - \tilde{\boldsymbol{\Omega}}_f\boldsymbol{T}_{fq}(\widetilde{\boldsymbol{I}_d^G\boldsymbol{T}_{qf}\boldsymbol{\Omega}_f})]\boldsymbol{\theta}^* + [\boldsymbol{T}_{fq}\boldsymbol{I}_d^G(\widetilde{\boldsymbol{T}_{qf}\dot{\boldsymbol{\Omega}}_f}) - \boldsymbol{T}_{fq}(\widetilde{\boldsymbol{I}_d^G\boldsymbol{T}_{qf}\dot{\boldsymbol{\Omega}}_f})]\boldsymbol{\theta}^* \\
&-\boldsymbol{T}_{fq}'[\boldsymbol{K}_{21}(\boldsymbol{\gamma}_q + \tilde{\boldsymbol{\gamma}}_q\boldsymbol{\theta}^* + \tilde{\boldsymbol{e}}_1\boldsymbol{\theta}^* + \tilde{\boldsymbol{k}}_q\boldsymbol{u}_q^* + \boldsymbol{u}_q^{*'}) + \boldsymbol{K}_{22}(\boldsymbol{k}_q - \boldsymbol{k}_l + \tilde{\boldsymbol{k}}_q\boldsymbol{\theta}^* + \boldsymbol{\theta}^{*'})] \\
&-\boldsymbol{T}_{fq}[\boldsymbol{K}_{21}(\boldsymbol{\gamma}_q + \tilde{\boldsymbol{\gamma}}_q\boldsymbol{\theta}^* + \tilde{\boldsymbol{e}}_1\boldsymbol{\theta}^* + \tilde{\boldsymbol{k}}_q\boldsymbol{u}_q^* + \boldsymbol{u}_q^{*'}) + \boldsymbol{K}_{22}(\boldsymbol{k}_q - \boldsymbol{k}_l + \tilde{\boldsymbol{k}}_q\boldsymbol{\theta}^* + \boldsymbol{\theta}^{*'})]' \\
&+\boldsymbol{T}_{fq}\tilde{\boldsymbol{e}}_d\tilde{\boldsymbol{k}}_q[\boldsymbol{K}_{11}(\boldsymbol{\gamma}_q + \tilde{\boldsymbol{\gamma}}_q\boldsymbol{\theta}^* + \tilde{\boldsymbol{e}}_1\boldsymbol{\theta}^* + \tilde{\boldsymbol{k}}_q\boldsymbol{u}_q^* + \boldsymbol{u}_q^{*'}) + \boldsymbol{K}_{12}(\boldsymbol{k}_q - \boldsymbol{k}_l + \tilde{\boldsymbol{k}}_q\boldsymbol{\theta}^* + \boldsymbol{\theta}^{*'})] \\
&+\boldsymbol{T}_{fq}\tilde{\boldsymbol{e}}_d[\boldsymbol{K}_{11}(\boldsymbol{\gamma}_q + \tilde{\boldsymbol{\gamma}}_q\boldsymbol{\theta}^* + \tilde{\boldsymbol{e}}_1\boldsymbol{\theta}^* + \tilde{\boldsymbol{k}}_q\boldsymbol{u}_q^* + \boldsymbol{u}_q^{*'}) + \boldsymbol{K}_{12}(\boldsymbol{k}_q - \boldsymbol{k}_l + \tilde{\boldsymbol{k}}_q\boldsymbol{\theta}^* + \boldsymbol{\theta}^{*'})]' \\
&-\boldsymbol{T}_{fq}(\tilde{\boldsymbol{\gamma}}_q + \tilde{\boldsymbol{e}}_1)[\boldsymbol{K}_{11}(\boldsymbol{\gamma}_q + \tilde{\boldsymbol{\gamma}}_q\boldsymbol{\theta}^* + \tilde{\boldsymbol{e}}_1\boldsymbol{\theta}^* + \tilde{\boldsymbol{k}}_q\boldsymbol{u}_q^* + \boldsymbol{u}_q^{*'}) + \boldsymbol{K}_{12}(\boldsymbol{k}_q - \boldsymbol{k}_l + \tilde{\boldsymbol{k}}_q\boldsymbol{\theta}^* + \boldsymbol{\theta}^{*'})]
\end{aligned} \tag{2.51}$$

in which $\boldsymbol{T}_{fq} = \boldsymbol{T}_{fl}\boldsymbol{T}_{lq}$. Eqs. (2.50) and (2.51) are a general Lagrangian formulation of the EOM's of MBBT that are linearized about a prescribed base configuration using separation of displacement. Geometric and kinematic nonlinearities are fully preserved for the base configuration. Inertial properties m and $\boldsymbol{I}_d^G$ can be evaluated either for the undeformed configuration, or evaluated for the base configuration such that differential inertial nonlinearities associated with base deformations are also preserved.

2.4.2 Discretized Matrix Formulation

A discretized FV representation of beam motions about a prescribed base configuration is derived from Eqs. (2.50) and (2.51) by applying the FV method, following the same steps as in Section 2.3.3. The resulting linear discretized EOM's are:

$$\begin{aligned}
&M^n[\boldsymbol{a}_f^W + (\dot{\tilde{\boldsymbol{\Omega}}} + \tilde{\boldsymbol{\Omega}}_f\tilde{\boldsymbol{\Omega}}_f)(\boldsymbol{R}_f^n + \boldsymbol{T}_{fl}^n\boldsymbol{U}_l^n + \boldsymbol{T}_{fq}^n\boldsymbol{e}^n) \\
&\quad + (\dot{\tilde{\boldsymbol{\Omega}}}_f + \tilde{\boldsymbol{\Omega}}_f\tilde{\boldsymbol{\Omega}}_f)\boldsymbol{T}_{fq}^n\boldsymbol{u}_q^{*,n} + 2\tilde{\boldsymbol{\Omega}}_f\boldsymbol{T}_{fq}^n\dot{\boldsymbol{u}}_q^{*,n} + \boldsymbol{T}_{fq}^n\ddot{\boldsymbol{u}}_q^{*,n} \\
&\quad - (\dot{\tilde{\boldsymbol{\Omega}}}_f + \tilde{\boldsymbol{\Omega}}_f\tilde{\boldsymbol{\Omega}}_f)\boldsymbol{T}_{fq}^n\tilde{\boldsymbol{e}}^n\boldsymbol{\theta}^{*,n} - 2\tilde{\boldsymbol{\Omega}}_f\boldsymbol{T}_{fq}^n\tilde{\boldsymbol{e}}^n\dot{\boldsymbol{\theta}}^{*,n} - \boldsymbol{T}_{fq}^n\tilde{\boldsymbol{e}}^n\ddot{\boldsymbol{\theta}}^{*,n}] \\
\approx\ &\boldsymbol{F}_f^{n,ext} - \boldsymbol{T}_{fq}^n\boldsymbol{T}_q^{nj}(\boldsymbol{K}_{11}^j\boldsymbol{\gamma}^j + \boldsymbol{K}_{12}^j\boldsymbol{\kappa}^j) + \boldsymbol{T}_{fq}^n\boldsymbol{T}_q^{nj+1}(\boldsymbol{K}_{11}^{j+1}\boldsymbol{\gamma}^{j+1} + \boldsymbol{K}_{12}^{j+1}\boldsymbol{\kappa}^{j+1})
\end{aligned} \tag{2.52}$$

$$\begin{aligned}
&\tilde{\boldsymbol{\Omega}}_f\boldsymbol{T}_{fq}^n\boldsymbol{I}^n\boldsymbol{T}_{qf}^n\boldsymbol{\Omega}_f + \boldsymbol{T}_{fq}^n\boldsymbol{I}^n\boldsymbol{T}_{qf}^n\dot{\boldsymbol{\Omega}}_f + \boldsymbol{T}_{fq}^n\boldsymbol{I}^n\ddot{\boldsymbol{\theta}}^{*,n} \\
&+[\tilde{\boldsymbol{\Omega}}_f\boldsymbol{T}_{fq}^n\boldsymbol{I}^n - \boldsymbol{T}_{fq}^n(\widetilde{\boldsymbol{I}^n\boldsymbol{T}_{qf}^n\boldsymbol{\Omega}_f}) + \boldsymbol{T}_{fq}^n\boldsymbol{I}^n(\widetilde{\boldsymbol{T}_{qf}^n\boldsymbol{\Omega}_f})]\dot{\boldsymbol{\theta}}^{*,n} \\
&+[\tilde{\boldsymbol{\Omega}}_f\boldsymbol{T}_{fq}^n\boldsymbol{I}^n(\widetilde{\boldsymbol{T}_{qf}^n\boldsymbol{\Omega}_f}) - \tilde{\boldsymbol{\Omega}}_f\boldsymbol{T}_{fq}^n(\widetilde{\boldsymbol{I}^n\boldsymbol{T}_{qf}^n\boldsymbol{\Omega}_f})]\boldsymbol{\theta}^{*,n} + [\boldsymbol{T}_{fq}^n\boldsymbol{I}^n(\widetilde{\boldsymbol{T}_{qf}^n\dot{\boldsymbol{\Omega}}_f}) - \boldsymbol{T}_{fq}^n(\widetilde{\boldsymbol{I}^n\boldsymbol{T}_{qf}^n\dot{\boldsymbol{\Omega}}_f})]\boldsymbol{\theta}^{*,n} \\
\approx\ &\boldsymbol{M}_f^{n,ext} + \boldsymbol{T}_{fq}^n(\tilde{\boldsymbol{e}}^n + \tilde{\boldsymbol{R}}_q^{P^jP^n})\boldsymbol{T}_q^{nj}(\boldsymbol{K}_{11}^j\boldsymbol{\gamma}^j + \boldsymbol{K}_{12}^j\boldsymbol{\kappa}^j) \\
&-\boldsymbol{T}_{fq}^n(\tilde{\boldsymbol{e}}^n - \tilde{\boldsymbol{R}}_q^{P^nP^{j+1}})\boldsymbol{T}_q^{nj+1}(\boldsymbol{K}_{11}^{j+1}\boldsymbol{\gamma}^{j+1} + \boldsymbol{K}_{12}^{j+1}\boldsymbol{\kappa}^{j+1}) \\
&-\boldsymbol{T}_{fq}^n\boldsymbol{T}_q^{nj}(\boldsymbol{K}_{21}^j\boldsymbol{\gamma}^j + \boldsymbol{K}_{22}^j\boldsymbol{\kappa}^j) + \boldsymbol{T}_{fq}^n\boldsymbol{T}_q^{nj+1}(\boldsymbol{K}_{21}^{j+1}\boldsymbol{\gamma}^{j+1} + \boldsymbol{K}_{22}^{j+1}\boldsymbol{\kappa}^{j+1})
\end{aligned} \tag{2.53}$$

in which $\boldsymbol{T}_{fq}^n = \frac{1}{M^n}\int_{s^j}^{s^{j+1}} m\boldsymbol{T}_{fl}\boldsymbol{T}_{lq}ds$ is the transformation matrix between coordinates f and q averaged over the nth segment; $\boldsymbol{U}_l^n = \int_{s^j}^{s^{j+1}} m\boldsymbol{T}_{fl}\boldsymbol{U}_l ds / \int_{s^j}^{s^{j+1}} m\boldsymbol{T}_{fl}ds$ is the base translational displacement averaged over the nth segment; $\boldsymbol{u}_q^{*,n} = \int_{s^j}^{s^{j+1}} m\boldsymbol{T}_{fq}\boldsymbol{u}_q^* ds / \int_{s^j}^{s^{j+1}} m\boldsymbol{T}_{fq}ds$ is the unknown averaged dynamic translational displacement of the nth segment, and $\boldsymbol{\theta}^{*,n}=\int_{s^j}^{s^{j+1}} m\boldsymbol{T}_{fq}\boldsymbol{\theta}^* ds / \int_{s^j}^{s^{j+1}} m\boldsymbol{T}_{fq} ds$ is the unknown averaged dynamic rotational displacement of the nth segment. Eqs. (2.52) and (2.53) are equivalent to Eqs. (2.40) and (2.41) with local undeformed coordinate l replaced by coordinate q such that dynamic displacements are relative to a base configuration.

The strain measures in Eqs. (2.52) and (2.53) include the effects associated with base deflections. These strain measures can be computed in a discretized form by applying linear interpolation to Eqs. (2.48) and (2.49).

$$\begin{aligned}
\boldsymbol{\kappa}^j &\approx \boldsymbol{k}_q^j - \boldsymbol{k}_l^j + \tilde{\boldsymbol{k}}_q^j \boldsymbol{\theta}^{*,j} + \frac{\boldsymbol{\theta}^{*,n} - \boldsymbol{\theta}^{*,n-1}}{\Delta s^j} \\
&= \boldsymbol{\kappa}_q^j + \frac{1}{\Delta s^j}(\Delta s^{jn}\tilde{\boldsymbol{k}}_q^j - \boldsymbol{I})\boldsymbol{\theta}^{*,n-1} + \frac{1}{\Delta s^j}(\Delta s^{n-1j}\tilde{\boldsymbol{k}}_q^j + \boldsymbol{I})\boldsymbol{\theta}^{*,n}
\end{aligned} \tag{2.54}$$

$$\begin{aligned}
\boldsymbol{\gamma}^j &\approx \boldsymbol{\gamma}_q^j + (\tilde{\boldsymbol{\gamma}}_q^j + \tilde{\boldsymbol{e}}_1)\boldsymbol{\theta}^{*,j} + \tilde{\boldsymbol{k}}_q^j \boldsymbol{u}_q^{*,j} + \frac{\boldsymbol{u}_q^{*,n} - \boldsymbol{u}_q^{*,n-1}}{\Delta s^j} \\
&= \boldsymbol{\gamma}_q^j + \frac{\Delta s^{jn}}{\Delta s^j}(\tilde{\boldsymbol{\gamma}}_q^j + \tilde{\boldsymbol{e}}_1)\boldsymbol{\theta}^{*,n-1} + \frac{\Delta s^{n-1j}}{\Delta s^j}(\tilde{\boldsymbol{\gamma}}_q^j + \tilde{\boldsymbol{e}}_1)\boldsymbol{\theta}^{*,n} \\
&\quad + \frac{1}{\Delta s^j}(\Delta s^{jn}\tilde{\boldsymbol{k}}_q^j - \boldsymbol{I})\boldsymbol{u}_q^{*,n-1} + \frac{1}{\Delta s^j}(\Delta s^{n-1j}\tilde{\boldsymbol{k}}_q^j + \boldsymbol{I})\boldsymbol{u}_q^{*,n}
\end{aligned} \tag{2.55}$$

where Δs^j, Δs^{n-1j}, Δs^{jn} are curvilinear distances: Δs^j=s^n-s^{n-1}; Δs^{n-1j}=s^j-s^{n-1}; Δs^{jn}=s^n-s^j, and $\boldsymbol{k}_q^j$ is the curvature vector of the prescribed base configuration at s^j (see Fig. 2.3). Eqs. (2.52) and (2.53) can be combined with strain measure interpolations, Eqs. (2.54) and (2.55), and then converted into conventional matrix form:

$$\begin{aligned}
&\left[\boldsymbol{M}_{equ}^n\right]\begin{bmatrix} \ddot{\boldsymbol{u}}_q^{*,n-1} \\ \ddot{\boldsymbol{\theta}}^{*,n-1} \\ \ddot{\boldsymbol{u}}_q^{*,n} \\ \ddot{\boldsymbol{\theta}}^{*,n} \\ \ddot{\boldsymbol{u}}_q^{*,n+1} \\ \ddot{\boldsymbol{\theta}}^{*,n+1} \end{bmatrix} + \left[\boldsymbol{C}_{equ}^n\right]\begin{bmatrix} \dot{\boldsymbol{u}}_q^{*,n-1} \\ \dot{\boldsymbol{\theta}}^{*,n-1} \\ \dot{\boldsymbol{u}}_q^{*,n} \\ \dot{\boldsymbol{\theta}}^{*,n} \\ \dot{\boldsymbol{u}}_q^{*,n+1} \\ \dot{\boldsymbol{\theta}}^{*,n+1} \end{bmatrix} + \left[\boldsymbol{K}_{equ}^n\right]\begin{bmatrix} \boldsymbol{u}_q^{*,n-1} \\ \boldsymbol{\theta}^{*,n-1} \\ \boldsymbol{u}_q^{*,n} \\ \boldsymbol{\theta}^{*,n} \\ \boldsymbol{u}_q^{*,n+1} \\ \boldsymbol{\theta}^{*,n+1} \end{bmatrix} \\
&= \left[\hat{\boldsymbol{F}}_f^{n,ine}\right] + \left[\hat{\boldsymbol{F}}_f^{n,ext}\right] + \left[\hat{\boldsymbol{F}}_f^{n,ela}\right]
\end{aligned} \tag{2.56}$$

The inertial properties of the nth beam segment can be represented as an equivalent mass matrix:

$$\left[\boldsymbol{M}_{equ}^{n}\right] = \begin{bmatrix} \mathbf{0} & \mathbf{0} & \boldsymbol{M}^{n}\boldsymbol{T}_{fq}^{n} & -\boldsymbol{M}^{n}\boldsymbol{T}_{fq}^{n}\tilde{\boldsymbol{e}}^{n} & \mathbf{0} & \mathbf{0} \\ \mathbf{0} & \mathbf{0} & \mathbf{0} & \boldsymbol{T}_{fq}^{n}\boldsymbol{I}^{n} & \mathbf{0} & \mathbf{0} \end{bmatrix} \tag{2.57}$$

where

$$\boldsymbol{M}^{n} = \text{Diag}(M^{n}, M^{n}, M^{n}) = \begin{bmatrix} M^{n} & 0 & 0 \\ 0 & M^{n} & 0 \\ 0 & 0 & M^{n} \end{bmatrix} \tag{2.58}$$

The stiffness properties of the nth beam element can be represented as an equivalent stiffness matrix:

$$\left[\boldsymbol{K}_{equ}^{n}\right] = \left[\boldsymbol{K}_{ela}^{n}\right] + \left[\boldsymbol{K}_{ine}^{n}\right] \tag{2.59}$$

where $[\boldsymbol{K}_{ela}^{n}]$ is the elastic stiffness and $[\boldsymbol{K}_{ine}^{n}]$ is the inertial stiffness representing the inertial effects on stiffness due to overall rigid-body motion. The elastic stiffness matrix can be computed from the cross-sectional constitutive matrices and the geometry of the undeformed configuration.

$$\left[\boldsymbol{K}_{ela}^{n}\right] = \begin{bmatrix} \boldsymbol{K}_{ela,11}^{n} & \boldsymbol{K}_{ela,12}^{n} & \boldsymbol{K}_{ela,13}^{n} & \boldsymbol{K}_{ela,14}^{n} & \boldsymbol{K}_{ela,15}^{n} & \boldsymbol{K}_{ela,16}^{n} \\ \boldsymbol{K}_{ela,21}^{n} & \boldsymbol{K}_{ela,22}^{n} & \boldsymbol{K}_{ela,23}^{n} & \boldsymbol{K}_{ela,24}^{n} & \boldsymbol{K}_{ela,25}^{n} & \boldsymbol{K}_{ela,26}^{n} \end{bmatrix}$$

in which the submatrices are explicitly computed from known structural properties and geometric configurations (see Appendix A). The inertial stiffness matrix can be computed as:

$$\left[\boldsymbol{K}_{ine}^{n}\right] = \begin{bmatrix} \mathbf{0} & \mathbf{0} & \boldsymbol{D}_{13}^{n} & \boldsymbol{D}_{14}^{n} & \mathbf{0} & \mathbf{0} \\ \mathbf{0} & \mathbf{0} & \mathbf{0} & \boldsymbol{D}_{24}^{n} & \mathbf{0} & \mathbf{0} \end{bmatrix} \tag{2.60}$$

where

$$
\begin{aligned}
\boldsymbol{D}^n_{13} &= \boldsymbol{M}^n \dot{\tilde{\boldsymbol{\Omega}}}_f \boldsymbol{T}^n_{fq} + \boldsymbol{M}^n \tilde{\boldsymbol{\Omega}}_f \tilde{\boldsymbol{\Omega}}_f \boldsymbol{T}^n_{fq} \\
\boldsymbol{D}^n_{14} &= -\boldsymbol{M}^n \dot{\tilde{\boldsymbol{\Omega}}}_f \boldsymbol{T}^n_{fq} \tilde{\boldsymbol{e}}^n - \boldsymbol{M}^n \tilde{\boldsymbol{\Omega}}_f \tilde{\boldsymbol{\Omega}}_f \boldsymbol{T}^n_{fq} \tilde{\boldsymbol{e}}^n \\
\boldsymbol{D}^n_{24} &= -\tilde{\boldsymbol{\Omega}}_f \boldsymbol{T}^n_{fq} (\widetilde{\boldsymbol{I}^n \boldsymbol{T}^n_{qf} \boldsymbol{\Omega}_f}) + \tilde{\boldsymbol{\Omega}}_f \boldsymbol{T}^n_{fq} \boldsymbol{I}^n (\widetilde{\boldsymbol{T}^n_{qf} \boldsymbol{\Omega}_f}) - \boldsymbol{T}^n_{fq} (\widetilde{\boldsymbol{I}^n \boldsymbol{T}^n_{qf} \dot{\boldsymbol{\Omega}}_f}) + \boldsymbol{T}^n_{fq} \boldsymbol{I}^n (\widetilde{\boldsymbol{T}^n_{qf} \dot{\boldsymbol{\Omega}}_f})
\end{aligned}
$$

The damping properties of the nth segment can also be represented as an equivalent damping matrix, $\left[\boldsymbol{C}^n_{equ}\right]$. Two types of velocity-proportional forces are accounted for in the effective damping terms. The first type captures conservative inertial effects associated with the overall rigid-body motion of the beam, $[\boldsymbol{C}^n_{ine}]$, which can introduce either positive or negative damping. The second type is traditional nonconservative structural damping, $[\boldsymbol{C}^n_{str}]$. Total effective damping can be assumed to be the sum of these two types, with the latter type proportional to the corresponding stiffness and mass matrices:

$$
\left[\boldsymbol{C}^n_{equ}\right] = [\boldsymbol{C}^n_{ine}] + [\boldsymbol{C}^n_{str}] = [\boldsymbol{C}^n_{ine}] + \mu_K \left[\boldsymbol{K}^n_{ela}\right] + \mu_M \left[\boldsymbol{M}^n_{equ}\right] \tag{2.61}
$$

in which μ_K and μ_M are stiffness and mass damping coefficients, and $[\boldsymbol{C}^n_{ine}]$ is computed as:

$$
[\boldsymbol{C}^n_{ine}] = \begin{bmatrix} \boldsymbol{0} & \boldsymbol{0} & \boldsymbol{C}^n_{13} & \boldsymbol{C}^n_{14} & \boldsymbol{0} & \boldsymbol{0} \\ \boldsymbol{0} & \boldsymbol{0} & \boldsymbol{0} & \boldsymbol{C}^n_{24} & \boldsymbol{0} & \boldsymbol{0} \end{bmatrix} \tag{2.62}
$$

where

$$
\begin{aligned}
\boldsymbol{C}^n_{13} &= 2\boldsymbol{M}^n \tilde{\boldsymbol{\Omega}}_f \boldsymbol{T}^n_{fq} \\
\boldsymbol{C}^n_{14} &= -2\boldsymbol{M}^n \tilde{\boldsymbol{\Omega}}_f \boldsymbol{T}^n_{fq} \tilde{\boldsymbol{e}}^n \\
\boldsymbol{C}^n_{24} &= \tilde{\boldsymbol{\Omega}}_f \boldsymbol{T}^n_{fq} \boldsymbol{I}^n + \boldsymbol{T}^n_{fq} \boldsymbol{I}^n (\widetilde{\boldsymbol{T}^n_{qf} \boldsymbol{\Omega}_f}) - \boldsymbol{T}^n_{fq} (\widetilde{\boldsymbol{I}^n \boldsymbol{T}^n_{qf} \boldsymbol{\Omega}_f})
\end{aligned}
$$

The internal forces and moments include linear contributions due to dynamic displacements plus nonlinear contributions due to base deflections. The linear contributions are represented by $[\boldsymbol{K}_{ela}^{n}]$. The internal forces and moments associated with the base deflections are generally nonlinear and are represented in the right-hand side of Eq. (2.56) by $\left[\hat{\boldsymbol{F}}_{f}^{n,ela}\right] = \left[\boldsymbol{F}_{f}^{n,ela}, \boldsymbol{M}_{f}^{n,ela}\right]^{T}$. Assuming linear elastic constitutive equations enables computation of $\boldsymbol{F}_{f}^{n,ela}$ and $\boldsymbol{M}_{f}^{n,ela}$ using cross-sectional stiffness matrices with base configuration strain measures:

$$\boldsymbol{F}_{f}^{n,ela}=\boldsymbol{T}_{fq}^{n}\boldsymbol{T}_{q}^{nj+1}[\boldsymbol{K}_{11}^{j+1}\boldsymbol{\gamma}_{q}^{j+1}+\boldsymbol{K}_{12}^{j+1}(\boldsymbol{k}_{q}^{j+1}-\boldsymbol{k}_{l}^{j+1})]-\boldsymbol{T}_{fq}^{n}\boldsymbol{T}_{q}^{nj}[\boldsymbol{K}_{11}^{j}\boldsymbol{\gamma}_{q}^{j}+\boldsymbol{K}_{12}^{j}(\boldsymbol{k}_{q}^{j}-\boldsymbol{k}_{l}^{j})] \tag{2.63}$$

$$\begin{aligned}\boldsymbol{M}_{f}^{n,ela}=&\boldsymbol{T}_{fq}^{n}(\tilde{\boldsymbol{e}}^{n}+\tilde{\boldsymbol{R}}_{q}^{P^{j}P^{n}})\boldsymbol{T}_{q}^{nj}[\boldsymbol{K}_{11}^{j}\boldsymbol{\gamma}_{q}^{j}+\boldsymbol{K}_{12}^{j}(\boldsymbol{k}_{q}^{j}-\boldsymbol{k}_{l}^{j})]\\&-\boldsymbol{T}_{fq}^{n}(\tilde{\boldsymbol{e}}^{n}-\tilde{\boldsymbol{R}}_{q}^{P^{n}P^{j+1}})\boldsymbol{T}_{q}^{nj+1}[\boldsymbol{K}_{11}^{j+1}\boldsymbol{\gamma}_{q}^{j+1}+\boldsymbol{K}_{12}^{j+1}(\boldsymbol{k}_{q}^{j+1}-\boldsymbol{k}_{l}^{j+1})]\\&-\boldsymbol{T}_{fq}^{n}\boldsymbol{T}_{q}^{nj}[\boldsymbol{K}_{21}^{j}\boldsymbol{\gamma}_{q}^{j}+\boldsymbol{K}_{22}^{j}(\boldsymbol{k}_{q}^{j}-\boldsymbol{k}_{l}^{j})]+\boldsymbol{T}_{fq}^{n}\boldsymbol{T}_{q}^{nj+1}[\boldsymbol{K}_{21}^{j+1}\boldsymbol{\gamma}_{q}^{j+1}+\boldsymbol{K}_{22}^{j+1}(\boldsymbol{k}_{q}^{j+1}-\boldsymbol{k}_{l}^{j+1})]\end{aligned} \tag{2.64}$$

The other two terms in the right-hand side of Eq. (2.56) represent two distinct quantities: $\left[\hat{\boldsymbol{F}}_{f}^{n,ext}\right] = \left[\boldsymbol{F}_{f}^{n,ext}, \boldsymbol{M}_{f}^{n,ext}\right]^{T}$ represents the externally applied loading on the nth beam segment, and $\left[\hat{\boldsymbol{F}}_{f}^{n,ine}\right] = \left[\boldsymbol{F}_{f}^{n,ine}, \boldsymbol{M}_{f}^{n,ine}\right]^{T}$ represents the inertial loading vector of the nth beam segment. The inertial loading results from the overall rigid-body motion of the beam:

$$\begin{aligned}\boldsymbol{F}_{f}^{n,ine} &= -\boldsymbol{M}^{n}\boldsymbol{a}_{f}^{W}-\boldsymbol{M}^{n}\dot{\tilde{\boldsymbol{\Omega}}}_{f}(\boldsymbol{R}_{f}^{n}+\boldsymbol{T}_{fl}^{n}\boldsymbol{U}_{l}^{n})-\boldsymbol{M}^{n}\dot{\tilde{\boldsymbol{\Omega}}}_{f}\boldsymbol{T}_{fq}^{n}\boldsymbol{e}^{n}\\&\quad -\boldsymbol{M}^{n}\tilde{\boldsymbol{\Omega}}_{f}\tilde{\boldsymbol{\Omega}}_{f}(\boldsymbol{R}_{f}^{n}+\boldsymbol{T}_{fl}^{n}\boldsymbol{U}_{l}^{n})-\boldsymbol{M}^{n}\tilde{\boldsymbol{\Omega}}_{f}\tilde{\boldsymbol{\Omega}}_{f}\boldsymbol{T}_{fq}^{n}\boldsymbol{e}^{n}\end{aligned} \tag{2.65}$$

$$\boldsymbol{M}_{f}^{n,ine} = -\tilde{\boldsymbol{\Omega}}_{f}\boldsymbol{T}_{fq}^{n}\boldsymbol{I}^{n}\boldsymbol{T}_{qf}^{n}\boldsymbol{\Omega}_{f}-\boldsymbol{T}_{fq}^{n}\boldsymbol{I}^{n}\boldsymbol{T}_{qf}^{n}\dot{\boldsymbol{\Omega}}_{f} \tag{2.66}$$

A matrix formulation for the undeformed beam configuration similar to Eq. (2.56) can be similarly obtained through Eqs. (2.57) - (2.66) by replacing $\boldsymbol{T}_{fq}^{n}/\boldsymbol{T}_{qf}^{n}$ with $\boldsymbol{T}_{fl}^{n}/\boldsymbol{T}_{lf}^{n}$, replacing $(\boldsymbol{R}_{f}^{n}+\boldsymbol{T}_{fl}^{n}\boldsymbol{U}_{l}^{n})$ with $\boldsymbol{R}_{f}^{n}$, and letting $\boldsymbol{\kappa}_{q}$ and $\boldsymbol{\gamma}_{q}$ equal to zero.

2.4.3 Implementation

The piecewise-linear MBBT can be implemented in the time-domain as a linearized updated Lagrangian formulation for large-displacement, nonlinear beams using separation of displacements. A time-stepping scheme is developed to solve the assembled system of Eq. (2.56) in which the base configuration for any time-step is selected as the configuration at the end of the prior time-step. Incremental time-steps are sufficiently small such that incremental dynamic displacements can be computed using the linearized MBBT. Quantities that need to be updated for each time-step are: the base translational displacement, ${}^{m}\boldsymbol{U}_l^n$; the transformation matrix between floating coordinate and local base coordinates, ${}^{m}\boldsymbol{T}_{fq}^n$; the transformation matrix between local coordinates along the base configuration, ${}^{m}\boldsymbol{T}_q^{nj}$ and ${}^{m}\boldsymbol{T}_q^{nj+1}$; the strain associated with base deflections, ${}^{m}\boldsymbol{\gamma}_q^j$; the curvature vector of the base configuration, ${}^{m}\boldsymbol{k}_q^j$, and vectors ${}^{m}\boldsymbol{R}_q^{P^jP^n}$ and ${}^{m}\boldsymbol{R}_q^{P^nP^{j+1}}$. The left superscript m denotes the quantity evaluated at the mth time-step; the right superscript indicates locations along the beam, e.g., ${}^{m}\boldsymbol{u}_q^{*,n}$ and ${}^{m}\boldsymbol{\theta}^{*,n}$ are the incremental displacements of the nth beam segment solved at the mth time-step based on the configuration updated from the (m-1)st time-step. These quantities are updated at the end of the mth time-step:

$$ {}^{m}\boldsymbol{T}_{lq}^n = {}^{m-1}\boldsymbol{T}_{lq}^n \, {}^{m}\boldsymbol{T}_{qd}^n = {}^{m-1}\boldsymbol{T}_{lq}^n(\boldsymbol{I} + {}^{m}\tilde{\boldsymbol{\theta}}^{*,n}) \tag{2.67} $$

$$ {}^{m}\boldsymbol{U}_l^n = {}^{m-1}\boldsymbol{U}_l^n + {}^{m}\boldsymbol{T}_{lq}^n \, {}^{m}\boldsymbol{u}_q^{*,n} \tag{2.68} $$

$$ {}^{m}\boldsymbol{T}_{fq}^n = \boldsymbol{T}_{fl}^n \, {}^{m}\boldsymbol{T}_{lq}^n \tag{2.69} $$

$$ {}^{m}\boldsymbol{T}_q^{nj} = {}^{m}\boldsymbol{T}_{ql}^n \, \boldsymbol{T}_l^{nj} \, {}^{m}\boldsymbol{T}_{lq}^j \tag{2.70} $$

$$ {}^{m}\boldsymbol{T}_q^{nj+1} = {}^{m}\boldsymbol{T}_{ql}^n \, \boldsymbol{T}_l^{nj+1} \, {}^{m}\boldsymbol{T}_{lq}^{j+1} \tag{2.71} $$

$$ {}^{m}\boldsymbol{R}_q^{P^jP^n} = {}^{m}\boldsymbol{T}_{ql}^n \, (\boldsymbol{R}_l^{P^jP^n} + {}^{m}\boldsymbol{U}_l^n - \boldsymbol{T}_l^{nj} \, {}^{m}\boldsymbol{U}_l^j) \tag{2.72} $$

$$ {}^{m}\boldsymbol{R}_q^{P^nP^{j+1}} = {}^{m}\boldsymbol{T}_{ql}^n \, (\boldsymbol{R}_l^{P^nP^{j+1}} - {}^{m}\boldsymbol{U}_l^n + \boldsymbol{T}_l^{nj+1} \, {}^{m}\boldsymbol{U}_l^{j+1}) \tag{2.73} $$

$$ {}^{m}\boldsymbol{\gamma}_q^j = {}^{m}\boldsymbol{T}_{ql}^j \left(\boldsymbol{e}_1 + \tilde{\boldsymbol{k}}_l^j \, {}^{m}\boldsymbol{U}_l^j + \frac{{}^{m}\boldsymbol{U}_l^n - {}^{m}\boldsymbol{U}_l^{n-1}}{\Delta s^j} \right) - \boldsymbol{e}_1 \tag{2.74} $$

$$ {}^{m}\tilde{\boldsymbol{k}}_q^j = {}^{m}\boldsymbol{T}_{ql}^j \tilde{\boldsymbol{k}}_l^j \, {}^{m}\boldsymbol{T}_{lq}^j + {}^{m}\boldsymbol{T}_{ql}^j \left(\frac{{}^{m}\boldsymbol{T}_{lq}^n - {}^{m}\boldsymbol{T}_{lq}^{n-1}}{\Delta s^j} \right) \tag{2.75} $$

in which ${}^{m}\boldsymbol{T}_{lq}^{j}$, ${}^{m}\boldsymbol{T}_{ql}^{j}$, and ${}^{m}\boldsymbol{U}_{l}^{j}$ are evaluated at the jth cross-section by linearly interpolating along the s axis:

$${}^{m}\boldsymbol{T}_{lq}^{j}=({}^{m}\boldsymbol{T}_{ql}^{j})^{T} = {}^{m-1}\boldsymbol{T}_{lq}^{j}\left[\frac{\Delta s^{n-1j}(\boldsymbol{I}+{}^{m}\tilde{\boldsymbol{\theta}}^{*,n}) - \Delta s^{jn}(\boldsymbol{I}+{}^{m}\tilde{\boldsymbol{\theta}}^{*,n-1})}{\Delta s^{j}}\right] \tag{2.76}$$

$${}^{m}\boldsymbol{U}_{l}^{j}= {}^{m-1}\boldsymbol{U}_{l}^{j} + {}^{m-1}\boldsymbol{T}_{lq}^{j}\left[\frac{\Delta s^{n-1j}({}^{m}\boldsymbol{u}_{q}^{*,n}) - \Delta s^{jn}({}^{m}\boldsymbol{u}_{q}^{*,n-1})}{\Delta s^{j}}\right] \tag{2.77}$$

The evolving base configuration is updated from the prior time-step including all nonlinear and large-angle effects. The coefficient matrices and loading vectors in Eq. (2.56) are renewed for the (m+1)st time-step at the end of the mth time-step using the updated quantities from Eqs. (2.67) - (2.77). Initial conditions for Eq. (2.56) are also renewed at each time-step. Initial displacements are set to zero because they are relative to the new base configuration. Initial velocities are obtained by transferring the velocities computed at the prior step to the newly updated base coordinates:

$${}^{m+1}_{initial}\dot{\boldsymbol{u}}_{q}^{*,n} = {}^{m}\boldsymbol{T}_{dq}^{n}\;{}^{m}\dot{\boldsymbol{u}}_{q}^{*,n} \tag{2.78}$$

$${}^{m+1}_{initial}\dot{\boldsymbol{\theta}}_{q}^{*,n} = {}^{m}\boldsymbol{T}_{dq}^{n}\;{}^{m}\dot{\boldsymbol{\theta}}_{q}^{*,n} \tag{2.79}$$

An explicit linear system of ordinary differential equations (ODE's) for the (m+1)st time-step is then established by assembling the renewed Eq. (2.56) for all beam segments, which can be solved explicitly for the renewed initial conditions using an existing ODE solver.

2.5 Numerical Examples

Two FV solvers are developed to solve the system of governing equations. The first solver is a piecewise-linear dynamic solver that computes beam motions based on piecewise-linear MBBT using a continuously evolving base configuration. The second solver is a static simplification of the dynamic solver, in which the mass and damping matrices are set to be zero and only the elastic and forcing terms are updated with solution steps. The dynamic solver uses the MATLAB "ode45" numerical integrator to integrate the locally linearized system within each time-step. The resulting incremental dynamic displacements are used to update the base configuration for the next time-step. The relative tolerance of ode45 is set to 10^{-6} in all examples. The fixed- and free-end boundary conditions are considered at cross-sections j=1 and j=N+1, respectively. The fixed end is simulated using an imaginary zeroth beam segment (n=0) at $s = -\Delta s^{11}$ with displacements $\boldsymbol{\theta}^0 = -\boldsymbol{\theta}^1$ and $\boldsymbol{u}_l^0 = -\boldsymbol{u}_l^1$, such that the fixed-end condition is enforced at the first cross-section. The free end is represented by the last cross-section that has zero stiffness: $\boldsymbol{K}_{11}^{N+1} = \boldsymbol{K}_{12}^{N+1} = \boldsymbol{K}_{21}^{N+1} = \boldsymbol{K}_{22}^{N+1} = \mathbf{0}$. A constant mass moment of inertia is selected for each beam segment as the mass moment evaluated for the undeformed segment. Four numerical examples are presented to demonstrate the effectiveness of the proposed MBBT solvers and the underlying theories.

2.5.1 Convergence and Order of Accuracy

The convergence and order of accuracy of the proposed piecewise-linear method are quantitatively verified. The benchmark problem used to verify the spatial convergence is pure bending of a cantilever beam subject to tip moment. This case is an established benchmark for which a nonlinear analytic static solution exists [25]. A straight cantilever beam of length 1 and uniform bending stiffness 2 is subject to static tip moment of 4π. The exact static solution predicts a closed circle with a diameter of $1/2\pi$. The static MBBT solver is used to compute this benchmark problem with seven progressively finer discretization models. The number of equal-length elements in each these beam models is 5, 10, 20, 50, 100, 200, and 500. Starting from the initial straight configuration, the static solver computes element displacements and updates the configuration until the root mean square of the residual of element displacements is less than 10^{-6}. All models are found to reach their convergent solutions within 20 iterations. The convergent solution of each model is compared to the exact solution using the root-mean-square error (RMSE). The RMSE is computed by taking the root mean square (RMS) of the errors between the exact translational element displacements predicted by the analytical circle and the numerical results predicted by MBBT. Fig. 2.5 shows that RMSE decreases with element size with second order of accuracy in spatial discretization.

The same benchmark problem is used to show convergence in temporal discretization. The cantilever beam now is provided with physical properties necessary to quantify dynamic effects:

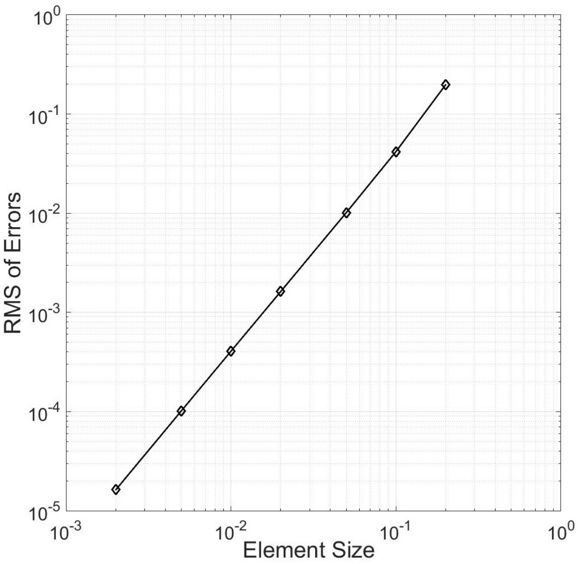

Figure 2.5: Change of root-mean-square error with element size.

the beam is 0.00331 m high, 0.00331 m wide, 1 m long, and is made of steel with Young's modulus of 200 GPa, shear modulus of 79.3 GPa, and density of 7850 kg/m^3. The stiffness and mass damping coefficients are set to 10^{-6} and 0 in the solver, respectively. The beam is discretized into 200 elements, and its deformation from the initial straight configuration at 0.0064 s is computed. The exact dynamic solution is unknown, so the solution computed using time-step size Δt=5×10^{-6} s is treated as a reference solution for analyses of ratios of differences between solutions computed with different time-step sizes. Table 2.1 shows the time-step sizes used and the convergence analyses, in which vector $\boldsymbol{u}_{\Delta t}$ includes all translational element displacements along the beam computed using time-step size of Δt. The results demonstrate the piecewise-linear scheme is consistently convergent in this case but large time-step size can lead to unacceptable solutions (Δt=128×10^{-5} s). The order of accuracy (the last column of Table 2.1) is not constant because the specified time-step is for the base configuration update. The ode45 integrator computes an explicit linear ODE system within each time-step, using a six-stage, fifth-order, Runge-Kutta method with its own adaptive internal steps.

Fig. 2.6 shows the static solutions computed using the 10-element and 200-element discretiza-

Table 2.1: Convergence analysis on time-step size.

Δt (s)	$RMS(\boldsymbol{u}_{\Delta t} - \boldsymbol{u}_{5e-6})$	$\frac{RMS(\boldsymbol{u}_{\Delta t}-\boldsymbol{u}_{5e-6})}{RMS(\boldsymbol{u}_{5e-6})}$	$RMS(\boldsymbol{u}_{\Delta t} - \boldsymbol{u}_{\Delta t/2})$	$\log_2[\frac{RMS(\boldsymbol{u}_{\Delta t}-\boldsymbol{u}_{\Delta t/2})}{RMS(\boldsymbol{u}_{\Delta t/2}-\boldsymbol{u}_{\Delta t/4})}]$
128e-5	7.480e-2	144%	7.913e-2	3.415
64e-5	7.948e-3	15.3%	7.418e-3	2.270
32e-5	1.286e-3	2.48%	1.538e-3	0.268
16e-5	1.014e-3	1.96%	1.277e-3	2.308
8e-5	2.988e-4	0.576%	2.580e-4	2.159
4e-5	6.982e-5	0.135%	5.778e-5	1.524
2e-5	3.308e-5	0.064%	2.009e-5	0.564
1e-5	1.359e-5	0.026%	1.359e-5	–

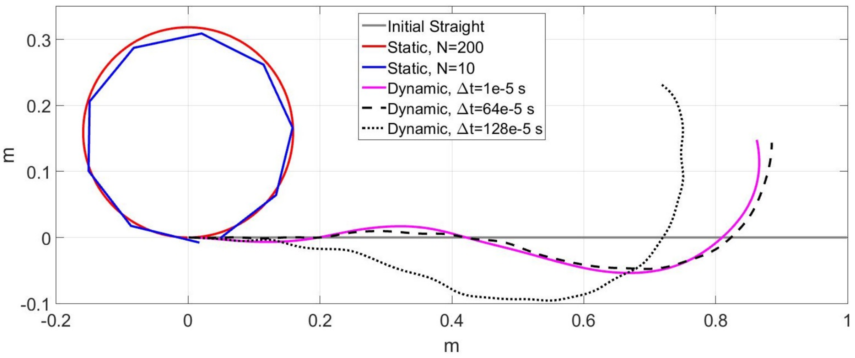

Figure 2.6: The cantilever beam subject to tip moment.

tions, and the dynamic solutions at 0.0064 s computed using the 200-element model with various time-step sizes. Convergence is verified for the finite volume discretization and the piecewise-linear MBBT method. The finite volume method is shown to have second-order accuracy and is used to demonstrate that conventional discretization methods are applicable without special treatment; other discretization methods could alternatively be used to improve accuracy or efficiency. The piecewise-linear time-stepping scheme is shown to be numerically stable when the time-steps are sufficiently small for incremental dynamic displacements to be small enough for linearization. Convergence should be tested for a particular problem to select a suitable time-step size. The time-step size needed for piecewise-linear models is expected to be smaller than needed for a non-linear iterative scheme, such as the Newton–Raphson method, though each step is expected to be less computationally intensive as no iteration is used.

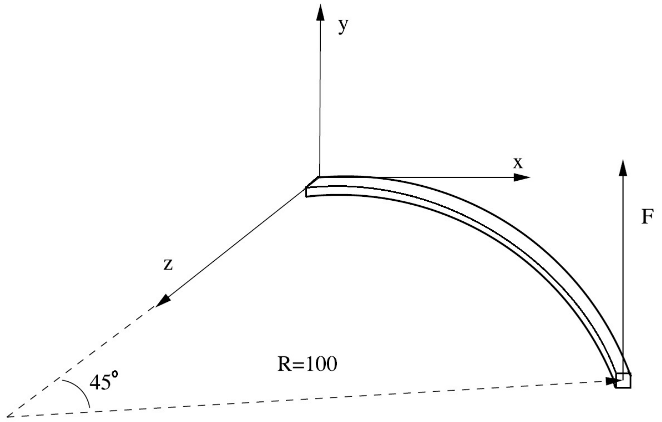

Figure 2.7: $45°$-curved cantilever beam.

2.5.2 Initially-curved Beam

A $45°$-curved cantilever beam subject to static tip load is another classical problem that was first presented by [141]. It includes bending, shear, torsion, and extension deformations of a 3D beam and has been studied in many articles on nonlinear beams with large deformations [25, 142, 31, 143]. The $45°$-curved cantilever has a radius of 100 with a unit square cross-section (Fig. 2.7). Young's modulus is 10^7, and shear modulus is 0.5×10^7. A static tip load F is applied in the positive y-direction with two different magnitudes: F=300 and F=600. The piecewise-linear static solver is used to compute the beam deflection using three different discretization models. The models differ only by the number of equal-length elements into which the beam is divided.

Table 2.2 shows the spatial coordinates of the tip computed using various non-linear beam theories and by ANSYS v18.2. Displacements are computed at the mass center of each element in the finite volume method. Therefore, the curved beam is modeled with its free-end extended by one half-element length and with the static load acting at the center node of that last element, such that the finite volume results are directly comparable with the FE results at the same tip node. The 2-node Timoshenko beam element used in ANSYS has the same second-order accuracy as the proposed finite volume method, and the results from these two methods converge similarly. The piecewise-linear MBBT solutions agree well with equivalent results from other non-linear beam

Table 2.2: Tip coordinates (x,y,z) of the deformed curved beam.

Tip load	$F = 300$	$F = 600$
Present (20 elements)	58.79, 40.23, 22.26	47.15, 53.43, 15.69
Present (40 elements)	58.78, 40.20, 22.25	47.15, 53.47, 15.69
Present (60 elements)	58.78, 40.20, 22.25	47.15, 53.47, 15.69
ANSYS (20 beam elements)	58.56, 40.45, 22.13	46.91, 53.59, 15.58
ANSYS (40 beam elements)	58.57, 40.44, 22.12	46.91, 53.60, 15.57
ANSYS (60 beam elements)	58.57, 40.44, 22.12	46.91, 53.60, 15.57
ANSYS (632 solid elements)	58.74, 40.22, 22.23	46.93, 53.59, 15.59
Simo and Vu-Quoc (1986)	58.84, 40.08, 22.33	47.23, 53.37, 15.79
Cardona and Geradin (1988)	58.64, 40.35, 22.14	47.04, 53.50, 15.55
Zupan and Saje (2003)	58.78, 40.16, 22.28	47.15, 53.43, 15.74
Romero (2008)	58.54, 40.48, 22.12	46.89, 53.60, 15.56

solvers, demonstrating capture of 3D large deformations of an initially-curved beam.

2.5.3 Rotating Straight Beam

Direct application of MBBT in a non-inertial frame is demonstrated in this example. The piecewise-linear dynamic solver and a nonlinear FE code are applied to simulate the response of a straight cantilever beam having an overall rotation of 10 rad/s about the y-axis at its fixed-end (Ω_y=10 rad/s). The cantilever beam is 0.5 m high, 0.25 m wide, 10 m long, and is made of steel with the same material properties as in Section 2.5.1. The beam is subject to 5000 kN static tip force in negative y-direction plus a dynamic load distributed uniformly along the beam: $w_y^{ext}(t) = W \sin(\omega t)$ kN/m. The dynamic loading frequency is selected as the natural frequency of the beam estimated using Timoshenko beam theory: $\omega = 25.6$ rad/s. The amplitude of the dynamic load is equivalent to application of five times the magnitude of gravity: $W = -48.13$ kN/m. The beam is discretized into 30 equal-length elements and the time-step size is 0.005 s in both the MBBT and ANSYS solvers.

Fig. 2.8 shows time-histories of tip displacements. Good agreement between solvers is observed in the x- and y-directions but not in the z-direction. Results from the MBBT solver show the expected Coriolis effect on response in the z-direction. This inertial effect caused by the beam rotation about its y-axis couples velocity in the x-direction with Coriolis force in the z-direction,

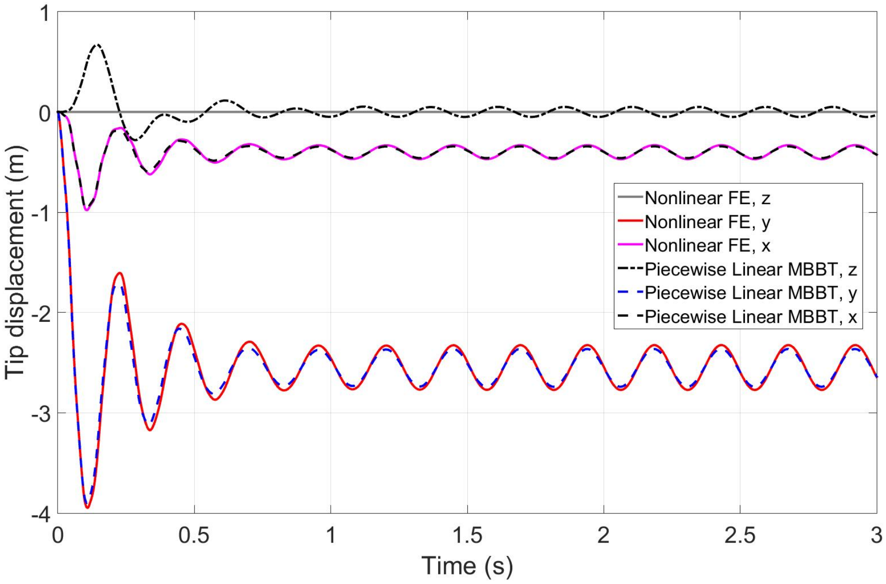

Figure 2.8: The cantilever beam subject to static and dynamic loads and rotation.

and velocity in the z-direction with Coriolis force in the x-direction. In this example, bending in the y-direction introduces axial motion in the x-direction due to foreshortening, and the resulting axial motion introduces Coriolis force in the z-direction. Coriolis force also exists in the x-direction, but the beam axial stiffness in this case is sufficiently large that the resulting deformation is minimal. The Coriolis effect demonstrated here is captured through the coupled inertial "damping term" in the MBBT formulation: $[\boldsymbol{C}_{13}^n]\,\dot{\boldsymbol{u}}_l^n = 2\boldsymbol{M}^n\tilde{\boldsymbol{\Omega}}_f\boldsymbol{T}_{fl}^n\dot{\boldsymbol{u}}_l^n$. This inertial term is proportional to velocity such that the Coriolis-excited response in the z-direction is out of phase with displacements in the other directions (Fig. 2.8).

2.5.4 Initially-twisted Wind Turbine Blade

Wind turbine blades are complex beam structures with varying cross-sections and twisted geometry. Blades used on floating offshore wind turbines also experience large irregular overall motions. The proposed beam theory is perfect for application to these complex beam structures in non-inertial frames. The theory is demonstrated on one blade of the National Renewable Energy Laboratory (NREL) 5-MW reference wind turbine [144]. The BeamDyn code is used as a bench-

Table 2.3: Comparisons of blade tip displacements.

Displacement (m)	Edgewise	Flapwise	Axial
RMS_{MBBT}	3.167e-1	5.730e-2	1.408e-3
$RMS_{BeamDyn}$	3.130e-1	5.553e-2	1.388e-3
$RMS_{diff.}$	3.861e-3	3.308e-3	2.773e-5
$\frac{RMS_{diff.}}{RMS_{BeamDyn}}$	1.23%	5.96%	2.00%

mark. BeamDyn is a modular code included in the FAST package made available by the NREL. BeamDyn is based on nonlinear FE formulation of GEBT [128, 138, 55]. The blade is 61.5-m long and is rotating about its root at 12.1 RPM in a vertical plane. Gravity is the only external load applied in this example ($g = 9.80665\ m/s^2$). The blade is discretized into 23 elements in the MBBT solver, and is represented by a single fifth-order Legendre spectral finite element in BeamDyn. The stiffness damping coefficient is set to 0.003 and the time-step is set to 0.005 s in both solvers.

Figs. 2.9 and 2.10 respectively show the blade tip displacements and root bending moments for the first minute of simulation. Table 2.3 lists the RMS of displacements of tip translation evaluated for the last 3 minutes of a 5-minute simulation to neglect startup transients. The results from two very different geometrically-exact beam solvers show excellent agreement. BeamDyn is based on an existing GEBT formulation, in which rotational quantities are total rotations referred to an inertial frame. Special treatment is used for discretization of rotational quantities. The rigid-body rotations of the blade and of each blade element are removed from the total rotation. The remaining relative rotation within each element is then interpolated using Lagrangian-interpolant shape functions. The total rotation of each element is restored afterwards to establish governing equations in an inertial frame [55]. The MBBT implementation is more straightforward. The overall rigid-body rotation is separated explicitly in the MBBT formulation and spatial discretization is applied directly to the linearized MBBT formulation in a floating non-inertial frame.

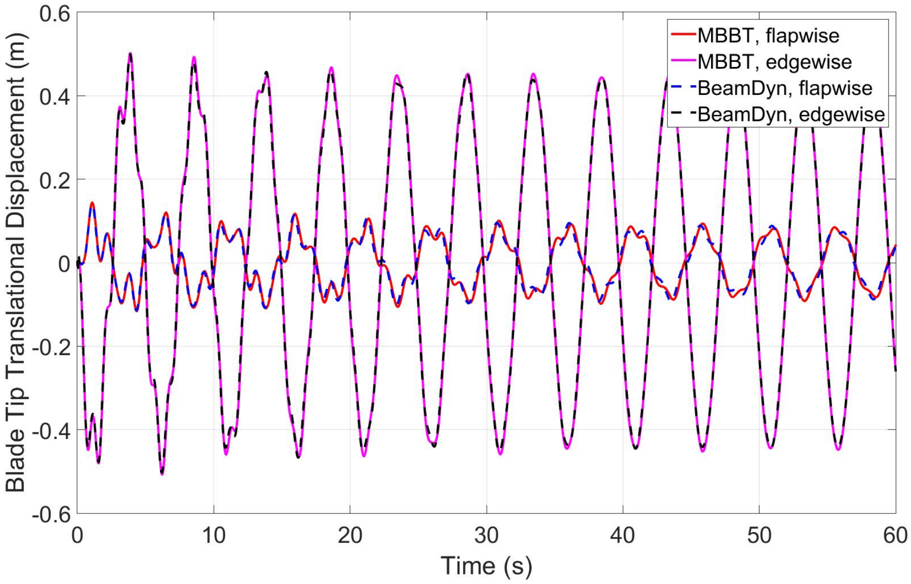

Figure 2.9: Time-histories of blade tip displacements.

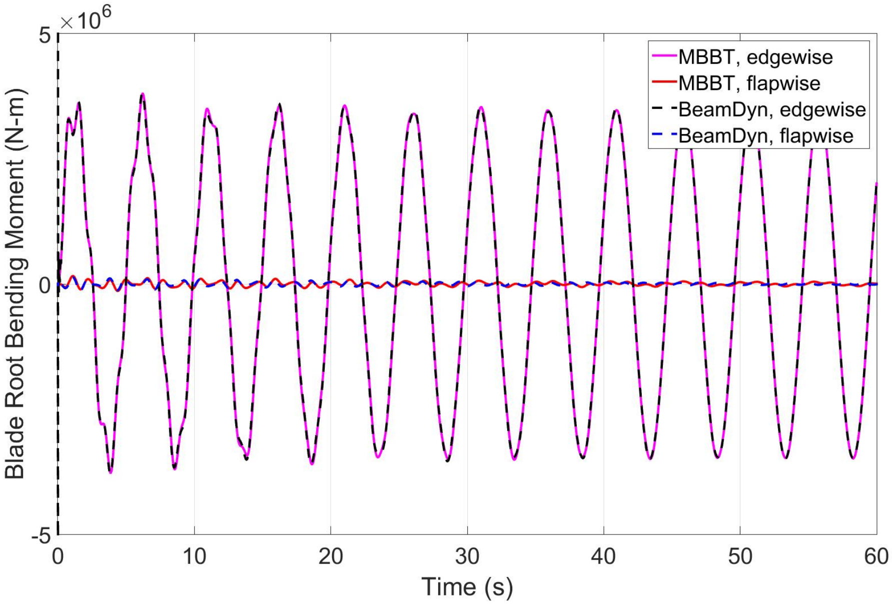

Figure 2.10: Time-histories of blade root bending moments.

2.6 Conclusions

A new momentum-based beam theory (MBBT) has been derived in a floating non-inertial frame for arbitrarily-shaped beams having large deformations and overall motions. MBBT is a geometrically-exact non-linear dynamic beam theory that fully addresses geometric and kinematic nonlinearities and inertial coupling effects. Expressing MBBT in an inertial frame has been shown to be mathematically equivalent to an existing formulation of GEBT. Specific advantages of the new theory have been demonstrated through linearization, simplification, and the development of a separation of displacements technique. Separation of displacements enables application of piecewise-linear MBBT to large non-linear dynamic displacements. The effectiveness of the theoretical developments has been demonstrated through numerical implementation. A finite volume formulation of linearized MBBT has been developed and implemented in two solvers: a piecewise-linear static solver, and a piecewise-linear dynamic solver that computes dynamic motion relative to a series of evolving base configurations in a non-inertial frame. The static MBBT solver has been shown to effectively capture geometric nonlinearities. The dynamic MBBT solver has been demonstrated to effectively capture non-linear geometric and kinematic behaviors and inertial coupling effects using only linear solutions without iteration at each time-step.

3. MOMENTUM-BASED THEORY FOR PIPES CONVEYING FLUID

3.1 Introduction

A new geometrically-exact nonlinear dynamic theory for pipes conveying fluid is developed using momentum-based approach. Conventional GEBT formulations are derived in inertial frames, mostly using the variational approach; the derivation method and resulting formulations are difficult to be expanded to include the dynamic effects of internal flow. MBBT is derived based on conservation of momentum in vector form using dynamic quantities relative to non-inertial frames. The particular derivation framework of MBBT allows it to be expanded to include fluid flow much more easily than other GEBT formulations. MBBT is expanded for pipes conveying fluid to include the geometric and kinematic nonlinearities for the pipe and inertial coupling effects between the pipe and fluid. The strength of the momentum-based approach is that the total momentum balance includes both the fluid and pipe, such that interaction forces between the fluid and pipe wall are implicitly included because internal forces do not affect the total momentum balance. The result is the first dynamic theory for pipes undergoing large deformations and overall motions that rigorously addresses geometric and kinematic nonlinearities and inertial coupling effects. The fully nonlinear differential governing equations are first derived in a total Lagrangian formulation in Section 3.2. The separation of displacements technique is applied in Section 3.3 to derive an updated Lagrangian formulation, which is further linearized using additional physical assumptions. A piecewise-linear time-stepping scheme and finite volume discretization are proposed for numerical implementation in Section 3.4. Several numerical examples are presented in Section 3.5 to demonstrate the effectiveness of the theoretical developments, including a rotating cantilever pipe, a semi-circular curved pipe, and a top-tensioned riser subject to imposed motions.

The coordinate systems, displacements and kinematics, strain measures, and separation of displacement technique are all applied to pipes conveying fluid in the same way as they were applied to MBBT, and are briefly repeated in this chapter for completeness of the derivation.

3.2 Governing Equations

3.2.1 Assumptions

The proposed theory is derived using several fundamental assumptions: (a) the pipe is slender and has a relatively thick wall, such that it can be modeled using beam theory and the pipe combined with conveying fluid can be reduced to a line model; (b) cross-sections are assumed to be circular and uniform along the pipe, such that eccentricity can be neglected; (c) cross-sectional deformations are assumed to be small, such that cross-sectional mass properties, mass and mass moment of inertia per unit length, are constant in time, and the cross-sectional area is also constant in time; (d) the cross-sectional elastic forces and moments are functions of strain measures and/or time derivatives of strain measures, such that the constitutive relations do not introduce other unknowns and the Poisson effect is neglected; (e) the fluid is assumed to be incompressible and homogeneous, such that the fluid density is constant; (f) fluid rotation around the axis of the pipe and flow eddies are negligible, and (g) the flow rate at the pipe inlet is assumed to be constant.

3.2.2 Coordinate Systems

An inertial Cartesian coordinate system, $\boldsymbol{XYZ}$, with origin O fixed to the earth, is denoted as global coordinate g. A non-inertial Cartesian coordinate, $\boldsymbol{xyz}$, is fixed to the undeformed pipe at point W, and is defined as floating coordinate f. Translations and rotations of f relative to g represent the overall rigid-body motion of an undeformed pipe. Curvilinear coordinate s is attached to the centerline of an undeformed pipe; another curvilinear coordinate S is similarly attached to the centerline of the deformed pipe. Two sets of local coordinates are defined at each point along s and S. The non-inertial local undeformed coordinate l is fixed to mass center G_0, and includes Cartesian coordinates $\boldsymbol{abc}$ with $\boldsymbol{b}$ and $\boldsymbol{c}$ on the cross-sectional plane and $\boldsymbol{a}$ tangent to the undeformed centerline s at G_0. Deformed local coordinate d includes Cartesian coordinates $\boldsymbol{ABC}$, with origin G fixed to the mass center of the displaced cross-section. Deformed local coordinate d rotates with the cross-section such that $\boldsymbol{B}$ and $\boldsymbol{C}$ remain on the cross-sectional plane and $\boldsymbol{A}$ is perpendicular to the plane but not generally tangent to the deformed centerline S.

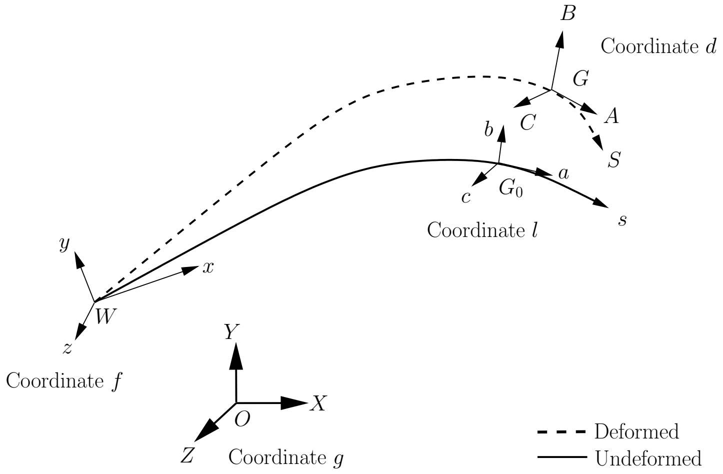

Figure 3.1: Coordinate systems of a pipe.

3.2.3 Displacements and Kinematics

The absolute displacement measured in global coordinate g of any point along the pipe can be expressed as a sum of two parts: the displacement resulting from a prescribed overall rigid-body motion of the undeformed pipe, plus the unknown displacements resulting from the pipe deformation. The unknown displacements are measured in local undeformed coordinate l: translational displacements $u_i(s,t)$ are the components of a vector from G_0 to G resolved onto the abc coordinates; rotational displacements $\theta_i(s,t)$ are defined here using the 1-2-3 sequenced Euler angles of finite rotations from coordinate l to d; other 3-variable rotation parameterizations could alternatively be used. Translational and rotational displacements can be expressed as 3D first-order tensors in vector form: $\boldsymbol{u}_l = [u_1, u_2, u_3]^T$; $\boldsymbol{\theta} = [\theta_1, \theta_2, \theta_3]^T$.

Rotational coordinate transformation matrices are used to transfer vectors from one coordinate system to another. The transformation matrices are orthogonal and can be computed based on the 1-2-3 Euler angle rotation sequence:

$$\boldsymbol{T}_{ld} = \begin{bmatrix} t_{11} & t_{12} & t_{13} \\ t_{21} & t_{22} & t_{23} \\ t_{31} & t_{32} & t_{33} \end{bmatrix} \tag{3.1}$$

in which:

$$
\begin{aligned}
t_{11} &= \cos\theta_2 \cos\theta_3 \\
t_{12} &= -\cos\theta_2 \sin\theta_3 \\
t_{13} &= \sin\theta_2 \\
t_{21} &= \cos\theta_1 \sin\theta_3 + \cos\theta_3 \sin\theta_1 \sin\theta_2 \\
t_{22} &= \cos\theta_1 \cos\theta_3 - \sin\theta_1 \sin\theta_2 \sin\theta_3 \\
t_{23} &= -\cos\theta_2 \sin\theta_1 \\
t_{31} &= \sin\theta_1 \sin\theta_3 - \cos\theta_1 \cos\theta_3 \sin\theta_2 \\
t_{32} &= \cos\theta_3 \sin\theta_1 + \cos\theta_1 \sin\theta_2 \sin\theta_3 \\
t_{33} &= \cos\theta_1 \cos\theta_2
\end{aligned}
$$

Angular velocities and accelerations are expressed using transformation matrices:

$$
\begin{aligned}
\tilde{\boldsymbol{\omega}}_d &= \boldsymbol{T}_{dl}\dot{\boldsymbol{T}}_{ld} && (3.2)\\
\tilde{\boldsymbol{\Omega}}_f &= \boldsymbol{T}_{fg}\dot{\boldsymbol{T}}_{gf} && (3.3)\\
\dot{\tilde{\boldsymbol{\omega}}}_d &= \frac{\partial}{\partial t}(\boldsymbol{T}_{dl}\dot{\boldsymbol{T}}_{ld}) = \dot{\boldsymbol{T}}_{dl}\dot{\boldsymbol{T}}_{ld} + \boldsymbol{T}_{dl}\ddot{\boldsymbol{T}}_{ld} && (3.4)\\
\dot{\tilde{\boldsymbol{\Omega}}}_f &= \frac{\partial}{\partial t}(\boldsymbol{T}_{fg}\dot{\boldsymbol{T}}_{gf}) = \dot{\boldsymbol{T}}_{fg}\dot{\boldsymbol{T}}_{gf} + \boldsymbol{T}_{fg}\ddot{\boldsymbol{T}}_{gf} && (3.5)
\end{aligned}
$$

in which vector $\boldsymbol{\omega}_d$ is the angular velocity of local deformation at a cross-section measured in coordinate d; vector $\boldsymbol{\Omega}_f$ is the angular velocity of overall rigid-body motion measured in coordinate f; $\dot{(\ )}$ and $\ddot{(\ )}$ denote the first and second time derivatives, and $\tilde{(\ )}$ denotes the skew-symmetric matrix of a vector, which can be used to represent cross products as matrix multiplications.

3.2.4 Strain Measures and Elastic Forces and Moments

The nonlinear relationships between displacements and strain measures are rigorously considered in the computation of angular and linear strains. The strains computation remains the same as in Section 2.2.4.

Two curvature vectors are used to describe the change in direction of curvilinear coordinates per unit length, $\boldsymbol{k}_l$ of the undeformed curvilinear coordinate s and $\boldsymbol{k}_d$ of the deformed curvilinear coordinate S, measured in the local Cartesian coordinates l and d respectively. The skew-symmetric matrix of the local curvature vector at any point can be computed as $\tilde{\boldsymbol{k}}_l = \boldsymbol{T}_{lf}\boldsymbol{T}'_{fl}$ or $\tilde{\boldsymbol{k}}_d = \boldsymbol{T}_{df}\boldsymbol{T}'_{fd}$, in which $\boldsymbol{T}_{df} = \boldsymbol{T}_{dl}\boldsymbol{T}_{lf}$ and $(\ )'$ denotes spatial derivatives with respect to s. The local angular strain, $\boldsymbol{\kappa}$, can be computed along the pipe as the difference between these curvature vectors:

$$\boldsymbol{\kappa} = \boldsymbol{k}_d - \boldsymbol{k}_l = \text{axial}(\boldsymbol{T}_{dl}\tilde{\boldsymbol{k}}_l\boldsymbol{T}_{ld} + \boldsymbol{T}_{dl}\boldsymbol{T}'_{ld} - \tilde{\boldsymbol{k}}_l) \tag{3.6}$$

where axial( ) denotes the axial vector computed from a skew-symmetric matrix.

Derivation of linear strain follows similar logic applied to differential position vectors instead of curvature vectors. Differential position vectors $\boldsymbol{r}'_l$ of the undeformed curvilinear coordinate s, and $\boldsymbol{r}'_d$ of deformed curvilinear coordinate S, each describe the change in shape of a differential element along the centerline, measured in the local Cartesian coordinates l and d respectively. Differential position vectors at a point can be computed as $\boldsymbol{r}'_l = \boldsymbol{T}_{lf}(\boldsymbol{R}_f^{WG_0})'$ and $\boldsymbol{r}'_d = \boldsymbol{T}_{df}(\boldsymbol{R}_f^{WG})'$. Transformation matrices $\boldsymbol{T}_{lf}$ and $\boldsymbol{T}_{df}$ effectively rotate the spatial derivatives of position vectors to the common coordinate system f (Fig. 3.2), such that these vectors become additive. The resulting linear strain, $\boldsymbol{\gamma}$, includes axial and shear strains and excludes rigid element rotations:

$$\boldsymbol{\gamma} = \boldsymbol{r}'_d - \boldsymbol{r}'_l = \boldsymbol{T}_{dl}(\boldsymbol{e}_1 + \tilde{\boldsymbol{k}}_l\boldsymbol{u}_l + \boldsymbol{u}'_l) - \boldsymbol{e}_1 \tag{3.7}$$

in which $\boldsymbol{r}'_l = \tilde{\boldsymbol{k}}_l\boldsymbol{R}_l^{WG_0} + (\boldsymbol{R}_l^{WG_0})' = \boldsymbol{e}_1$ and $\boldsymbol{e}_1 = [1, 0, 0]^T$ is a unit vector, because $\boldsymbol{r}'_l$ yields a tangent unit vector that is always aligned with the $\boldsymbol{a}$-direction of local undeformed coordinate l. Vector $\boldsymbol{r}'_d$ is similarly tangent to the deformed centerline but is not always aligned with the $\boldsymbol{A}$-direction.

Eqs. (3.6) and (3.7) represent the strain measures of a beam-type structure subject to large angular and translational deflections, and include full consideration of geometrical nonlinearities. These

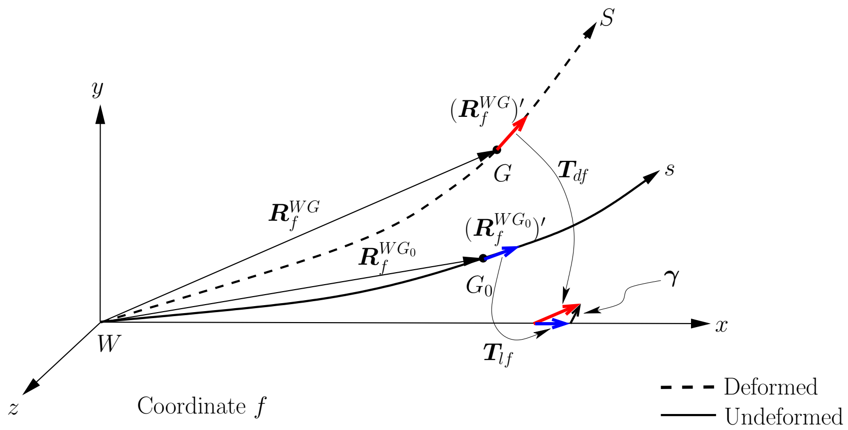

Figure 3.2: Linear strain of a pipe.

strain measures are invariant with rigid-body motions. The resultant elastic force and moment of a cross-section at s are assumed to be functions of strain measures and/or the time derivatives of strain measures:

$$\boldsymbol{F}_d(s,t) = \boldsymbol{F}_d(\boldsymbol{\gamma}, \boldsymbol{\kappa}, \dot{\boldsymbol{\gamma}}, \dot{\boldsymbol{\kappa}}) \tag{3.8}$$

$$\boldsymbol{M}_d(s,t) = \boldsymbol{M}_d(\boldsymbol{\gamma}, \boldsymbol{\kappa}, \dot{\boldsymbol{\gamma}}, \dot{\boldsymbol{\kappa}}) \tag{3.9}$$

in which $\boldsymbol{F}_d$ is the elastic force measured in deformed local coordinate d, and $\boldsymbol{M}_d$ is the elastic moment about mass center in coordinate d. Eqs. (3.8) and (3.9) represent the constitutive relations for the pipe, and are applicable for linear elastic, hyperelasic, or viscoelastic material models.

3.2.5 Flow Model

The internal fluid is assumed to flow along the deformed curvilinear coordinate S while flow eddies are assumed to be negligible. The positive flow is in the $+S$ direction and tangent to the deformed centerline of the pipe. The full range of deformations of the pipe are considered; the flow direction is generally not perpendicular to each cross-section ($\boldsymbol{BC}$-plane) of the deformed pipe as the result of shear deformation. The actual flow direction can be expressed using the tangent unit vector of the centerline measured in local deformed coordinate d:

$$\boldsymbol{e}_d^f = \frac{\boldsymbol{r}'_d}{|\boldsymbol{r}'_d|} = \frac{\boldsymbol{T}_{dl}(\boldsymbol{e}_1 + \tilde{\boldsymbol{k}}_l \boldsymbol{u}_l + \boldsymbol{u}'_l)}{|\boldsymbol{T}_{dl}(\boldsymbol{e}_1 + \tilde{\boldsymbol{k}}_l \boldsymbol{u}_l + \boldsymbol{u}'_l)|} = \boldsymbol{T}_{dl} \frac{\boldsymbol{e}_1 + \tilde{\boldsymbol{k}}_l \boldsymbol{u}_l + \boldsymbol{u}'_l}{|\boldsymbol{e}_1 + \tilde{\boldsymbol{k}}_l \boldsymbol{u}_l + \boldsymbol{u}'_l|} \tag{3.10}$$

The fluid velocity, $\boldsymbol{V}_l = V\boldsymbol{e}_1$, is perpendicular to the cross-sections in the undeformed pipe, the fluid-passing area of which is A^f and is assumed to be constant as per the small cross-sectional deformation assumption. The combined assumptions of incompressible and homogeneous fluid and constant flow rate indicate the mass flow rate in the deformed pipe must remain the same as in the undeformed condition: $Q = \rho^f A^f V = \rho^f A_d^f(s) V_d(s)$, in which Q is the constant mass flow rate; ρ^f is the fluid density; $\boldsymbol{V}_d(s) = V_d(s)\boldsymbol{e}_{\boldsymbol{d}}$ is the flow velocity along the deformed centerline, and $A_d^f(s)$ is the actual fluid-passing area perpendicular to the flow velocity along the deformed centerline. The value of $A_d^f(s)$ can be computed as the projection of A^f using the dot product of their normal unit vectors, $A_d^f(s) = (\boldsymbol{e}_d^f \cdot \boldsymbol{e}_1)A^f$, such that:

$$V_d(s) = \frac{Q}{\rho^f A_d^f(s)} = \frac{Q}{(\boldsymbol{e}_d^f \cdot \boldsymbol{e}_1)\rho^f A^f} \tag{3.11}$$

A differential cross-section attached to the pipe is considered as a control volume including both the solid and fluid. Pipe deformation and overall rigid-body motion induce lateral motion to the fluid and changes the direction of the axial flow. The motion of the fluid inside a control volume consists of the motion of the control volume plus the relative motion between the pipe and fluid in the axial direction. The absolute fluid velocity relative to the inertial coordinate g can be written as:

$$\boldsymbol{v}_g^f = \boldsymbol{v}_g^W + \dot{\boldsymbol{T}}_{gf}(\boldsymbol{R}_f^{WG_0} + \boldsymbol{T}_{fl}\boldsymbol{u}_l) + \boldsymbol{T}_{gf}\boldsymbol{T}_{fl}\dot{\boldsymbol{u}}_l - \boldsymbol{T}_{gf}\boldsymbol{T}_{fl}\boldsymbol{T}_{ld}(\boldsymbol{T}_{dl}\dot{\boldsymbol{u}}_l \cdot \boldsymbol{e}_d^f)\boldsymbol{e}_d^f + \boldsymbol{T}_{gf}\boldsymbol{T}_{fl}\boldsymbol{T}_{ld}\boldsymbol{V}_d \tag{3.12}$$

in which $\boldsymbol{v}_g^W = \dot{\boldsymbol{R}}_g^{OW}$. The first three terms on the right-hand-side taken together represent the absolute velocity of a control volume attached to a pipe cross-section. The last two terms represent the relative motion between the pipe and fluid. Time derivatives of $\boldsymbol{R}_f^{WG_0}$ and $\boldsymbol{T}_{fl}$ are zero because there is no relative motion between the local undeformed coordinates and floating coordinate f. Fluid is constrained laterally by the pipe wall but flows independently in the axial direction with velocity V_d. The axial flow velocity relative to the pipe is given by $(V_d - \boldsymbol{T}_{dl}\dot{\boldsymbol{u}}_l \cdot \boldsymbol{e}_d^f)$, and the momentum flux through a pipe-attached control volume can be computed in inertial coordinate g as: $m^f \boldsymbol{T}_{gf}\boldsymbol{T}_{fl}\boldsymbol{T}_{ld}(V_d - \boldsymbol{T}_{dl}\dot{\boldsymbol{u}}_l \cdot \boldsymbol{e}_d^f)\boldsymbol{e}_d^f$, in which $m^f = \rho^f A^f$ is the mass of fluid per unit length.

The fluid pressure $P(s)$ along the pipe is a primary unknown variable, for which a scalar governing equation can be derived along the deformed centerline. The pressure difference along the pipe is used to compute the pipe flow: the sum of pressure difference, pipe friction force, and gravity force in the axial direction is equal to the fluid mass multiplied by fluid axial acceleration. The Darcy–Weisbach formulation is used to compute friction loss:

$$-A^f \frac{\partial}{\partial s}[(P\boldsymbol{e}_1) \cdot \boldsymbol{e}_d^f] - f_D \frac{VQ}{2D} + m^f(\boldsymbol{T}_{dl}\boldsymbol{T}_{lf}\boldsymbol{T}_{fg}\boldsymbol{g}) \cdot \boldsymbol{e}_d^f = m^f a_d^f \tag{3.13}$$

where D is the inner diameter of the pipe; f_D is the Darcy friction factor, and a_d^f is the absolute axial acceleration of the fluid measured in local deformed coordinate d and computed using Eq. (3.12):

$$\begin{aligned} a_d^f &= [\boldsymbol{T}_{dl}\boldsymbol{T}_{lf}\boldsymbol{T}_{fg}\frac{\partial}{\partial t}(\boldsymbol{v}_g^f)] \cdot \boldsymbol{e}_d^f \\ &= [\boldsymbol{T}_{dl}\boldsymbol{T}_{lf}\boldsymbol{a}_f^W + \boldsymbol{T}_{dl}\boldsymbol{T}_{lf}(\dot{\tilde{\boldsymbol{\Omega}}}_f + \tilde{\boldsymbol{\Omega}}_f\tilde{\boldsymbol{\Omega}}_f)(\boldsymbol{R}_f^{WG_0} + \boldsymbol{T}_{fl}\boldsymbol{u}_l) + 2\boldsymbol{T}_{dl}\boldsymbol{T}_{lf}\tilde{\boldsymbol{\Omega}}_f\boldsymbol{T}_{fl}\dot{\boldsymbol{u}}_l + \boldsymbol{T}_{dl}\ddot{\boldsymbol{u}}_l] \cdot \boldsymbol{e}_d^f \\ &\quad + \frac{\partial}{\partial t}(V_d - \boldsymbol{T}_{dl}\dot{\boldsymbol{u}}_l \cdot \boldsymbol{e}_d^f) \end{aligned} \tag{3.14}$$

in which $\boldsymbol{a}_f^W = \boldsymbol{T}_{fg}\dot{\boldsymbol{v}}_g^W$ is the translational acceleration of the overall rigid-body motion.

3.2.6 Momentum Balance

The absolute linear and angular momenta of a coupled cross-sectional control volume that includes both the pipe and fluid can be expressed in inertial coordinate g as:

$$\boldsymbol{L}_g = (m^p + m^f)(\boldsymbol{v}_g^W + \dot{\boldsymbol{T}}_{gf}\boldsymbol{R}_f^{WG_0} + \dot{\boldsymbol{T}}_{gf}\boldsymbol{T}_{fl}\boldsymbol{u}_l + \boldsymbol{T}_{gf}\boldsymbol{T}_{fl}\dot{\boldsymbol{u}}_l) + m^f\boldsymbol{T}_{gf}\boldsymbol{T}_{fl}\boldsymbol{T}_{ld}(V_d - \boldsymbol{T}_{dl}\dot{\boldsymbol{u}}_l \cdot \boldsymbol{e}_d^f)\boldsymbol{e}_d^f \tag{3.15}$$

$$\boldsymbol{H}_g = \boldsymbol{T}_{gf}\boldsymbol{T}_{fl}\boldsymbol{T}_{ld}\boldsymbol{I}_d\boldsymbol{T}_{dl}\boldsymbol{T}_{lf}\boldsymbol{\Omega}_f + \boldsymbol{T}_{gf}\boldsymbol{T}_{fl}\boldsymbol{T}_{ld}\boldsymbol{I}_d\boldsymbol{\omega}_d \tag{3.16}$$

in which m^p is the mass of pipe per unit length, and $\boldsymbol{I}_d = \text{Diag}(J^p, I_B^p + I_B^f, I_C^p + I_C^f)$ is the mass moment of inertia of the differential control volume, where J^p is the polar moment of inertia of the pipe cross-section; I_B^p and I_C^p are the second moments of inertia of the pipe cross-section about axes B and C respectively; I_B^f and I_C^f are the second moments of inertia of the fluid cross-section about axes B and C respectively.

Momentum balance is applied to the absolute momenta of the pipe-fluid system, measured in an inertial coordinate system. The interactions between the fluid and pipe wall within a control volume, such as wall pressure and wall friction, are internal effects that do not affect the total momentum balance of the control volume. Any change in momentum results from the change of momentum flux of the fluid and from the sum of forces and moments acting on each differential control volume:

$$\dot{\boldsymbol{L}}_g = \sum \boldsymbol{F}_g = \boldsymbol{F}_g^{ext} + \boldsymbol{F}_g^{int} - (V_d - \boldsymbol{T}_{dl}\dot{\boldsymbol{u}}_l \cdot \boldsymbol{e}_d^f)\frac{\partial}{\partial s}[m^f\boldsymbol{T}_{gf}\boldsymbol{T}_{fl}\boldsymbol{T}_{ld}(V_d - \boldsymbol{T}_{dl}\dot{\boldsymbol{u}}_l \cdot \boldsymbol{e}_d^f)\boldsymbol{e}_d^f] \tag{3.17}$$

$$\dot{\boldsymbol{H}}_g = \sum \boldsymbol{M}_g = \boldsymbol{M}_g^{ext} + \boldsymbol{M}_g^{int} \tag{3.18}$$

in which $\boldsymbol{F}_g^{ext}$ and $\boldsymbol{M}_g^{ext}$ are the total forces and moments about G resulting from external loads; $\boldsymbol{F}_g^{int}$ and $\boldsymbol{M}_g^{int}$ are the total internal forces and moments resulting from pipe deformation and fluid pressure. The last term in Eq. (3.17) represents the changing rate of momentum flux through the differential control volume.

Computing the time derivative of $\boldsymbol{L}_g$ and multiplying Eq. (3.17) by $\boldsymbol{T}_{fg}$ yields a physically-intuitive equation representing the change in linear momentum in non-inertial coordinate f:

$$\begin{aligned}
&\boldsymbol{F}_f^{ext} + \boldsymbol{F}_f^{int} \\
=\ & (m^p + m^f)[\boldsymbol{a}_f^W + \dot{\tilde{\boldsymbol{\Omega}}}_f(\boldsymbol{R}_f^{WG_0} + \boldsymbol{T}_{fl}\boldsymbol{u}_l) + \tilde{\boldsymbol{\Omega}}_f\tilde{\boldsymbol{\Omega}}_f(\boldsymbol{R}_f^{WG_0} + \boldsymbol{T}_{fl}\boldsymbol{u}_l) + 2\tilde{\boldsymbol{\Omega}}_f\boldsymbol{T}_{fl}\dot{\boldsymbol{u}}_l + \boldsymbol{T}_{fl}\ddot{\boldsymbol{u}}_l] \\
& + m^f\tilde{\boldsymbol{\Omega}}_f\boldsymbol{T}_{fl}\boldsymbol{T}_{ld}(V_d - \boldsymbol{T}_{dl}\dot{\boldsymbol{u}}_l \cdot \boldsymbol{e}_d^f)\boldsymbol{e}_d^f + m^f\boldsymbol{T}_{fl}\frac{\partial}{\partial t}[\boldsymbol{T}_{ld}(V_d - \boldsymbol{T}_{dl}\dot{\boldsymbol{u}}_l \cdot \boldsymbol{e}_d^f)\boldsymbol{e}_d^f] \\
& + m^f(V_d - \boldsymbol{T}_{dl}\dot{\boldsymbol{u}}_l \cdot \boldsymbol{e}_d^f)\frac{\partial}{\partial s}[\boldsymbol{T}_{fl}\boldsymbol{T}_{ld}(V_d - \boldsymbol{T}_{dl}\dot{\boldsymbol{u}}_l \cdot \boldsymbol{e}_d^f)\boldsymbol{e}_d^f] \qquad (3.19)
\end{aligned}$$

The derivation for the angular momentum balance in floating coordinate f follows the same logic: computing the time derivative of $\boldsymbol{H}_g$ and multiplying Eq. (3.18) by $\boldsymbol{T}_{fg}$ yields:

$$\begin{aligned}
\boldsymbol{M}_f^{ext} + \boldsymbol{M}_f^{int} &= \tilde{\boldsymbol{\Omega}}_f\boldsymbol{T}_{fl}\boldsymbol{T}_{ld}\boldsymbol{I}_d(\boldsymbol{T}_{dl}\boldsymbol{T}_{lf}\boldsymbol{\Omega}_f + \boldsymbol{\omega}_d) + \boldsymbol{T}_{fl}\boldsymbol{T}_{ld}\tilde{\boldsymbol{\omega}}_d\boldsymbol{I}_d(\boldsymbol{T}_{dl}\boldsymbol{T}_{lf}\boldsymbol{\Omega}_f + \boldsymbol{\omega}_d) \\
&\quad + \boldsymbol{T}_{fl}\boldsymbol{T}_{ld}\boldsymbol{I}_d(\boldsymbol{T}_{dl}\boldsymbol{T}_{lf}\dot{\boldsymbol{\Omega}}_f + \dot{\boldsymbol{\omega}}_d) - \boldsymbol{T}_{fl}\boldsymbol{T}_{ld}\boldsymbol{I}_d\tilde{\boldsymbol{\omega}}_d\boldsymbol{T}_{dl}\boldsymbol{T}_{lf}\boldsymbol{\Omega}_f \qquad (3.20)
\end{aligned}$$

The total internal force exerted on a control volume can be computed directly as the sum of the pipe elastic forces and fluid pressure forces. Internal forces are exerted at each end of a differential control volume (s^- and s^+), such that the total internal force is:

$$\boldsymbol{F}_f^{int} = (\boldsymbol{T}'_{fl}\boldsymbol{T}_{ld} + \boldsymbol{T}_{fl}\boldsymbol{T}'_{ld})(\boldsymbol{F}_d - A^f\boldsymbol{P}) + \boldsymbol{T}_{fl}\boldsymbol{T}_{ld}(\boldsymbol{F}'_d - A^f\boldsymbol{P}') \qquad (3.21)$$

in which $\boldsymbol{P} = P\boldsymbol{e}_1$. The sum of the internal moments exerted at each end of a differential control volume is:

$$\boldsymbol{M}_f^{int} = (\boldsymbol{T}'_{fl}\boldsymbol{T}_{ld} + \boldsymbol{T}_{fl}\boldsymbol{T}'_{ld})\boldsymbol{M}_d + \boldsymbol{T}_{fl}\boldsymbol{T}_{ld}\boldsymbol{M}'_d + \boldsymbol{T}_{fl}\boldsymbol{T}_{ld}(\tilde{\gamma} + \tilde{\boldsymbol{e}}_1)(\boldsymbol{F}_d - A^f\boldsymbol{P}) \qquad (3.22)$$

Translational and rotational equations of motion (EOM's) in non-inertial coordinate f are derived based on the total momentum balance of a control volume by substituting Eqs. (3.21) and

(3.22) into Eqs. (3.19) and (3.20), respectively:

$$\begin{aligned}
& \boldsymbol{F}_f^{ext} + (\boldsymbol{T}'_{fl}\boldsymbol{T}_{ld} + \boldsymbol{T}_{fl}\boldsymbol{T}'_{ld})(\boldsymbol{F}_d - A^f\boldsymbol{P}) + \boldsymbol{T}_{fl}\boldsymbol{T}_{ld}(\boldsymbol{F}'_d - A^f\boldsymbol{P}') \\
= \;& (m^p + m^f)[\boldsymbol{a}_f^W + \dot{\tilde{\boldsymbol{\Omega}}}_f(\boldsymbol{R}_f^{WG_0} + \boldsymbol{T}_{fl}\boldsymbol{u}_l) + \tilde{\boldsymbol{\Omega}}_f\tilde{\boldsymbol{\Omega}}_f(\boldsymbol{R}_f^{WG_0} + \boldsymbol{T}_{fl}\boldsymbol{u}_l) + 2\tilde{\boldsymbol{\Omega}}_f\boldsymbol{T}_{fl}\dot{\boldsymbol{u}}_l + \boldsymbol{T}_{fl}\ddot{\boldsymbol{u}}_l] \\
& + m^f\tilde{\boldsymbol{\Omega}}_f\boldsymbol{T}_{fl}\boldsymbol{T}_{ld}(V_d - \boldsymbol{T}_{dl}\dot{\boldsymbol{u}}_l\cdot\boldsymbol{e}_d^f)\boldsymbol{e}_d^f + m^f\boldsymbol{T}_{fl}\frac{\partial}{\partial t}[\boldsymbol{T}_{ld}(V_d - \boldsymbol{T}_{dl}\dot{\boldsymbol{u}}_l\cdot\boldsymbol{e}_d^f)\boldsymbol{e}_d^f] \\
& + m^f(V_d - \boldsymbol{T}_{dl}\dot{\boldsymbol{u}}_l\cdot\boldsymbol{e}_d^f)\frac{\partial}{\partial s}[\boldsymbol{T}_{fl}\boldsymbol{T}_{ld}(V_d - \boldsymbol{T}_{dl}\dot{\boldsymbol{u}}_l\cdot\boldsymbol{e}_d^f)\boldsymbol{e}_d^f]
\end{aligned} \tag{3.23}$$

$$\begin{aligned}
& \boldsymbol{M}_f^{ext} + (\boldsymbol{T}'_{fl}\boldsymbol{T}_{ld} + \boldsymbol{T}_{fl}\boldsymbol{T}'_{ld})\boldsymbol{M}_d + \boldsymbol{T}_{fl}\boldsymbol{T}_{ld}\boldsymbol{M}'_d + \boldsymbol{T}_{fl}\boldsymbol{T}_{ld}(\tilde{\gamma} + \tilde{e}_1)(\boldsymbol{F}_d - A^f\boldsymbol{P}) \\
= \;& \tilde{\boldsymbol{\Omega}}_f\boldsymbol{T}_{fl}\boldsymbol{T}_{ld}\boldsymbol{I}_d(\boldsymbol{T}_{dl}\boldsymbol{T}_{lf}\boldsymbol{\Omega}_f + \boldsymbol{\omega}_d) + \boldsymbol{T}_{fl}\boldsymbol{T}_{ld}\tilde{\boldsymbol{\omega}}_d\boldsymbol{I}_d(\boldsymbol{T}_{dl}\boldsymbol{T}_{lf}\boldsymbol{\Omega}_f + \boldsymbol{\omega}_d) \\
& + \boldsymbol{T}_{fl}\boldsymbol{T}_{ld}\boldsymbol{I}_d(\boldsymbol{T}_{dl}\boldsymbol{T}_{lf}\dot{\boldsymbol{\Omega}}_f + \dot{\boldsymbol{\omega}}_d) - \boldsymbol{T}_{fl}\boldsymbol{T}_{ld}\boldsymbol{I}_d\tilde{\boldsymbol{\omega}}_d\boldsymbol{T}_{dl}\boldsymbol{T}_{lf}\boldsymbol{\Omega}_f
\end{aligned} \tag{3.24}$$

Eqs. (3.23) and (3.24) are the nonlinear six-degree-of-freedom (6-DOF) EOM's expressed using transformation matrices in the floating frame. The complete formulation of the proposed geometrically-exact pipe-fluid model is represented by the EOM's of Eqs. (3.23) (3.24), strain measures of Eqs. (3.6) (3.7), constitutive relations of Eqs. (3.8) (3.9), fluid model of Eqs. (3.10) (3.11) (3.13), angular motions of Eqs. (3.2) - (3.5), and the Euler angle rotation formulations of Eq. (3.1). The primary unknown variables are pipe displacements $\boldsymbol{u}_l$ and $\boldsymbol{\theta}$ and fluid pressure P. The proposed nonlinear model is formulated as in a total Lagrangian formulation in vector form with dynamic quantities relative to the non-inertial undeformed frame. Overall rigid-body motions introduce significant inertial forces and moments, which are explicitly included in the EOM's through translational acceleration, $\boldsymbol{a}_f^W$, rotational velocity, $\boldsymbol{\Omega}_f$, and rotational acceleration, $\dot{\boldsymbol{\Omega}}_f$. Gravity is included in the external force term $\boldsymbol{F}_f^{ext}$. The external moment does not include gravitational effects because the angular EOM is established about the center of mass.

3.3 Separation of Displacements and Linearization

A major advantage of MBBT is that the EOM's can be formulated with dynamic quantities relative to arbitrary non-inertial frames using separation of displacements. The same technique is applied here to refer all dynamic quantities to a continuously evolving quasi-static configuration, which allows the fully nonlinear pipe-fluid model to be rigorously reduced into a series of piecewise-linear models. The fully nonlinear system of governing equations is first derived for an arbitrary quasi-static base configuration using separation of displacements, and then the resulting system is linearized using several additional assumptions.

3.3.1 Separation of Displacements

Total deformations are separated into a quasi-static base configuration whose time derivatives equal zero, plus dynamic displacements relative to that quasi-static base configuration. This separation of displacements is a purely mathematical manipulation: an arbitrary pipe configuration without any particular physical significance can be selected as the base configuration and considered to be quasi-static. Time derivatives of the dynamic displacements represent the total velocities and accelerations relative to the undeformed configuration. The total translational and rotational displacements are each separated into a quasi-static displacement plus a dynamic displacement:

$$\boldsymbol{u}_l(s,t) = \boldsymbol{U}_l(s) + \boldsymbol{u}_l^*(s,t) \tag{3.25}$$

$$\boldsymbol{\phi}_l(s,t) = \boldsymbol{\Phi}_l(s) + \boldsymbol{\phi}_l^*(s,t) \tag{3.26}$$

in which $\boldsymbol{U}_l(s)$ is the quasi-static portion of the translational displacement measured from undeformed coordinate l; $\boldsymbol{u}_l^*(s,t)$ is the dynamic part of the translational displacement; total rotation vector $\boldsymbol{\phi}_l(s,t)$ describes the rotation of a differential element from its undeformed to deformed configurations; rotation vector $\boldsymbol{\Phi}_l(s)$ represents the rotation from the undeformed configuration to the base configuration, and vector $\boldsymbol{\phi}_l^*(s,t)$ is the dynamic rotation vector.

The base configuration is represented by an additional curvilinear coordinate system denoted as coordinate Q (Fig. 3.3). Coordinate Q shares the same origin as curvilinear coordinates s and S, but its curvilinear axis is the centerline of a prescribed base configuration. Coordinate Q is displaced from s by quasi-static displacement $\boldsymbol{U}_l(s)$. A local element-fixed Cartesian coordinate system, $\boldsymbol{a}^*\boldsymbol{b}^*\boldsymbol{c}^*$, is introduced as coordinate q, with origin at the cross-sectional center G^* and

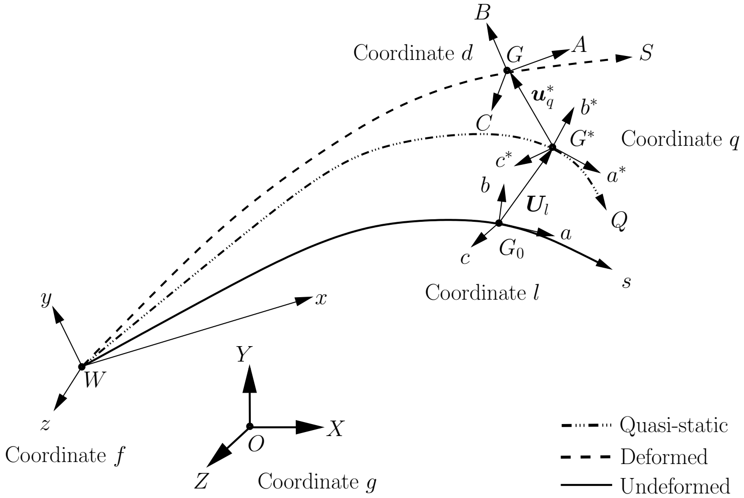

Figure 3.3: Base configuration and coordinate systems of a pipe.

with directions described by rotation vector $\boldsymbol{\Phi}_l(s)$ (Fig. 3.3). The transformation matrices between coordinate q and coordinates l and d are given by $\boldsymbol{T}_{ld} = \boldsymbol{T}_{lq}\boldsymbol{T}_{qd}$ and $\boldsymbol{T}_{dl} = \boldsymbol{T}_{dq}\boldsymbol{T}_{ql}$. Euler angles of the dynamic rotational displacements ($\theta_1^*, \theta_2^*, \theta_3^*$) measured from coordinate q are employed for $\boldsymbol{T}_{dq}$ and $\boldsymbol{T}_{qd}$ based on the same Euler angle rotation formulation as in Section 3.2.3. Eqs. (3.2), (3.4), and (3.25) then can be rewritten as:

$$\tilde{\boldsymbol{\omega}}_d = \boldsymbol{T}_{dq}\dot{\boldsymbol{T}}_{qd} \tag{3.27}$$

$$\dot{\tilde{\boldsymbol{\omega}}}_d = \dot{\boldsymbol{T}}_{dq}\dot{\boldsymbol{T}}_{qd} + \boldsymbol{T}_{dq}\ddot{\boldsymbol{T}}_{qd} \tag{3.28}$$

$$\boldsymbol{u}_l(s,t) = \boldsymbol{U}_l(s) + \boldsymbol{T}_{lq}(s)\boldsymbol{u}_q^*(s,t) \tag{3.29}$$

in which $\boldsymbol{u}_q^* = [u_1^*, u_2^*, u_3^*]^T$ is the dynamic translational displacement measured in coordinate q, and $\dot{\boldsymbol{T}}_{lq} = \ddot{\boldsymbol{T}}_{lq} = \boldsymbol{0}$. Taking time derivatives of Eq. (3.29) yields the translational velocity and acceleration:

$$\dot{\boldsymbol{u}}_l = \frac{\partial}{\partial t}(\boldsymbol{U}_l + \boldsymbol{T}_{lq}\boldsymbol{u}_q^*) = \boldsymbol{T}_{lq}\dot{\boldsymbol{u}}_q^* \tag{3.30}$$

$$\ddot{\boldsymbol{u}}_l = \frac{\partial^2}{\partial t^2}(\boldsymbol{U}_l + \boldsymbol{T}_{lq}\boldsymbol{u}_q^*) = \boldsymbol{T}_{lq}\ddot{\boldsymbol{u}}_q^* \tag{3.31}$$

where $\dot{\boldsymbol{U}}_l = \ddot{\boldsymbol{U}}_l = \boldsymbol{0}$.

The governing equations formulated using separation of displacements technique can be obtained by substituting Eqs. (3.27) - (3.31) into Eqs. (3.13), (3.23) and (3.24):

$$\begin{aligned}
&-A^f \frac{\partial}{\partial s}[(P\boldsymbol{e}_1) \cdot \boldsymbol{e}_d^f] - f_D \frac{VQ}{2D} + m^f(\boldsymbol{T}_{qf}\boldsymbol{T}_{fg}\boldsymbol{g}) \cdot \boldsymbol{e}_q \\
= \; & m^f[\boldsymbol{T}_{qf}\boldsymbol{a}_f^W + \boldsymbol{T}_{qf}(\dot{\tilde{\boldsymbol{\Omega}}}_f + \tilde{\boldsymbol{\Omega}}_f\tilde{\boldsymbol{\Omega}}_f)(\boldsymbol{R}_f^{WG_0} + \boldsymbol{T}_{fl}\boldsymbol{U}_l + \boldsymbol{T}_{fq}\boldsymbol{u}_q^*) + 2\boldsymbol{T}_{qf}\tilde{\boldsymbol{\Omega}}_f\boldsymbol{T}_{fq}\dot{\boldsymbol{u}}_q^* + \ddot{\boldsymbol{u}}_q^*] \cdot \boldsymbol{e}_q \\
&+m^f \frac{\partial}{\partial t}(V_d - \dot{\boldsymbol{u}}_q^* \cdot \boldsymbol{e}_q)
\end{aligned} \tag{3.32}$$

$$\begin{aligned}
&\boldsymbol{F}_f^{ext} + (\boldsymbol{T}_{fq}'\boldsymbol{T}_{qd} + \boldsymbol{T}_{fq}\boldsymbol{T}_{qd}')(\boldsymbol{F}_d - A^f\boldsymbol{P}) + \boldsymbol{T}_{fq}\boldsymbol{T}_{qd}(\boldsymbol{F}_d' - A^f\boldsymbol{P}') \\
= \; & (m^p + m^f)[\boldsymbol{a}_f^W + (\dot{\tilde{\boldsymbol{\Omega}}}_f + \tilde{\boldsymbol{\Omega}}_f\tilde{\boldsymbol{\Omega}}_f)(\boldsymbol{R}_f^{WG_0} + \boldsymbol{T}_{fl}\boldsymbol{U}_l + \boldsymbol{T}_{fq}\boldsymbol{u}_q^*) + 2\tilde{\boldsymbol{\Omega}}_f\boldsymbol{T}_{fq}\dot{\boldsymbol{u}}_q^* + \boldsymbol{T}_{fq}\ddot{\boldsymbol{u}}_q^*] \\
&+m^f\tilde{\boldsymbol{\Omega}}_f\boldsymbol{T}_{fq}(V_d - \dot{\boldsymbol{u}}_q^* \cdot \boldsymbol{e}_q)\boldsymbol{e}_q + m^f\boldsymbol{T}_{fq}\frac{\partial}{\partial t}[(V_d - \dot{\boldsymbol{u}}_q^* \cdot \boldsymbol{e}_q)\boldsymbol{e}_q] \\
&+m^f(V_d - \dot{\boldsymbol{u}}_q^* \cdot \boldsymbol{e}_q)\frac{\partial}{\partial s}[\boldsymbol{T}_{fq}(V_d - \dot{\boldsymbol{u}}_q^* \cdot \boldsymbol{e}_q)\boldsymbol{e}_q]
\end{aligned} \tag{3.33}$$

$$\begin{aligned}
&\boldsymbol{M}_f^{ext} + (\boldsymbol{T}_{fq}'\boldsymbol{T}_{qd} + \boldsymbol{T}_{fq}\boldsymbol{T}_{qd}')\boldsymbol{M}_d + \boldsymbol{T}_{fq}\boldsymbol{T}_{qd}\boldsymbol{M}_d' + \boldsymbol{T}_{fq}\boldsymbol{T}_{qd}(\tilde{\boldsymbol{\gamma}} + \tilde{\boldsymbol{e}}_1)(\boldsymbol{F}_d - A^f\boldsymbol{P}) \\
= \; & \tilde{\boldsymbol{\Omega}}_f\boldsymbol{T}_{fq}\boldsymbol{T}_{qd}\boldsymbol{I}_d(\boldsymbol{T}_{dq}\boldsymbol{T}_{qf}\boldsymbol{\Omega}_f + \boldsymbol{\omega}_d) + \boldsymbol{T}_{fq}\boldsymbol{T}_{qd}\tilde{\boldsymbol{\omega}}_d\boldsymbol{I}_d(\boldsymbol{T}_{dq}\boldsymbol{T}_{qf}\boldsymbol{\Omega}_f + \boldsymbol{\omega}_d) \\
&+\boldsymbol{T}_{fq}\boldsymbol{T}_{qd}\boldsymbol{I}_d(\boldsymbol{T}_{dq}\boldsymbol{T}_{qf}\dot{\boldsymbol{\Omega}}_f + \dot{\boldsymbol{\omega}}_d) - \boldsymbol{T}_{fl}\boldsymbol{T}_{ld}\boldsymbol{I}_d\tilde{\boldsymbol{\omega}}_d\boldsymbol{T}_{dq}\boldsymbol{T}_{qf}\boldsymbol{\Omega}_f
\end{aligned} \tag{3.34}$$

in which $\boldsymbol{T}_{fq} = \boldsymbol{T}_{fl}\boldsymbol{T}_{lq}$; $\boldsymbol{e}_q = \boldsymbol{T}_{qd}\boldsymbol{e}_d^f$ is the unit tangent vector of the deformed centerline measured in coordinate q, and $\boldsymbol{T}_{dq}\boldsymbol{u}_q^* \cdot \boldsymbol{e}_d^f = \boldsymbol{u}_q^* \cdot \boldsymbol{T}_{qd}\boldsymbol{e}_d^f$ using a property of the dot product. This system of governing equations includes seven coupled scalar equations that are used to solve for the seven unknown variables: P, u_1^*, u_2^*, u_3^*, θ_1^*, θ_2^*, and θ_3^*. These unknown dynamic displacements are relative to an arbitrarily prescribed base configuration. The governing equations of Eqs. (3.32), (3.33), and (3.34) provide a general Lagrangian formulation expressed in floating coordinate f, and they are equivalent to the total Lagrangian formulation of Eqs. (3.13), (3.23), and (3.24), respectively, if the base configuration is selected as the undeformed pipe configuration.

3.3.2 Piecewise Linearization

Piecewise linearization can be used in the time-domain to compute the dynamic motions for pipes conveying fluid. The base configuration for a time-step can be selected as the configuration at the end of the prior time-step, such that the dynamic displacements ($\boldsymbol{u}_q^*$, $\boldsymbol{\theta}_q^*$) are the incremental displacements occurring at the current time-step. Three additional assumptions are applied to enable the nonlinear model of a pipe conveying fluid to be linearized about an evolving base configuration: (a) incremental dynamic displacements ($\boldsymbol{u}_q^*$, $\boldsymbol{\theta}_q^*$) along the pipe can be assumed small within one time-step; (b) constitutive relationships for the pipe are assumed to be linear elastic, and (c) the flow direction is assumed to be perpendicular to the local deformed pipe cross-section such that the effect on flow direction due to pipe shear deformation can be neglected.

Transformation matrices $\boldsymbol{T}_{qd}$ and $\boldsymbol{T}_{dq}$ can be simplified considerably if the magnitudes of rotational displacements are assumed small. Setting $\sin(\theta_i^*) \approx \theta$ and $\cos(\theta_i^*) \approx 1$ in the Euler angle formulation yields expressions for transformation matrices $\boldsymbol{T}_{qd}$ and $\boldsymbol{T}_{dq}$ simplified for small angles:

$$\boldsymbol{T}_{qd} \approx \boldsymbol{I} + \tilde{\boldsymbol{\theta}}^* \tag{3.35}$$

$$\boldsymbol{T}_{dq} = \boldsymbol{T}_{qd}^T \approx \boldsymbol{I} - \tilde{\boldsymbol{\theta}}^* \tag{3.36}$$

in which $\boldsymbol{I}$ is the identity matrix. The linearized angular velocity and acceleration are obtained by substituting Eqs. (3.35) - (3.36) into Eqs. (3.27) and (3.28) and neglecting all terms of second-order and higher in θ_i^*, $\dot{\theta}_i^*$, and $\ddot{\theta}_i^*$:

$$\boldsymbol{\omega}_d \approx \left[\dot{\theta}_1^*, \dot{\theta}_2^*, \dot{\theta}_3^*\right]^T = \dot{\boldsymbol{\theta}}^* \tag{3.37}$$

$$\dot{\boldsymbol{\omega}}_d \approx \left[\ddot{\theta}_1^*, \ddot{\theta}_2^*, \ddot{\theta}_3^*\right]^T = \ddot{\boldsymbol{\theta}}^* \tag{3.38}$$

Strain measures are computed for the total displacements relative to the undeformed configuration using the sum of quasi-static base displacements plus incremental dynamic displacements. Strain measures can be assumed linear near the base configuration for small dynamic displacements. The total curvature vector is then computed as: $\tilde{\boldsymbol{k}}_d = \boldsymbol{T}_{dq}\boldsymbol{T}_{ql}\boldsymbol{T}_{lf}\boldsymbol{T}'_{fl}\boldsymbol{T}_{lq}\boldsymbol{T}_{qd} + \boldsymbol{T}_{dq}\boldsymbol{T}_{ql}(\boldsymbol{T}_{lq}\boldsymbol{T}_{qd})' \approx \tilde{\boldsymbol{k}}_q - \tilde{\boldsymbol{\theta}}^*\tilde{\boldsymbol{k}}_q + \tilde{\boldsymbol{k}}_q\tilde{\boldsymbol{\theta}}^* + \tilde{\boldsymbol{\theta}}^{*'}$ in which $\tilde{\boldsymbol{k}}_q = \boldsymbol{T}_{qf}\boldsymbol{T}'_{fq} = \boldsymbol{T}_{ql}\boldsymbol{T}_{lf}\boldsymbol{T}'_{fl}\boldsymbol{T}_{lq} + \boldsymbol{T}_{ql}\boldsymbol{T}'_{lq}$ is the skew-symmetric matrix of the local curvature vector of the base configuration. Angular strain linearized near the base configuration is computed by substituting $\tilde{\boldsymbol{k}}_d$ into Eq. (3.6):

$$\boldsymbol{\kappa} = \text{axial}(\tilde{\boldsymbol{k}}_d - \tilde{\boldsymbol{k}}_l) \approx \boldsymbol{\kappa}_q + \tilde{\boldsymbol{k}}_q\boldsymbol{\theta}^* + \boldsymbol{\theta}^{*'} \tag{3.39}$$

where $\boldsymbol{\kappa}_q = \boldsymbol{k}_q - \boldsymbol{k}_l$ is the angular strain associated with deflection of the base configuration. The linear strain is treated in a similar fashion: substituting Eq. (3.29) into Eq. (3.7) and assuming small dynamic displacements. Linearizing the resulting equation yields an expression for strain linearized near the base configuration:

$$\boldsymbol{\gamma} \approx \boldsymbol{\gamma}_q + (\tilde{\boldsymbol{\gamma}}_q + \tilde{\boldsymbol{e}}_1)\boldsymbol{\theta}^* + \tilde{\boldsymbol{k}}_q\boldsymbol{u}_q^* + \boldsymbol{u}_q^{*'} \tag{3.40}$$

in which $\boldsymbol{\gamma}_q = \boldsymbol{T}_{ql}(\boldsymbol{e}_1 + \tilde{\boldsymbol{k}}_l\boldsymbol{U}_l + \boldsymbol{U}'_l) - \boldsymbol{e}_1$ is the strain associated with deflection of the base configuration. Only the dynamic strain measures are assumed small and linearized in Eqs. (3.39) and (3.40). Strain measures computed for the base configuration are finite strains that preserve the nonlinearities associated with large deformations from the original undeformed configuration.

Elastic forces and moments can be computed using the strain measures and constitutive matrices assuming linear elasticity, such that Eqs. (3.8) and (3.9) are expressed as:

$$\begin{bmatrix} \boldsymbol{F}_d(s,t) \\ \boldsymbol{M}_d(s,t) \end{bmatrix} = \boldsymbol{K} \begin{bmatrix} \boldsymbol{\gamma}(s,t) \\ \boldsymbol{\kappa}(s,t) \end{bmatrix} = \begin{bmatrix} \boldsymbol{K}_{11} & \boldsymbol{K}_{12} \\ \boldsymbol{K}_{21} & \boldsymbol{K}_{22} \end{bmatrix} \begin{bmatrix} \boldsymbol{\gamma}(s,t) \\ \boldsymbol{\kappa}(s,t) \end{bmatrix} \tag{3.41}$$

in which $\boldsymbol{K}$ is the cross-sectional constitutive matrix, which is constant in time.

The internal flow direction is assumed to be perpendicular to the local deformed cross-section, such that the unit vector representing the flow direction is the unit vector in the $\boldsymbol{A}$-direction:

$$\boldsymbol{e}_q = \boldsymbol{T}_{qd}\boldsymbol{e}_d^f \approx \boldsymbol{T}_{qd}\boldsymbol{e}_1 \tag{3.42}$$

Substituting $\boldsymbol{e}_d^f \approx \boldsymbol{e}_1$ into Eq. (3.11) indicates constant flow along the pipe:

$$\boldsymbol{V}_d \approx V\boldsymbol{e}_1 \tag{3.43}$$

The governing equations linearized about a quasi-static base configuration are derived by substituting Eqs. (3.35) - (3.43) into Eqs. (3.32) - (3.34), and then neglecting the second- and higher-order terms in incremental dynamic displacements:

$$\begin{aligned}
&-A^f P' - f_D \frac{VQ}{2D} + m^f(\boldsymbol{T}_{qf}\boldsymbol{T}_{fg}\boldsymbol{g}) \cdot \boldsymbol{e}_1 + m^f(\boldsymbol{T}_{qf}\boldsymbol{T}_{fg}\boldsymbol{g}) \cdot (\tilde{\boldsymbol{\theta}}^* \boldsymbol{e}_1) \\
\approx& m^f[\boldsymbol{T}_{qf}\boldsymbol{a}_f^W + \boldsymbol{T}_{qf}(\dot{\tilde{\boldsymbol{\Omega}}}_f + \tilde{\boldsymbol{\Omega}}_f\tilde{\boldsymbol{\Omega}}_f)(\boldsymbol{R}_f^{WG_0} + \boldsymbol{T}_{fl}\boldsymbol{U}_l + \boldsymbol{T}_{fq}\boldsymbol{u}_q^*) + 2\boldsymbol{T}_{qf}\tilde{\boldsymbol{\Omega}}_f\boldsymbol{T}_{fq}\dot{\boldsymbol{u}}_q^*] \cdot \boldsymbol{e}_1 \\
&+m^f[\boldsymbol{T}_{qf}\boldsymbol{a}_f^W + \boldsymbol{T}_{qf}(\dot{\tilde{\boldsymbol{\Omega}}}_f + \tilde{\boldsymbol{\Omega}}_f\tilde{\boldsymbol{\Omega}}_f)(\boldsymbol{R}_f^{WG_0} + \boldsymbol{T}_{fl}\boldsymbol{U}_l)] \cdot (\tilde{\boldsymbol{\theta}}^* \boldsymbol{e}_1)
\end{aligned} \tag{3.44}$$

$$\begin{aligned}
&\boldsymbol{F}_f^{ext} + \boldsymbol{T}'_{fq}[\boldsymbol{K}_{11}(\boldsymbol{\gamma}_q + \tilde{\boldsymbol{\gamma}}_q\boldsymbol{\theta}^* + \tilde{\boldsymbol{e}}_1\boldsymbol{\theta}^* + \tilde{\boldsymbol{k}}_q\boldsymbol{u}_q^* + \boldsymbol{u}_q^{*'}) + \boldsymbol{K}_{12}(\boldsymbol{k}_q - \boldsymbol{k}_l + \tilde{\boldsymbol{k}}_q\boldsymbol{\theta}^* + \boldsymbol{\theta}^{*'}) - A^f P\boldsymbol{e}_1] \\
&+\boldsymbol{T}_{fq}[\boldsymbol{K}_{11}(\boldsymbol{\gamma}_q + \tilde{\boldsymbol{\gamma}}_q\boldsymbol{\theta}^* + \tilde{\boldsymbol{e}}_1\boldsymbol{\theta}^* + \tilde{\boldsymbol{k}}_q\boldsymbol{u}_q^* + \boldsymbol{u}_q^{*'})' + \boldsymbol{K}_{12}(\boldsymbol{k}_q - \boldsymbol{k}_l + \tilde{\boldsymbol{k}}_q\boldsymbol{\theta}^* + \boldsymbol{\theta}^{*'})' - A^f P'\boldsymbol{e}_1] \\
\approx&(m^p + m^f)[\boldsymbol{a}_f^W + (\dot{\tilde{\boldsymbol{\Omega}}}_f + \tilde{\boldsymbol{\Omega}}_f\tilde{\boldsymbol{\Omega}}_f)(\boldsymbol{R}_f^{WG_0} + \boldsymbol{T}_{fl}\boldsymbol{U}_l + \boldsymbol{T}_{fq}\boldsymbol{u}_q^*) + 2\tilde{\boldsymbol{\Omega}}_f\boldsymbol{T}_{fq}\dot{\boldsymbol{u}}_q^* + \boldsymbol{T}_{fq}\ddot{\boldsymbol{u}}_q^*] \\
&+m^f V\tilde{\boldsymbol{\Omega}}_f\boldsymbol{T}_{fq}\boldsymbol{e}_1 - m^f V\tilde{\boldsymbol{\Omega}}_f\boldsymbol{T}_{fq}\tilde{\boldsymbol{e}}_1\boldsymbol{\theta}^* - m^f\tilde{\boldsymbol{\Omega}}_f\boldsymbol{T}_{fq}(\boldsymbol{e}_1\boldsymbol{e}_1^T)\dot{\boldsymbol{u}}_q^* - m^f V\boldsymbol{T}_{fq}\tilde{\boldsymbol{e}}_1\dot{\boldsymbol{\theta}}^* - m^f\boldsymbol{T}_{fq}(\boldsymbol{e}_1\boldsymbol{e}_1^T)\ddot{\boldsymbol{u}}_q^* \\
&+m^f V[V\boldsymbol{T}_{fq}(\boldsymbol{e}_1 - \tilde{\boldsymbol{e}}_1\boldsymbol{\theta}^*) - \boldsymbol{T}_{fq}(\boldsymbol{e}_1\boldsymbol{e}_1^T)\dot{\boldsymbol{u}}_q^*)]' - m^f V(\dot{\boldsymbol{u}}_q^* \cdot \boldsymbol{e}_1)(\boldsymbol{T}_{fq}\boldsymbol{e}_1)'
\end{aligned} \tag{3.45}$$

$$\begin{aligned}
&\boldsymbol{M}_f^{ext} + \boldsymbol{T}'_{fq}[\boldsymbol{K}_{21}(\boldsymbol{\gamma}_q + \tilde{\boldsymbol{\gamma}}_q\boldsymbol{\theta}^* + \tilde{\boldsymbol{e}}_1\boldsymbol{\theta}^* + \tilde{\boldsymbol{k}}_q\boldsymbol{u}_q^* + \boldsymbol{u}_q^{*'}) + \boldsymbol{K}_{22}(\boldsymbol{k}_q - \boldsymbol{k}_l + \tilde{\boldsymbol{k}}_q\boldsymbol{\theta}^* + \boldsymbol{\theta}^{*'})] \\
&+\boldsymbol{T}_{fq}[\boldsymbol{K}_{21}(\boldsymbol{\gamma}_q + \tilde{\boldsymbol{\gamma}}_q\boldsymbol{\theta}^* + \tilde{\boldsymbol{e}}_1\boldsymbol{\theta}^* + \tilde{\boldsymbol{k}}_q\boldsymbol{u}_q^* + \boldsymbol{u}_q^{*'})' + \boldsymbol{K}_{22}(\boldsymbol{k}_q - \boldsymbol{k}_l + \tilde{\boldsymbol{k}}_q\boldsymbol{\theta}^* + \boldsymbol{\theta}^{*'})'] \\
&+\boldsymbol{T}_{fq}(\tilde{\boldsymbol{\gamma}}_q + \tilde{\boldsymbol{e}}_1)[\boldsymbol{K}_{11}(\boldsymbol{\gamma}_q + \tilde{\boldsymbol{\gamma}}_q\boldsymbol{\theta}^* + \tilde{\boldsymbol{e}}_1\boldsymbol{\theta}^* + \tilde{\boldsymbol{k}}_q\boldsymbol{u}_q^* + \boldsymbol{u}_q^{*'}) + \boldsymbol{K}_{12}(\boldsymbol{k}_q - \boldsymbol{k}_l + \tilde{\boldsymbol{k}}_q\boldsymbol{\theta}^* + \boldsymbol{\theta}^{*'}) - A^f P\boldsymbol{e}_1] \\
\approx&\tilde{\boldsymbol{\Omega}}_f\boldsymbol{T}_{fq}\boldsymbol{I}_d\boldsymbol{T}_{qf}\boldsymbol{\Omega}_f + \boldsymbol{T}_{fq}\boldsymbol{I}_d\boldsymbol{T}_{qf}\dot{\boldsymbol{\Omega}}_f + \boldsymbol{T}_{fq}\boldsymbol{I}_d\ddot{\boldsymbol{\theta}}^* + [\tilde{\boldsymbol{\Omega}}_f\boldsymbol{T}_{fq}\boldsymbol{I}_d - \boldsymbol{T}_{fq}(\widetilde{\boldsymbol{I}_d\boldsymbol{T}_{qf}\boldsymbol{\Omega}_f}) + \boldsymbol{T}_{fq}\boldsymbol{I}_d(\widetilde{\boldsymbol{T}_{qf}\boldsymbol{\Omega}_f})]\dot{\boldsymbol{\theta}}^* \\
&+[\tilde{\boldsymbol{\Omega}}_f\boldsymbol{T}_{fq}\boldsymbol{I}_d(\widetilde{\boldsymbol{T}_{qf}\boldsymbol{\Omega}_f}) - \tilde{\boldsymbol{\Omega}}_f\boldsymbol{T}_{fq}(\widetilde{\boldsymbol{I}_d\boldsymbol{T}_{qf}\boldsymbol{\Omega}_f}) + \boldsymbol{T}_{fq}\boldsymbol{I}_d(\widetilde{\boldsymbol{T}_{qf}\dot{\boldsymbol{\Omega}}_f}) - \boldsymbol{T}_{fq}(\widetilde{\boldsymbol{I}_d\boldsymbol{T}_{qf}\dot{\boldsymbol{\Omega}}_f})]\boldsymbol{\theta}^*
\end{aligned} \tag{3.46}$$

in which the following vector manipulations are employed: $\tilde{\boldsymbol{\alpha}}\boldsymbol{\beta} = -\tilde{\boldsymbol{\beta}}\boldsymbol{\alpha}$; $(\boldsymbol{\alpha} \cdot \boldsymbol{\beta})\boldsymbol{\eta} = (\boldsymbol{\eta}\boldsymbol{\beta}^T)\boldsymbol{\alpha}$, and $\boldsymbol{\alpha}, \boldsymbol{\beta}, \boldsymbol{\eta}$ are arbitrary 3D vectors. Eqs. (3.44) - (3.46) are the EOM's of momentum-based theory for pipes conveying fluid linearized about a quasi-static base configuration using separation of displacement with the three additional assumptions. Geometric and kinematic nonlinearities remain preserved for the base configuration. No additional equations are required to solve for the unknown variables $\boldsymbol{u}_q^*$, $\boldsymbol{\theta}^*$, and P, because the linearized rotation formulations and strain measures have been substituted into these EOM's. Eqs. (3.44) - (3.46) become a linearized updated Lagrangian formulation if the quasi-static base configuration is selected as the configuration computed from the prior time-step. A time-stepping scheme is developed in the next section, in which the displacement results computed at each time-step are used to update the evolving base configuration.

3.4 Numerical Implementation

A time-stepping scheme is developed that allows a nonlinear pipe-fluid model to be reduced into a series of piecewise-linear models. The piecewise-linear governing equations are spatially discretized using the finite volume method, resulting in a system of ordinary differential equations (OED's) which can be numerically solved using an existing ODE solver and appropriate boundary conditions.

3.4.1 Finite Volume Discretization

The spatial discretization used for the piecewise-linear model is derived using the finite volume method. Application of the finite volume method is convenient in this case because the underlying theory is based on a conservation law. The governing equations could alternately be discretized using the finite element method. A finite control volume attached to a deformed pipe segment is shown in Fig. 3.4. The jth and (j+1)st cross-sections are end boundaries of the nth segment, and G^n is the center of mass of the nth segment. The discretized governing equations for the nth segment can be derived based on Eqs. (3.44) - (3.46):

$$\begin{aligned}
&A^fP^j - A^fP^{j+1} - \frac{f_D V Q \Delta s^n}{2D} + m^{f,n}(\boldsymbol{T}^n_{qf}\boldsymbol{T}_{fg}\boldsymbol{g})\cdot\boldsymbol{e}_1 + m^{f,n}(\boldsymbol{T}^n_{qf}\boldsymbol{T}_{fg}\boldsymbol{g})\cdot(\tilde{\boldsymbol{\theta}}^{*,n}\boldsymbol{e}_1)\\
\approx& m^{f,n}[\boldsymbol{T}^n_{qf}\boldsymbol{a}^W_f + \boldsymbol{T}^n_{qf}(\dot{\tilde{\boldsymbol{\Omega}}}_f + \tilde{\boldsymbol{\Omega}}_f\tilde{\boldsymbol{\Omega}}_f)(\boldsymbol{R}^n_f + \boldsymbol{T}^n_{fl}\boldsymbol{U}^n_l + \boldsymbol{T}^n_{fq}\boldsymbol{u}^{*,n}_q) + 2\boldsymbol{T}^n_{qf}\tilde{\boldsymbol{\Omega}}_f\boldsymbol{T}^n_{fq}\dot{\boldsymbol{u}}^{*,n}_q]\cdot\boldsymbol{e}_1\\
&+m^{f,n}[\boldsymbol{T}^n_{qf}\boldsymbol{a}^W_f + \boldsymbol{T}^n_{qf}(\dot{\tilde{\boldsymbol{\Omega}}}_f + \tilde{\boldsymbol{\Omega}}_f\tilde{\boldsymbol{\Omega}}_f)(\boldsymbol{R}^n_f + \boldsymbol{T}^n_{fl}\boldsymbol{U}^n_l)]\cdot(\tilde{\boldsymbol{\theta}}^{*,n}\boldsymbol{e}_1)
\end{aligned} \tag{3.47}$$

$$\begin{aligned}
&\boldsymbol{F}^{ext,n}_f - \boldsymbol{T}^n_{fq}\boldsymbol{T}^{nj}_q(\boldsymbol{K}_{11}\boldsymbol{\gamma}^j + \boldsymbol{K}_{12}\boldsymbol{\kappa}^j - A^fP^j\boldsymbol{e}_1) + \boldsymbol{T}^n_{fq}\boldsymbol{T}^{nj+1}_q(\boldsymbol{K}_{11}\boldsymbol{\gamma}^{j+1} + \boldsymbol{K}_{12}\boldsymbol{\kappa}^{j+1} - A^fP^{j+1}\boldsymbol{e}_1)\\
\approx&(m^{p,n}+m^{f,n})[\boldsymbol{a}^W_f + (\dot{\tilde{\boldsymbol{\Omega}}}_f + \tilde{\boldsymbol{\Omega}}_f\tilde{\boldsymbol{\Omega}}_f)(\boldsymbol{R}^n_f + \boldsymbol{T}^n_{fl}\boldsymbol{U}^n_l + \boldsymbol{T}^n_{fq}\boldsymbol{u}^{*,n}_q) + 2\tilde{\boldsymbol{\Omega}}_f\boldsymbol{T}^n_{fq}\dot{\boldsymbol{u}}^{*,n}_q + \boldsymbol{T}^n_{fq}\ddot{\boldsymbol{u}}^{*,n}_q]\\
&+m^{f,n}V\tilde{\boldsymbol{\Omega}}_f\boldsymbol{T}^n_{fq}\boldsymbol{e}_1 - m^{f,n}V\tilde{\boldsymbol{\Omega}}_f\boldsymbol{T}^n_{fq}\tilde{\boldsymbol{e}}_1\boldsymbol{\theta}^{*,n} - m^{f,n}\tilde{\boldsymbol{\Omega}}_f\boldsymbol{T}^n_{fq}(\boldsymbol{e}_1\boldsymbol{e}_1^T)\dot{\boldsymbol{u}}^{*,n}_q - m^{f,n}V\boldsymbol{T}^n_{fq}\tilde{\boldsymbol{e}}_1\dot{\boldsymbol{\theta}}^{*,n}\\
&-m^{f,n}\boldsymbol{T}^n_{fq}(\boldsymbol{e}_1\boldsymbol{e}_1^T)\ddot{\boldsymbol{u}}^{*,n}_q - A^f\rho^f\boldsymbol{T}^n_{fq}\boldsymbol{T}^{nj}_q[V^2\boldsymbol{e}_1 - V^2\tilde{\boldsymbol{e}}_1\boldsymbol{\theta}^{*,n} - 2V(\boldsymbol{e}_1\boldsymbol{e}_1^T)\dot{\boldsymbol{u}}^{*,n}_q]\\
&+A^f\rho^f\boldsymbol{T}^n_{fq}\boldsymbol{T}^{nj+1}_q[V^2\boldsymbol{e}_1 - V^2\tilde{\boldsymbol{e}}_1\boldsymbol{\theta}^{*,n} - 2V(\boldsymbol{e}_1\boldsymbol{e}_1^T)\dot{\boldsymbol{u}}^{*,n}_q]
\end{aligned} \tag{3.48}$$

$$\begin{aligned}
&\boldsymbol{M}^{ext,n}_f - \boldsymbol{T}^n_{fq}\boldsymbol{T}^{nj}_q(\boldsymbol{K}_{21}\boldsymbol{\gamma}^j + \boldsymbol{K}_{22}\kappa^j) + \boldsymbol{T}^n_{fq}\boldsymbol{T}^{nj+1}_q(\boldsymbol{K}_{21}\boldsymbol{\gamma}^{j+1} + \boldsymbol{K}_{22}\kappa^{j+1})\\
&-\boldsymbol{T}^n_{fq}\tilde{\boldsymbol{R}}^{nj}_q\boldsymbol{T}^{nj}_q(\boldsymbol{K}_{21}\boldsymbol{\gamma}^j + \boldsymbol{K}_{22}\kappa^j - A^fP^j\boldsymbol{e}_1)\\
&+\boldsymbol{T}^n_{fq}\tilde{\boldsymbol{R}}^{nj+1}_q\boldsymbol{T}^{nj+1}_q(\boldsymbol{K}_{21}\boldsymbol{\gamma}^{j+1} + \boldsymbol{K}_{22}\kappa^{j+1} - A^fP^{j+1}\boldsymbol{e}_1)\\
\approx&\tilde{\boldsymbol{\Omega}}_f\boldsymbol{T}^n_{fq}\boldsymbol{I}^n\boldsymbol{T}^n_{qf}\boldsymbol{\Omega}_f + \boldsymbol{T}^n_{fq}\boldsymbol{I}^n\boldsymbol{T}^n_{qf}\dot{\boldsymbol{\Omega}}_f + \boldsymbol{T}^n_{fq}\boldsymbol{I}^n\ddot{\boldsymbol{\theta}}^{*,n}\\
&+[\tilde{\boldsymbol{\Omega}}_f\boldsymbol{T}^n_{fq}\boldsymbol{I}^n - \boldsymbol{T}^n_{fq}(\widetilde{\boldsymbol{I}^n\boldsymbol{T}^n_{qf}\boldsymbol{\Omega}_f}) + \boldsymbol{T}^n_{fq}\boldsymbol{I}^n(\widetilde{\boldsymbol{T}^n_{qf}\boldsymbol{\Omega}_f})]\dot{\boldsymbol{\theta}}^{*,n}\\
&+[\tilde{\boldsymbol{\Omega}}_f\boldsymbol{T}^n_{fq}\boldsymbol{I}^n(\widetilde{\boldsymbol{T}^n_{qf}\boldsymbol{\Omega}_f}) - \tilde{\boldsymbol{\Omega}}_f\boldsymbol{T}^n_{fq}(\widetilde{\boldsymbol{I}^n\boldsymbol{T}^n_{qf}\boldsymbol{\Omega}_f}) + \boldsymbol{T}^n_{fq}\boldsymbol{I}^n(\widetilde{\boldsymbol{T}^n_{qf}\dot{\boldsymbol{\Omega}}_f}) - \boldsymbol{T}^n_{fq}(\widetilde{\boldsymbol{I}^n\boldsymbol{T}^n_{qf}\dot{\boldsymbol{\Omega}}_f})]\boldsymbol{\theta}^{*,n}
\end{aligned} \tag{3.49}$$

in which P^j and P^{j+1} are the fluid pressures at the jth and (j+1)st cross-sections; $\Delta s^n = s^{j+1} - s^j$ is the curvilinear length of the nth segment; $m^{f,n} = \rho^f A^f \Delta s^n$ is the fluid mass within the control volume; $m^{p,n}$ is the pipe mass of the nth segment; $\boldsymbol{I}^n$ is the mass moment of inertia of the nth segment excluding the fluid torsional inertia; $\boldsymbol{T}^n_{qf}$ and $\boldsymbol{T}^n_{fq}$ are the transformation matrices between floating coordinate f and the local base coordinate q at the center of the nth segment; $\boldsymbol{T}^{nj}_q$ and $\boldsymbol{T}^{nj+1}_q$ are the transformation matrices among different local base coordinates at the jth and (j+1)st cross-sections and the center of the nth segment; $\boldsymbol{R}^n_f = \boldsymbol{R}^{WG^n}_f$ is the position vector of

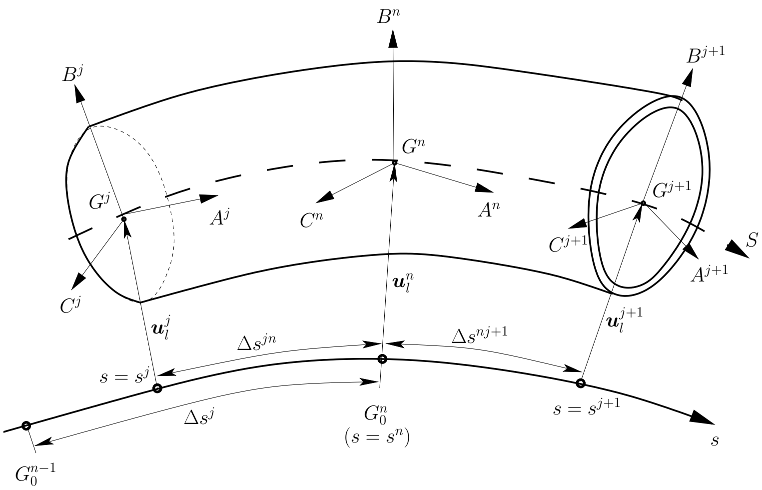

Figure 3.4: The nth pipe finite control volume.

the nth segment; $\boldsymbol{R}_q^{nj}$ and $\boldsymbol{R}_q^{nj+1}$ are vectors pointing from mass center G^n to the centers of the jth and (j+1)st cross-sections; $\boldsymbol{F}_f^{ext,n}$ and $\boldsymbol{M}_f^{ext,n}$ are the total external force and external moment about G^n exerted on the nth segment, respectively; $\boldsymbol{u}_q^{*,n}$ and $\boldsymbol{\theta}^{*,n}$ are the incremental dynamic displacements of the nth segment, and the strain measures at cross-sections can be computed based on Eqs. (3.39) and (3.40) using linear interpolation:

$$\boldsymbol{\kappa}^j \approx \boldsymbol{k}_q^j - \boldsymbol{k}_l^j + \tilde{\boldsymbol{k}}_q^j \frac{\Delta s^{jn}\boldsymbol{\theta}^{*,n-1} + \Delta s^{n-1j}\boldsymbol{\theta}^{*,n}}{\Delta s^j} + \frac{\boldsymbol{\theta}^{*,n} - \boldsymbol{\theta}^{*,n-1}}{\Delta s^j} \tag{3.50}$$

$$\boldsymbol{\gamma}^j \approx \boldsymbol{\gamma}_q^j + (\tilde{\boldsymbol{\gamma}}_q^j + \tilde{\boldsymbol{e}}_1)\frac{\Delta s^{jn}\boldsymbol{\theta}^{*,n-1} + \Delta s^{n-1j}\boldsymbol{\theta}^{*,n}}{\Delta s^j} + \tilde{\boldsymbol{k}}_q^j \frac{\Delta s^{jn}\boldsymbol{u}_q^{*,n-1} + \Delta s^{n-1j}\boldsymbol{u}_q^{*,n}}{\Delta s^j} + \frac{\boldsymbol{u}_q^{*,n} - \boldsymbol{u}_q^{*,n-1}}{\Delta s^j} \tag{3.51}$$

where Δs^j, Δs^{n-1j}, Δs^{jn} are curvilinear distances: Δs^j=s^n-s^{n-1}; Δs^{n-1j}=s^j-s^{n-1}; Δs^{jn}=s^n-s^j (see Fig. 3.4).

3.4.2 Evolving Base Configuration

The separation of displacements technique is combined with linearization of the dynamic system to represent large nonlinear displacements as a series of piecewise-linear displacements. A time-stepping scheme is developed to solve Eqs. (3.47) - (3.49), in which the base configuration for any time-step is selected as the configuration computed at the end of the prior time-step with velocities from that time-step. The evolving base configuration is updated from the prior time-step including all nonlinear and large-angle effects. Quantities that need to be updated for each time-step are: the base translational displacement, ${}^{m}\boldsymbol{U}_l^n$; the transformation matrix between floating coordinate and local base coordinates, ${}^{m}\boldsymbol{T}_{fq}^n$; the transformation matrix between local coordinates along the base configuration, ${}^{m}\boldsymbol{T}_q^{nj}$ and ${}^{m}\boldsymbol{T}_q^{nj+1}$; the linear strain associated with base deflections, ${}^{m}\boldsymbol{\gamma}_q^j$; the curvature vector of the base configuration, ${}^{m}\boldsymbol{k}_q^j$, and vectors ${}^{m}\boldsymbol{R}_q^{nj}$ and ${}^{m}\boldsymbol{R}_q^{nj+1}$. The left superscript m denotes the quantity evaluated at the mth time-step; the right superscript indicates locations along the beam, e.g., ${}^{m}\boldsymbol{u}_q^{*,n}$ and ${}^{m}\boldsymbol{\theta}^{*,n}$ are the incremental displacements of the nth beam segment solved at the mth time-step based on the configuration updated from the (m-1)st time-step. These quantities are updated at the end of the mth time-step:

$$ {}^{m}\boldsymbol{T}_{lq}^n = {}^{m-1}\boldsymbol{T}_{lq}^n \, {}^{m}\boldsymbol{T}_{qd}^n = {}^{m-1}\boldsymbol{T}_{lq}^n (\boldsymbol{I} + {}^{m}\tilde{\boldsymbol{\theta}}^{*,n}) \tag{3.52} $$

$$ {}^{m}\boldsymbol{U}_l^n = {}^{m-1}\boldsymbol{U}_l^n + {}^{m}\boldsymbol{T}_{lq}^n \, {}^{m}\boldsymbol{u}_q^{*,n} \tag{3.53} $$

$$ {}^{m}\boldsymbol{T}_{fq}^n = \boldsymbol{T}_{fl}^n \, {}^{m}\boldsymbol{T}_{lq}^n \tag{3.54} $$

$$ {}^{m}\boldsymbol{T}_q^{nj} = {}^{m}\boldsymbol{T}_{ql}^n \, \boldsymbol{T}_l^{nj} \, {}^{m}\boldsymbol{T}_{lq}^j \tag{3.55} $$

$$ {}^{m}\boldsymbol{T}_q^{nj+1} = {}^{m}\boldsymbol{T}_{ql}^n \, \boldsymbol{T}_l^{nj+1} \, {}^{m}\boldsymbol{T}_{lq}^{j+1} \tag{3.56} $$

$$ {}^{m}\boldsymbol{R}_q^{nj} = {}^{m}\boldsymbol{T}_{ql}^n \, (\boldsymbol{R}_l^{nj} - {}^{m}\boldsymbol{U}_l^n + \boldsymbol{T}_l^{nj} \, {}^{m}\boldsymbol{U}_l^j) \tag{3.57} $$

$$ {}^{m}\boldsymbol{R}_q^{nj+1} = {}^{m}\boldsymbol{T}_{ql}^n \, (\boldsymbol{R}_l^{nj+1} - {}^{m}\boldsymbol{U}_l^n + \boldsymbol{T}_l^{nj+1} \, {}^{m}\boldsymbol{U}_l^{j+1}) \tag{3.58} $$

$$ {}^{m}\boldsymbol{\gamma}_q^j = {}^{m}\boldsymbol{T}_{ql}^j \left(\boldsymbol{e}_1 + \tilde{\boldsymbol{k}}_l^j \, {}^{m}\boldsymbol{U}_l^j + \frac{{}^{m}\boldsymbol{U}_l^n - {}^{m}\boldsymbol{U}_l^{n-1}}{\Delta s^j} \right) - \boldsymbol{e}_1 \tag{3.59} $$

$$ {}^{m}\tilde{\boldsymbol{k}}_q^j = {}^{m}\boldsymbol{T}_{ql}^j \tilde{\boldsymbol{k}}_l^j \, {}^{m}\boldsymbol{T}_{lq}^j + {}^{m}\boldsymbol{T}_{ql}^j \left(\frac{{}^{m}\boldsymbol{T}_{lq}^n - {}^{m}\boldsymbol{T}_{lq}^{n-1}}{\Delta s^j} \right) \tag{3.60} $$

in which ${}^{m}\boldsymbol{T}^{j}_{lq}$, ${}^{m}\boldsymbol{T}^{j}_{ql}$, and ${}^{m}\boldsymbol{U}^{j}_{l}$ are evaluated at the jth cross-section by linear interpolation:

$${}^{m}\boldsymbol{T}^{j}_{lq}=({}^{m}\boldsymbol{T}^{j}_{ql})^{T} = {}^{m-1}\boldsymbol{T}^{j}_{lq}\left[\frac{\Delta s^{n-1j}(\boldsymbol{I}+{}^{m}\tilde{\boldsymbol{\theta}}^{*,n}) - \Delta s^{jn}(\boldsymbol{I}+{}^{m}\tilde{\boldsymbol{\theta}}^{*,n-1})}{\Delta s^{j}}\right] \tag{3.61}$$

$${}^{m}\boldsymbol{U}^{j}_{l}= {}^{m-1}\boldsymbol{U}^{j}_{l} + {}^{m-1}\boldsymbol{T}^{j}_{lq}\left[\frac{\Delta s^{n-1j}({}^{m}\boldsymbol{u}^{*,n}_{q}) - \Delta s^{jn}({}^{m}\boldsymbol{u}^{*,n-1}_{q})}{\Delta s^{j}}\right] \tag{3.62}$$

The base configuration is updated including nonlinear effects after each time-step. The governing equations are renewed for the (m+1)st time-step at the end of the mth time-step using the updated quantities from Eqs. (3.52) - (3.62). Initial conditions are also renewed at each time-step. Initial displacements (${}^{m+1}_{initial}\boldsymbol{u}^{*,n}_{q}$ and ${}^{m+1}_{initial}\boldsymbol{\theta}^{*,n}$) are set to zero because they are relative to the new base configuration. Initial velocities are obtained by transferring the velocities from the prior step to the newly updated base coordinates:

$${}^{m+1}_{initial}\dot{\boldsymbol{u}}^{*,n}_{q} = {}^{m}\boldsymbol{T}^{n}_{dq}\;{}^{m}\dot{\boldsymbol{u}}^{*,n}_{q}, \qquad {}^{m+1}_{initial}\dot{\boldsymbol{\theta}}^{*,n} = {}^{m}\boldsymbol{T}^{n}_{dq}\;{}^{m}\dot{\boldsymbol{\theta}}^{*,n} \tag{3.63}$$

The governing equation of fluid pressure, Eq. (3.47), can be solved in a weakly-coupled manner. Eq. (3.47) is solved algebraically with respect to P between time-steps using the values updated from the prior time-step. The pressures computed between time-steps along the pipe are then treated as known constants in Eqs. (3.48) and (3.49) for the current time-step.

3.4.3 Boundary Conditions and Assembled System

The fixed-end boundary condition at the first cross-section (j=1) is imposed using an imaginary zeroth beam segment (n=0) at $s = -\Delta s^{11}$ with displacements $\boldsymbol{\theta}^{0} = -\boldsymbol{\theta}^{1}$ and $\boldsymbol{u}^{0}_{l} = -\boldsymbol{u}^{1}_{l}$, such that displacements at the first cross-section are effectively zero. The free-end boundary condition at the (N+1)st cross-section is imposed by setting the stiffness matrices of the (N+1)st cross-section to zero: $\boldsymbol{K}^{N+1}_{11} = \boldsymbol{K}^{N+1}_{12} = \boldsymbol{K}^{N+1}_{21} = \boldsymbol{K}^{N+1}_{22} = \boldsymbol{0}$. Fluid pressures along the pipe are computed algebraically through the evolving base configuration assuming constant flow, such that the boundary pressure can be applied at either end of the pipe.

The complete pipe-fluid model is represented using an assembled system of ODE's. The system of ODE's with respect to 6×N incremental dynamic displacements results from substituting Eqs. (3.50) - (3.51) into governing Eqs. (3.48) - (3.49) and assembling the resulting equations for each of the N segments. Structural damping effects can be modeled by including a damping matrix that is assumed to be proportional to the stiffness and mass matrices. The resulting system of ODE's is linear and explicit, which can be solved for 6×N unknown displacements using an existing ODE solver at each time-step. The governing system of ODE's and fluid pressures are updated between time-steps for each evolving quasi-static base configuration.

3.5 Numerical Examples

The combined pipe-fluid theory and piecewise linearization are demonstrated through a series of numerical examples. The MATLAB "ode45" solver is used to solve the evolving system of ODE's at each time-step, with relative tolerance set to 10^{-6} in all examples. The Haaland equation [145] is employed to compute the Darcy friction factor. The linear elastic stiffness matrix is adopted for the pipe cross-section: $\boldsymbol{K} = \text{diag}(EA^p, EI, EI, 2GI, GA^p, GA^p)$, in which A^p is the cross-sectional area of the pipe wall; I is the moment of inertia of the pipe cross-section; E and G are Young's modulus and the shear modulus, respectively. The following dimensionless quantities are introduced to enable direct comparison with reference results:

$$\mu_m = \frac{m^f}{m^f + m^p}, \quad \mu_A = \frac{A^p L^2}{I}, \quad \mu_V = VL\sqrt{\frac{m^f}{EI}}, \quad \mu_\Omega = \Omega L^2\sqrt{\frac{m^p}{EI}}, \quad \mu_\omega = \omega L^2\sqrt{\frac{m^f + m^p}{EI}} \tag{3.64}$$

$$\mu_V^* = VR\sqrt{\frac{m^f}{EI}}, \quad \mu_\Omega^* = \Omega R^2\sqrt{\frac{m^p}{EI}}, \quad \mu_\omega^* = \omega R^2\sqrt{\frac{m^f + m^p}{EI}} \quad \text{(for semi-circular curved pipes)} \tag{3.65}$$

in which L is the length of a pipe; R is the radius of a semi-circle curved pipe; Ω is the magnitude of the overall pipe rotation velocity (rad/s), and ω is the circular frequency of pipe vibrations.

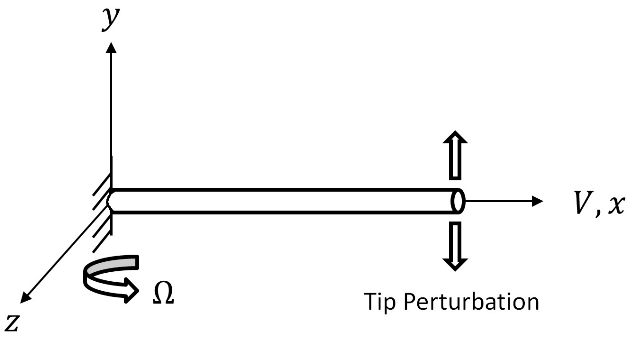

Figure 3.5: Rotating cantilever pipe conveying fluid.

3.5.1 Rotating Cantilever Pipe

The effectiveness of the new pipe-fluid combined model is verified through comparison with several reference results [94, 146, 147]. A white-noise, small-amplitude perturbation is applied to the tip of the cantilever pipe (Fig. 3.5), and the power spectral density of the tip response is computed. The resulting peak frequencies approximate the natural frequencies of the cantilever pipe. The pipe is discretized into 40 elements and the time-step size is set to 0.0005 s; these parameters were selected using convergence tests. Direct comparison with the reference results is enabled by assuming inviscid fluid and zero fluid pressures throughout the pipe.

The natural frequencies are assessed using the new methodology for cantilever pipe without fluid but subject to overall rotation. The left-hand half of Table 3.1 shows the lowest three dimensionless frequencies computed using other methodologies, including an ANSYS model based on 20 Timoshenko beam elements and an Euler-Bernoulli beam model with nonlinear strains [94]. The natural frequencies match well when there is no rotation (μ_Ω=0) and consistently increase with rotation speed. The first natural frequency computed using the new geometrically-exact model increases faster with rotation speed than that computed using the Euler-Bernoulli model, indicating that the new combined model could more accurately capture geometric stiffening effects.

The natural frequencies are assessed for a non-rotating cantilever pipe conveying fluid over a range of flow velocities. The right-hand half of Table 3.1 shows the comparison among experimental results [146], numerical results based on linear Timoshenko beam theory [147], and the

Table 3.1: Dimensionless frequencies, μ_ω, of a cantilever pipe.

Rotating without flow (μ_A=3.90×10^3, μ_m=0)	1st	2nd	3rd	Non-rotating with flow (μ_A=1.80×10^4, μ_m=0.5035)	1st	2nd	3rd
μ_Ω=0, μ_V=0				μ_Ω=0, μ_V=0			
Combined model	3.49	21.49	59.53	Combined model	3.51	21.98	61.03
Yoon and Son, [94]	3.34	22.02	–	Zhai et al., [147]	3.51	21.94	61.28
ANSYS	3.50	22.49	58.28	Sinha et al., [146] (μ_m=0.5156)	3.15	19.68	54.80
μ_Ω=1, μ_V=0				μ_Ω=0, μ_V=0.27			
Combined model	3.66	21.78	59.76	Combined model	3.39	21.88	61.03
Yoon and Son, [94]	3.37	22.14	–	Zhai et al., [147]	3.46	21.91	61.25
μ_Ω=2, μ_V=0				μ_Ω=0, μ_V=0.81			
Combined model	4.10	22.15	60.14	Combined model	3.39	21.75	61.03
Yoon and Son, [94]	3.44	22.52	–	Zhai et al., [147]	3.00	21.61	60.97
μ_Ω=3, μ_V=0				μ_Ω=0, μ_V=1.35			
Combined model	4.69	22.87	60.76	Combined model	3.82	21.00	60.30
Yoon and Son, [94]	3.56	23.12	–	Zhai et al., [147]	1.79	21.01	60.42

new combined model results. Natural frequencies agree well for the higher orders and when flow velocity is zero. However, the first natural frequency computed using the new model does not consistently decrease with flow velocity like the results computed using the linear Timoshenko model.

This example is next expanded to include the effects of both fluid flow and overall rotation. Fig. 3.6 shows static deformations of the rotating pipe subject to different rotation speeds with dimensionless fluid parameters μ_m=0.5035 and μ_V=1.35. The bending deformation increases with rotation speed in this case: the bending of the pipe in its rotating plane is caused by the Coriolis force induced by the flowing fluid in a rotating frame and is slightly offset by centrifugal force.

3.5.2 Semi-circular Curved Pipe

The new pipe-fluid combined model is next assessed through computation of the dynamic vibrations of a curved pipe conveying fluid. A semi-circular curved pipe with two fixed supports is modeled (Fig. 3.7). The pipe is discretized into 25 elements and the time-step size is set to 0.0001 s, based on convergence tests. The natural frequencies of in-plane vibrations are investigated as in Section 3.5.1: white-noise, small-amplitude perturbations are applied in the x-direction at the 6th element and in the z-direction at the 16th element to excite in-plane vibration. These elements

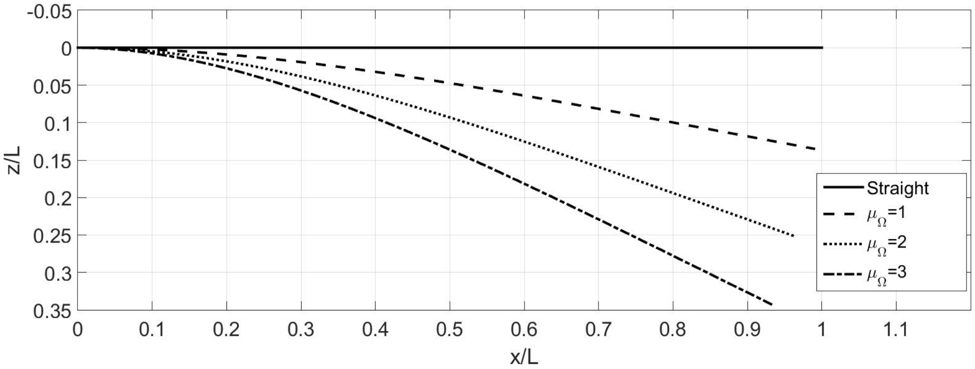

Figure 3.6: Static deformation of rotating cantilever pipe conveying fluid.

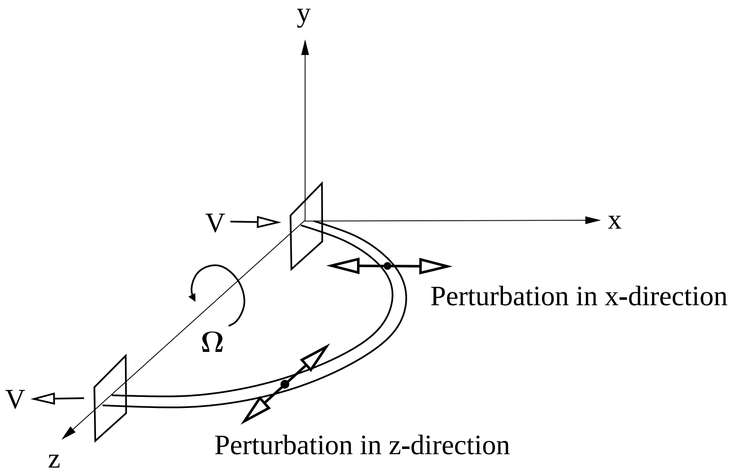

Figure 3.7: Semi-circular curved pipe conveying fluid.

are selected as being close to the quarter-point and point of trisection. The fluid is assumed to be inviscid and fluid pressures throughout the pipe are set to zero for comparison with existing reference results.

Table 3.2 presents the natural frequencies of the in-plane vibration identified from power spectral densities computed at various locations along the curved pipe. The results computed using the new combined model agree well with two sets of established reference results: a small-strain Euler-Bernoulli beam with an extensible centerline [84], and an Euler-Bernoulli model with nonlinear Lagrange strains [87].

Table 3.2: Dimensionless frequencies, μ_ω^*, for in-plane vibration of a semi-circular pipe.

μ_A=1.00 × 10^4, μ_m=0.50	1st	2nd	3rd	μ_A=7.36 × 10^3, μ_m=0.26	1st	2nd
μ_Ω^*=0, μ_V^*=0				μ_Ω^*=0, μ_V^*=0		
Combined model	4.79	9.44	18.00	Combined model	4.55	9.00
Misra et al., [84]	4.67	9.84	18.05	Jung and Chung, [87]	4.38	9.60
μ_Ω^*=0, μ_V^*=1				μ_Ω^*=0, μ_V^*=1		
Combined model	4.70	9.57	17.17	Combined model	4.46	9.04
Misra et al., [84]	4.53	9.88	17.90	Jung and Chung, [87]	4.32	9.66
μ_Ω^*=0, μ_V^*=2				μ_Ω^*=0, μ_V^*=2		
Combined model	4.45	9.83	16.67	Combined model	4.29	9.17
Misra et al., [84]	4.30	9.92	17.62	Jung and Chung, [87]	4.21	9.64
μ_Ω^*=0, μ_V^*=3				μ_Ω^*=0, μ_V^*=3		
Combined model	4.08	10.17	16.13	Combined model	4.03	9.30
Misra et al., [84]	3.95	9.77	17.19	Jung and Chung, [87]	4.00	9.66
μ_Ω^*=0, μ_V^*=4				μ_Ω^*=0, μ_V^*=4		
Combined model	3.68	10.34	15.88	Combined model	3.68	9.34
Misra et al., [84]	3.57	9.65	17.17	Jung and Chung, [87]	3.76	9.62

The effectiveness of capturing 3D deformations and inertial effects in non-inertial frames is demonstrated through a semi-circular pipe conveying fluid (μ_A=10^4, μ_m=0.5, μ_V^*=1) subject to overall rotation about the z-axis (Fig. 3.7). Fig. 3.8 and Fig. 3.9 respectively show the static in-plane and out-of-plane deformations with the pipe subject to various rotation speeds. The in-plane deformation is significantly affected by centrifugal force: the pipe deforms further outwards from the rotating axis as rotation speed increases (Fig. 3.8). The Coriolis effect induces out-of-plane deformations: the Coriolis force acts in the negative y-direction when the fluid flows away from the rotating axis and acts in the positive y-direction when the fluid flows towards to the z-axis, which causes deformation in the opposite direction (Fig. 3.9).

3.5.3 Top-tensioned Riser

Marine risers are long steel pipes conveying fluid from the seabed to the water surface, which are critical structures in the offshore oil and gas industry. Top-tensioned risers are supported only at the top and bottom; the long span can be subject to significant dynamic effects. The new pipe-fluid combined model is demonstrated through application to a typical top-tensioned production riser conveying oil. The outer diameter of the riser is 254 mm; the inner diameter is 228.6 mm; the

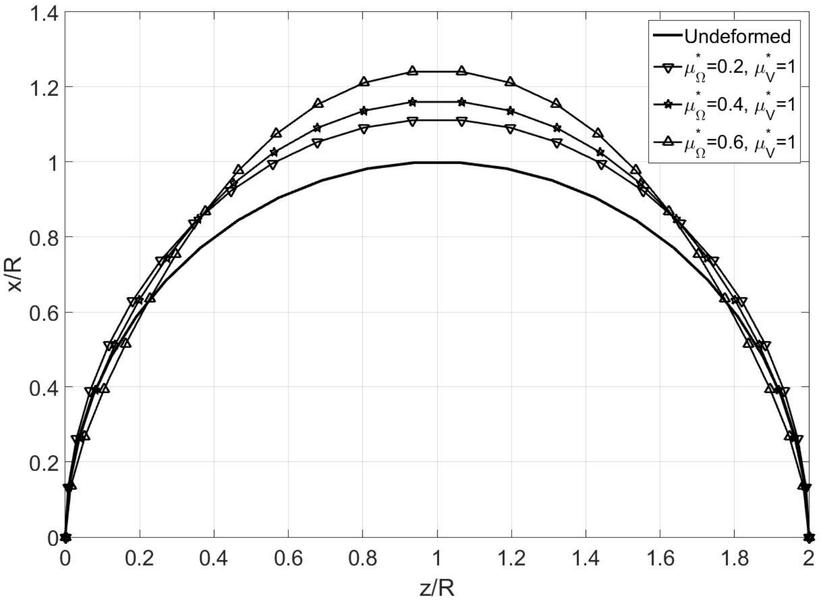

Figure 3.8: In-plane deformation of rotating semi-circular pipe conveying fluid. (Deformation is magnified by a factor of 20.)

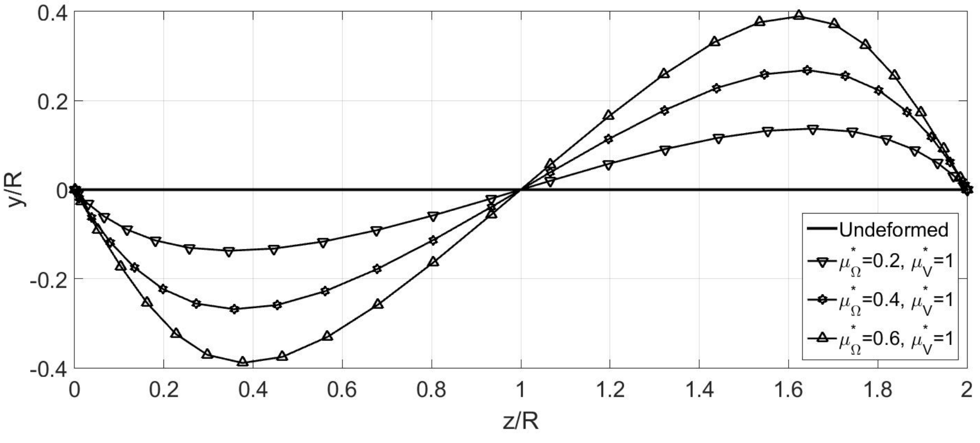

Figure 3.9: Out-of-plane deformation of rotating semi-circular pipe conveying fluid. (Deformation is magnified by a factor of 20.)

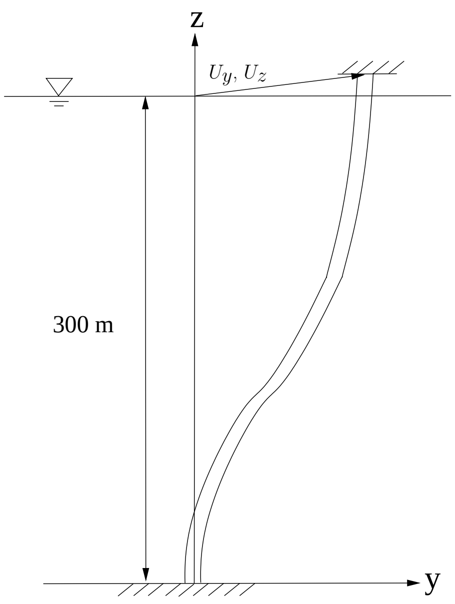

Figure 3.10: Top-tensioned riser.

unstretched length is 300 m; Young's modulus is 209 GPa; pipe density is 7800 kg/m^3; oil density is 900 kg/m^3; oil dynamic viscosity is 0.009 Pa-s; pipe wall roughness is 0.05 mm; pipe Poisson's ratio is 0.3, and the stiffness damping coefficient is set to 0.001. The wellhead pressure is assumed to be 20.68 MPa ($\approx$3000 psi); a production rate of 50,000 barrels per day is measured with a flow velocity of 2.242 m/s. The connection at the lower end of the riser is treated as a fixed connection at the wellhead on the seabed, and the upper end is treated as a fixed connection at the deck of the floating platform (Fig.3.10). The riser is subject to gravity, buoyancy, external hydrodynamic forces caused by moving through the sea water, with the top end of the riser forced through a prescribed time-history. The hydrodynamic loads are computed using Morison's equation with inertia coefficient of 1.8 and drag coefficient of 1.0. The riser is discretized into 100 elements and the time-step size is set to 0.001 s, based on convergence tests.

The new pipe-fluid combined model is shown to capture the effects of top tension, flow velocity, and fluid pressure through application to four different cases: (a) the riser under a common operational condition, in which the upper end undergoes axial stretching prescribed by Eq. (3.66) combined with sinusoidal lateral motion prescribed by Eq. (3.67); (b) the riser subject to the lateral motion prescribed by Eq. (3.67) but the axial stretching is neglected; (c) the riser without axial stretching and the upper end valve closed, such that there is fluid pressure within the riser but zero flow velocity, and (d) the riser without axial stretching and the lower end valve closed, such that the flow velocity is zero and the upper end fluid pressure is atmospheric.

$$U_z(t) = \begin{cases} 0.3t & \text{if } 0 < t < 1s, \\ 0.3 & \text{if } t \geq 1s. \end{cases} \tag{3.66}$$

$$U_y(t) = \begin{cases} 0 & \text{if } 0 < t < 1s, \\ 5\sin[0.2\pi(t-1)] & \text{if } t \geq 1s. \end{cases} \tag{3.67}$$

Fig. 3.11 shows the riser deformations for each of the four cases at various time-steps. Comparing the results from Cases (a) and (b) shows that the riser is significantly stiffer when subject to large axial tension. The results from Cases (b) and (c) are nearly identical, implying that the flow velocity in this example (μ_v=1.072) has negligible effect on riser deformations. Comparing the results from Cases (c) and (d) shows that internal fluid pressure significantly affects the riser dynamics in the absence of large axial tension: the riser is more flexible and experiences sharper bending deformations when it is subject to higher internal pressure. Fig. 3.12 shows the maxima of the computed bending moments along the length observed at any time throughout the periodic lateral motion of the upper end. The largest bending moments are formed at each of the two fixed-ends. Increased axial tension is shown to reduce bending while increased fluid pressure increases bending, which conforms to conventional understanding of riser behavior.

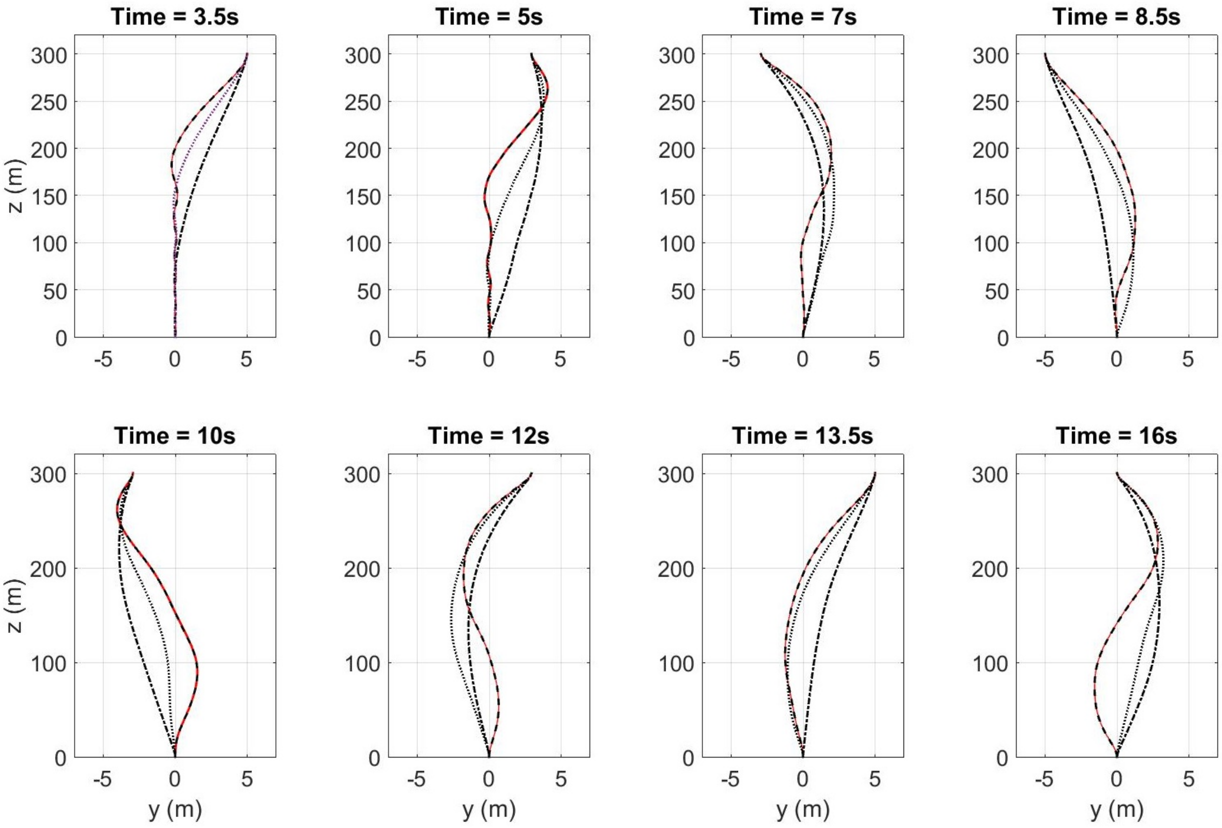

Figure 3.11: Riser deformations at various time-steps.
(Case (a): dash-dot line; Case (b) red solid line; Case (c): dashed line; Case (d): dotted line.)

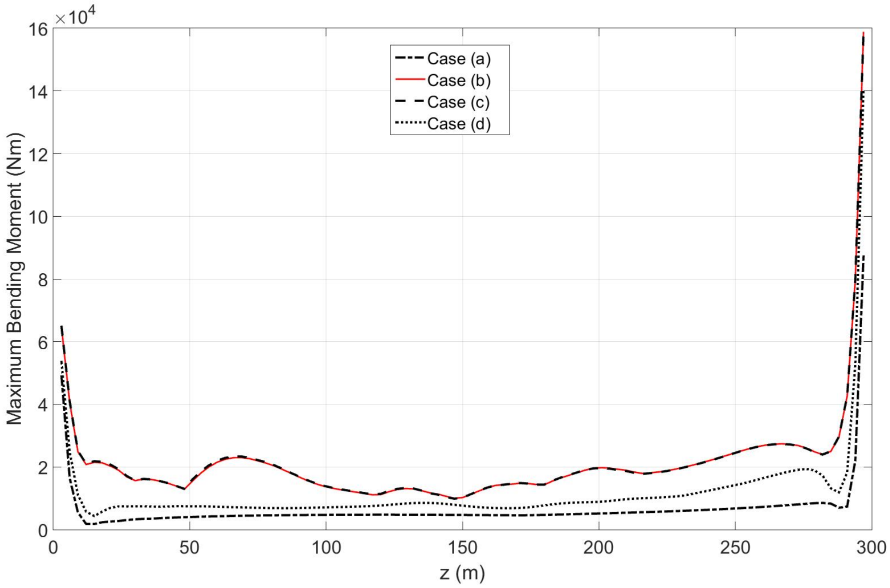

Figure 3.12: Maximum bending moments along the riser.

3.6 Conclusions

A geometrically-exact theory has been developed for pipes conveying fluid using a momentum-based approach. Pipe dynamics is computed similarly to the geometrically-exact momentum-based beam theory. The dynamic equations of motion of the pipe are derived including the momentum of both the pipe and the fluid moving within it. The flow model allows for viscous fluid effects, but the fluid is assumed to be incompressible and homogeneous. The proposed theory rigorously addresses geometric and kinematic nonlinearities of the pipe, and the dynamic coupling between the fluid and pipe is implicitly considered through the combined momentum. Fully nonlinear governing equations are formulated in floating non-inertial frames. A linearized updated Lagrangian formulation is derived to solve these equations of motion in the time-domain, which allows large-displacement nonlinear dynamics to be reduced to a series of piecewise-linear models and enables conventional discretized methods, such as finite volume and finite element, to be directly applied. The resulting methodology has been shown to be effective for large deformations and non-inertial frames. The resulting time-stepping scheme is implemented using the finite volume method and is used to simulate several recognized academic examples, plus a more practical simulation of a top-tensioned marine riser. Internal flow in the moving pipes has been shown to significantly affect the dynamic behavior of the pipe-fluid system. The pipe-fluid combined model has also been shown to quantify the dynamic effects of axial tension and internal fluid pressure for a typical marine riser. The newly developed theory is the first theory that enables the dynamics of a combined pipe-fluid system directly formulated in non-inertial frames and includes a geometrically-exact representation of the pipe.

4. NONLINEAR COUPLED DYNAMICS OF FLOATING OFFSHORE WIND TURBINES

4.1 Introduction

The latest developments in nonlinear beam theory and multibody dynamics are combined in this chapter to enable fully-coupled dynamic analyses for FOWT systems. The value of combining momentum-based beam theory (MBBT) and momentum cloud method (MCM) is demonstrated through a numerical investigation of the coupling effects between blade vibration and platform motions. The OC3-Hywind spar with 5-MW reference turbine (NREL [144, 148]) is modeled as a system consisting of three rigid bodies (spar/tower, nacelle, and hub) and three flexible blades. Two different floater designs, the original OC3-Hywind spar and a truncated highly-compliant spar, are each simulated for realistic environmental conditions. The floating platform and turbine blades have substantially different mass and stiffness, which combined with the spin of the rotor results in a multi-scale problem: blade vibration, turbine spin, and platform motions each have distinctively different frequency ranges. A multi-time-scale coupling scheme between rigid and flexible bodies is developed as part of this work. The MCM is used to solve the three-rigid-body system with a relatively large time-step, and MBBT is applied between these larger steps to compute the vibration and reactions of the flexible blades with a smaller time-step size. Response time-histories are computed for six different cases. The resulting time-histories of blade response are investigated using singular value decomposition (SVD) and computing power spectral densities of proper orthogonal modes. SVD has been shown to be effective on nonlinear beam vibration [149, 150] and superior to eigenmodes or Lanczos modes for wind turbine blades [151]. Nonlinearities associated with FOWT systems and the blades are discussed in Sections 4.2 and 4.3. The numerical framework of the proposed method is presented in Section 4.4. Structural configurations, simulation conditions, and validation tests are presented in Section 4.5. Results are analyzed and discussed in Section 4.6, including key findings on dynamic coupling between blades and platform motions, dynamic coupling effects on fatigue loading, and observation on the highly-compliant FOWT concept.

4.2 Nonlinear FOWT Systems

FOWT systems are highly nonlinear, and the associated nonlinearities are closely coupled. Time-domain simulation is required to accurately model these complicated dynamic effects. Fig. 4.1 shows the nonlinearities associated with FOWT systems. Irregular winds are generated using linear (Gaussian process) turbulence models. Nonlinear aerodynamic loads are computed for the instantaneous wind velocity and angle of attack relative to each of the moving blade elements. These loads are computed using the blade element momentum method, such that aeroelastic effects are included. Nonlinear turbine control actively adjusts the pitch angle of the blades, which directly impacts the wind forces on the turbine. Nonlinear hydrostatic effects are included by computing the buoyancy force and the location of the center of buoyancy using the instantaneous position of the platform, including the changes of the water plane and to the submerged portion due to platform motion. Nonlinear hydrodynamics are included by computing the hydrodynamic forces using Morison's equation and the instantaneous fluid velocity and acceleration relative to each of the moving spar segments. The fluid motions induced by irregular waves are computed using linear wave theory and are considered in the computation of hydrodynamics. Nonlinear restoring forces and moments provided by the mooring lines are computed using the instantaneous relative positions between the platform and the anchor points, but the mooring line themselves are modeled as linear springs. A quasi-static model is used for each mooring line, in which the inertial and dynamic effects and sag of the mooring line are neglected. Nonlinear multibody dynamics are included using the MCM, in which the Euler angle formulation is used to represent the instantaneous configuration and exact kinematics of the multibody system. Gyroscopic effects of the whirling blades are captured implicitly through the dynamic coupling between the flexible blades and the multibody system, with the gyroscopic moments resulting from summing the inertial effects of the elements of each blade in a moving reference frame. Nonlinear blade dynamics and the dynamic coupling scheme between the blades and the multibody system are presented in Sections 4.3 and 4.4, respectively.

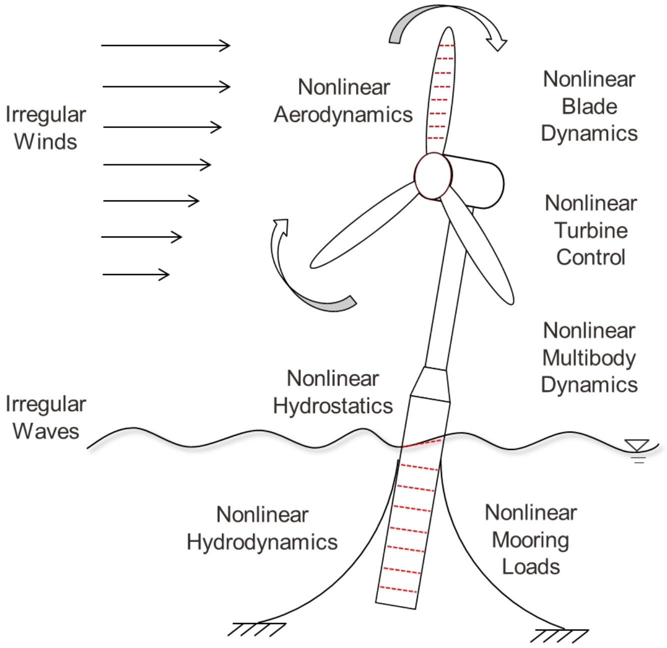

Figure 4.1: Nonlinearities associated with FOWT systems.

4.3 Nonlinear Blade Dynamics

Kinematic and geometric nonlinearities are highly critical to accurate modeling of FOWT blade dynamics, while constitutive, damping, and differential inertial nonlinearities can reasonably be neglected for the blades. Kinematic nonlinearities primarily result from the blades being subject to overall turbine rotations and platform motions, which introduces significant nonlinear inertial loads through kinematic nonlinearities, such as centrifugal and Coriolis forces. Geometric nonlinearities primarily result from the blades being subject to geometric stiffening effects due to the large axial tensions induced by centrifugal forces; nonlinear strain measures are shown to be necessary to address the axial foreshortening effect for capturing the geometric stiffening of spinning blades. Table 4.1 shows how different beam models address kinematic and geometric nonlinearities for the blades. The inertial loads associated with the overall rigid-body motion of a blade are computed for the linearly-deformed configuration in the linearized MBBT, such that kinematic nonlinearities are partially included. However, the linearized strain measures are computed in the linearized MBBT including only the initial twist and curvature associated the undeformed beam, such that

Table 4.1: Blade models.

	Linearized MBBT	Piecewise-linear MBBT		Nonlinear MBBT
		Incremantal deformation	Evolving base configuration	
Displacements	Linear solutions	Linear solutions	Nonlinearly updated	Nonlinear solutions
Velocities	Linear solutions	Linear solutions	Nonlinearly updated	Nonlinear solutions
Inertial effects assoc. with overall rigid-body motion	Computed based on linear deformation	Computed based on evolving deformation		Computed based on nonlinear deformation
Inertial effects assoc. with beam deformation	Linearized	Computed based on evolving deformation		Computed based on nonlinear deformation
Strain measures	Linearized	Linearized	Nonlinear	Nonlinear

the nonlinear geometric stiffening effects are neglected. Both inertial loads and strain measures are computed including nonlinear effects for the evolving base configuration in the piecewise-linear MBBT formulation. The evolving base configuration is updated between time-steps in a nonlinear geometrically-exact manner, including kinematic and geometric nonlinearities associated with the evolving configuration. The result is that the piecewise-linear MBBT solver is able to accurately capture the nonlinear blade dynamics if the time-step size used is sufficiently small for piecewise linearization, and it is used in the following coupled FOWT simulations.

4.4 Dynamic Coupling

4.4.1 Rigid-flexible-body Coupling

A spar-type FOWT is modeled as a multibody system that consists of three flexible blades plus three rigid bodies: the floating spar and tower, nacelle, and hub. The three-rigid-body system is solved using an existing in-house code based on the MCM, and blade dynamics are solved using the new beam solver based on the piecewise-linear model implementation of MBBT.

System motions of the three-rigid-body system are computed using external loads resulting from gravity, hydrostatic and hydrodynamic loads on the floater, loads from mooring lines, and loads from the blades acting on the rotating hub. Blade dynamics are computed using the external loads acting on the blades ($\boldsymbol{F}_f^{ext}$ and $\boldsymbol{M}_f^{ext,G}$) and floating frame motions ($\boldsymbol{A}_f^W$, $\boldsymbol{\Omega}_f$, and $\dot{\boldsymbol{\Omega}}_f$). The external loads acting on the blades are gravity and aerodynamic loads. The floating frame motions represent the blade overall rigid-body motions resulting from the moving platform and rotating hub. Inertial effects caused by the floating frame motions, such as centrifugal and Coriolis forces, are not considered as external loads because they are included as inertial terms in MBBT.

Each blade is modeled as a cantilever beam having a fixed-end boundary at its root, which is attached to the moving hub. Blade deflections due to external loads and the floating frame motions are computed using the MBBT solver. The resulting deflections are used to compute the resultant forces and moments at the roots of the blades, which are returned to the MCM code as external loads on the hub. The motion of the base body (spar/tower) is computed using the MCM code, and combined with the relative motions along the kinematic chain to compute the translational acceleration ($\boldsymbol{A}_f^W$) and the rotational velocity and acceleration ($\boldsymbol{\Omega}_f$, $\dot{\boldsymbol{\Omega}}_f$) of the overall rigid-body motion for each blade. These motions combined with gravity and aerodynamic loading are used in the MBBT solution for blade vibration and response. All inertial effects are coupled explicitly by the inertial terms in MBBT, and the root forces and moments acting on the multibody system inherently include gyroscopic effects of the whirling blades.

4.4.2 Computational Method

The framework of the fully-coupled FOWT analysis is shown as Fig. 4.2. Aerodynamic loads on each blade element are computed using AeroDyn v13, which is based on blade element momentum theory and developed by NREL [152]. Wave loads on the spar are computed using Morison's equation considering the instantaneous position and motion of the spar. Hydrostatic restoring forces and moments are computed using the buoyancy of the spar based on its instantaneous position. Mooring forces are computed by representing each taut-leg mooring lines as a massless linear spring along the axis of the line. Large angular displacements of the floater are rigorously considered in the hydrodynamic, hydrostatic, mooring, and multibody modules. The DISCON control routine developed for the OC3-Hywind 5-MW turbine by NREL activates shaft torque control or blade pitch control depending on wind loading. Power output and instantaneous hub spin are computed using a single differential equation to represent the turbine drivetrain.

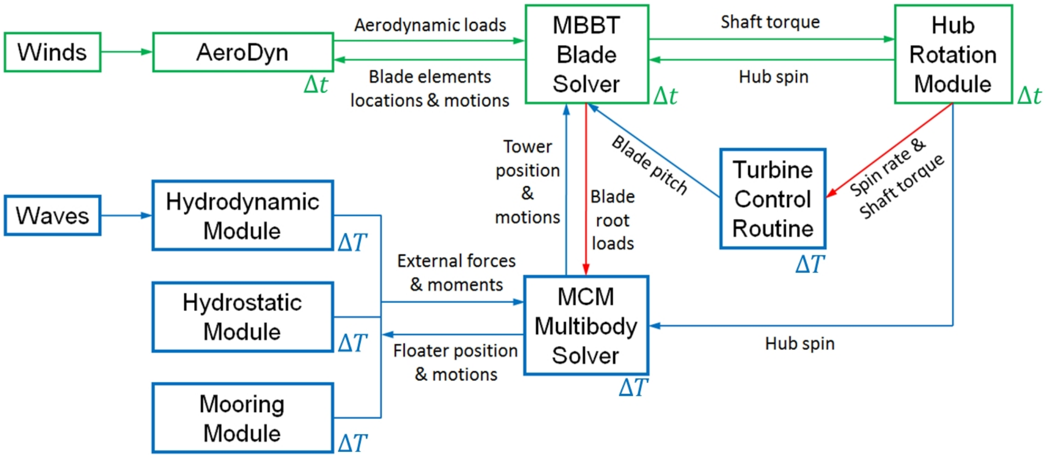

Figure 4.2: Coupling framework.

The proposed coupling framework is implemented as a multi-scale and weakly-coupled model. Two different time-step sizes are applied because the blade vibration has much higher natural frequencies than the global platform motions. Aerodynamics and dynamics of the blades and hub rotations are computed using a smaller time-step size (Δt) than that used in the multibody system and its related modules including turbine control routine (ΔT). The forces and moments acting at the blade roots are computed at multiple small time-steps and are averaged over each large time-step to apply at the averaged root positions in the multibody system. The dynamic model is described as weakly coupled as no iteration is performed between the MBBT and MCM solvers.

4.5 Simulations

4.5.1 Structure Configurations

All simulation examples use numerical models based on the NREL 5-MW OC3-Hywind floating wind turbine design [144, 148]. The 5-MW OC3-Hywind model is a spar-type conceptual FOWT design that is commonly used as a reference example in academic studies. The cut-in, rated, and cut-out wind speeds of the 5-MW wind turbine are 3 m/s, 11.4 m/s, and 25 m/s, respectively, and the rated rotor speed is 12.1 revolutions per minute (RPM). The OC3-Hywind model was originally designed with a 120 m draft and three catenary mooring lines. A family of six

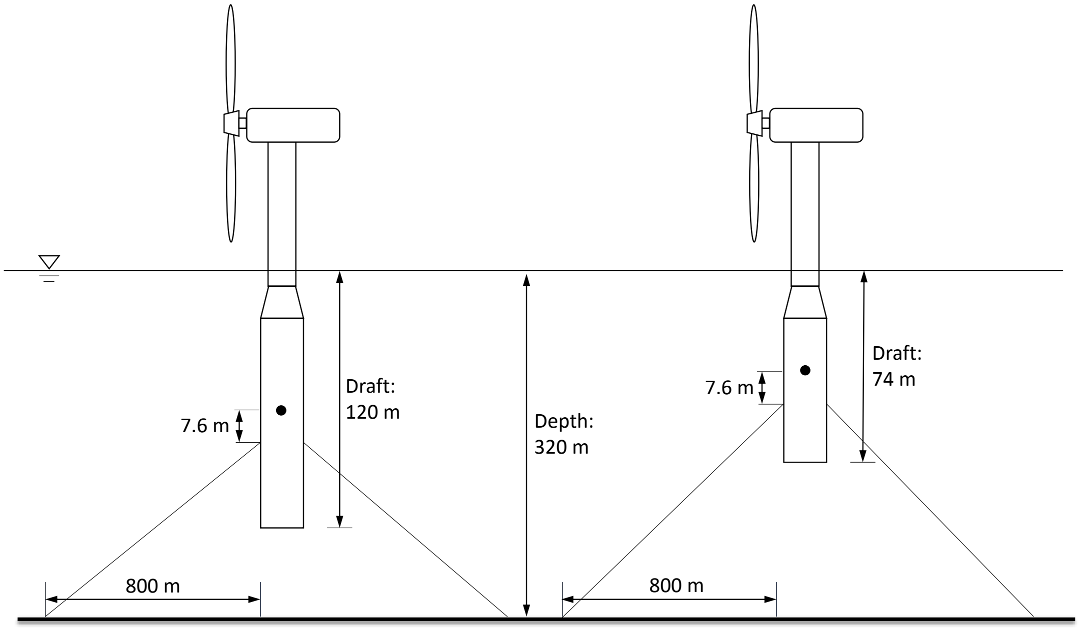

Figure 4.3: 120-m spar design and 74-m truncated spar design.

new spar platform designs have been developed based on the OC3-Hywind model by Gao and Sweetman [4] with drafts ranging from 62 m to 97 m. These truncated spar designs conform to the industry standard structural guide, API Bulletin 2U, and have significantly lower stiffnesses in pitch and roll, making them highly-compliant relative to the original design. Truncated designs offer reduced manufacture and installation costs at the expense of reduced power output. A spar draft of about 74 m was found to optimize the trade-off between cost and electricity harvest [4]. Dynamic coupling effects are investigated through comparison between the dynamic responses of the original stiff 120-m spar design and a compliant 74-m truncated design (Fig. 4.3).

The mooring system is modified from the original three catenary line system to a four taut-leg mooring system. The mooring lines are anchored 804.7 m away from the spar centerline (spar diameter of 9.4 m) and 320 m below the still water level. They are attached to the spar 7.6 m below the center of mass of the spar/tower (Fig. 4.3). The taut-leg mooring lines are assumed to have axial stiffness of 384,243,000 N per unit strain. Additional yaw stiffness of 98,340,000 Nm/rad and additional yaw damping of 13,000,000 Nm/(rad/s) are numerically applied to both spar models, as were applied in the original OC3-Hywind numerical modeling at NREL [148].

4.5.2 Environmental Conditions

Two load cases are simulated in this study. The first load case represents a typical operational condition, which is equivalent to an industry-standard Design Load Case, DLC 1.2 in IEC 61400-3 [153]. An irregular wind field is numerically simulated using the TurbSim code from NREL [154] using the normal turbulence model (NTM). The mean wind speed is 11.4 m/s at the 90 m hub height, which is the rated wind speed of the 5-MW turbine. The model is also subject to irregular waves, which are generated with significant wave height of 1.8 m, peak period of 6.1 s, and conforming to the JONSWAP spectrum assuming a fully-developed sea. The second load case represents an extreme operational condition, equivalent to DLC 1.6a in IEC 61400-3. The irregular winds have a mean wind speed of 25 m/s, which is the cut-off wind speed of the turbine. An extreme irregular wave process representing the 50-year extreme in the western region of the Gulf of Mexico is selected: the significant wave height is 11.3 m with peak period 14.4 s as per the industry standard, API-2INT-MET. The directions of waves and winds are assumed to be co-directional in both load cases.

4.5.3 Validation Test

The new dynamic method that couples MBBT and the MCM is verified through benchmarking against the widely recognized FAST package for the 120-m OC3-Hywind FOWT with the modified mooring system. A time-domain simulation is performed using FAST (version 8) and the fully-coupled MBBT-MCM model. The validation test is to model the FOWT starting with zero initial displacements and the rotor spinning at a constant 12.1 RPM. A constant force of 1000 kN is applied to the tower in the positive surge direction at the still water level, in absence of waves or winds (Fig. 4.4). Each blade in the MBBT model is discretized into 23 elements; each blade in FAST BeamDyn is represented by single fifth-order Legendre spectral finite element. A convergence test was performed to verify each of the two time-step sizes used in flexible blade dynamics and multibody system dynamics. Results computed using 0.02 s for the MCM code and 0.005 s

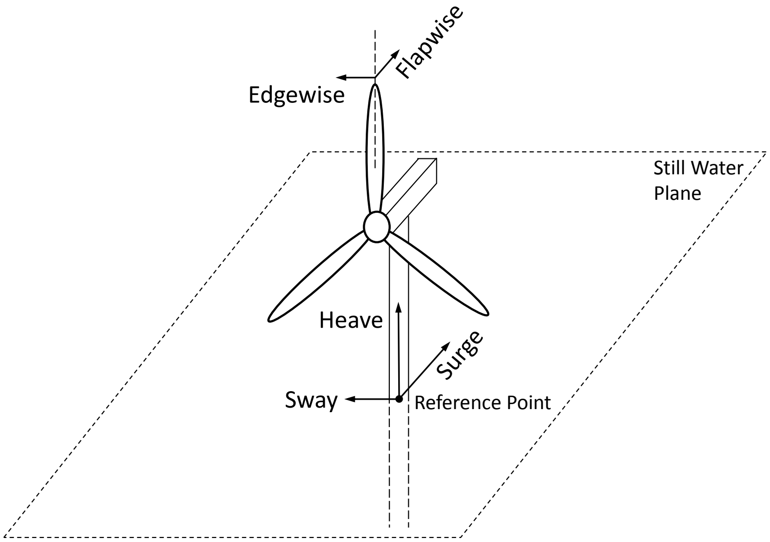

Figure 4.4: Directions of motions.

for the MBBT solver are nearly identical to those computed using 0.003 s for both solvers. The time-step sizes are set to be 0.02 s and 0.005 s for all remaining examples.

Figs. 4.5 and 4.6 show the platform and blade responses computed by FAST and the new MBBT-MCM coupled model. The test results show good agreement, despite the two methods being based on different numerical models for the blade, mooring, hydrostatics, and hydrodynamics.

4.5.4 Simulation Cases

The MBBT-MCM couple model combined with the aerodynamic solver (AeroDyn) and control routine (DISCON) from the FAST package are used to simulate six different cases (Table 4.2). The FOWT's with the 120-m spar and the 74-m spar are each simulated subject to the typical and extreme operational conditions specified in Section 4.5.2. Two fixed cases are also included, in which the spar/tower is held fixed throughout the simulation. The position at which each case is fixed is selected as the mean angular position computed from a fully-dynamic simulation. The "120-m fixed" case has platform roll, pitch, and yaw angles are each fixed to the steady-state mean value computed from the 120-m floating spar subject to the typical operational condition. The "74-m fixed" case has a platform roll, pitch, and yaw angles fixed to the steady-state mean values as the 74-m floating spar simulated subject to the typical operational condition. All simulation cases are

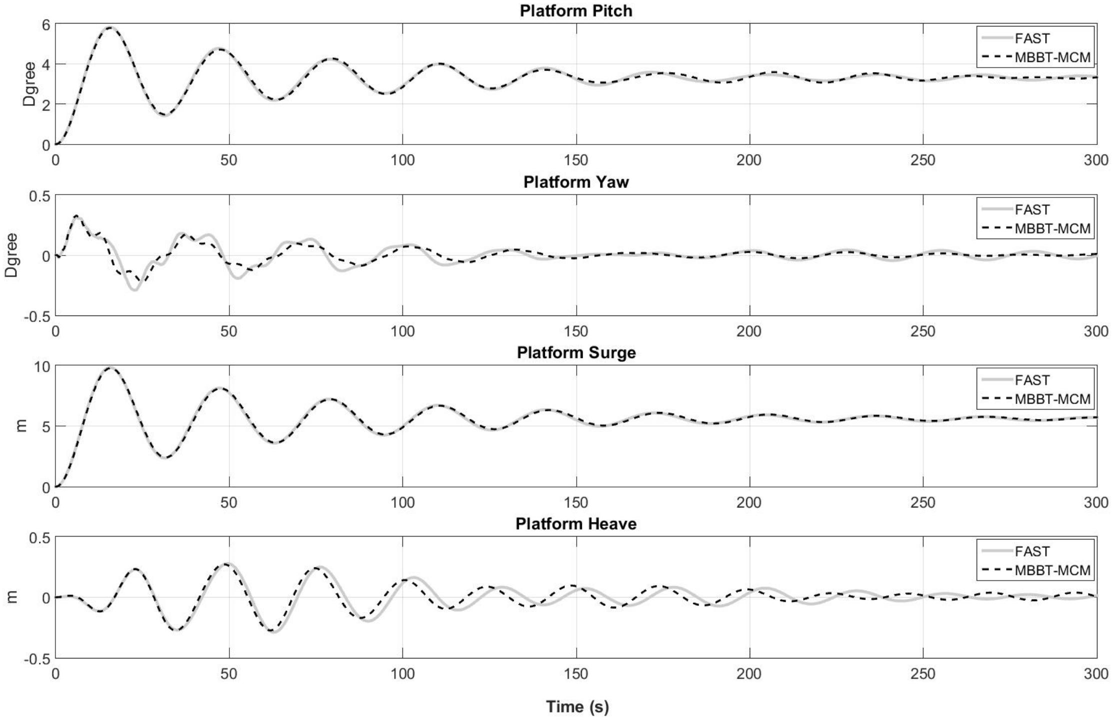

Figure 4.5: Platform motions in validation tests.

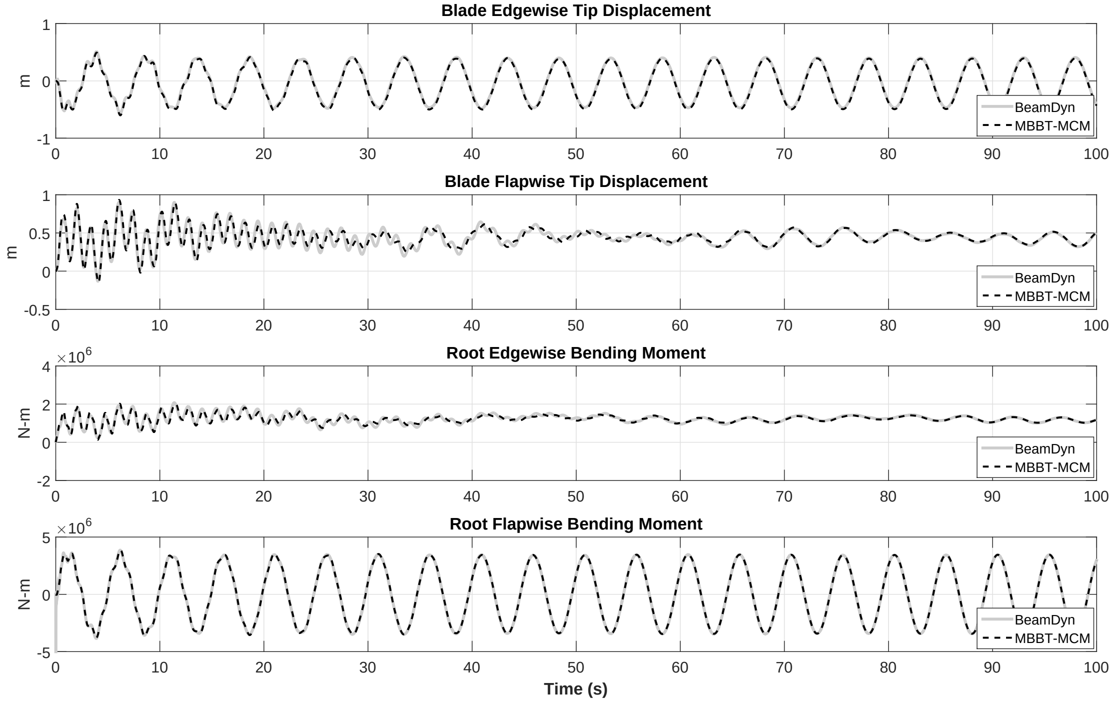

Figure 4.6: Blade responses and reactions in validation tests.

Table 4.2: Simulation cases.

Case	120-m Typical	120-m Extreme	120-m Fixed	74-m Typical	74-m Extreme	74-m Fixed
Structure	120-m Floating Spar	120-m Floating Spar	Fixed Tower	74-m Floating Spar	74-m Floating Spar	Fixed Tower
Wind	11.4 m/s @90 m, NTM	25 m/s @90 m, NTM	11.4 m/s @90 m, NTM	11.4 m/s @90 m, NTM	25m/s @90 m, NTM	11.4 m/s @90 m, NTM
Wave	T_p=6.1 s, H_s=1.8 m	T_p=14.4 s, H_s=11.3 m	–	T_p=6.1 s, H_s=1.8 m	T_p=14.4 s, H_s=11.3 m	–

computed in the time-domain for 800 s, including the startup transition; the platform and blades have zero initial displacement and zero initial turbine rotation speed.

4.6 Results and Discussion

4.6.1 Highly-compliant FOWT

The feasibility of the highly-compliant FOWT design with the 74-m spar is demonstrated through the simulation cases including the floating spar subject to both the typical and extreme operational conditions. The compliant FOWT does not experience substantial oscillatory motions when subject to the typical operational condition and survives in the extreme operational condition.

Fig. 4.7 shows the turbine start-up and steady-state operation when subject to the typical condition. Blade pitch remains zero because aerodynamic torque is below the activation threshold of blade pitch control. Fig. 4.8 shows the platform motions, including a large steady-state mean pitch angle of $16.2°$. The compliant platform barely oscillates under the typical wind and wave excitations.

Acceptable dynamic system performance of the highly-compliant design is verified in the extreme operational condition. Fig. 4.9 shows benign behaviors for both FOWT designs in the steady-state. The power output is regulated by the control system to between 5 to 5.5 MW by increasing blade pitch angle to around $23°$. The 74-m spar experiences larger platform pitch angles and greater surge oscillation than the 120-m spar. The wind turbine on the compliant platform operates normally despite the platform motions. The mean platform pitch angle in the extreme condition for the compliant design is smaller than that in the typical condition, because the increased blade pitch significantly reduces the wind thrust force per megawatt generated.

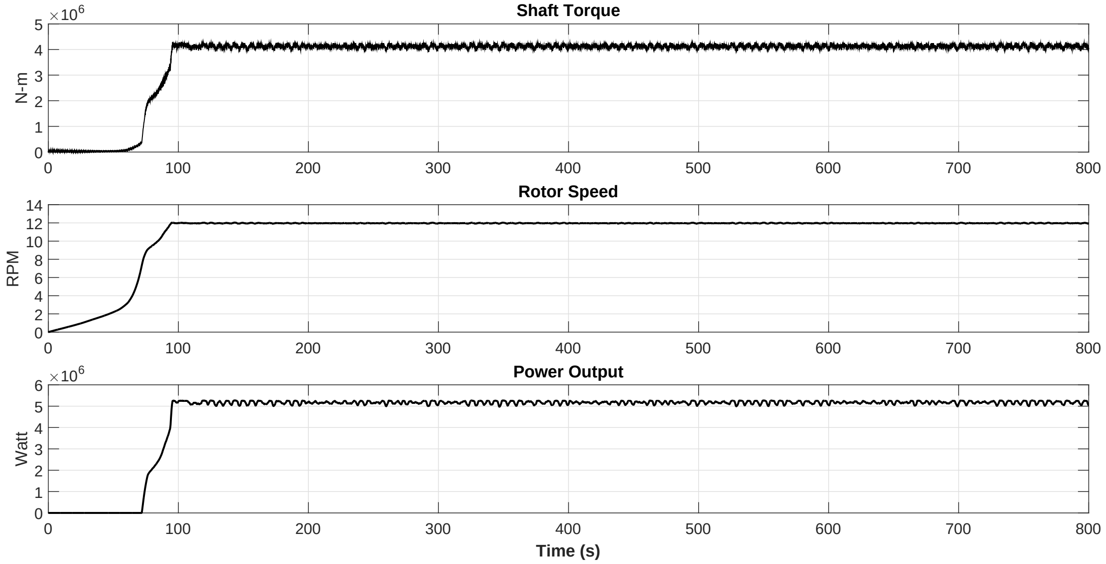

Figure 4.7: Turbine performance of 74-m spar in the typical operational condition.

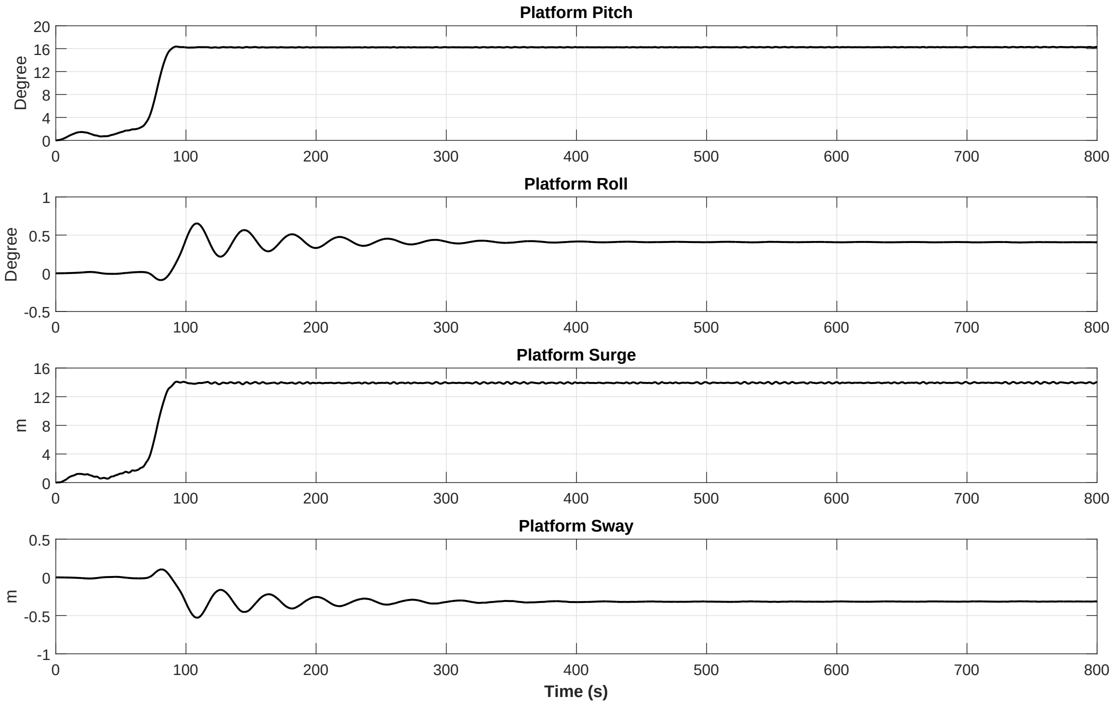

Figure 4.8: Platform motions of 74-m spar in the typical operational condition.

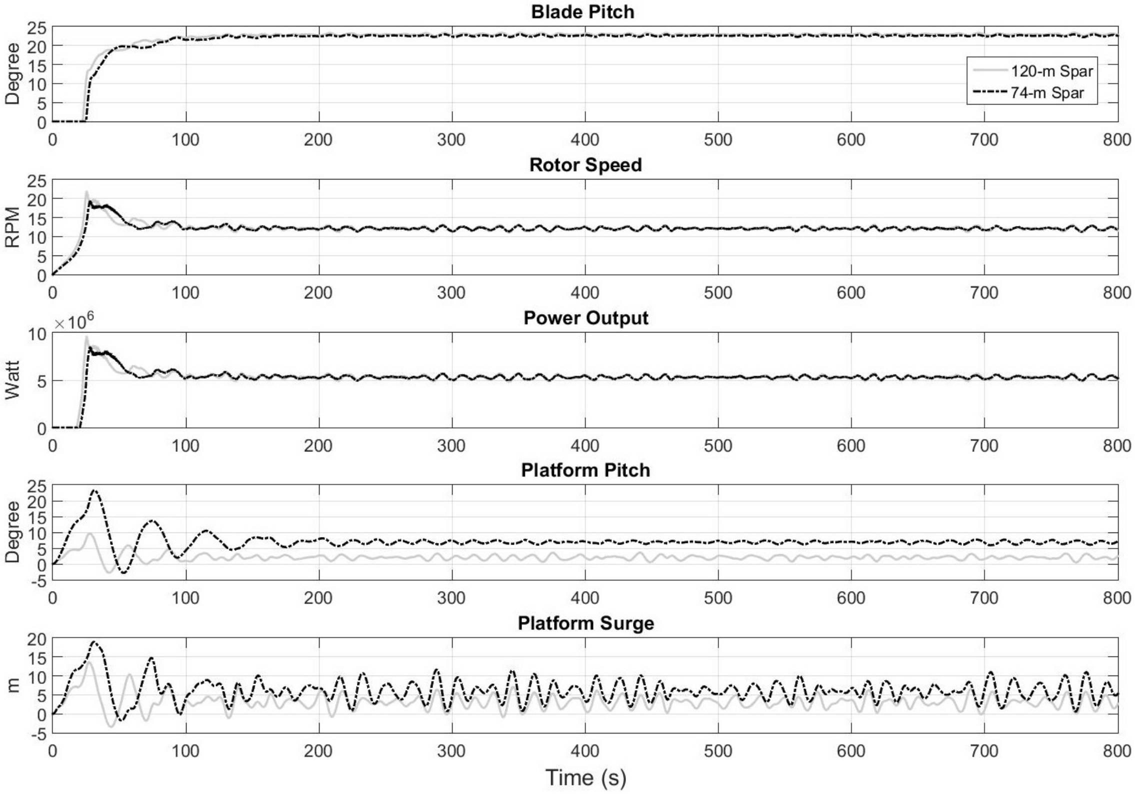

Figure 4.9: 120-m spar and 74-m spar in the extreme operational condition.

4.6.2 Control-induced Platform Oscillations

Blade pitch control is shown to cause substantial platform oscillations in the simulation case of the 120-m floating spar subject to the typical operational condition. Fig. 4.10 shows the dynamic coupling between active blade pitch control and platform motions. The FOWT experiences strong oscillatory platform motions when blade pitch control is active, but only minimal oscillations if the blades remain at a fixed angle relative to the hub. Constant blade pitch angle results in a nearly-constant aerodynamic drag coefficient. Therefore, wind thrust increases as the platform pitches upwind because the relative wind speed on the rotor increases, and the wind thrust decreases as the platform pitches downwind, resulting in a strong damping effect. The active control algorithm increases the blade pitch angle at times of high wind to protect gearbox and generator, which also effectively changes the drag coefficient and wind thrust of the rotor. Fig. 4.11 shows the mechanism of the dynamic coupling. The blade pitch angle increases with the apparent wind associated with the tower pitching into the wind; as the tower pitches downwind the blade pitch is decreased to maximize generator output in the reduced apparent wind. This behavior results in an oscillatory wind thrust force coupled with tower pitch motion, and leads to a control-induced resonance. This dynamic coupling phenomenon has been observed and studied, e.g. [155, 156]. The control routine for a FOWT system should be designed and tested including its effects on overall platform dynamics, and blade pitch control can be used to control floating platform motions [157, 158].

4.6.3 Imbalanced Aerodynamic Loads

Significant dynamic responses observed in the simulation case of the 74-m floating spar in the typical condition are found to be caused by imbalanced aerodynamic loads. Fig. 4.12 shows the power spectral densities (PSD's) of platform pitch, roll, and yaw motions in steady-state (200 to 800 s). Wave loading excites platform pitch oscillation, and pitch and yaw motions are coupled by gyroscopic effects. The peak of the wave spectrum can be seen in the PSD's of pitch and yaw at about 0.16 Hz (1/6.1 s). The highest peak in the PSD of platform roll is at about 0.03 Hz, which is roll natural frequency. Multiple peaks in these PSD's are also observed at 0.6, 1.2, and 1.8 Hz,

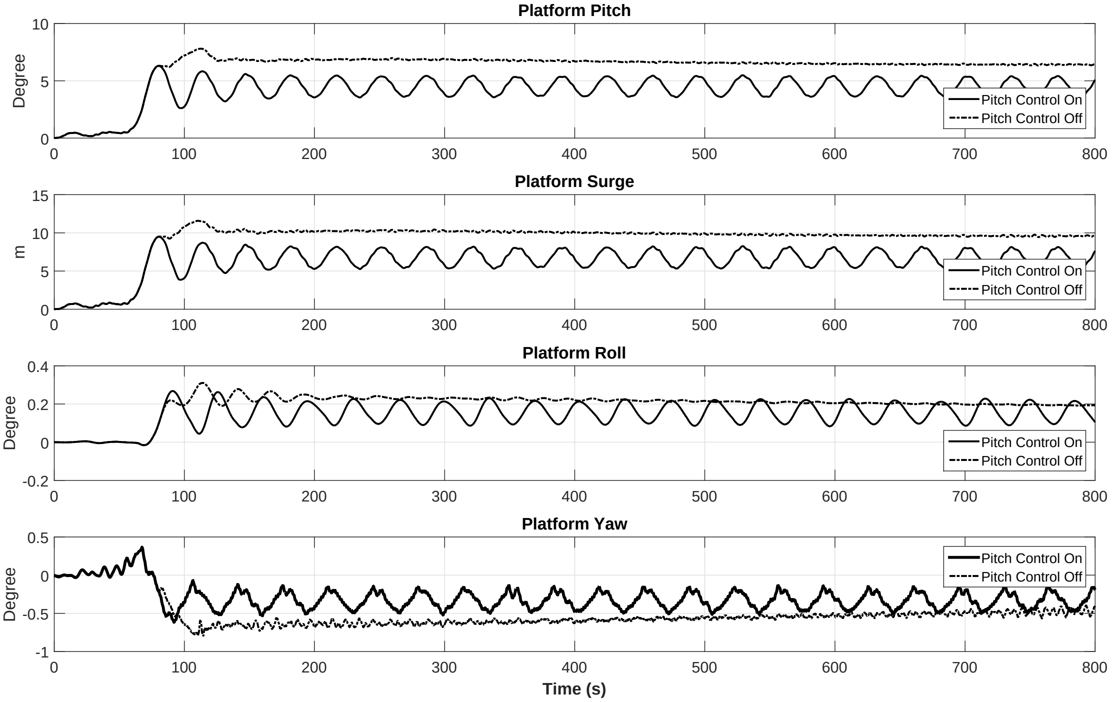

Figure 4.10: Platform motions of 120-m spar in the typical operational condition.

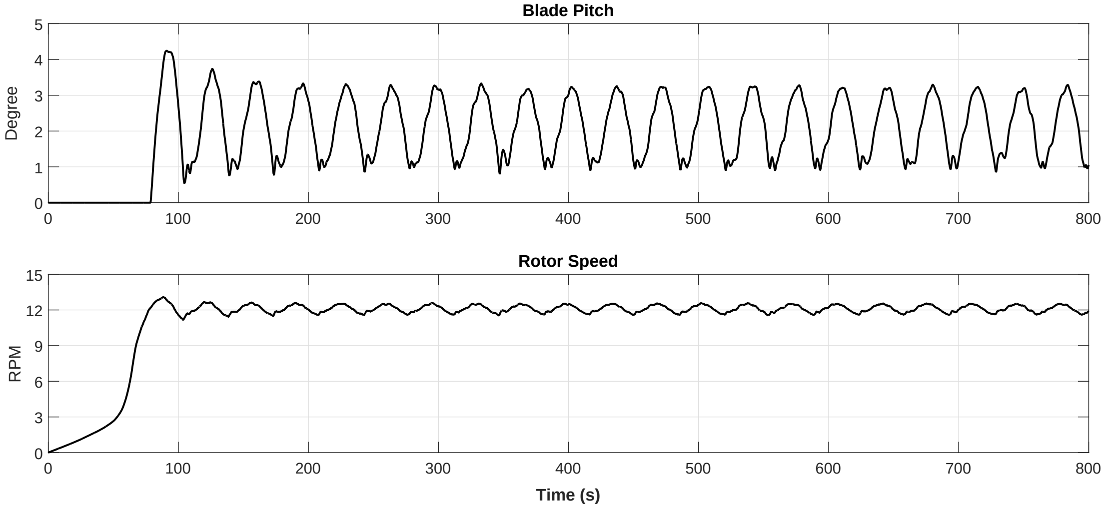

Figure 4.11: Turbine performance of 120-m spar in the typical operational condition.

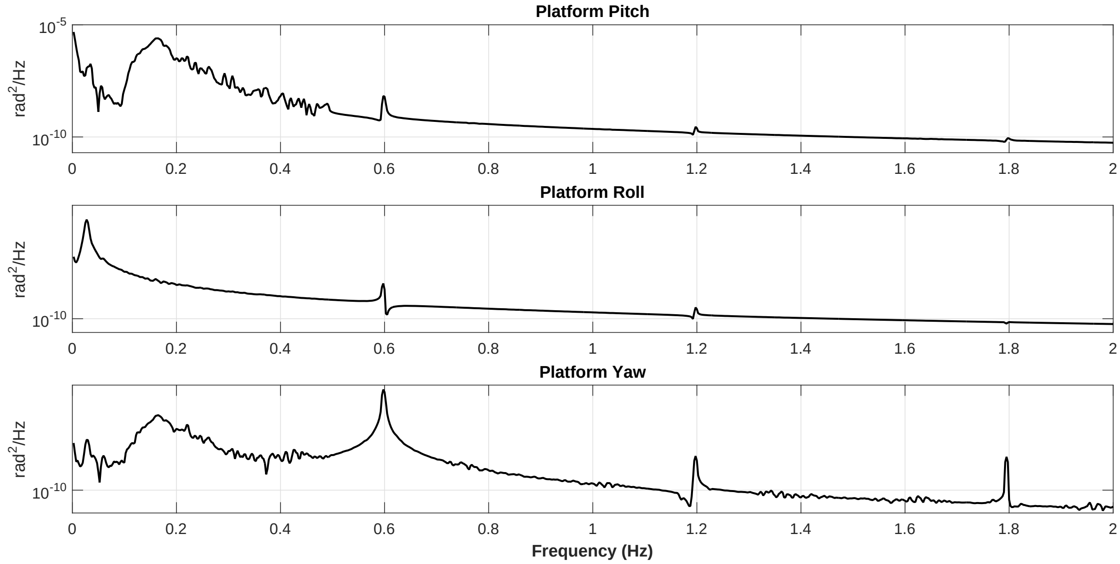

Figure 4.12: PSD's of 74-m spar in the typical operational condition.

especially for yaw motion. These responses are found to be caused by the imbalance of turbine aerodynamic loads acting on the top of tower, which are associated with blade rotation at 12 RPM (3×12/60 s = 0.6 Hz).

The imbalanced aerodynamic loads are found to be induced by the axial-asymmetric deflections of blades. Individual blade deflects differently at various position in single revolution, such that the three-blade turbine cannot be considered as an axial-symmetric body. Two special cases are simulated to demonstrate the cause of the imbalanced aerodynamic loads. The 5-MW wind turbine is simulated without precone or shaft tilt on a upright fixed tower in a 13 m/s uniform wind field, such that the turbine rotates on a vertical plane. Gravity is considered in the first case while is neglected in the second one. Fig. 4.13 shows the time-history of the aerodynamic yaw moment at steady-state, in which non-zero mean and periodic variation are observed in the first case. The blades deflecting differently subject to gravity about the spinning axis creates axial asymmetry in the uniform wind field, which generates axial-asymmetrical aerodynamic loading. The resulting aerodynamic effects of the loading asymmetry is most prominent in the yaw direction because yaw moments would be zero for an axial-symmetric turbine rotating in an uniform wind field,

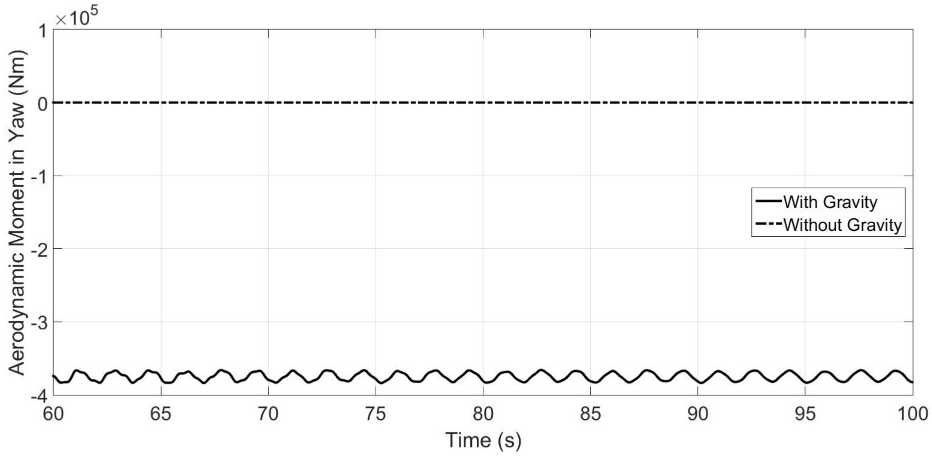

Figure 4.13: Comparison of resultant aerodynamic yaw moment.

and because yaw stiffness and damping are very low for a spar floater. The axial-asymmetric deflections of blades also affect aerodynamic forces and moments in all other directions. Similar axial-asymmetric blade deflections and imbalanced aerodynamic loads could also result from wind shear profile or a tilted rotor plane.

4.6.4 Coupled Dynamics

The couped dynamics of FOWT systems are investigated using power spectral analysis of singular value decomposition (SVD) results. SVD is a common method to orthogonally decompose discretized data, which can be used to numerically extract proper orthogonal modes (POM's) from vibratory displacements. The resulting POM's are orthogonal mode shapes that are mathematically optimized representations of a data set. The displacements of N DOF's of a structure are expressed as column vectors $\boldsymbol{x}(t)$ making up a $N \times M$ matrix that includes time-histories of M time-steps:

$$\boldsymbol{X} = \begin{bmatrix} \boldsymbol{x}(t_1) & \dots & \boldsymbol{x}(t_M) \end{bmatrix} = \begin{bmatrix} x_1(t_1) & \dots & x_1(t_M) \\ \vdots & \ddots & \vdots \\ x_N(t_1) & \dots & x_N(t_M) \end{bmatrix} \tag{4.1}$$

The SVD of matrix $\boldsymbol{X}$ can be computed as:

$$\boldsymbol{X} = \boldsymbol{U}\boldsymbol{S}\boldsymbol{V}^T \tag{4.2}$$

in which $\boldsymbol{U}$ is a $N \times N$ orthonormal matrix of eigenvectors of $\boldsymbol{X}\boldsymbol{X}^T$; $\boldsymbol{V}$ is an $M \times M$ orthonormal matrix of eigenvectors of $\boldsymbol{X}^T\boldsymbol{X}$; and $\boldsymbol{S}$ is a $N \times M$ matrix whose main diagonal has non-negative real numbers that are the singular values of matrix $\boldsymbol{X}$. The POM's are given by the column vectors in matrix $\boldsymbol{U}$, and the time-histories of the magnitude of each POM are given by the first N column vectors in matrix $\boldsymbol{V}$. The ratio of the singular value associated with each POM to the sum of all singular values indicates the percentage that the corresponding mode contributes to the total response. POM's differ from conventional eigenmodes in that they are not solely dependent on structure properties but also include load effects, and they are not associated with any particular frequencies. Time-histories of the magnitude of each POM can be extracted from simulation results, and spectral analysis of these POM's can be used to reveal the main frequency features of nonlinear blade vibration.

The 120-m floating case subject to the typical condition and experiencing control-induced oscillations is investigated to assess the dynamic coupling between blade vibration and platform oscillations. SVD is applied to compute the singular values and POM's of a blade for the last 10 minutes of simulation (200 to 800 s). The ratios of singular values of the first three POM's are 92.8$\%$, 6.1$\%$, and 0.6$\%$, respectively, indicating the first two POM's are accounted for nearly 99$\%$ of the blade deflections. Fig. 4.14 shows the PSD's of the first two POM's. Dynamic coupling between blade vibration and overall system is demonstrated as the peaks at the frequency of the wind-pitch resonance (0.03 Hz) are observed in both PSD's. Dynamic coupling between blade vibration and rotor spin is also demonstrated: the second, third, and fourth peaks of the first POM (0.4, 0.2, and 0.6 Hz) and the first peak of the second POM (0.2 Hz) are all associated with turbine rotation. The peak at 1.04 Hz is associated with the first edgewise bending natural frequency of the blade [159].

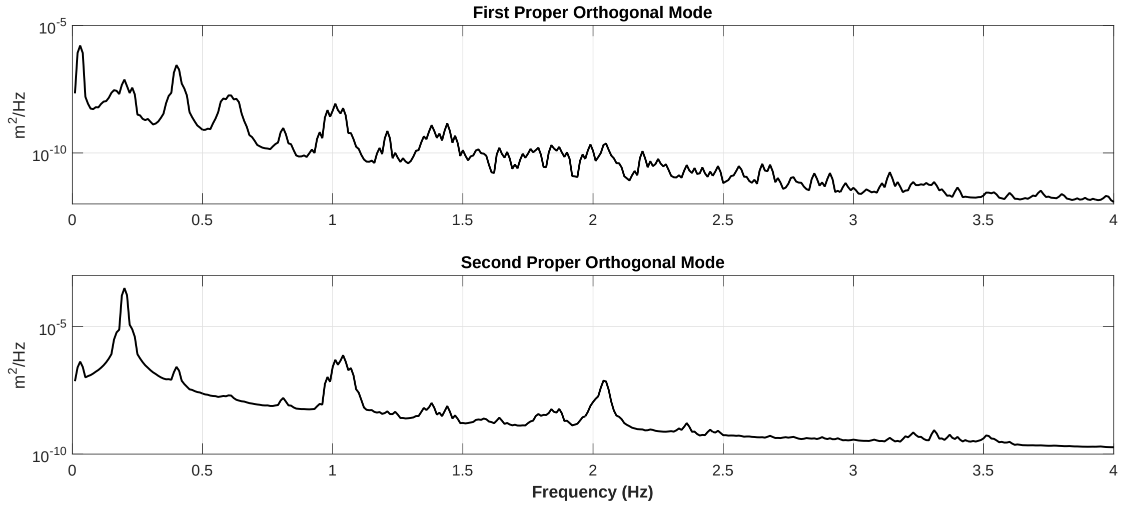

Figure 4.14: PSD's of the blade POM's for 120-m spar in the typical operational condition.

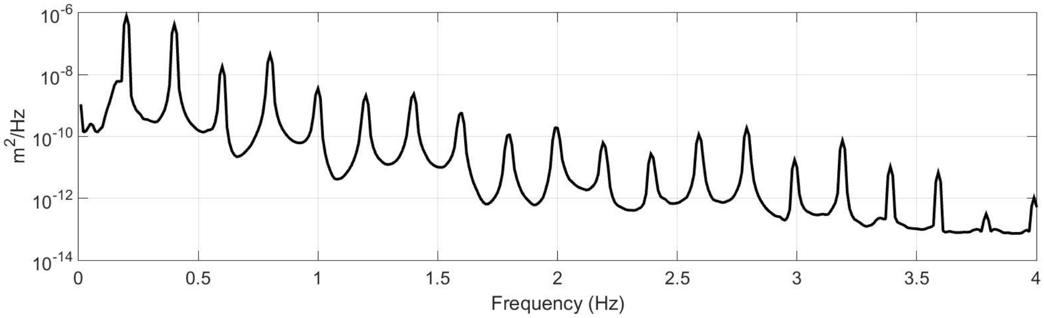

Figure 4.15: PSD of the first blade POM for 74-m spar in the typical operational condition.

The 74-m floating case subject to the typical condition is also investigated. The ratios of singular values of the first three POM's of a blade are 94.5%, 4.8%, and 0.3%, respectively. Fig. 4.15 shows the PSD of the first POM. Blade dynamics are closely coupled with rotor spin when the platform hardly oscillates: frequency peaks of the first POM are spaced evenly with a 0.2 Hz interval.

4.6.5 Fatigue Loading Comparison

The simulation results computed using the MBBT-MCM coupled model for the six cases are found to capture important dynamic behaviors of FOWT systems, and are further used for fatigue analysis. The effects of coupled dynamics on fatigue loading are investigated by comparing the short-term damage-equivalent loads (DEL's). The short-term DEL's of the loads at blade roots and turbine shaft are computed using the MLife code from NREL [160, 161] for 10-minute results (200 to 800 s) of all six simulation cases. Miner's rule, rainflow cycle counting, and Goodman correction with Goodman exponent equal to one are used in MLife for damage computation. DEL is the one-sided amplitude of an oscillatory load that has a set mean value and a set frequency and causes the same fatigue damage as a given load time-history. All the DEL's are computed based on mean value equal to zero and frequency equal to 1 Hz, and applying the Goodman correction for mean stress. The ultimate loads are estimated from maximum loading in the extreme condition simulations and a total safety factor of 1.755 (1.35 loading safety factor combined with 1.3 material safety factor) [159]. The Whöler exponent is set to be 10 for composite blade or 3 for steel shaft, as is common practice.

Table 4.3 shows the short-term DEL's of flapwise-edgewise combined bending moment, combined shear force, and axial force at the root of a blade, and the shaft torque. The estimated ultimate loads are 1.775e7 Nm, 6.475e5 N, 1.481e6 N, and 8.909e6 Nm, respectively. The 120-m fixed case has a tower pitch angle of $4.5°$; the 74-m fixed case has a tower pitch angle of $16.2°$. Fatigue damage at blade root predicted for the fixed cases is compared and tower pitch is found to be adverse to fatigue life, because gravity loading in the flapwise bending has an increased mean. Fatigue damage predicted for the fixed cases and the floating cases is compared for the typical operational condition. Platform oscillations are found to adversely affect fatigue life. The 120-m floating case experiencing the wind-pitch resonance has larger DEL's than its fixed counterpart, while the DEL's for the 74-m floating spar that barely oscillates are similar to those for the fixed case. Fatigue damage predicted for the original 120-m spar and the compliant 74-m spar is found to be similar for the extreme operational condition. These results reflect only the DEL's at the blade root and the shaft for a very limited number of cases. A more detailed fatigue assessment would need to consider fatigue damage along the blade and at other fatigue-sensitive locations on a FOWT structure, and to include substantially more environmental conditions.

Table 4.3: Short-term damage-equivalent loads.

	120-m Fixed	120-m Typical	120-m Extreme	74-m Fixed	74-m Typical	74-m Extreme
Bending Moment (Nm)	2.208e6	3.242e6	4.757e6	3.200e6	3.562e6	4.759e6
Shear force (N)	7.576e4	9.207e4	1.733e5	9.708e4	1.029e5	1.679e5
Axial force (N)	2.201e5	2.369e5	2.682e5	2.021e5	1.987e5	2.560e5
Shaft Torque (Nm)	1.762e5	3.646e5	8.679e5	1.552e5	1.998e5	9.955e5

4.7 Conclusions

A multi-scale dynamic coupling method has been developed that combines momentum-based beam theory (MBBT) with multibody momentum cloud method (MCM). The MBBT-MCM coupled model has been shown to be an effective numerical tool for simulating the coupled dynamics of floating offshore wind turbines. Six cases are simulated with each being subject to either an typical or an extreme operational condition. The proposed multi-scale coupling scheme has been demonstrated to effectively capture various coupling dynamic behaviors of FOWT systems. A highly-compliant FOWT design has been found feasible for the typical and extreme operational conditions simulated in this study. An improperly-designed blade pitch control has been shown to induce platform oscillations through wind-pitch resonance. Imbalanced aerodynamic loads have found to be induced by axial-asymmetric deflections of the blades. Turbine rotation and floating platform motions have been shown to significantly affect blade vibration. The damage-equivalent-loads computed for the six simulation cases have used to show that large platform oscillations adversely affect fatigue life.

5. SUMMARY

5.1 Conclusions

A geometrically-exact beam formulation, momentum-based beam theory (MBBT), and a nonlinear geometrically-exact dynamic theory for pipes conveying fluid are derived in this dissertation. Separation of displacements and local linearization techniques are used with these theories to develop piecewise-linear models for computation of large-displacement nonlinear dynamics. The new theoretical and numerical developments are implemented in ocean engineering applications, including floating offshore wind turbines (FOWT's) and a top-tensioned marine riser.

MBBT is derived in Chapter 2, in which coordinate transformation matrices are used throughout the derivation to rigorously consider geometric and kinematic nonlinearities. The resulting theory is different from other existing geometrically-exact beam formulations in that it is derived based on momentum conservation in vector form and it can be expressed with respect to arbitrary non-inertial reference frames. The vector-based formulation enables easy application of practical engineering assumptions, which leads to linearized and simplified versions of the fully nonlinear MBBT. These simplified theories bridge the gap between the classical Timoshenko beam theory and modern geometrically-exact beam theories, allowing users to select a beam theory suitable for their particular applications. The formulation in non-inertial frames enables separation of displacement and easy coupling with multibody models. Combining linearization and separation of displacement techniques enables the development of a piecewise-linear formulation and a time-stepping scheme, allowing nonlinear dynamics to be reduced into a series of piecewise-linear models, in which conventional discretization methods are applicable. A piecewise-linear finite volume beam solver is developed and shown to effectively solve dynamics of beams having large deformations and overall motions.

A momentum-based dynamic theory for pipes conveying fluid is derived in Chapter 3. The methodology used to derive MBBT is modified to include dynamic effects of the internal flow, in which the total momentum is computed as a sum over both the fluid and pipe. The resulting theory is the first model that rigorously addresses geometric and kinematic nonlinearities and inertial coupling effects for pipes conveying fluid and having large deformations and overall motions. The fluid is viscous and assumed to be incompressible and homogeneous, and fluid pressures along the pipe are the primary variables in this model. The linearization and separation of displacements techniques are adopted for application to the pipe theory. The resulting piecewise-linear finite volume pipe solver is applied to rotating pipes and a top-tensioned marine risers to demonstrate the significant effects of inertial coupling and internal pressure.

A multi-scale weakly-coupled method is developed in Chapter 4 to combine MBBT and a multibody model for application to FOWT's. The piecewise-linear MBBT beam solver is used to compute blade dynamics by modeling each blade as a cantilever beam with the fixed-end attached to the moving hub. The existing in-house multibody code based on the momentum cloud method is used to compute the coupled dynamics of the three-rigid-body system consisting of the spar/tower, nacelle, and hub. An advanced numerical tool is developed for fully-coupled aero-hydro-servo-elastic simulation of FOWT systems, which is used to demonstrate the effectiveness of the proposed coupling method. Two different spar-type FOWT designs are investigated, one of which is a highly-compliant design. Each design is subject to two time-domain simulations, representing a typical and an extreme operational conditions. Various coupling dynamic effects are investigated, including the coupling between blade vibration and platform motions, the coupling between blade pitch control and platform motions, and the coupling between blade vibration and turbine rotation. Aerodynamic imbalance loading cause by axial-asymmetric deflections of blades is analyzed. Fatigue effects are quantified as short-term damage-equivalent-loads, and platform motions are shown to adversely affect blade fatigue performance.

5.2 Future Work

Several potential future developments have been identified.

(a) A finite element discretization method for the piecewise-linear beam or pipe model may be developed to enhance the likelihood of the new theory gaining widespread acceptance through compatibility with conventional finite element analysis and design tools. A finite element discretization might also enable better accuracy and/or efficiency than the finite volume method.

(b) A fully nonlinear numerical method may be developed to directly solve the geometrically-exact nonlinear governing equations for beams or pipes without relying on the piecewise-linear models.

(c) A linearized model for pipes conveying fluid and having large overall motions may be derived by further simplifying the proposed pipe theory with additional assumptions.

(d) The theory for pipes conveying fluid may be expanded to include the Poisson effect of pipe walls. A single combined element may be a very efficient method to model nonlinear dynamic pipe-fluid systems.

(e) A new methodology to assess fatigue damage on FOWT blades for different FOWT designs may be developed, in which fatigue estimations are based on the proposed fully-coupled simulation tool.

(f) Physical experiments on beams and pipes subject to large overall motions would be valuable for verification of the new nonlinear dynamic beam and pipe theories.

REFERENCES

[1] Wikipedia, “Hywind Scotland.” https://en.wikipedia.org/wiki/Hywind_Scotland, (accessed February 2019).

[2] L. Wang and B. Sweetman, “Simulation of large-amplitude motion of floating wind turbines using conservation of momentum,” *Ocean Engineering*, vol. 42, pp. 155–164, 2012.

[3] B. Sweetman and L. Wang, “Floating offshore wind turbine dynamics: Large-angle motins in Euler-space,” *Journal of Offshore Mechanics and Arctic Engineering*, vol. 134, 2012.

[4] J. Gao and B. Sweetman, “Design optimization of hull size for spar-based floating offshore wind turbines,” *Journal of Ocean Engineering and Marine Energy*, vol. 4, no. 3, pp. 217–229, 2018.

[5] L. Wang and B. Sweetman, “Multibody dynamics of floating wind turbines with large-amplitude motion,” *Applied Ocean Research*, vol. 43, pp. 1–10, 2013.

[6] B. Sweetman and L. Wang, “Momentum cloud method for dynamic simulation of rigid body systems,” *Journal of Engineering Mechanics*, vol. 140, pp. 257–267, 2014.

[7] T. R. Kane, R. Ryan, and A. K. Banerjee, “Dynamics of a cantilever beam attached to a moving base,” *Journal of Guidance, Control, and Dynamics*, vol. 10, pp. 139–151, 1987.

[8] I. Sharf, “Geometric stiffening in multibody dynamics formulations,” *Journal of Guidance, Control, and Dynamics*, vol. 18, no. 4, pp. 882–890, 1995.

[9] H. Kim, H. H. Yoo, and J. Chung, “Dynamic model for free vibration and response analysis of rotating beams,” *Journal of Sound and Vibration*, vol. 332, no. 22, pp. 5917–5928, 2013.

[10] G. Zhao and Z. Wu, “Coupling vibration analysis of rotating three-dimensional cantilever beam,” *Computers & Structures*, vol. 179, pp. 64–74, 2017.

[11] D. H. Hodges, "A mixed variational formulation based on exact intrinsic equations for dynamics of moving beams," *International Journal of Solids and Structures*, vol. 26, no. 11, pp. 1253–1273, 1990.

[12] D. H. Hodges, "Geometrically exact, intrinsic theory for dynamics of curved and twisted anisotropic beams," *AIAA Journal*, vol. 41, no. 6, pp. 1131–1137, 2003.

[13] J. C. Simo and L. Vu-Quoc, "On the dynamics in space of rods undergoing large motions - A geometrically exact approach," *Computer Methods in Applied Mechanics and Engineering*, vol. 66, pp. 125–161, 1988.

[14] A. Ibrahimbegović, "On finite element implementation of geometrically nonlinear Reissner's beam theory: three-dimensional curved beam elements," *Computer Methods in Applied Mechanics and Engineering*, vol. 122, no. 1-2, pp. 11–26, 1995.

[15] G. Jelenić and M. A. Crisfield, "Geometrically exact 3D beam theory: implementation of a strain-invariant finite element for statics and dynamics," *Computer Methods in Applied Mechanics and Engineering*, vol. 171, no. 1-2, pp. 141–171, 1999.

[16] E. Zupan, M. Saje, and D. Zupan, "The quaternion-based three-dimensional beam theory," *Computer Methods in Applied Mechanics and Engineering*, vol. 198, no. 49, pp. 3944–3956, 2009.

[17] V. Sonneville, A. Cardona, and O. Brüls, "Geometrically exact beam finite element formulated on the special Euclidean group SE (3)," *Computer Methods in Applied Mechanics and Engineering*, vol. 268, pp. 451–474, 2014.

[18] M. A. Crisfield and G. Jelenić, "Objectivity of strain measures in the geometrically exact three-dimensional beam theory and its finite-element implementation," in *Proceedings of the Royal Society of London A: Mathematical, Physical and Engineering Sciences*, vol. 455, pp. 1125–1147, The Royal Society, 1999.

[19] D. H. Hodges, *Nonlinear Composite Beam Theory*. American Institute of Aeronautics and Astronautics, 2006.

[20] O. A. Bauchau, *Flexible Multibody Dynamics*. Springer, 2011.

[21] E. Reissner, “On one-dimensional finite-strain beam theory: the plane problem,” *Journal of Applied Mathematics and Physics*, vol. 23, pp. 795–804, 1972.

[22] E. Reissner, “On one-dimensional large-displacement finite-strain beam theory,” *Studies in Applied Mathematics*, vol. 52, no. 2, pp. 87–95, 1973.

[23] E. Reissner, “On finite deformations of space-curved beams,” *Journal of Applied Mathematics and Physics*, vol. 32, pp. 734–744, 1981.

[24] J. C. Simo, “A finite strain beam formulation. the three-dimensional dynamic problem. Part I,” *Computer Methods in Applied Mechanics and Engineering*, vol. 49, pp. 55–70, 1985.

[25] J. C. Simo and L. Vu-Quoc, “A three-dimensional finite-strain rod model. Part II: Computational aspects,” *Computer Methods in Applied Mechanics and Engineering*, vol. 58, pp. 79–116, 1986.

[26] J. C. Simo and L. Vu-Quoc, “A geometrically-exact rod model incorporating shear and torsion-warping deformation,” *International Journal of Solids and Structures*, vol. 27, no. 3, pp. 371–393, 1991.

[27] O. A. Bauchau and C. H. Hong, “Large displacement analysis of naturally curved and twisted composite beams,” *AIAA journal*, vol. 25, no. 11, pp. 1469–1475, 1987.

[28] O. A. Bauchau and C. H. Hong, “Nonlinear composite beam theory,” *Journal of Applied Mechanics*, vol. 55, pp. 156–163, 1988.

[29] D. A. Danielson and D. H. Hodges, “Nonlinear beam kinematics by decomposition of the rotation tensor,” *Journal of Applied Mechanics*, vol. 54, pp. 258–262, 1987.

[30] D. A. Danielson and D. H. Hodges, “A beam theory for large global rotation, moderate local rotation, and small strain,” *Journal of Applied Mechanics*, vol. 55, pp. 179–184, 1988.

[31] D. Zupan and M. Saje, “Finite-element formulation of geometrically exact three-dimensional beam theories based on interpolation of strain measures,” *Computer Methods in Applied Mechanics and Engineering*, vol. 192, pp. 5209–5248, 2003.

[32] W. Su and C. E. S. Cesnik, “Strain-based geometrically nonlinear beam formulation for modeling very flexible aircraft,” *International Journal of Solids and Structures*, vol. 48, pp. 2349–2360, 2011.

[33] C. E. S. Cesnik and D. H. Hodges, “Variational-asymptotical analysis of initially curved and twisted composite beams,” *Applied Mechanics Reviews*, vol. 46, no. 11/2, pp. S211–S220, 1993.

[34] C. E. S. Cesnik and D. H. Hodges, “VABS: A new concept for composite rotor blade cross-sectional modeling,” *Journal of the American Helicopter Society*, vol. 42, no. 1, pp. 27–38, 1997.

[35] W. Yu, D. H. Hodges, V. Volovoi, and C. E. S. Cesnik, “On Timoshenko-like modeling of initially curved and twisted composite beams,” *International Journal of Solids and Structures*, vol. 39, pp. 5101–5121, 2002.

[36] W. Yu, V. Volovoi, D. H. Hodges, and X. Hong, “Validation of the variational asymptotic beam sectional analysis (VABS),” *AIAA Journal*, vol. 40, no. 10, pp. 2015–2113, 2002.

[37] W. Yu and D. H. Hodges, “Elasticity solutions versus asymptotic sectional analysis of homogeneous, isotropic, prismatic beams,” *Journal of Applied Mechanics*, vol. 71, no. 1, pp. 15–23, 2004.

[38] D. H. Hodges and W. Yu, “A rigorous, engineer-friendly approach for modelling realistic, composite rotor blades,” *Wind Energy*, vol. 10, no. 2, pp. 179–193, 2007.

[39] Y. Jonnalagadda and J. D. Whitcomb, “Calculation of effective section stiffness properties for wind turbine blades using homogenization,” *Wind Energy*, vol. 17, pp. 297–316, 2014.

[40] H. Yang, J. Hong, and Z. Yu, “Dynamics modelling of a flexible hub–beam system with a tip mass,” *Journal of Sound and Vibration*, vol. 266, no. 4, pp. 759–774, 2003.

[41] J. B. Yang, L. J. Jiang, and D. C. Chen, “Dynamic modelling and control of a rotating Euler-Bernoulli beam,” *Journal of sound and vibration*, vol. 274, no. 3-5, pp. 863–875, 2004.

[42] S. K. Sinha, “Non-linear dynamic response of a rotating radial Timoshenko beam with periodic pulse loading at the free-end,” *International Journal of Non-Linear Mechanics*, vol. 40, no. 1, pp. 113–149, 2005.

[43] S. Y. Lee and J. J. Sheu, “Free vibration of an extensible rotating inclined Timoshenko beam,” *Journal of Sound and Vibration*, vol. 304, no. 3-5, pp. 606–624, 2007.

[44] C. L. Huang, W. Y. Lin, and K. M. Hsiao, “Free vibration analysis of rotating Euler beams at high angular velocity,” *Computers & structures*, vol. 88, no. 17-18, pp. 991–1001, 2010.

[45] M. H. Tsai, W. Y. Lin, Y. C. Zhou, and K. M. Hsiao, “Investigation on steady state deformation and free vibration of a rotating inclined Euler beam,” *International Journal of Mechanical Sciences*, vol. 53, no. 12, pp. 1050–1068, 2011.

[46] Z. Zhao, C. Liu, and W. Ma, “Characteristics of steady vibration in a rotating hub-beam system,” *Journal of Sound and Vibration*, vol. 363, pp. 571–583, 2016.

[47] J. C. Simo and L. Vu-Quoc, “On the dynamics of flexible beams under large overall motions - The plane case: Part I,” *Journal of Applied Mechanics*, vol. 53, no. 4, pp. 849–854, 1986.

[48] J. C. Simo and L. Vu-Quoc, “The role of non-linear theories in transient dynamic analysis of flexible structures,” *Journal of Sound and Vibration*, vol. 119, no. 3, pp. 487–508, 1987.

[49] H. H. Yoo, R. R. Ryan, and R. A. Scott, “Dynamics of flexible beams undergoing overall motions,” *Journal of Sound and vibration*, vol. 181, no. 2, pp. 261–278, 1995.

[50] J. L. Meek and H. Liu, “Nonlinear dynamics analysis of flexible beams under large overall motions and the flexible manipulator simulation,” *Computers & structures*, vol. 56, no. 1, pp. 1–14, 1995.

[51] J. Y. Liu and J. Z. Hong, “Dynamics of three-dimensional beams undergoing large overall motion,” *European Journal of Mechanics-A/Solids*, vol. 23, no. 6, pp. 1051–1068, 2004.

[52] J. Y. Liu and J. Z. Hong, "Geometric stiffening effect on rigid-flexible coupling dynamics of an elastic beam," *Journal of sound and Vibration*, vol. 278, no. 4-5, pp. 1147–1162, 2004.

[53] M. J. Patil and D. H. Hodges, "Variable-order finite elements for nonlinear, fully intrinsic beam equations," *Journal of Mechanics of Materials and Structures*, vol. 6, no. 1, pp. 479–493, 2011.

[54] E. Zupan, M. Saje, and D. Zupan, "Dynamics of spatial beams in quaternion description based on the Newmark integration scheme," *Computational Mechanics*, vol. 51, no. 1, pp. 47–64, 2013.

[55] Q. Wang, M. A. Sprague, J. Jonkman, N. Johnson, and B. Jonkman, "BeamDyn: a high-fidelity wind turbine blade solver in the FAST modular framework," *Wind Energy*, vol. 20, no. 8, pp. 1439–1462, 2017.

[56] A. A. Shabana, "Flexible multibody dynamics: review of past and recent developments," *Multibody system dynamics*, vol. 1, no. 2, pp. 189–222, 1997.

[57] J. D. Downer, K. C. Park, and J. C. Chiou, "Dynamics of flexible beams for multibody systems: A computational procedure," *Computer Methods in Applied Mechanics and Engineering*, vol. 96, no. 3, pp. 373–408, 1992.

[58] A. K. Banerjee and S. Nagarajan, "Efficient simulation of large overall motion of beams undergoing large deflection," *Multibody System Dynamics*, vol. 1, no. 1, pp. 113–126, 1997.

[59] I. Romero, "The interpolation of rotations and its application to finite element models of geometrically exact rods," *Computational Mechanics*, vol. 34, no. 2, pp. 121–133, 2004.

[60] A. A. Shabana and R. Y. Yakoub, "Three dimensional absolute nodal coordinate formulation for beam elements: theory," *Journal of Mechanical Design*, vol. 123, pp. 606–613, 2001.

[61] R. Y. Yakoub and A. A. Shabana, "Three dimensional absolute nodal coordinate formulation for beam elements: implementation and applications," *Journal of Mechanical Design*, vol. 123, pp. 614–621, 2001.

[62] J. Gerstmayr, M. K. Matikainen, and A. M. Mikkola, “A geometrically exact beam element based on the absolute nodal coordinate formulation,” *Multibody System Dynamics*, vol. 20, no. 4, pp. 359–384, 2008.

[63] M. P. Païdoussis, “Flow-induced instabilities of cylindrical structures,” *Applied Mechanics Reviews*, vol. 40, no. 2, pp. 163–175, 1987.

[64] M. P. Païdoussis and G. X. Li, “Pipes conveying fluid: a model dynamical problem,” *Journal of Fluids and Structures*, vol. 7, no. 2, pp. 137–204, 1993.

[65] R. A. Ibrahim, “Overview of mechanics of pipes conveying fluids—Part I: Fundamental studies,” *Journal of Pressure Vessel Technology*, vol. 132, no. 3, p. 034001, 2010.

[66] R. A. Ibrahim, “Mechanics of pipes conveying fluids—Part II: Applications and fluidelastic problems,” *Journal of Pressure Vessel Technology*, vol. 133, no. 2, p. 024001, 2011.

[67] S. Li, B. W. Karney, and G. Liu, “FSI research in pipeline systems–A review of the literature,” *Journal of Fluids and Structures*, vol. 57, pp. 277–297, 2015.

[68] M. P. Païdoussis, *Fluid-structure interactions: slender structures and axial flow*, vol. 1. Academic Press, London, 1998.

[69] M. P. Païdoussis, *Fluid-structure interactions: slender structures and axial flow*, vol. 2. Elsevier Academic Press, London, 2003.

[70] C. Semler, G. X. Li, and M. P. Païdoussis, “The non-linear equations of motion of pipes conveying fluid,” *Journal of Sound and Vibration*, vol. 169, no. 5, pp. 577–599, 1994.

[71] M. Stangl, J. Gerstmayr, and H. Irschik, “An alternative approach for the analysis of non-linear vibrations of pipes conveying fluid,” *Journal of Sound and Vibration*, vol. 310, no. 3, pp. 493–511, 2008.

[72] M. H. Ghayesh, M. P. Païdoussis, and M. Amabili, “Nonlinear dynamics of cantilevered extensible pipes conveying fluid,” *Journal of Sound and Vibration*, vol. 332, no. 24, pp. 6405–6418, 2013.

[73] M. Wadham-Gagnon, M. P. Païdoussis, and C. Semler, “Dynamics of cantilevered pipes conveying fluid. Part 1: Nonlinear equations of three-dimensional motion,” *Journal of Fluids and Structures*, vol. 23, no. 4, pp. 545–567, 2007.

[74] M. P. Païdoussis, C. Semler, M. Wadham-Gagnon, and S. Saaid, “Dynamics of cantilevered pipes conveying fluid. Part 2: Dynamics of the system with intermediate spring support,” *Journal of Fluids and Structures*, vol. 23, no. 4, pp. 569–587, 2007.

[75] M. H. Ghayesh and M. P. Païdoussis, “Three-dimensional dynamics of a cantilevered pipe conveying fluid, additionally supported by an intermediate spring array,” *International Journal of Non-Linear Mechanics*, vol. 45, no. 5, pp. 507–524, 2010.

[76] Y. Modarres-Sadeghi, C. Semler, M. Wadham-Gagnon, and M. P. Païdoussis, “Dynamics of cantilevered pipes conveying fluid. Part 3: Three-dimensional dynamics in the presence of an end-mass,” *Journal of Fluids and Structures*, vol. 23, no. 4, pp. 589–603, 2007.

[77] M. H. Ghayesh, M. P. Païdoussis, and Y. Modarres-Sadeghi, “Three-dimensional dynamics of a fluid-conveying cantilevered pipe fitted with an additional spring-support and an end-mass,” *Journal of Sound and Vibration*, vol. 330, no. 12, pp. 2869–2899, 2011.

[78] Y. Modarres-Sadeghi and M. P. Païdoussis, “Chaotic oscillations of long pipes conveying fluid in the presence of a large end-mass,” *Computers & Structures*, vol. 122, pp. 192–201, 2013.

[79] Y. Modarres-Sadeghi and M. P. Païdoussis, “Nonlinear dynamics of extensible fluid-conveying pipes, supported at both ends,” *Journal of Fluids and Structures*, vol. 25, no. 3, pp. 535–543, 2009.

[80] G. Liu and Y. Li, “Vibration analysis of liquid-filled pipelines with elastic constraints,” *Journal of sound and vibration*, vol. 330, no. 13, pp. 3166–3181, 2011.

[81] M. Kheiri, M. P. Païdoussis, G. C. Del Pozo, and M. Amabili, “Dynamics of a pipe conveying fluid flexibly restrained at the ends,” *Journal of Fluids and Structures*, vol. 49, pp. 360–385, 2014.

[82] T. Zhang, H. Ouyang, Y. O. Zhang, and B. L. Lv, “Nonlinear dynamics of straight fluid-conveying pipes with general boundary conditions and additional springs and masses,” *Applied Mathematical Modelling*, vol. 40, no. 17-18, pp. 7880–7900, 2016.

[83] A. K. Misra, M. P. Païdoussis, and K. S. Van, “On the dynamics of curved pipes transporting fluid. Part I: inextensible theory,” *Journal of Fluids and Structures*, vol. 2, no. 3, pp. 221–244, 1988.

[84] A. K. Misra, M. P. Païdoussis, and K. S. Van, “On the dynamics of curved pipes transporting fluid. Part II: Extensible theory,” *Journal of Fluids and Structures*, vol. 2, no. 3, pp. 245–261, 1988.

[85] C. Dupuis and J. Rousselet, “The equations of motion of curved pipes conveying fluid,” *Journal of Sound and Vibration*, vol. 153, no. 3, pp. 473–489, 1992.

[86] C. Dupuis and J. Rousselet, “Hamilton’s principle and the governing equations of fluid-conveying curved pipes,” *Journal of Sound Vibration*, vol. 160, pp. 172–174, 1993.

[87] D. Jung and J. Chung, “In-plane and out-of-plane motions of an extensible semi-circular pipe conveying fluid,” *Journal of Sound and Vibration*, vol. 311, no. 1-2, pp. 408–420, 2008.

[88] H. L. Dai, L. Wang, Q. Qian, and J. Gan, “Vibration analysis of three-dimensional pipes conveying fluid with consideration of steady combined force by transfer matrix method,” *Applied Mathematics and Computation*, vol. 219, no. 5, pp. 2453–2464, 2012.

[89] Q. Ni, M. Tang, Y. Wang, and L. Wang, “In-plane and out-of-plane dynamics of a curved pipe conveying pulsating fluid,” *Nonlinear Dynamics*, vol. 75, no. 3, pp. 603–619, 2014.

[90] A. Zare, M. Eghtesad, and F. Daneshmand, “An isogeometric analysis approach to the stability of curved pipes conveying fluid,” *Marine Structures*, vol. 59, pp. 321–341, 2018.

[91] J. Łuczko and A. Czerwiński, “Nonlinear three-dimensional dynamics of flexible pipes conveying fluids,” *Journal of Fluids and Structures*, vol. 70, pp. 235–260, 2017.

[92] A. Czerwiński and J. Łuczko, "Non-planar vibrations of slightly curved pipes conveying fluid in simple and combination parametric resonances," *Journal of Sound and Vibration*, vol. 413, pp. 270–290, 2018.

[93] D. A. Panussis and A. D. Dimarogonas, "Linear in-plane and out-of-plane lateral vibrations of a horizontally rotating fluid-tube cantilever," *Journal of Fluids and structures*, vol. 14, no. 1, pp. 1–24, 2000.

[94] H. I. Yoon and I. S. Son, "Dynamic response of rotating flexible cantilever pipe conveying fluid with tip mass," *International journal of mechanical sciences*, vol. 49, no. 7, pp. 878–887, 2007.

[95] D. Meng, H. Y. Guo, and S. P. Xu, "Non-linear dynamic model of a fluid-conveying pipe undergoing overall motions," *Applied Mathematical Modelling*, vol. 35, no. 2, pp. 781–796, 2011.

[96] G. H. Chang and Y. Modarres-Sadeghi, "Flow-induced oscillations of a cantilevered pipe conveying fluid with base excitation," *Journal of Sound and Vibration*, vol. 333, no. 18, pp. 4265–4280, 2014.

[97] S. Chucheepsakul, T. Monprapussorn, and T. Huang, "Large strain formulations of extensible flexible marine pipes transporting fluid," *Journal of Fluids and Structures*, vol. 17, no. 2, pp. 185–224, 2003.

[98] S. Kaewunruen, J. Chiravatchradej, and S. Chucheepsakul, "Nonlinear free vibrations of marine risers/pipes transporting fluid," *Ocean engineering*, vol. 32, no. 3-4, pp. 417–440, 2005.

[99] C. Athisakul, T. Monprapussorn, and S. Chucheepsakul, "A variational formulation for three-dimensional analysis of extensible marine riser transporting fluid," *Ocean engineering*, vol. 38, no. 4, pp. 609–620, 2011.

[100] I. K. Chatjigeorgiou, "On the effect of internal flow on vibrating catenary risers in three dimensions," *Engineering Structures*, vol. 32, no. 10, pp. 3313–3329, 2010.

[101] I. K. Chatjigeorgiou, “Three dimensional nonlinear dynamics of submerged, extensible catenary pipes conveying fluid and subjected to end-imposed excitations,” *International Journal of Non-Linear Mechanics*, vol. 45, no. 7, pp. 667–680, 2010.

[102] M. Abdulkadir, V. Hernandez-Perez, I. S. Lowndes, B. J. Azzopardi, and S. Dzomeku, “Experimental study of the hydrodynamic behaviour of slug flow in a vertical riser,” *Chemical Engineering Science*, vol. 106, pp. 60–75, 2014.

[103] L. Wang, Y. Yang, Y. Li, and Y. Wang, “Dynamic behaviours of horizontal gas-liquid pipes subjected to hydrodynamic slug flow: Modelling and experiments,” *International Journal of Pressure Vessels and Piping*, vol. 161, pp. 50–57, 2018.

[104] D. P. Lannes and A. L. Gama, “On the relationship between pipe accelerance and the void fraction of internal two-phase flow,” *Journal of Fluids and Structures*, vol. 80, pp. 350–369, 2018.

[105] D. J. Montoya-Hernández, A. O. Vázquez-Hernández, R. Cuamatzi, and M. A. Hernandez, “Natural frequency analysis of a marine riser considering multiphase internal flow behavior,” *Ocean Engineering*, vol. 92, pp. 103–113, 2014.

[106] C. An and J. Su, “Dynamic behavior of pipes conveying gas–liquid two-phase flow,” *Nuclear Engineering and Design*, vol. 292, pp. 204–212, 2015.

[107] I. K. Chatjigeorgiou, “Hydroelastic response of marine risers subjected to internal slug-flow,” *Applied Ocean Research*, vol. 62, pp. 1–17, 2017.

[108] Q. Li, M. Duan, *et al.*, “On the interaction between severe slug buildup and dynamic response of a submerged top-tensioned riser,” *Ocean Engineering*, vol. 164, pp. 683–697, 2018.

[109] D. Meng and L. Chen, “Nonlinear free vibrations and vortex-induced vibrations of fluid-conveying steel catenary riser,” *Applied Ocean Research*, vol. 34, pp. 52–67, 2012.

[110] H. L. Dai, A. Abdelkefi, and L. Wang, “Modeling and nonlinear dynamics of fluid-conveying risers under hybrid excitations,” *International Journal of Engineering Science*, vol. 81, pp. 1–14, 2014.

[111] J. Wang and M. Duan, “A nonlinear model for deepwater steel lazy-wave riser configuration with ocean current and internal flow,” *Ocean Engineering*, vol. 94, pp. 155–162, 2015.

[112] F. He, H. Dai, Z. Huang, and L. Wang, “Nonlinear dynamics of a fluid-conveying pipe under the combined action of cross-flow and top-end excitations,” *Applied Ocean Research*, vol. 62, pp. 199–209, 2017.

[113] Y. Bazilevs, M. C. Hsu, J. Kiendl, R. Wüchner, and K. U. Bletzinger, “3D simulation of wind turbine rotors at full scale. Part II: Fluid–structure interaction modeling with composite blades,” *International Journal for Numerical Methods in Fluids*, vol. 65, no. 1-3, pp. 236–253, 2011.

[114] J. C. Dai, Y. P. Hu, D. S. Liu, and X. Long, “Aerodynamic loads calculation and analysis for large scale wind turbine based on combining bem modified theory with dynamic stall model,” *Renewable Energy*, vol. 36, no. 3, pp. 1095–1104, 2011.

[115] M. C. Hsu and Y. Bazilevs, “Fluid–structure interaction modeling of wind turbines: simulating the full machine,” *Computational Mechanics*, vol. 50, no. 6, pp. 821–833, 2012.

[116] M. Carrión, R. Steijl, M. Woodgate, G. N. Barakos, X. Munduate, and S. Gomez-Iradi, “Aeroelastic analysis of wind turbines using a tightly coupled CFD-CSD method,” *Journal of Fluids and Structures*, vol. 50, pp. 392–415, 2014.

[117] D. O. Yu and O. J. Kwon, “Predicting wind turbine blade loads and aeroelastic response using a coupled CFD-CSD method,” *Renewable Energy*, vol. 70, pp. 184–196, 2014.

[118] X. Liu, C. Lu, S. Liang, A. Godbole, and Y. Chen, “Vibration-induced aerodynamic loads on large horizontal axis wind turbine blades,” *Applied Energy*, vol. 185, pp. 1109–1119, 2017.

[119] D. Tang, S. Bao, L. Luo, J. Mao, B. Lv, and H. Guo, “Study on the aeroelastic responses of a wind turbine using a coupled multibody-FVW method,” *Energy*, vol. 141, pp. 2300–2313, 2017.

[120] T. Tran, D. Kim, and J. Song, “Computational fluid dynamic analysis of a floating offshore wind turbine experiencing platform pitching motion,” *Energies*, vol. 7, no. 8, pp. 5011–5026, 2014.

[121] T. T. Tran and D. H. Kim, “The coupled dynamic response computation for a semi-submersible platform of floating offshore wind turbine,” *Journal of Wind Engineering and Industrial Aerodynamics*, vol. 147, pp. 104–119, 2015.

[122] T. T. Tran and D. H. Kim, “Fully coupled aero-hydrodynamic analysis of a semi-submersible fowt using a dynamic fluid body interaction approach,” *Renewable Energy*, vol. 92, pp. 244–261, 2016.

[123] T. T. Tran and D. H. Kim, “A CFD study of coupled aerodynamic-hydrodynamic loads on a semisubmersible floating offshore wind turbine,” *Wind Energy*, vol. 21, no. 1, pp. 70–85, 2018.

[124] V. Leble and G. N. Barakos, “A coupled floating offshore wind turbine analysis with high-fidelity methods,” *Energy Procedia*, vol. 94, pp. 523–530, 2016.

[125] Y. Liu, Q. Xiao, A. Incecik, and D. Wan, “Investigation of the effects of platform motion on the aerodynamics of a floating offshore wind turbine,” *Journal of Hydrodynamics*, vol. 28, no. 1, pp. 95–101, 2016.

[126] Y. Liu, Q. Xiao, A. Incecik, C. Peyrard, and D. Wan, “Establishing a fully coupled CFD analysis tool for floating offshore wind turbines,” *Renewable Energy*, vol. 112, pp. 280–301, 2017.

[127] A. Cordle and J. Jonkman, “State of the art in floating wind turbine design tools,” in *The Twenty-first International Offshore and Polar Engineering Conference*, International Society of Offshore and Polar Engineers, 2011.

[128] B. Jonkman and J. Jonkman, "FAST v8. 16.00 a–bjj," tech. rep., National Renewable Energy Lab, Golden, CO, USA, 2016.

[129] J. Jonkman, T. Larsen, A. Hansen, T. Nygaard, K. Maus, M. Karimirad, Z. Gao, T. Moan, and I. Fylling, "Offshore code comparison collaboration within IEA wind task 23: Phase IV results regarding floating wind turbine modeling; preprint," tech. rep., National Renewable Energy Lab, Golden, CO, USA, 2010.

[130] A. Robertson, J. Jonkman, F. Vorpahl, W. Popko, J. Qvist, L. Frøyd, X. Chen, J. Azcona, E. Uzunoglu, C. G. Soares, *et al.*, "Offshore code comparison collaboration continuation within IEA wind task 30: Phase II results regarding a floating semisubmersible wind system," in *ASME 2014 33rd International Conference on Ocean, Offshore and Arctic Engineering*, American Society of Mechanical Engineers, 2014.

[131] A. Robertson, F. Wendt, J. Jonkman, W. Popko, H. Dagher, S. Gueydon, J. Qvist, F. Vittori, J. Azcona, E. Uzunoglu, *et al.*, "OC5 project Phase II: Validation of global loads of the deepcwind floating semisubmersible wind turbine," *Energy Procedia*, vol. 137, pp. 38–57, 2017.

[132] L. Wang, X. Liu, and A. Kolios, "State of the art in the aeroelasticity of wind turbine blades: Aeroelastic modelling," *Renewable and Sustainable Energy Reviews*, vol. 64, pp. 195–210, 2016.

[133] M. Rafiee, F. Nitzsche, and M. Labrosse, "Dynamics, vibration and control of rotating composite beams and blades: A critical review," *Thin-Walled Structures*, vol. 119, pp. 795–819, 2017.

[134] S. Øye, "FLEX5 user manual," tech. rep., Technical University of Denmark, 1999.

[135] J. M. Jonkman and M. L. J. Buhl, *FAST User's Guide*. National Renewable Energy Laboratory, CO, USA, 2005.

[136] "Bladed theory manual version 4.7," tech. rep., Garrad Hassan & Partners Ltd, 2015.

[137] T. Kim, A. M. Hansen, and K. Branner, "Developmetn of an anisotropic beam finite element for composite wind turbine blades in multibody system," *Rnewable Energy*, vol. 59, pp. 172–183, 2013.

[138] Q. Wang, J. Jonkman, M. Sprague, and B. Jonkman, *BeamDyn User's Guide and Theory Manual.* National Renewable Energy Laboratory, CO, USA), 2016.

[139] Q. Wang and W. Yu, "Geometrically nonlinear analysis of composite beams using wiener-milenković parameters," *Journal of Renewable and Sustainable Energy*, vol. 9, no. 3, p. 033306, 2017.

[140] Y. B. Yang, J. D. Yau, and L. J. Leu, "Recent developments in geometrically nonlinear and postbuckling analysis of framed structures," *Applied Mechanics Reviews*, vol. 56, no. 4, pp. 431–449, 2003.

[141] K. J. Bathe and S. Bolourchi, "Large displacement analysis of three-dimensional beam structures," *International Journal for Numerical Methods in Engineering*, vol. 14, no. 7, pp. 961–986, 1979.

[142] A. Cardona and M. Geradin, "A beam finite element non-linear theory with finite rotations," *International journal for numerical methods in engineering*, vol. 26, no. 11, pp. 2403–2438, 1988.

[143] I. Romero, "A comparison of finite elements for nonlinear beams: the absolute nodal coordinate and geometrically exact formulations," *Multibody System Dynamics*, vol. 20, no. 1, pp. 51–68, 2008.

[144] J. Jonkman, S. Butterfield, W. Musial, and G. Scott, "Definition of a 5-MW reference wind turbine for offshore system development," tech. rep., National Renewable Energy Laboratory, Golden, CO, USA, 2009.

[145] S. E. Haaland, "Simple and explicit formulas for the friction factor in turbulent pipe flow," *Journal of Fluids Engineering*, vol. 105, no. 1, pp. 89–90, 1983.

[146] J. K. Sinha, S. Singh, and A. R. Rao, "Finite element simulation of dynamic behaviour of open-ended cantilever pipe conveying fluid," *Journal of Sound and Vibration*, vol. 240, no. 1, pp. 189–194, 2001.

[147] H. B. Zhai, Z. Y. Wu, Y. S. Liu, and Z. F. Yue, "Dynamic response of pipeline conveying fluid to random excitation," *Nuclear Engineering and Design*, vol. 241, no. 8, pp. 2744–2749, 2011.

[148] J. Jonkman, "Definition of the floating system for Phase IV of OC3," tech. rep., National Renewable Energy Lab, Golden, CO, USA, 2010.

[149] V. Lenaerts, G. Kerschen, and J. C. Golinval, "Proper orthogonal decomposition for model updating of non-linear mechanical systems," *Mechanical Systems and Signal Processing*, vol. 15, no. 1, pp. 31–43, 2001.

[150] M. Azeez and A. F. Vakakis, "Proper orthogonal decomposition (POD) of a class vibroimpact oscillations," *Journal of Sound and Vibration*, vol. 240, no. 5, pp. 859–889, 2001.

[151] M. Meyer and H. G. Matthies, "Efficient model reduction in non-linear dynamics using the Karhunen-Loeve expansion and dual-weighted-residual methods," *Computational Mechanics*, vol. 31, pp. 179–191, 2003.

[152] B. J. Jonkman and J. M. Jonkman, *Addendum to the user's guides for FAST, A2AD, and AeroDyn released March 2010-February 2013*. National Renewable Energy Laboratory, CO, USA, 2013.

[153] IEC, "Wind turbines - Part 3: Design requirements for offshore wind turbines," Tech. Rep. IEC 61400-3 ed. 1.0, International Electrotechnical Commission, 2009.

[154] B. J. Jonkman and L. Kilcher, *TurbSim User's Guide: Version 1.06.00 (Draft)*. National Renewable Energy Laboratory, CO, USA, 2012.

[155] F. G. Nielsen, T. D. Hanson, and B. Skaare, "Integrated dynamic analysis of floating offshore wind turbines," in *25th International Conference on Offshore Mechanics and Arctic Engineering*, pp. 671–679, American Society of Mechanical Engineers, 2006.

[156] J. Jonkman, “Influence of control on the pitch damping of a floating wind turbine,” in *46th AIAA Aerospace Sciences Meeting and Exhibit*, p. 1306, 2008.

[157] T. J. Larsen and T. D. Hanson, “A method to avoid negative damped low frequent tower vibrations for a floating, pitch controlled wind turbine,” in *Journal of Physics: Conference Series*, vol. 75, p. 012073, IOP Publishing, 2007.

[158] M. A. Lackner, “Controlling platform motions and reducing blade loads for floating wind turbines,” *Wind Engineering*, vol. 33, no. 6, pp. 541–553, 2009.

[159] B. R. Resor, “Definition of a 5MW/61.5 m wind turbine blade reference model,” tech. rep., Sandia National Laboratories, NM, USA, 2013.

[160] G. J. Hayman, *MLife theory manual for version 1.00.* National Renewable Energy Laboratory, CO, USA, 2012.

[161] G. J. Hayman and M. Buhl Jr, *MLife user’s guide for version 1.00.* National Renewable Energy Laboratory, CO, USA, 2012.

APPENDIX A

ELASTIC STIFFNESS MATRICES OF A BASE CONFIGURATION

$$\boldsymbol{K}^n_{ela,11}{=}\boldsymbol{T}^n_{fl}\boldsymbol{T}^{nj}_l\boldsymbol{T}^j_{lq}\boldsymbol{K}^j_{11}\frac{(\Delta s^{jn}\tilde{\boldsymbol{k}}^j_q-\boldsymbol{I})}{\Delta s^j} \tag{A.1}$$

$$\begin{aligned}\boldsymbol{K}^n_{ela,12}{=}&\boldsymbol{T}^n_{fl}\boldsymbol{T}^{nj}_l\boldsymbol{T}^j_{lq}\boldsymbol{K}^j_{11}\frac{\Delta s^{jn}(\tilde{\boldsymbol{\gamma}}^j_q+\tilde{\boldsymbol{e}}_1)}{\Delta s^j}\\&+\boldsymbol{T}^n_{fl}\boldsymbol{T}^{nj}_l\boldsymbol{T}^j_{lq}\boldsymbol{K}^j_{12}\frac{(\Delta s^{jn}\tilde{\boldsymbol{k}}^j_q-\boldsymbol{I})}{\Delta s^j}\end{aligned} \tag{A.2}$$

$$\begin{aligned}\boldsymbol{K}^n_{ela,13}{=}&\boldsymbol{T}^n_{fl}\boldsymbol{T}^{nj}_l\boldsymbol{T}^j_{lq}\boldsymbol{K}^j_{11}\frac{(\Delta s^{n-1j}\tilde{\boldsymbol{k}}^j_q+\boldsymbol{I})}{\Delta s^j}\\&-\boldsymbol{T}^n_{fl}\boldsymbol{T}^{nj+1}_l\boldsymbol{T}^j_{lq}\boldsymbol{K}^{j+1}_{11}\frac{(\Delta s^{j+1n+1}\tilde{\boldsymbol{k}}^{j+1}_q-\boldsymbol{I})}{\Delta s^{j+1}}\end{aligned} \tag{A.3}$$

$$\begin{aligned}\boldsymbol{K}^n_{ela,14}{=}&\boldsymbol{T}^n_{fl}\boldsymbol{T}^{nj}_l\boldsymbol{T}^j_{lq}\boldsymbol{K}^j_{11}\frac{\Delta s^{n-1j}(\tilde{\boldsymbol{\gamma}}^j_q+\tilde{\boldsymbol{e}}_1)}{\Delta s^j}\\&+\boldsymbol{T}^n_{fl}\boldsymbol{T}^{nj}_l\boldsymbol{T}^j_{lq}\boldsymbol{K}^j_{12}\frac{(\Delta s^{n-1j}\tilde{\boldsymbol{k}}^j_q+\boldsymbol{I})}{\Delta s^j}\\&-\boldsymbol{T}^n_{fl}\boldsymbol{T}^{nj+1}_l\boldsymbol{T}^{j+1}_{lq}\boldsymbol{K}^{j+1}_{11}\frac{\Delta s^{j+1n+1}(\tilde{\boldsymbol{\gamma}}^{j+1}_q+\tilde{\boldsymbol{e}}_1)}{\Delta s^{j+1}}\\&-\boldsymbol{T}^n_{fl}\boldsymbol{T}^{nj+1}_l\boldsymbol{T}^{j+1}_{lq}\boldsymbol{K}^{j+1}_{12}\frac{(\Delta s^{j+1n+1}\tilde{\boldsymbol{k}}^{j+1}_q-\boldsymbol{I})}{\Delta s^{j+1}}\end{aligned} \tag{A.4}$$

$$\boldsymbol{K}^n_{ela,15}{=}-\boldsymbol{T}^n_{fl}\boldsymbol{T}^{nj+1}_l\boldsymbol{T}^{j+1}_{lq}\boldsymbol{K}^{j+1}_{11}\frac{(\Delta s^{nj+1}\tilde{\boldsymbol{k}}^{j+1}_q+\boldsymbol{I})}{\Delta s^{j+1}} \tag{A.5}$$

$$\begin{aligned}\boldsymbol{K}^n_{ela,16}=&-\boldsymbol{T}^n_{fl}\boldsymbol{T}^{nj+1}_l\boldsymbol{T}^{j+1}_{lq}\boldsymbol{K}^{j+1}_{11}\frac{\Delta s^{nj+1}(\tilde{\boldsymbol{\gamma}}^{j+1}_q+\tilde{\boldsymbol{e}}_1)}{\Delta s^{j+1}}\\&-\boldsymbol{T}^n_{fl}\boldsymbol{T}^{nj+1}_l\boldsymbol{T}^{j+1}_{lq}\boldsymbol{K}^{j+1}_{12}\frac{(\Delta s^{nj+1}\tilde{\boldsymbol{k}}^{j+1}_q+\boldsymbol{I})}{\Delta s^{j+1}}\end{aligned}\tag{A.6}$$

$$\begin{aligned}\boldsymbol{K}^n_{ela,21}=&\boldsymbol{T}^n_{fl}\boldsymbol{T}^{nj}_l\boldsymbol{T}^j_{lq}\boldsymbol{K}^j_{21}\frac{(\Delta s^{jn}\tilde{\boldsymbol{k}}^j_q-\boldsymbol{I})}{\Delta s^j}\\&-\boldsymbol{T}^n_{fl}\boldsymbol{T}^n_{lq}\tilde{\boldsymbol{e}}^n\boldsymbol{T}^n_{ql}\boldsymbol{T}^{nj}_l\boldsymbol{T}^j_{lq}\boldsymbol{K}^j_{11}\frac{(\Delta s^{jn}\tilde{\boldsymbol{k}}^j_q-\boldsymbol{I})}{\Delta s^j}\\&-\boldsymbol{T}^n_{fl}(\boldsymbol{R}^{P^jP^n}_l\widetilde{+\boldsymbol{U}^n_l}-\boldsymbol{T}^{nj}_l\boldsymbol{U}^j_l)\boldsymbol{T}^{nj}_l\boldsymbol{T}^j_{lq}\boldsymbol{K}^j_{11}\frac{(\Delta s^{jn}\tilde{\boldsymbol{k}}^j_q-\boldsymbol{I})}{\Delta s^j}\end{aligned}\tag{A.7}$$

$$\begin{aligned}\boldsymbol{K}^n_{ela,22}=&\boldsymbol{T}^n_{fl}\boldsymbol{T}^{nj}_l\boldsymbol{T}^j_{lq}[\boldsymbol{K}^j_{21}\frac{\Delta s^{jn}(\tilde{\boldsymbol{\gamma}}^j_q+\tilde{\boldsymbol{e}}_1)}{\Delta s^j}+\boldsymbol{K}^j_{22}\frac{(\Delta s^{jn}\tilde{\boldsymbol{k}}^j_q-\boldsymbol{I})}{\Delta s^j}]\\&-\boldsymbol{T}^n_{fl}\boldsymbol{T}^n_{lq}\tilde{\boldsymbol{e}}^n\boldsymbol{T}^n_{ql}\boldsymbol{T}^{nj}_l\boldsymbol{T}^j_{lq}\boldsymbol{K}^j_{11}\frac{\Delta s^{jn}(\tilde{\boldsymbol{\gamma}}^j_q+\tilde{\boldsymbol{e}}_1)}{\Delta s^j}\\&-\boldsymbol{T}^n_{fl}\boldsymbol{T}^n_{lq}\tilde{\boldsymbol{e}}^n\boldsymbol{T}^n_{ql}\boldsymbol{T}^{nj}_l\boldsymbol{T}^j_{lq}\boldsymbol{K}^j_{12}\frac{(\Delta s^{jn}\tilde{\boldsymbol{k}}^j_q-\boldsymbol{I})}{\Delta s^j}\\&-\boldsymbol{T}^n_{fl}(\boldsymbol{R}^{P^jP^n}_l\widetilde{+\boldsymbol{U}^n_l}-\boldsymbol{T}^{nj}_l\boldsymbol{U}^j_l)\boldsymbol{T}^{nj}_l\boldsymbol{T}^j_{lq}\boldsymbol{K}^j_{11}\frac{\Delta s^{jn}(\tilde{\boldsymbol{\gamma}}^j_q+\tilde{\boldsymbol{e}}_1)}{\Delta s^j}\\&-\boldsymbol{T}^n_{fl}(\boldsymbol{R}^{P^jP^n}_l\widetilde{+\boldsymbol{U}^n_l}-\boldsymbol{T}^{nj}_l\boldsymbol{U}^j_l)\boldsymbol{T}^{nj}_l\boldsymbol{T}^j_{lq}\boldsymbol{K}^j_{12}\frac{(\Delta s^{jn}\tilde{\boldsymbol{k}}^j_q-\boldsymbol{I})}{\Delta s^j}\end{aligned}\tag{A.8}$$

$$\begin{aligned}\boldsymbol{K}^n_{ela,23}=&\boldsymbol{T}^n_{fl}\boldsymbol{T}^{nj}_l\boldsymbol{T}^j_{lq}\boldsymbol{K}^j_{21}\frac{(\Delta s^{n-1j}\tilde{\boldsymbol{k}}^j_q+\boldsymbol{I})}{\Delta s^j}\\&-\boldsymbol{T}^n_{fl}\boldsymbol{T}^n_{lq}\tilde{\boldsymbol{e}}^n\boldsymbol{T}^n_{ql}\boldsymbol{T}^{nj}_l\boldsymbol{T}^j_{lq}\boldsymbol{K}^j_{11}\frac{(\Delta s^{n-1j}\tilde{\boldsymbol{k}}^j_q+\boldsymbol{I})}{\Delta s^j}\\&-\boldsymbol{T}^n_{fl}(\boldsymbol{R}^{P^jP^n}_l\widetilde{+\boldsymbol{U}^n_l}-\boldsymbol{T}^{nj}_l\boldsymbol{U}^j_l)\boldsymbol{T}^{nj}_l\boldsymbol{T}^j_{lq}\boldsymbol{K}^j_{11}\frac{(\Delta s^{n-1j}\tilde{\boldsymbol{k}}^j_q+\boldsymbol{I})}{\Delta s^j}\\&-\boldsymbol{T}^n_{fl}\boldsymbol{T}^{nj+1}_l\boldsymbol{T}^{j+1}_{lq}\boldsymbol{K}^{j+1}_{21}\frac{(\Delta s^{j+1n+1}\tilde{\boldsymbol{k}}^{j+1}_q-\boldsymbol{I})}{\Delta s^{j+1}}\\&+\boldsymbol{T}^n_{fl}\boldsymbol{T}^n_{lq}\tilde{\boldsymbol{e}}^n\boldsymbol{T}^n_{ql}\boldsymbol{T}^{nj+1}_l\boldsymbol{T}^{j+1}_{lq}\boldsymbol{K}^{j+1}_{11}\frac{(\Delta s^{j+1n+1}\tilde{\boldsymbol{k}}^{j+1}_q-\boldsymbol{I})}{\Delta s^{j+1}}\\&-\boldsymbol{T}^n_{fl}(\boldsymbol{R}^{P^n\widetilde{P^{j+1}}}_l-\boldsymbol{U}^n_l)\boldsymbol{T}^{nj+1}_l\boldsymbol{T}^{j+1}_{lq}\boldsymbol{K}^{j+1}_{11}\frac{(\Delta s^{j+1n+1}\tilde{\boldsymbol{k}}^{j+1}_q-\boldsymbol{I})}{\Delta s^{j+1}}\\&-\boldsymbol{T}^n_{fl}(\widetilde{\boldsymbol{T}^{nj+1}_l\boldsymbol{U}^{j+1}_l})\boldsymbol{T}^{nj+1}_l\boldsymbol{T}^{j+1}_{lq}\boldsymbol{K}^{j+1}_{11}\frac{(\Delta s^{j+1n+1}\tilde{\boldsymbol{k}}^{j+1}_q-\boldsymbol{I})}{\Delta s^{j+1}}\end{aligned}\tag{A.9}$$

$$
\begin{aligned}
\boldsymbol{K}_{ela,24}^{n} = & \boldsymbol{T}_{fl}^{n}\boldsymbol{T}_{l}^{nj}\boldsymbol{T}_{lq}^{j}[\boldsymbol{K}_{21}^{j}\frac{\Delta s^{n-1j}(\tilde{\boldsymbol{\gamma}}_{q}^{j}+\tilde{\boldsymbol{e}}_{1})}{\Delta s^{j}}+\boldsymbol{K}_{22}^{j}\frac{(\Delta s^{n-1j}\tilde{\boldsymbol{k}}_{q}^{j}+\boldsymbol{I})}{\Delta s^{j}}] \\
& -\boldsymbol{T}_{fl}^{n}\boldsymbol{T}_{lq}^{n}\tilde{\boldsymbol{e}}^{n}\boldsymbol{T}_{ql}^{n}\boldsymbol{T}_{l}^{nj}\boldsymbol{T}_{lq}^{j}\boldsymbol{K}_{11}^{j}\frac{\Delta s^{n-1j}(\tilde{\boldsymbol{\gamma}}_{q}^{j}+\tilde{\boldsymbol{e}}_{1})}{\Delta s^{j}} \\
& -\boldsymbol{T}_{fl}^{n}\boldsymbol{T}_{lq}^{n}\tilde{\boldsymbol{e}}^{n}\boldsymbol{T}_{ql}^{n}\boldsymbol{T}_{l}^{nj}\boldsymbol{T}_{lq}^{j}\boldsymbol{K}_{12}^{j}\frac{(\Delta s^{n-1j}\tilde{\boldsymbol{k}}_{q}^{j}+\boldsymbol{I})}{\Delta s^{j}} \\
& -\boldsymbol{T}_{fl}^{n}(\widetilde{\boldsymbol{R}_{l}^{P^{j}P^{n}}+\boldsymbol{U}_{l}^{n}}-\boldsymbol{T}_{l}^{nj}\boldsymbol{U}_{l}^{j})\boldsymbol{T}_{l}^{nj}\boldsymbol{T}_{lq}^{j}\boldsymbol{K}_{11}^{j}\frac{\Delta s^{n-1j}(\tilde{\boldsymbol{\gamma}}_{q}^{j}+\tilde{\boldsymbol{e}}_{1})}{\Delta s^{j}} \\
& -\boldsymbol{T}_{fl}^{n}(\widetilde{\boldsymbol{R}_{l}^{P^{j}P^{n}}+\boldsymbol{U}_{l}^{n}}-\boldsymbol{T}_{l}^{nj}\boldsymbol{U}_{l}^{j})\boldsymbol{T}_{l}^{nj}\boldsymbol{T}_{lq}^{j}\boldsymbol{K}_{12}^{j}\frac{(\Delta s^{n-1j}\tilde{\boldsymbol{k}}_{q}^{j}+\boldsymbol{I})}{\Delta s^{j}} \\
& -\boldsymbol{T}_{fl}^{n}\boldsymbol{T}_{l}^{nj+1}\boldsymbol{T}_{lq}^{j+1}\boldsymbol{K}_{21}^{j+1}\frac{\Delta s^{j+1n+1}(\tilde{\boldsymbol{\gamma}}_{q}^{j+1}+\tilde{\boldsymbol{e}}_{1})}{\Delta s^{j+1}} \\
& -\boldsymbol{T}_{fl}^{n}\boldsymbol{T}_{l}^{nj+1}\boldsymbol{T}_{lq}^{j+1}\boldsymbol{K}_{22}^{j+1}\frac{(\Delta s^{j+1n+1}\tilde{\boldsymbol{k}}_{q}^{j+1}-\boldsymbol{I})}{\Delta s^{j+1}} \\
& +\boldsymbol{T}_{fl}^{n}\boldsymbol{T}_{lq}^{n}\tilde{\boldsymbol{e}}^{n}\boldsymbol{T}_{ql}^{n}\boldsymbol{T}_{l}^{nj+1}\boldsymbol{T}_{lq}^{j+1}\boldsymbol{K}_{11}^{j+1}\frac{\Delta s^{j+1n+1}(\tilde{\boldsymbol{\gamma}}_{q}^{j+1}+\tilde{\boldsymbol{e}}_{1})}{\Delta s^{j+1}} \\
& +\boldsymbol{T}_{fl}^{n}\boldsymbol{T}_{lq}^{n}\tilde{\boldsymbol{e}}^{n}\boldsymbol{T}_{ql}^{n}\boldsymbol{T}_{l}^{nj+1}\boldsymbol{T}_{lq}^{j+1}\boldsymbol{K}_{12}^{j+1}\frac{(\Delta s^{j+1n+1}\tilde{\boldsymbol{k}}_{q}^{j+1}-\boldsymbol{I})}{\Delta s^{j+1}} \\
& -\boldsymbol{T}_{fl}^{n}(\widetilde{\boldsymbol{R}_{l}^{P^{n}P^{j+1}}}-\boldsymbol{U}_{l}^{n})\boldsymbol{T}_{l}^{nj+1}\boldsymbol{T}_{lq}^{j+1}\boldsymbol{K}_{11}^{j+1}\frac{\Delta s^{j+1n+1}(\tilde{\boldsymbol{\gamma}}_{q}^{j+1}+\tilde{\boldsymbol{e}}_{1})}{\Delta s^{j+1}} \\
& -\boldsymbol{T}_{fl}^{n}(\widetilde{\boldsymbol{R}_{l}^{P^{n}P^{j+1}}}-\boldsymbol{U}_{l}^{n})\boldsymbol{T}_{l}^{nj+1}\boldsymbol{T}_{lq}^{j+1}\boldsymbol{K}_{12}^{j+1}\frac{(\Delta s^{j+1n+1}\tilde{\boldsymbol{k}}_{q}^{j+1}-\boldsymbol{I})}{\Delta s^{j+1}} \\
& -\boldsymbol{T}_{fl}^{n}(\widetilde{\boldsymbol{T}_{l}^{nj+1}\boldsymbol{U}_{l}^{j+1}})\boldsymbol{T}_{l}^{nj+1}\boldsymbol{T}_{lq}^{j+1}\boldsymbol{K}_{11}^{j+1}\frac{\Delta s^{j+1n+1}(\tilde{\boldsymbol{\gamma}}_{q}^{j+1}+\tilde{\boldsymbol{e}}_{1})}{\Delta s^{j+1}} \\
& -\boldsymbol{T}_{fl}^{n}(\widetilde{\boldsymbol{T}_{l}^{nj+1}\boldsymbol{U}_{l}^{j+1}})\boldsymbol{T}_{l}^{nj+1}\boldsymbol{T}_{lq}^{j+1}\boldsymbol{K}_{12}^{j+1}\frac{(\Delta s^{j+1n+1}\tilde{\boldsymbol{k}}_{q}^{j+1}-\boldsymbol{I})}{\Delta s^{j+1}}
\end{aligned}
\tag{A.10}
$$

$$
\begin{aligned}
\boldsymbol{K}_{ela,25}^{n} = & -\boldsymbol{T}_{fl}^{n}\boldsymbol{T}_{l}^{nj+1}\boldsymbol{T}_{lq}^{j+1}\boldsymbol{K}_{21}^{j+1}\frac{(\Delta s^{nj+1}\tilde{\boldsymbol{k}}_{q}^{j+1}+\boldsymbol{I})}{\Delta s^{j+1}} \\
& +\boldsymbol{T}_{fl}^{n}\boldsymbol{T}_{lq}^{n}\tilde{\boldsymbol{e}}^{n}\boldsymbol{T}_{ql}^{n}\boldsymbol{T}_{l}^{nj+1}\boldsymbol{T}_{lq}^{j+1}\boldsymbol{K}_{11}^{j+1}\frac{(\Delta s^{nj+1}\tilde{\boldsymbol{k}}_{q}^{j+1}+\boldsymbol{I})}{\Delta s^{j+1}} \\
& -\boldsymbol{T}_{fl}^{n}(\widetilde{\boldsymbol{R}_{l}^{P^{n}P^{j+1}}}-\boldsymbol{U}_{l}^{n})\boldsymbol{T}_{l}^{nj+1}\boldsymbol{T}_{lq}^{j+1}\boldsymbol{K}_{11}^{j+1}\frac{(\Delta s^{nj+1}\tilde{\boldsymbol{k}}_{q}^{j+1}+\boldsymbol{I})}{\Delta s^{j+1}} \\
& -\boldsymbol{T}_{fl}^{n}(\widetilde{\boldsymbol{T}_{l}^{nj+1}\boldsymbol{U}_{l}^{j+1}})\boldsymbol{T}_{l}^{nj+1}\boldsymbol{T}_{lq}^{j+1}\boldsymbol{K}_{11}^{j+1}\frac{(\Delta s^{nj+1}\tilde{\boldsymbol{k}}_{q}^{j+1}+\boldsymbol{I})}{\Delta s^{j+1}}
\end{aligned}
\tag{A.11}
$$

$$
\begin{aligned}
\boldsymbol{K}^n_{ela,26} = &-\boldsymbol{T}^n_{fl}\boldsymbol{T}^{nj+1}_l\boldsymbol{T}^{j+1}_{lq}\boldsymbol{K}^{j+1}_{21}\frac{\Delta s^{nj+1}(\tilde{\boldsymbol{\gamma}}^{j+1}_q+\tilde{\boldsymbol{e}}_1)}{\Delta s^{j+1}} \\
&-\boldsymbol{T}^n_{fl}\boldsymbol{T}^{nj+1}_l\boldsymbol{T}^{j+1}_{lq}\boldsymbol{K}^{j+1}_{22}\frac{(\Delta s^{nj+1}\tilde{\boldsymbol{k}}^{j+1}_q+\boldsymbol{I})}{\Delta s^{j+1}} \\
&+\boldsymbol{T}^n_{fl}\boldsymbol{T}^n_{lq}\tilde{\boldsymbol{e}}^n\boldsymbol{T}^n_{ql}\boldsymbol{T}^{nj+1}_l\boldsymbol{T}^{j+1}_{lq}\boldsymbol{K}^{j+1}_{11}\frac{\Delta s^{nj+1}(\tilde{\boldsymbol{\gamma}}^{j+1}_q+\tilde{\boldsymbol{e}}_1)}{\Delta s^{j+1}} \\
&+\boldsymbol{T}^n_{fl}\boldsymbol{T}^n_{lq}\tilde{\boldsymbol{e}}^n\boldsymbol{T}^n_{ql}\boldsymbol{T}^{nj+1}_l\boldsymbol{T}^{j+1}_{lq}\boldsymbol{K}^{j+1}_{12}\frac{(\Delta s^{nj+1}\tilde{\boldsymbol{k}}^{j+1}_q+\boldsymbol{I})}{\Delta s^{j+1}} \\
&-\boldsymbol{T}^n_{fl}(\boldsymbol{R}^{\widetilde{P^nP^{j+1}}}_l-\boldsymbol{U}^n_l)\boldsymbol{T}^{nj+1}_l\boldsymbol{T}^{j+1}_{lq}\boldsymbol{K}^{j+1}_{11}\frac{\Delta s^{nj+1}(\tilde{\boldsymbol{\gamma}}^{j+1}_q+\tilde{\boldsymbol{e}}_1)}{\Delta s^{j+1}} \\
&-\boldsymbol{T}^n_{fl}(\boldsymbol{R}^{\widetilde{P^nP^{j+1}}}_l-\boldsymbol{U}^n_l)\boldsymbol{T}^{nj+1}_l\boldsymbol{T}^{j+1}_{lq}\boldsymbol{K}^{j+1}_{12}\frac{(\Delta s^{nj+1}\tilde{\boldsymbol{k}}^{j+1}_q+\boldsymbol{I})}{\Delta s^{j+1}} \\
&-\boldsymbol{T}^n_{fl}(\widetilde{\boldsymbol{T}^{nj+1}_l\boldsymbol{U}^{j+1}_l})\boldsymbol{T}^{nj+1}_l\boldsymbol{T}^{j+1}_{lq}\boldsymbol{K}^{j+1}_{11}\frac{\Delta s^{nj+1}(\tilde{\boldsymbol{\gamma}}^{j+1}_q+\tilde{\boldsymbol{e}}_1)}{\Delta s^{j+1}} \\
&-\boldsymbol{T}^n_{fl}(\widetilde{\boldsymbol{T}^{nj+1}_l\boldsymbol{U}^{j+1}_l})\boldsymbol{T}^{nj+1}_l\boldsymbol{T}^{j+1}_{lq}\boldsymbol{K}^{j+1}_{12}\frac{(\Delta s^{nj+1}\tilde{\boldsymbol{k}}^{j+1}_q+\boldsymbol{I})}{\Delta s^{j+1}}
\end{aligned}
\tag{A.12}
$$